

University of Nottingham
UK | CHINA | MALAYSIA

Three Dimensional Printed Immunomodulatory Scaffolds with Controlled Drug Release for Bone Regeneration

Submitted by

Majed Abdullah Majrashi

Thesis submitted to the University of Nottingham for the degree of Doctor of Philosophy

July 2023

Abstract

Large bone defects pose significant challenges in orthopaedic surgery, necessitating the exploration of innovative repair technologies beyond traditional treatments like autografts, allografts, and synthetic substitutes, each fraught with specific challenges. Tissue engineering and regenerative medicine have emerged as promising fields, employing bioactive materials, growth factors, and cellular components to emulate natural bone properties and functions. Notably, additive manufacturing techniques contribute to these advancements by customising 3D-printed scaffolds enhancing patient-specific treatments.

Recent studies underscore the significant influence of immune responses in bone regeneration, an area still in its infancy. Particularly, the modulation of immune reactions through specialised biomaterials and the strategic delivery of anti-inflammatory agents like dexamethasone present a novel approach to support bone healing processes, avoiding the systemic side effects of traditional drug administration.

In this thesis, novel inks were developed to sustain the release of dexamethasone from a 3D-printed scaffold to modulate the immune response and osteogenesis. Excipients with surfactant properties, including the poloxamers F127, F68, L31, sorbitan monooleate Span80, and sucrose acetate isobutyrate (SAIB), were added to PCL to test their ability to sustain drug release. All these inks were fabricated into scaffolds by using direct ink writing 3D printing technique. The fabricated

scaffolds were then characterised by SEM, DSC, FTIR, and ToF-SIMS. Macrophages and mesenchymal stem cells (MSCs) were cocultured to investigate the effects of the controlled release of dexamethasone on the modulation of macrophage polarisation and osteogenic differentiation of MSCs.

Notably, blending PCL with 40% wt/wt (SAIB) has improved dexamethasone-cyclodextrin dispersal and facilitated a sustained 35-day release dominated by first-ordered and Higuchi models. In this modified environment, investigations into macrophage-mesenchymal stem cell (MSC) interactions revealed that controlled dexamethasone release significantly influenced macrophage behaviour and MSC osteogenic differentiation. M1 macrophages boosted early alkaline phosphatase production (ALP) at (7 days), while later stages (21 days) saw dexamethasone's predominance. Bone morphogenic protein-2 (BMP-2) was significantly increased at day 21; meanwhile, interleukin-6 (IL-6) decreased at the same time. Moreover, the released dexamethasone switched the phenotype of macrophages from M1 to M2 at day 21, evidenced by the increased level of mannose receptor and decreased expression of calprotectin receptor. These results offer new insight into macrophage-MSC cross-talk and demonstrate the potential of drug-release scaffolds to modulate inflammation and enhance bone regeneration.

Declaration

I hereby declare that this thesis is original as it was conducted and written by myself during my PhD studies at the School of Pharmacy, University of Nottingham, and its contents are the result of my own work conducted at the University of Nottingham between February 2019 and July 2023 under the supervision of Dr Jing Yang and Professor Amir Ghaemmaghami. No part of my work has been submitted for another degree at Nottingham University or any other institution. When I quote from the work of others, I always provide the source. Assistance from others is acknowledged as appropriate.

Publications and conference proceedings

Manuscript in preparation

- Sustained release of dexamethasone from 3D printed scaffolds modulates macrophage activation and enhances osteogenic differentiation.

  Majed Majrashi, Anna Kotowska, David Scurr, Amir Ghaemmaghami, Jing Yang

Conferences Proceeding

- Poster presentation at the 3rd Postgraduate Allied Health Research Conference (AHPGR) 2021, University of Nottingham, UK
- Poster presentation Tissue Engineering and Regenerative Medicine International Society (TERMIS) European Chapter Conference 2022 in Krakow, Poland

Acknowledgement

The presented work would not have been possible without the assistance, encouragement, and direction of numerous individuals and institutions. In light of this, I would like to thank my supervisors, Dr Jing Yang and Professor Amir Ghaemmaghami. Throughout the duration of my doctoral studies, their invaluable supervision, guidance, suggestions, and forbearance were indispensable to my development as an independent research scientist. I would like to thank the Biodiscovery Institute for providing me with a platform and the chance to pursue doctoral studies. Thank you to the members of my thesis committee for your contributions to the success of my research.

To former and current members of the regenerative medicine and cellular thereby, immunology and immuno-bioengineering, and the Laboratory of Biophysics and Surface Analysis. I'd like to thank and recognise the postdocs Dr Matthew Vasey, Dr Constantine Tanase, Dr Leanne Fisher, Dr Arsalan Latif, and Dr Lisa Kammerling for discussing scientific challenges, providing new perspectives on research approaches, and offering infinite feedback on experimental design. Together with the other members of the group, they fostered an atmosphere conducive to scientific discourse and innovative thought.

I would like to express my gratitude to Dr Anna Kotwoska, a Research Fellow at the Faculty of Science. I would also like to acknowledge the laboratory technicians, Mrs Teresa Marshal, Mrs Ann Williams, Mr Paul Cooling, Mr Thomas Booth, and Miss. Esme Ireson, for their advice, training, and assistance throughout the lab work.

I would also like to express my gratitude to my family members, particularly my father and mother, who have supported and cared for me throughout my studies. My wife, son, and daughter are always by my side and offer me encouragement, particularly during my studies in the United Kingdom. I also appreciate my siblings for their encouragement and support. Not forgetting all my friends Dr Awaji Safhi, Dr Walid Rizq, Abdullah Aljasser, Saqer Alarifi, and Ahmad Albuloshi for their unwavering support and encouragement throughout my PhD study and inspiration during both challenging and joyful moments of this journey.

Finally, I would like to express my gratitude to King Abdulaziz City for Science and Technology (KACST) for providing me with the opportunity to pursue my higher education in the UK. I would also like to thank the Saudi Arabia Cultural Bureau in London for their unlimited support.

TABLE OF CONTENTS

Abstract i

Declaration iii

Publications and conference proceedings iv

Acknowledgement v

List of figures xiii

List of tables xx

List of abbreviations xxi

1. Chapter one: Literatures review 1

1.1. Introduction 1

1.2. Bone Physiology and Biology 3

1.2.1. Structures of the Bone 3

1.2.2. Bone cells 6

1.3. Bone self-regeneration 14

1.4. Bone formation and the immune system 20

1.4.1. Macrophage and bone formation 24

1.5. Bone regeneration via tissue engineering 28

1.5.1. Bone tissue engineering 28

1.5.2. Scaffolds 31

1.6. Biomaterial selection for 3D scaffolds 34

1.7. Scaffolds fabrication 37

1.7.1. Conventional methods 37
1.7.2. 3D printing techniques 43
1.8. Immunological response of biomaterials 50
1.9. Scaffold-based techniques for regulating the bone-regeneration immune microenvironment 55
1.9.1. Physical and chemical properties 57
1.9.2. Immunomodulatory drugs released from scaffolds 62
1.10. Aims and objectives of the thesis 68
2. Chapter two: General Material and methods 70
2.1 Extrusion-based 3D printing 70
2.2 Scanning Electron microscope (SEM) 70
2.3 Differential scanning calorimetry (DSC) 72
2.4 Attenuated Total Reflectance-Fourier Transformed Infrared Spectroscopy (ATR-FTIR) 73
2.5 Time of Flight Secondary Ion Mass Spectroscopy (ToF-SIMS) 74
2.6 Mesenchymal stem cells (MSCs) culturing 76
2.7 Immunofluorescence assay 77
2.7.1 Immunocytochemistry 78
2.7.2 Fluorescence microscopy 79
2.7.3 Enzyme-linked immunosorbent assay (ELISA) 81
2.8 Polymerase Chain Reaction (PCR) 83

3. Chapter Three: Developing 3D printed scaffolds for the controlled release of dexamethasone 86

3.1 Introduction 86

3.2 Materials and Methods 91

3.2.1 Chemicals 91

3.2.2 Ink preparation and 3D printing of scaffolds loaded with DEX-CYD 91

3.2.3 Dexamethasone Microcrystals preparation 92

3.2.4 Dexamethasone Microcrystal Characterisation. 92

3.2.5 Surface characterisation of 3D printed scaffolds 93

3.2.6 SEM Images analysis 93

3.2.7 Differential Scanning Calorimetry 94

3.2.8 Attenuated Total Reflectance- Fourier Transform Infra-Red Spectroscopy (ATR-FTIR) 94

3.2.9 Time of Flight Secondary Ion Mass Spectroscopy (ToF-SIMS) 95

3.2.10 *In vitro* release of dexamethasone 96

3.2.11 Drug release kinetics 97

3.3 Results 98

3.3.1 Ink preparation and 3D printed scaffold characterisation 98

3.3.2 Fabrication of 3D printed PCL scaffolds with high drug loading using dexamethasone microcrystal (DEX-MC) 109

3.3.3 Ink preparation and 3D printing of PCL/DEX-MC 112

3.3.4 Characterisation of 3D printed PCL/ DEX-MC scaffolds 114

3.3.5 Thermal Characterisation 117

3.3.6 Chemical Characterisation by FTIR 120

3.3.7 *In vitro* release of dexamethasone from 3D printed scaffolds 125

3.3.8 Drug release Kinetics 140

3.3.9 Distribution of drugs in 3D printed scaffolds 149

3.4 Discussion 153

3.5 Summary 168

4. Chapter Four: Control release of dexamethasone from 3D printed scaffolds promotes M2-like macrophage and enhances osteogenic differentiation of MSCs 169

4.1 Introduction 169

4.2 Materials and Methods 173

4.2.1 Materials 173

4.2.2 Ink preparation and 3D printing of scaffolds 174

4.2.3 Thermogravimetric (TGA) analysis 174

4.2.4 THP1 culturing and Polarisation to macrophage 174

4.2.5 Immunomodulation dexamethasone does on the polarisation of M1 macrophages. 175
4.2.6 Polarisation of M1 macrophage by released dexamethasone. 175
4.2.7 Bioactivity of released dexamethasone from PCL/SAIB/DEX-CYD 176
4.2.8 MSCs expansion and osteogenic differentiation 177
4.2.9 Macrophages polarisation and co-culture with MSCs. 178
4.2.10 Cytotoxicity 179
4.2.11 Cell proliferation 179
4.2.12 Alkaline phosphatase (ALP) activity 180
4.2.13 Alizarin red staining (ARS) 180
4.2.14 RUNX2 gene expression 180
4.2.15 Cytokines release analysis 181
4.2.16 Immunofluorescent staining of macrophages 182
4.2.17 Fluorescent intensity measurement 182
4.2.18 Statistical Analysis 182
4.3 Results 183
4.3.1 Thermogravimetric (TGA) analysis 183
4.3.2 Polarisation of macrophages in RPMI single media, and co-culture mix media 185
4.3.3 Cytotoxicity of controlled release scaffolds 188

4.3.4 Immunomodulation of macrophages by controlled release of dexamethasone 192

4.3.5 Osteogenic differentiation and macrophage polarisation in co-cultures 199

4.4 Discussion 206

4.5 Summary 211

5. Chapter Five: Conclusion and future works 213

5.1 Conclusion 213

5.2 Future work 218

6. Chapter Six: References 221

7. Chapter Seven: Appendices 262

List of figures

Figure 1-1: The hierarchical structure of bone 4

Figure 1-2: Image of a bone regeneration region 7

Figure 1-3: Optical micrographs of rat alveolar bone fragments 9

Figure 1-4: Scanning electron micrograph of osteocytes..... 11

Figure 1-5:Controlling osteoclast differentiation 13

Figure 1-6: Stages of bone fracture healing. 20

Figure 1-7: Involvement of immune cells in fracture repair 24

Figure 1-8: Soluble factors that polarize macrophages to M1 and M2 phenotypes. 26

Figure 1-9: Tissue engineering components 29

Figure 1-10: The basic elements of bone tissue engineering 31

Figure 1-11: Common methodologies employed in the fabrication of scaffolds. 43

Figure 1-12: Common 3D printing methods..... 46

Figure 1-13: Foreign-body reaction timeline.. 54

Figure 1-14: Various strategies to modulate macrophages include 56

Figure 2-1: Schematic diagram of the SEM component. 71

Figure 2-2: Schematic diagram representation of the DSC. 73

Figure 2-3: An ATR-FTIR system is depicted in a schematic representation 74

Figure 2-4: Data acquisition by Time-of-Flight Secondary Ion Mass Spectrometry (ToF-SIMS) 76

Figure 2-5: Direct and indirect immunofluorescent procedures. 79

Figure 2-6: Schematic diagram visually represents the epifluorescence microscope..... 81
Figure 2-7: Various enzyme-linked immunosorbent assay (ELISA) techniques encompass direct, indirect, and sandwich assays. .. 82
Figure 2-8 Depiction of the steps involved in reverse transcription-quantitative polymerase chain reaction (RT qPCR). 85
Figure 3-1: Schematic diagram showing PCL ink preparation, 3D printing. 99
Figure 3-2: Images of different concentrations of dexamethasone-cyclodextrin dissolved with PCL in DCM. 100
Figure 3-3: 3D printed lattice PCL scaffold composed of 0.1% wt/wt of dexamethasone, showing the top view (A) and side view (B). . 101
Figure 3-4: Nozzle clogged during printing with PCL ink. 102
Figure 3-5: SEM micrographs for 3D printed PCL/DEX-CYD scaffolds. 106
Figure 3-6: Strut diameter measurements and pore sizes..... 108
Figure 3-7: Schematic diagram of microcrystal preparation. 110
Figure 3-8: SEM micrographs of dexamethasone microcrystals 112
Figure 3-9: Solubility of DEX-CYD and DEX-MC in dichloromethane (DCM). 113
Figure 3-10: Effect of PCL on DEX-MC solubility. 114
Figure 3-11: SEM micrographs for 3D printed PCL/DEXMC scaffolds. 115
Figure 3-12: Strut diameters and pore sizes..... 116
Figure 3-13: DSC thermograph for 3D printed PCL scaffolds..... 119

Figure 3-14: FTIR graphs representing absorbance of 3D printed scaffolds containing 0.17% wt/wt DEX-CYD. (A) PCL/DEX-CYD. (B) PCL/F127/DEX-CYD. (C) PCL/F68/DEX-CYD. (D) PCL/L31/DEX-CYD. (E) PCL/SAIB/DEX-CYD. (F) PCL/Span80/DEX-CYD. (G) PCL/DEX-MC, and PCL/SAIB/DEX-MC. 125

Figure 3-15: Cumulative release percentage of 3D printed PCL scaffolds loaded with 0.05%, 0.1%, and 0.17% wt/wt of dexamethasone-cyclodextrin. 127

Figure 3-16: Cumulative release percentage of 3D printed scaffolds of PCL, PCL/F127 (70:30), and PCL/F127 (60:40) loaded with 0.17% wt/wt of DEX-CYD. 129

Figure 3-17: Cumulative release percentage of 3D printed scaffolds of PCL/F68 (70:30) and PCL/F68 (60:40) loaded with 0.17% wt/wt of DEX-CYD. 130

Figure 3-18: Cumulative release percentage of 3D printed scaffolds of PCL, PCL/L31 (70:30), and PCL/L31 (60:40) loaded with 0.17% wt/wt of DEX-CYD. 132

Figure 3-19: Cumulative release percentage of 3D printed scaffolds of PCL, PCL/Span80 (70:30), and PCL/Span80 (60:40) loaded with 0.17% wt/wt of DEX-CYD. 134

Figure 3-20: Cumulative release percentage of 3D printed scaffolds of PCL/SAIB (70:30)/DEX-CYD and PCL/SAIB (60:40)/DEX-CYD. 136

Figure 3-21: Cumulative release percentage of 3D printed scaffolds of PCL/DEX-MC (0.17% wt/wt), PCL/DEX-MC (0.7% wt/wt) and PCL/SAIB (60:40)/DEX-MC (0.7% wt/wt). 139

Figure 3-22: Dexamethasone release kinetics of 3D printed PCL scaffolds loaded with 0.05% wt/wt, 0.1% wt/wt, and 0.17% wt/wt 142

Figure 3-23: Dexamethasone release kinetics of 3D printed PCL scaffolds loaded with 0.17% wt/wt of dexamethasone cyclodextrin. PCL/F127 (70:30) and PCL/F127 (60:40). 143

Figure 3-24: Dexamethasone release kinetics of 3D printed PCL scaffolds loaded with 0.17% wt/wt of dexamethasone cyclodextrin. PCL/F68 (70:30) and PCL/F68 (60:40) 144

Figure 3-25: Dexamethasone release kinetics of 3D printed PCL scaffolds loaded with 0.17% wt/wt of dexamethasone cyclodextrin. PCL/L31 (70:30) and PCL/L31 (60:40) 145

Figure 3-26: Dexamethasone release kinetics of 3D printed PCL scaffolds loaded with 0.17% wt/wt of dexamethasone cyclodextrin. PCL/Span80 (70:30)and PCL/Span80 (60:40)..... 146

Figure 3-27: Dexamethasone release kinetics of 3D printed PCL scaffolds loaded with 0.17% wt/wt of dexamethasone cyclodextrin. PCL/SAIB (70:30) and PCL/SAIB (60:40) 147

Figure 3-28: Dexamethasone release kinetics of 3D printed PCL scaffolds loaded with various concentrations of dexamethasone microcrystal (DEX-MC) 0.17% wt/wt , 0.7% wt/wt, and PCL/SAIB (60:40) loaded with 0.7% wt/wt DEX-MC..... 148

Figure 3-29: Dexamethasone distribution within polymer struts was analysed by using ToF SIMS. 151

Figure 3-30: Depth profiles of dexamethasone molecular ion $C22H27FO5^-$ (orange) and fragment $C21H26FO4^-$ (blue), F^- (grey), PCL marker $C6H9O2^-$ (yellow), and SAIB marker $C34H53O17^-$ (green) in A) PCL + dexamethasone 0.17% wt/wt B) PCL+dexamethasone 0.17% wt/wt + SAIB, and C) PCL + SAIB scaffolds. 152

Figure 4-1: Thermogravimetric analysis (TGA) spectra of 3D printed scaffolds 184

Figure 4-2: The polarisation of M0, M1 and M2 macrophages derived from THP-1 monocytes and M0, M1, and M2 cytokine expression. in RPMI single-media 186

Figure 4-3: The polarisation of M0, M1 and M2 macrophages derived from THP-1 monocytes and M0, M1, and M2 cytokine expression. A) Immunostaining of macrophages polarised at days 3 and 7 in a mixed-media (RPMI:α-MEM) 187

Figure 4-4: THP-1 Cell viability was determined by ToxiLight™ cytotoxicity assay, and Cell proliferation was determined by Quanti-iTTM Picogreen® 189

Figure 4-5: Viability and proliferation of MSCs in α-MEM and co-culture media with or without drug-loaded scaffolds PCL/SAIB (60:40)/DEX-CYD (0.17% wt/wt).. 191

Figure 4-6: Effect of dexamethasone concentration on macrophage polarisation and viability. 193

Figure 4-7: Quantification of pro-inflammatory TNF-α and IL-6, and anti-inflammatory cytokines IL-10 and TGF-β1 cytokines in macrophage culture 195
Figure 4-8: UV–vis absorbance of dexamethasone as received and released from 3D printed PCL/SAIB (60:40)/DEX-CYD scaffold at different time points after 15, 25, and 35 days, respectively in basal RPMI media. 197
Figure 4-9: Bioactivity of the released dexamethasone from PCL/SAIB (60:40)/DEX-CYD.. 198
Figure 4-10: (A) ALP activity, (B) Alizarin red staining, (C) Quantification of Alizarin red staining.(D) Gene expression of RUNX2. (E) BMP-2 level in co-cultures. 202
Figure 4-11: Macrophage activation status in co-cultures. 205
Figure 7-1: Routins of image analysis by imageJ. 262
Figure 7-2: Dexamethasone-cyclodextrin standard curve 263
Figure 7-3: DSC thermograph. (A) DEX-CYD, (B) PCL with 0.05%, 0.1%, and 0.25% wt/wt DEX-CYD..... 264
Figure 7-4: Cumulative and actual release of dexamethasone from 2D PCL films incubated in 10 ml of PBS. (A) Cumulative release percentage of 2D PCL films loaded with 0.2%, 0.7%, and 1% wt/wt of dexamethasone-cyclodextrin. 266
Figure 7-5: Dexamethasone release kinetics of 2D PCL films..... 267
Figure 7-6: 3D printed scaffold mass loss after 35 days..... 268
Figure 7-7: Dexamethasone release kinetics of 3D printed PCL scaffolds loaded with 0.17% wt/wt of dexamethasone. PCL/SAIB (70:30)

(blue), and PCL/SAIB (60:40) (red), fitted the zero-order model at 24h. 269
Figure 7-8: Image analysis by imageJ. (A) Schematic analysis of cell count. (B) Schematic procedure of measuring mean fluorescent intensity. 272
Figure 7-9: The representative stress-strain curves. 273

List of tables

Table 1-1: Conventional methods for 3D scaffold fabrication 40

Table 1-2: AM techniques being used in bone tissue engineering. 47

Table 3-1: Dexamethasone microcrystal preparation method 111

Table 3-2: Thermal properties of 3D printed scaffolds..... 120

Table 3-3: R^2 drug release kinetics values 148

Table 4-1: Primers used to study osteogenesis..... 181

Table 7-1: Drug lodging in all 3D-prented..... 263

Table 7-2: Thermal properties of PCL loaded with DEX-CYD. 265

Table 7-3: R^2 drug release kinetics values for all 2D PCL films..... 267

Table 7-4: Media composition for αMEM and RPMI 269

Table 7-5: The correspondent concentration of dexamethasone measured by UV-vis..... 271

Abbreviations

AK	Adenylate kinase
ALP	Alkaline phosphatase
AM	Additive manufacturing
ANOVA	Analysis of variance
ATR-	Attenuated Total Reflectance-Fourier Transformed
FTIR	Infrared Spectroscopy
BMP	Bone morphogenetic protein
CAD	Computer-aided design
cDNA	Complementary DNA
CT	Computed tomography
DAMPS	Damage-associated molecular patterns
DAPI	4,6-diamidino-2-phenylindole
DCM	Dichloromethane
DIW	Direct-ink writing
dH_2O	Distilled water
DMEM	Dulbecco’s modified Eagle’s medium
DNA	Deoxyribonucleic acid
DSC	Differential scanning calorimeter
ECM	Extracellular matrix
EDTA	Ethylenediaminetetraacetic acid
ELISA	Enzyme-linked immunosorbent
FBR	Foreign body response
FBS	Fetal bovine serum
FDA	Food and Drug Administration

FDM	Fused deposition modelling
FGF	Fibroblastic growth factor
GAPDH	Glyceraldehyde-3-phosphate dehydrogenase
HA	Hydroxyapatite
HRP	Horse radish peroxidase
IFN-γ	Interferon-gamma
IL-1β	Interleukin-1 beta
IR	Infrared
MEM	Minimum Essential Medium Eagles
MRI	magnetic resonance imaging
MSCs	Mesynchymal Stem Cells
nH	nano-hydroxyapatite
OPG	Osteoprotegerin
OPN	Osteopontin
OSM	Oncostatin M
PAMP	Pathogen-associated molecular patterns
PBS	Phosphate buffer saline
PCL	Poly(Ɛ-caprolactone)
PCR	Polymerase chain reaction
PDLLA	Poly(D,L-lactic acid) or poly(D,L-lactide)
PDMS	Polydimethylsiloxane
PEG	Poly(ethylene glycol)
PEO	Poly-ethylene oxide
PHBV	Poly(3-hydroxybutyrate-co-3-hydroxyvalerate)
PLGA	Poly(lactic-co-glycolic acid)

PLLA	poly(L-lactic acid) or poly(L-lactide)
PPO	Poly-propylene oxide
PTFE	Polytetrafluoroethylene
PVA	Poly(vinyl alcohol)
RANKL	Receptor activator of nuclear factor-kappa-B ligand
Runx2	Runt-related transcription factor 2
SD	Standard diviation
SEM	Scanning electron microscope
SF	Spinal fusion
SLA	Stereolithography
SLS	Selective laser sintering
TCP	Tricalcium Phosphate
T_g	Glass transition temperature
TGA	Thermogarovometric analysis
TGF-β1	Transforming growth factor beta 1
Th2	T helper cells type 2
TNF-α	Tumor necrosis factor-alpha
UV	Ultraviolet
VEGF	Vascular endothelial growth factor
V/V	Volume by volume
W/V	Weight by volume

1. Chapter one: Literatures review

1.1. Introduction

The skeletal system plays a crucial role in safeguarding internal organs and supporting the body's weight during daily activities [1]. However, bone defects that result from injury, trauma, diseases, or tumours can result in disability and a decline in quality of life overall. Bones are characterised by their self-healing capacity [2]; substantial bone defects, known as "non-union fractures," present a considerable clinical challenge, as their regenerative capacity becomes impaired when the defect (gap) exceeds a critical size, typically 3 cm or more in humans. In spite of surgical interventions, delayed healing, or "non-union," occurs in 5–10% of bone fractures, with a rate approaching 100% for segmental bone defects [3].

The current treatment for large bone defects consists of autologous and allogeneic bone graft transplantations [3]. However, it has been elucidated that there are significant deficiencies, limitations, and side effects of existing clinical interventions for bone repair and regeneration [4]. Autografts are regarded as the standard for bone grafts due to their histocompatibility, non-immunogenic character, and possession of the fundamental features required for good bone graft materials. In particular, autografts contain essential components that promote osteoinduction, e.g., bone morphogenetic proteins (BMP2, BMP7) and osteoprogenitor cells. However, autografts require bone harvesting from the patient's iliac crest, which can result in significant donor site injury, morbidity, deformity, scarring, and numerous surgical risks, including

haemorrhage, inflammation, infection, and chronic pain. In addition, autografts may not be an option when the defect site requires larger bone volumes than are available or feasible [5, 6].

Allografts, the second most prevalent method for bone grafting, involve the transplantation of bone tissue from deceased donors. Allogeneic bone grafts are also likely to be histocompatible, and they come in different forms depending on what the recipient site needs. These forms include demineralised bone matrix, cancellous fragments, cortical grafts, osteochondral segments, and whole-bone segments. However, immunoreactions and infection transmission are more likely to occur with allografts than with autografts. Furthermore, due to irradiation or freeze-drying, their osteoinductive properties are diminished, and they lack biological components. Allografts have fewer drawbacks than autografts, but they still present significant financial obstacles. In addition, allograft bone graft material is in limited supply, resulting in an imbalance between supply and demand in the bone grafting industry [5].

Bone tissue engineering (BTE) is focused on exploring alternative therapeutic strategies to overcome the inherent challenges of current clinical interventions. The conventional approach to BTE typically involves three main components: (1) employing a biocompatible scaffold that mimics the characteristics of the extracellular matrix in bone, (2) utilizing osteogenic cells responsible for depositing bone tissue matrix, and (3) incorporating morphogenic signals to guide cell differentiation towards the desired phenotype [5, 7, 8].

However, despite significant progress in the field, several significant obstacles need to be addressed before implementing BTE in clinical practice. One crucial area of research that has gained attention in recent years is the study of interactions between osteogenic cells, immune cells, and the inflammatory response generated by the implanted scaffolds. The role of immune cells in bone repair and homeostasis is now widely recognized [9]. The immune response to bone biomaterials can have both beneficial and detrimental effects on osteogenesis control. A favourable immune response can create an environment conducive to osteogenesis, while an improper immune response may lead to chronic inflammation and the formation of a fibrous capsule around the implant.

1.2. Bone Physiology and Biology

Bone is a highly active organ that is constantly remodelled. Matrix resorption and deposition occur simultaneously in an intricate and well-balanced cycle. It is necessary to understand bone biology and development to develop procedures for bone regeneration and comprehend bone illness.

1.2.1. Structures of the Bone

Bones are composed of two forms of tissues: cortical (compact) and cancellous (trabecular or spongy) bones (**Figure 1-1)**. Cortical bone forms the outer part of the bone and is considered the hardest, with thickness ranging from a tenth of a millimetre to several millimetres and a porosity of about 6%. Cortical bones comprise nearly 80% of the skeleton’s total bone mass and have a mechanical function and a high mineral content. Cancellous bone forms the internal part of the bone and

has a porosity of about 80%. It has a delicate lattice structure packed with bone marrow, blood vessels, and fat [10]. The interactions between osteocytes, osteoblasts, and osteoclasts control the bone resorption and remodelling processes [11].

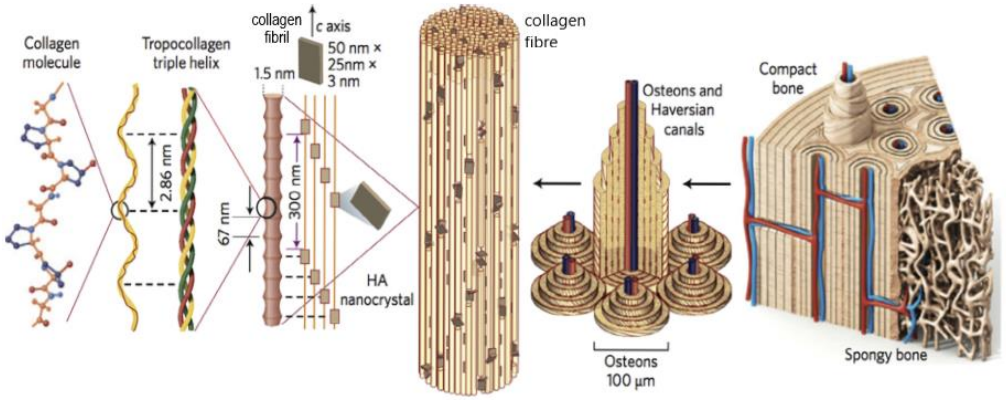


Figure 1-1: The hierarchical structure of bone shows the cortical and spongy bone, osteons, and collagen fibre from right to left. Adapted from [12].

On the other hand, the lamella is an arrangement of mineralized collagen fibres with a width of 3-7 µm [13]. In compact bone, lamellae wrap around central canals, forming a concentric layer of about 3–8 lamellae. This arrangement is called the osteon or Haversian system (**Figure 1-1**). Osteons are cylindrical and packed in parallel to the long axis of the bone. In cancellous bone, mineralized collagen fibres form a lattice-like network called trabeculae (**Figure 1-1**). The trabeculae appear to be a random network [10].

Mineralized collagen fibre is the primary structural component of bones (**Figure 1-1**). Each fibril has a diameter of 100 nm and is made of

collagen molecules of roughly 300 nm in length and 1.5 nm in width. Type I collagen is the primary component of bone. Osteoblasts produce collagen, which undergoes self-assembly to form tropocollagen triple helixes, collagen fibrils, and collagen fibres. It appears that collagen fibrils are longitudinally compacted with a space between each fibril. Crystals of apatite form in the space between collagen fibrils. The growth of crystals is constrained by collagen fibrils, causing them to separate and cease. In addition, crystals appear regularly and sequentially alongside fibrils, with an estimated recurrence distance of 67 nm [14]. The nanoscale organisation of lamellae and collagen is believed to endow bone with isotropic properties, inhibit the propagation of cracks, and increase its toughness [15].

The formation of apatite within collagen fibrils is referred to as "biomineralization." The phases of bone development, bone fracture, and senescence influence bone mineralization. Bones undergo nucleation when anionic proteins and collagen type I fibrils come into contact. This interaction provides the stereochemical orientation of the negatively charged group necessary for hydroxyapatite nucleation. There are two stages of mineralization: primary mineralization, which occurs when the bone matrix is formed; this stage is rapid, and up to 70% of the bone’s matrix is mineralized at this stage. Afterwards, secondary mineralization of the remaining 30% of the matrix takes several years to complete [16].

Calcium phosphate is considered the primary contributor to bone tissue's durability, hardness, stiffness, and strong resistance to compression stress. Collagen fibrils, in contrast, are responsible for elasticity. Cortical

bone has Young's modulus of E = 7–30 GPa, a tensile strength of 50–150 MPa, a compressive strength of 167–193 MPa, a strain of 1–3 percent, and fracture toughness of KIC = 2–12 MPa.$m^{1/2}$ in the longitudinal direction. In contrast, cancellous bone has Young's modulus between 50 and 500 MPa, a tensile strength between 1.2 and 20 MPa, a compressive strength between 1.9 and 10 MPa, a strain between 5 and 7 percent, and fracture toughness of KIC = 0.1 MPa.$m^{1/2}$ [17, 18].

1.2.2. Bone cells

Bone cells can be categorised into osteoprogenitor (osteogenic) cells, osteoblasts, osteocytes, and osteoclasts.

1.2.2.1. Osteoprogenitor cells (Osteogenic)

Osteoprogenitor cells, which are considered unspecialized mesenchymal stem cells. Under the right conditions, they differentiate to form osteoblasts; also, these cells are capable of differentiating into fibroblasts, adipocytes, chondrocytes, and muscle cells. These cells are situated on the endosteal, periosteal, and inner surfaces of the Haversian canals of the bone (**Figure 1-2)**. During bone remodelling or repair, osteoprogenitor cells are activated; these cells move and develop into osteoblasts. Transcription factors, including core binding factor a-1 (cbfa-1), Runt-related transcription factor 2 (Runx2), and osteoblast-specific genes like bone morphogenic factor (BMP) and transforming growth factor-β (TGF-β), have an essential role in activation and development processes [19]. Runt-related transcription factor 2 (Runx2) plays a vital role in skeletal development. It has been discovered that mice born missing the Runx2 gene perish shortly after birth due to a skeletal

ossification defect [20]. In addition, TAZ (transcription co-activator with PDZ-binding motif) serves to determine osteoblast fate in bipotent osteoblast/adipocyte stem cells by activating Runx2 and inhibiting Peroxisome proliferator-activated receptor-γ (PPAR-γ), a key adipogenesis-related transcription factor [21]. Several additional transcription factors regulate osteoblast differentiation, such as distal-less homeobox 5 (Dlx-5) and osterix (OSX) [22].

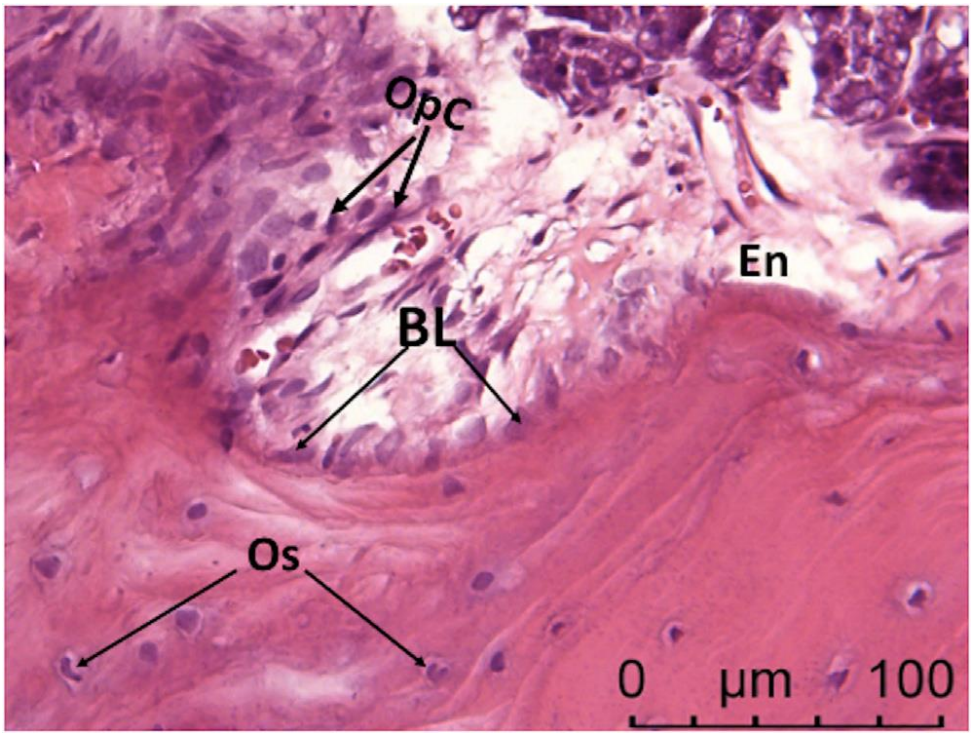


Figure 1-2: Hematoxylin and eosin image of a bone regeneration region show bone endosteum (**En**), bone lining cells (**BL**), and osteoprogenitor cells (**OpC**). This image is adapted from [19].

1.2.2.2. Osteoblasts

Osteoblasts are developed from osteogenic cells and are responsible for bone formation. These cells are mononuclear and are located along the superficial region of the bone. It comprises approximately 4% to 6% of

total cells in healthy bones (**Figure 1-3A**). The bone matrix is synthesised in two steps: collagen matrix deposition, produced by the osteoblasts, followed by the mineralization process [23]. Osteoblast development requires the expression of certain genes, including Runx2, distal-less homeobox 5 (Dlx5), and osterix (Osx), in addition to the production of bone morphogenetic proteins (BMPs) and Wingless (Wnt) pathway components [22]. Runx2 has been demonstrated to be the master gene responsible for osteoblast differentiation. Runx2 has been demonstrated to upregulate osteoblast-associated genes, such as collagen type 1 alpha 1 (COL1A1), alkaline phosphatase (ALP), and osteocalcin (OCN) [24].

Once the expression of Runx2 and ColIA1 is established during osteoblast development, osteoblast progenitors increase ALP activity and are classified as preosteoblasts [22]. Then, osteoblast maturation is marked by an increase in Osx expression and the release of bone matrix proteins, including OCN, bone sialoprotein (BSP) I/II, and collagen type I [25]. After osteoblast cells differentiate, they surround themselves with the extracellular matrix and start the calcification process. The calcium-binding activity of bone-specific proteins such as ALP, OCN, and osteopontin (OPN) leads to the deposition of hydroxyapatite crystals in the mineralized matrix. The majority of osteoblasts transform into osteocytes, whereas a few become bone-lining cells covering bone surfaces. This process is partly regulated by BMP-2 and regulates the quantity and function of osteoblasts (**Figure 1-3B**) [26].

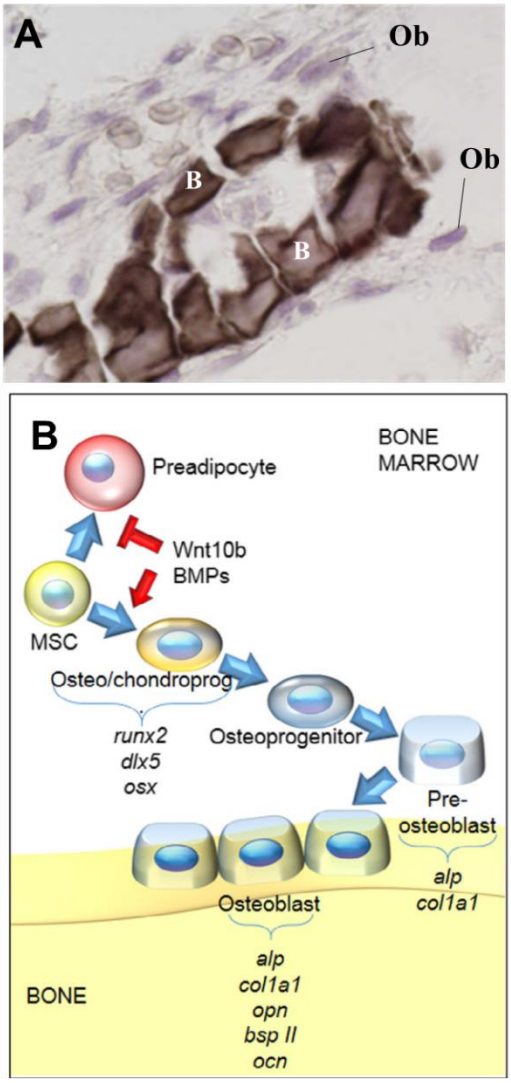


Figure 1-3: (**A**) Optical micrographs of rat alveolar bone fragment Using the Gomori technique for the detection of ALP, an undecalcified section shows a section of bone matrix (**B** = bone) that is positive for ALP (in brown/black). (**Ob**= osteoblasts). (**B**) Schematic representation of the multistep process of osteoblast differentiation (MSC = mesenchymal stem cell). Adapted from [22, 23].

1.2.2.3. Osteocytes

Osteocytes constitute 90–95 percent of all bone cells and have the longest lifespan [27]. Osteocytes are derived from osteoblasts that have

differentiated from mesenchymal stem cells. This procedure comprises four stages: osteoid-osteocyte, pre-osteocyte, young osteocyte, and mature osteocyte [27]. At the conclusion of the bone production cycle, a subset of osteoblasts becomes osteocytes and is integrated into the bone matrix. Several previously expressed osteoblast indicators, including OCN, BSPII, collagen type I, and ALP, are inhibited after the mature osteocytes become imprisoned within the calcified bone matrix.

Notably, osteocytes are situated in mineralized bone matrix-surrounded lacunae and have a dendritic appearance (**Figures 1-4A**) [28]. The osteocyte cell body remains within the lacuna, while its cytoplasmic processes (up to 50 per cell) traverse canaliculi that emerge from the lacuna space to form the osteocyte lacuna-canalicular system (**Figure 1-4B**) [29]. These cytoplasmic processes are connected to the cytoplasmic processes of nearby osteocytes, osteoblasts, and bone surface lining cells via gap junctions, thereby allowing the intercellular transit of signalling molecules such as prostaglandins and nitric oxide [30]. In addition, the lacuna-canalicular system of osteocytes is near to the vascular supply, allowing oxygen and nutrients to reach osteocytes [28]. Also, osteocytes function as mechanosensory because their interconnected network can sense mechanical pressures and loads, thus aiding bone adaptation to everyday mechanical forces [29]. Osteocytes appear to orchestrate bone remodelling and homeostasis by regulating osteoblast and osteoclast activities [28].

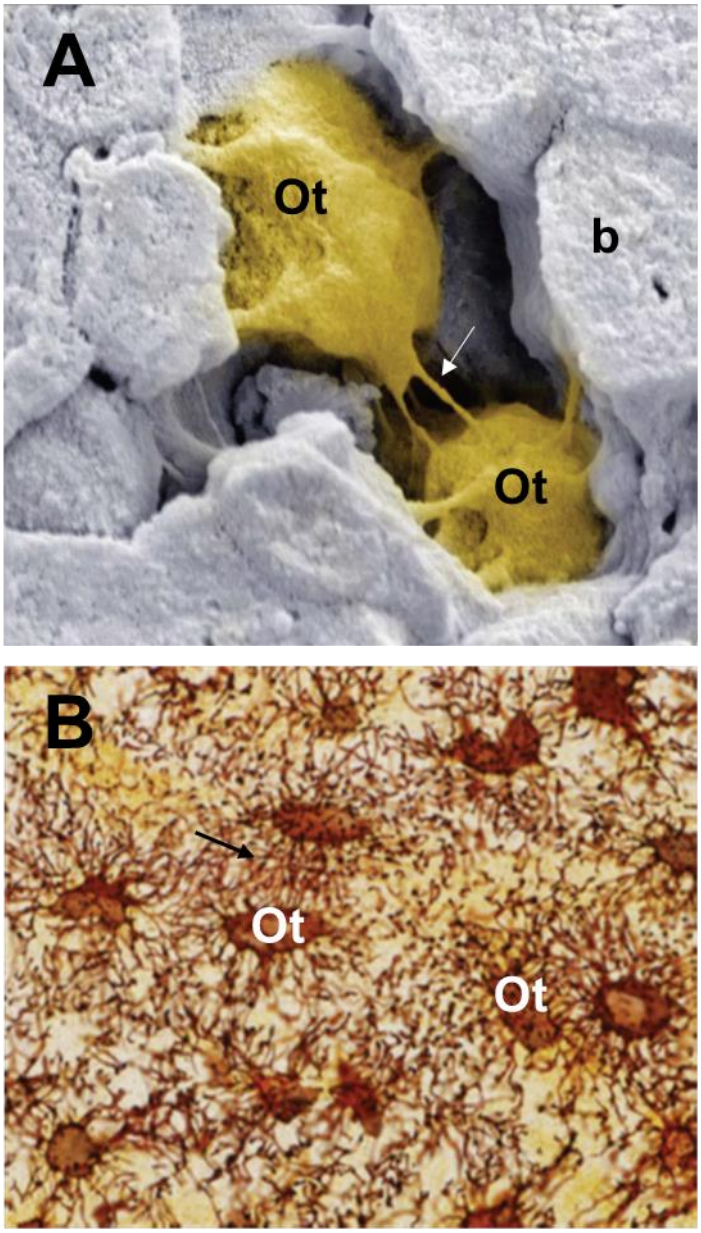


Figure 1-4: (**A**) Scanning electron micrograph of two osteocytes (**Ot**) surrounded by bone matrix (**b**). The arrow denotes cytoplasmic processes observed between the osteocytes (**Ot**) forming a network. (**B**) Image of a bone segment obtained and treated using the silver impregnation procedure. The arrow denotes the cytoplasmic

processes connecting the osteocytes (**Ot**). Adapted from [23].

1.2.2.4. Osteoclast

Osteoclasts are multinucleated macrophage-derived cells that are responsible for bone resorption in bone homeostasis. Also, osteoclasts maintain the equilibrium between bone formation and bone resorption at sites of bone remodelling or destruction. Osteoclasts are present on bone surfaces that are undergoing resorption [31]. On these surfaces, osteoclasts are found in shallow depressions known as "resorption bays" (Howship's lacunae). Osteoclasts erode the underlying bone, resulting in the formation of resorption bays. The bottom border of an osteoclast exhibits finger-like processes due to the presence of deep infoldings of the cell membrane; this border is termed the "ruffled border." (**Figure 1-5A-C**) [32].

Osteoclasts differentiate when mononuclear hematopoietic stem cells interact with osteoblast-secreted monocyte/macrophage colony-stimulating factor (M-CSF) and tumour necrosis factor α (TNF-α). During this interaction, the nuclear factor kappa-light chain enhancer of activated B cells (NFB) and c-Fos transcription factors are activated, leading to the production of receptor activator for nuclear factor κ B (RANK) on the osteoclast surface membrane [33]. The mutual interaction of RANK and its ligand stimulates the development of osteoclasts via many signalling pathways. In order to prevent excessive bone resorption, osteoblasts create an additional protein known as osteoprotegerin

(OPG). During bone resorption, osteoclasts assist in the formation of new bone by communicating with osteoblasts through OPG [34].

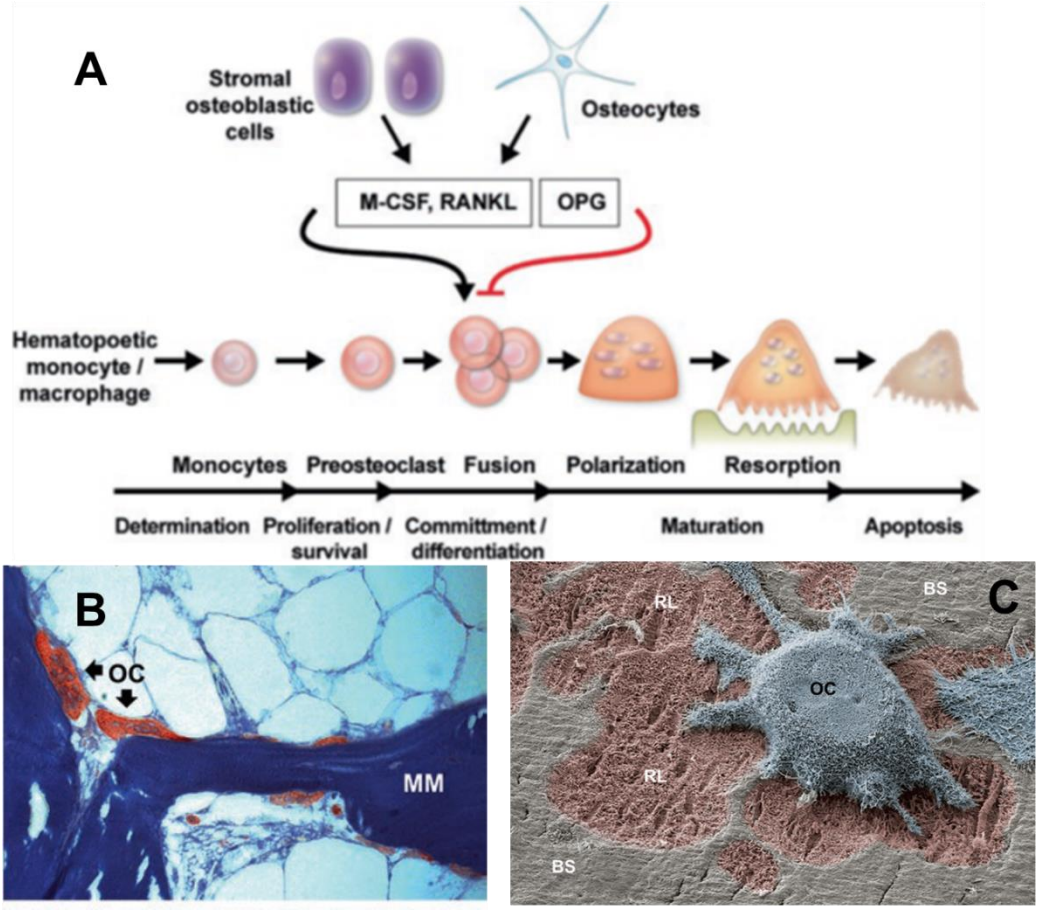


Figure 1-5: (**A**) Controlling osteoclast differentiation is the responsibility of RANKL, M-CSF, and other cytokines released by osteoblasts and osteocytes that govern successive stages of osteoclastogenesis. OPG, which is also secreted by osteoblasts and osteocytes, inhibits osteoclast formation by functioning as a decoy receptor for the receptor activator for nuclear factor κ B ligand (RANKL). (**B**) shows rat multinucleated osteoclasts (**OC**) stained with tartrate-resistant acid phosphatase (TRAP) on a trabecular surface of mineralized material (MM). (**C**) Coloured SEM image showing osteoclast (**OC**). Resorption pit (**RL**) and "intact" bone surface (**BS**). Adapted from [35].

1.3. Bone self-regeneration

Bones can regenerate (repair) after damage and throughout skeletal growth or continual remodelling during the human life span. Bone regeneration is an intricate process that involves a series of biological processes involving several cell types and intracellular and extracellular molecular-signalling pathways, with a specified spatial and temporal order, to maximise bone regeneration and restore bone function [4]. However, fracture healing is the most prevalent type of bone regeneration in the clinical environment. Bone fractures are healed via a mechanism that recapitulates several events of both intramembranous and endochondral bone formation but without the development of scar tissue [36].

Bone regeneration is a complex process that can be categorised as primary (direct) or secondary (indirect). Direct bone repair is an uncommon process and happens under extremely strict fixation without any movement of bone fragments [36]. When an exact fixation is achieved where there is no gap, the direct contact of the bone leads to healing in a process that resembles normal bone remodelling. During the healing process, bone resorption is driven by osteoclasts that proceed straight through the fracture line, followed by the deposition of new bone mediated by osteoblasts, resulting in the direct re-establishment of the Haversian system. In contrast, where bones are in the same mechanically stable state but with a slightly bigger gap between the bone pieces, in this situation, the gap is filled by direct deposition of intramembranous woven bone, and the Haversian system is re-

established by osteoclast-mediated remodelling. This is referred to as "gap healing." [37]. However, total stiffness is not attained, resulting in increased mobility at the fracture site and some periodic displacement between the bone ends [38].

Indirect bone repair is the most common type of fracture repair, characterised by a multi-staged process of healing progress [38]. In general, the secondary bone healing process is defined by initial hematoma development, followed by an immune response that plays a role in the production of several signalling cytokines (e.g., IL-6, TNF-α, FGFs, BMPs, VEGF, etc.) that are involved in the regulation of new bone growth. At the cortex and periosteum, there is immediate intramembranous bone growth. The exterior soft tissues anchor the fracture by forming a callus, which then undergoes chondrogenesis in a process comparable to endochondral ossification. In particular, chondrocyte proliferation decreases as tissues develop (i.e., hypertrophy) and calcify the matrix after the formation of a callus. Chondroclasts are necessary for resorbing calcified cartilage, while osteoblastic progenitors induce the formation of new bone. Finally, the mechanical aspect of the cortex is reached through the further remodelling of the newly produced bone (**Figure 1-6**) [39, 40].

1.3.1. Stages of bone fracture healing

1.3.1.1. Inflammatory phase

A bone fracture is followed immediately by an inflammatory reaction. The trauma induces the bursting of blood vessels inside and around the fracture site, resulting in a hematoma (**Figures 1–6 (1)**). Initially, the microenvironment of a hematoma is marked by hypoxia, acidity, a decrease in temperature, and a high concentration of calcium and lactic acid. The hematoma acts as a scaffold for the recruitment of inflammatory cells and cytokines such as IL-1, IL6, TNF-α, and CCL2 to initiate the inflammatory cascade. Following the recruitment of polymorphonuclear leukocytes (PMNs), monocytes/macrophages penetrate the fracture zone [41, 42]. After macrophage infiltration, macrophages are polarised into the M1 phenotype. Then, the immune response switches to adaptive immunity, which is characterised by lymphocyte invasion into the fracture site. Furthermore, this is followed by the removal of dead cells and debris by PMNs and macrophages, which results in the resolution of inflammation, which is considered a complicated and well-controlled process. In this phase, the inflammatory interaction and the production of pro-inflammatory cytokines are inhibited, and immune cells are gradually eliminated from the tissue.

During the resolution of acute inflammation, anti-inflammatory cytokines such as IL4, IL10, and IL13 play a role in stimulating macrophage polarisation from the M1 to M2 phenotype. Furthermore, local cytokines such as TNF-α [43] and stromal cell-derived factor 1 (SDF1), interchangeably known as the chemokine C-X-C motif chemokine ligand

12 (CXCL12), attract bone marrow mesenchymal stem cells (BM-MSCs). In order to initiate osteogenesis, recruited BM-MSCs and inflammatory cells engage in crucial inter-cellular communication mediated by numerous pro-inflammatory cytokines, anti-inflammatory cytokines, and growth factors, including transforming growth factor β (TGFβ), bone morphogenetic proteins (BMPs), vascular endothelial growth factor (VEGF), platelet-derived growth factor (PDGF), and fibroblast growth factor-2 (FGF-2) [44]. This procedure may also generate a reparative granuloma, which serves as a template for further callus production. During this phase, the acute inflammatory response reaches its peak within 24–48 hours and subsides around one week post-fracture [45].

1.3.1.2. Repair Phase

The callus's formation and the collagen matrix's deposition occur during the repair phase. Callus formation involves two kinds of mechanisms: intramembranous ossification and endochondral ossification [46]. At the periosteum, intramembranous ossification creates a hard callus immediately. Periosteal mesenchymal stem cells (MSCs) develop into osteoprogenitor cells, proliferating and differentiating into osteoblasts that produce woven bone directly. Endosteum and bone marrow undergo endochondral ossification, which has a soft callus and, later, a hard callus. BM-MSCs undergo differentiation into chondrocytes and then produce a cartilage matrix to create a cartilaginous template. Following hypertrophic differentiation, chondrocytes mineralize the surrounding matrix to generate a cartilaginous callus (**Figure 1-6 (2a)**). Once

hypertrophic chondrocytes undergo apoptosis, vascular invasion and osteoblast migration ensue [46].

The cartilage matrix eventually transforms into a bone matrix (**Figure 1-6 (2b)**) [46]. During this phase, proinflammatory cytokines such as IL1 and IL6 are lacking. Additionally, TNF-α decreases during the early healing phase but rises during the late repair phase. TNF-α stimulates chondrocyte death, resorption of mineralized cartilage, and vascularization during the endochondral ossification process. Low levels of TNF-α promote osteoblast growth, but excessive levels hinder these activities [43, 47]. In addition, osteomacs, a distinct macrophage subtype identified in bone tissues, are distributed throughout bone lining cells in both the endosteum and periosteum and contribute to bone homeostasis. In addition, osteomacs can detect the initial damaging input and trigger the inflammatory cascade; they also serve as a source of substances that stimulate the essential cellular processes necessary for bone regeneration [48]. In contrast, osteoclasts are multinucleated, highly specialised cells that breakdown bone [32].

1.3.1.3. Remodelling phase

During the last stage of bone healing, the bone restores its previous structure and mechanical properties via remodelling (**Figure 1-6 (3)**). The equilibrium between osteoclast bone resorption and osteoblast bone deposition plays a crucial role during the remodelling phase. Bone remodelling units are groupings of nearby osteoblasts and osteoclasts that coordinate the process. This mechanism is mediated locally by different growth factors and cytokines. Multiple pro-inflammatory

cytokines, including IL1, IL6, and TNF-α, are significantly secreted [45, 47]. Osteoclasts resorb the matrix from the erosion cavity, after which osteoblast precursor cells develop into osteoblasts and deposit a fresh matrix. Bone undergoes remodelling to maintain its shape and function in response to mechanical pressure and stress. Reduced bone loading may result in reduced bone mineral density (BMD). Such an issue occurs in fracture patients and those exposed to extended periods of low gravity, such as astronauts [49]. The presence of microfractures in the bone, resulting from regular everyday activity and stress, often initiates bone remodelling. The microdamage generates signals that play a role in the activation of the remodelling units, allowing control over BMD and routine fatigue damage [50]. It seems that bone remodelling is mediated by a feedback mechanism in which bone cells may detect environmental stress and respond by producing or removing bone. Calcium, glutamate, nitric oxide, and prostaglandins have been identified as signalling molecules that contribute to the adaptive response of bones to mechanical strain [51, 52].

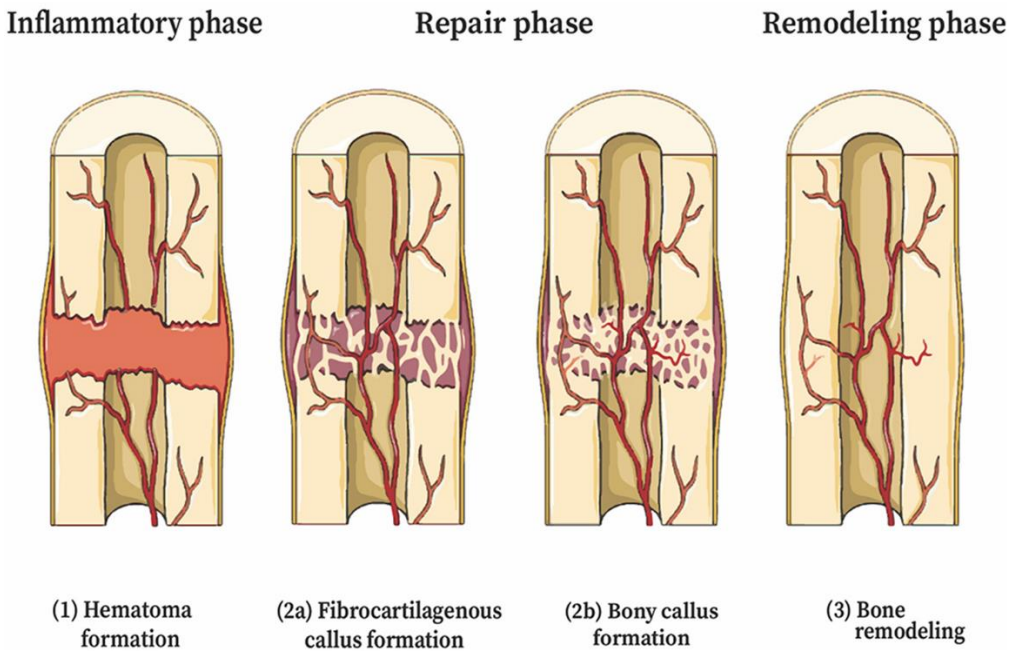


Figure 1-6: Stages of bone fracture healing. (**1**) Inflammatory phase, characterised by coagulation and an acute inflammatory response (**2**) The repair phase is characterised by (**a**) soft cartilage callus formation, followed by (**b**) hard bony callus formation. (**3**) The remodelling phase is characterised by the deposition of lamellar bone and the restoration of pre-injury anatomical proportions. Adapted from [53].

1.4. Bone formation and the immune system

There is a tight relationship between bone metabolism and immunological function. This relationship contributed to the development of the field of osteoimmunology [54], as it was recognised and acknowledged in several publications [55-57]. In healthy and pathological settings, this interdisciplinary subject explores the interplay between the immune and skeletal systems. These studies examine the interactions between osteoblasts, osteoclasts, lymphocytes, and hematopoietic cells during bone fracture repair (**Figure 1-7**) [58]. Shortly

after the injury, thrombin produced by the wounded vasculature activates the circulating platelets, leading to the platelets creating fibrin thrombus. Platelets generate inflammatory cytokines (IL-1, IL-6, and TNF-α) and growth factors (PDGF and TGF-β) in order to recruit immune cells (neutrophils and monocytes) and mesenchymal progenitor cells [59].

The role of neutrophils is still elucidated, but it has been shown to deposit the fibronectin matrix on the fibrin thrombus during early inflammation and remove thrombus and tissue debris in the late inflammatory phase [60]. Neutrophils also secrete cytokines that attract monocytes, such as IL-1, IL-6, IL-10, TNF-α, MCP-1, CXCL-1, and MIP-1 [61]. On the other hand, natural killer cells (NK cells) are lymphoid-derived hematopoietic cells. NK cells have the immunological role of identifying foreign or virally contaminated cells and inducing apoptosis or cell lysis through cytotoxic granules. NK cells generate IFN-γ and RANKL, suggesting they attract inflammatory cells and osteoclasts to the injured tissue [62]. Moreover, CXCL7-secreting NK cells may attract mesenchymal progenitor cells for deposition later in fracture healing [63].

At the conclusion of the inflammatory phase and during the mineralisation phase, T and B cells seem to perform cell-signalling functions. During the last stages of the inflammatory phase, T cells secrete RANKL to recruit, mature, and activate osteoclasts in an effort to remove the fibrin thrombus in preparation for the cartilaginous callus. On the other hand, B cells are implicated in inhibiting the pro-inflammatory signals IFN-γ, TNF-α, and IL-2 during this period [64].

The discovery that RANKL enhances T-cell growth and dendritic cell activity initially captured scientific interest in the intricate interplay between the immune and skeletal systems. RANKL, belonging to the TNF superfamily and serving as a cell surface cytokine, is conventionally produced by osteoblasts, osteocytes, activated T cells, and neutrophils [55, 58]. In the realm of osteoclast biology, RANKL interacts with RANK receptors situated on the osteoclast precursor cell membrane, playing an indispensable role in facilitating the activation process of osteoclasts. RANK activation is induced by transducing signals to activate the NF-kB and c-Jun N-terminal kinase (JNK) pathways to improve osteoclast survival and encourage maturation [55, 65]. Moreover, RANKL signalling specifically stimulates the production of nuclear factor of activated T cells cytoplasmic 1 (NFATc1), the main regulator of osteoclast development and activation [55, 56]. Osteoprotegerin (OPG), on the other hand, is a soluble decoy receptor expressed by B cells, dendritic cells, MSCs, and osteoblasts, which plays a role in inhibiting osteoclast activation by binding competitively to RANKL. Thus, the RANKL/OPG ratio is a key determinant of osteoclast activity [57, 66]. In young mice, deletion of NFATc1 was associated with osteoporosis and the suppression of osteoclastogenesis *in vivo* and *in vitro*. Both macrophage colony-stimulating factor (M-CSF) and RANKL encourage osteoclast differentiation. Specifically, M-CSF is essential for the survival and proliferation of myeloid cells and also promotes a high level of RANK expression. Conversely, when osteoclast precursor cells are exposed to RANKL, they merge and develop into active osteoclasts [55, 58].

L-6 and oncostatin M (OSM) belong to the cytokines within the interleukin-6 class, and they play a crucial role in stimulating the generation and function of osteoclasts. It is widely postulated that IL-6 exerts a favorable regulatory influence on osteoclastogenesis by enhancing the expression of RANKL on the osteoblast surface, thereby initiating the RANK signaling pathway in osteoclast precursors [67]. Interferon-γ (IFN γ), in contrast, increases the degradation of TRAF6, which is a crucial intermediary in the RANKL/RANK pathway, hence limiting significant bone loss during inflammation [6]. Also, TNF-α is, defined as a pro-inflammatory cytokine, was discovered to stimulate RANKL expression in bone marrow mesenchymal stem cells [68, 69]. Prolonged excessive inflammation is characterised by continuous production of pro-inflammatory cytokines (IL-6, TNF-α, and IL-1), often accompanied by a decreased RANKL/OPG ratio and high osteoclast activity. Consequently, bone remodelling shifts toward osteoclast-mediated progressive bone erosion, which is characterised by mineral and organic component disruption, resulting in excessive bone loss and functional impairment [57, 58]. In addition, immune cells participate in promoting osteogenesis through the production and release of several regulatory cytokines, including inflammatory cytokines, bone morphogenetic protein 2 (BMP2), transforming growth factor β (TGF-β), and vascular endothelial growth factor (VEGF) [70].

Besides the roles of T and B cells, macrophages have recently grabbed attention. Due to their similar origins, cells of the macrophage and MSC (osteoblast) lineages can engage in a broad spectrum of dynamic cross-

talk [58]. In addition to their role in body surveillance and pathogen combat, collective studies have shown that macrophages play a vital role in bone metabolism and bone tissue formation. Osteoclasts originate from macrophages and are known as resident macrophages of the bone. Furthermore, macrophages can also induce mineralization and osteoblast differentiation *in vivo*. However, macrophage depletion also reduced osteoblast numbers *in vivo* [71, 72].

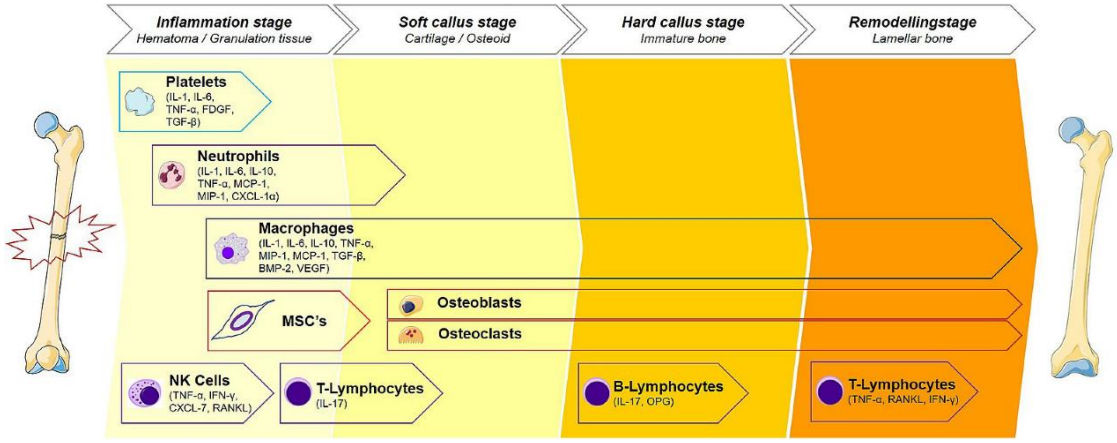


Figure 1-7: Involvement of immune cells in fracture repair. Immune cells at the fracture site change during bone regeneration. Platelets start a cascade of events that change the bone from inflammatory to proliferative, with soft and hard callus formation and reparative cells like osteoblasts and osteoclasts. The remodelling process supports the healing site. Macrophages are crucial throughout the healing cascade. Adapted from [53].

1.4.1. Macrophage and bone formation

Macrophages are derived from the myeloid cell lineage in the bone marrow and are considered highly heterogeneous cells. Macrophages have an essential role in the defence against pathogens and

inflammation. Moreover, it can be classified into resident macrophages and inflammatory macrophages [73]. The resident macrophage can be found in all tissues all over the body, functioning as an immune patrol, maintaining homeostasis, and playing a part in tissue repair [74, 75]. Inflammatory macrophages are derived from monocytes, which circulate through the bloodstream to the inflammation sites and undergo polarisation [76]. Macrophage polarisation is classified into M1 (classically activated), which is defined as pro-inflammatory macrophages, and M2 (alternatively activated), which is defined as anti-inflammatory macrophages [76]. Pro-inflammatory M1 macrophages contribute to the defence against pathogens [77]; This type of cell can be polarised by IFN-γ, granulocyte-macrophage colony-stimulating factor (GM-CSF), or other toll-like receptor (TLR) ligands such as lipopolysaccharide (LPS). In addition, M1 produces different pro-inflammatory cytokines and surface markers, including IL-1β, IL-12, IL-6, TNF-α, chemokine (C-C motif) receptor 7 (CCR7), CCR2, calprotectin, and superoxide anions, which in turn activate Th1 cells [78, 79].

On the other hand, M2 anti-inflammatory macrophages have a role in tissue repair and inflammation recovery. IL-4 and IL-13 can activate M2-like macrophages. IL-10, IL-1RA, and TGF-β are produced after M2 activation, as are mannose receptor and scavenger receptor CD163, which lead to Th2 activation [80]. M2 is considered the dominant phenotype for macrophages in healthy conditions, and this helps in tissue homeostasis and maintenance [81]. **Figure 1-8** demonstrates

macrophage phenotypes' characteristic properties after polarisation into M1 or M2 phenotypes.

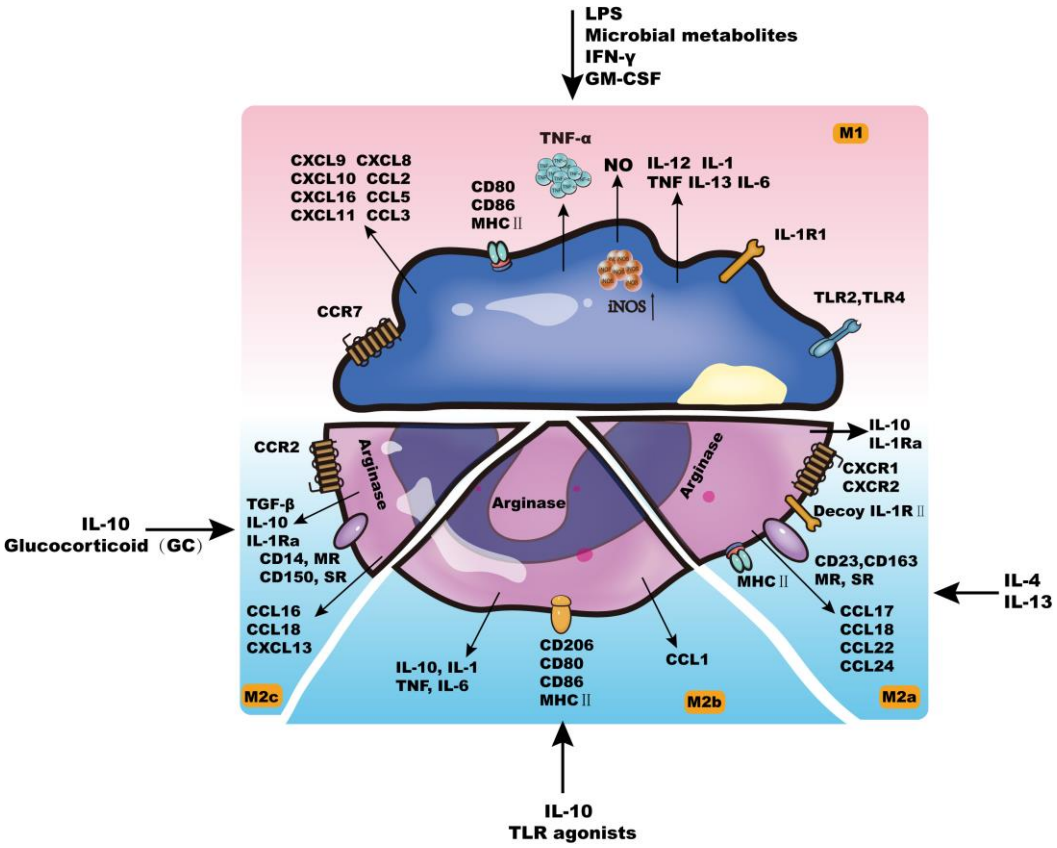


Figure 1-8: Soluble factors that polarize macrophages to M1 and M2 phenotypes. Adapted from [82].

At the fracture site, neutrophils infiltrate and produce cytokines that help recruit macrophages to the injury site. Consequently, macrophages are activated into M1 macrophages, which then contribute to eliminating dead cells and producing various cytokines, including TNF-α, IL-1β, IL-6, and C-C chemokine ligand 2. TNF-α is also implicated in cell recruitment and the activation of subsequent inflammatory signalling. IL-1β produced by macrophages stimulates angiogenesis, IL-6 production, and the creation of primary cartilaginous calluses [83]. On the other hand, IL-6 is able to attract MSCs to the site of damage and induce

angiogenesis and osteoblast development [84]. Also, M1 macrophages produce oncostatin M (OSM), which has a role in promoting osteogenesis and mineralization in mesenchymal stem cells (MSCs) *in vitro* [85].

Many studies have demonstrated the role of resident and inflammatory macrophages in impacting bone development. The osteoclast is usually considered a resident macrophage in bones. Interestingly, a large number have been identified as bone-resident macrophages in the periosteal and endosteal regions of the bone. These macrophages are called osteomacs and constitute about one-sixth of all cells in the bone marrow. Notably, on the endosteal surface of the bone, osteomacs are adjacent to the osteoblast, which suggests that osteomacs may support the osteoblast and promote bone formation [86]. Chang *et al*. demonstrated the positive role of osteomacs. They reported that when removing osteomacs from primary calvaria osteoblast culture, osteoblast mineralization was reduced by about 23-fold. In contrast, mineralization can increase when osteomacs are added to purified osteoblasts. Osteomacs can control the maturation of osteoblasts. Osteoblast immaturation can take place when osteomacs are depleted, which in turn reduces bone formation [71].

During inflammation recovery, macrophages get polarised to M2, reducing pro-inflammatory cytokine release, clearing debris, and restoring hemostasis. Also, M2 macrophages stimulate osteogenesis by secreting cytokines such as bone morphogenetic protein 2, bone morphogenetic protein 4, and TGF-β1 [87]. Interestingly, in a co-culture

study, M2 macrophages were able to stimulate the proliferation and osteogenic differentiation of MSCs [87]. Also, Wu *et al.* illustrated that a significant quantity of M1 could be noticed in the initial phase of osteonecrosis, whereas M2 is mostly found in the late stage along with new bone development [88].

1.5. Bone regeneration via tissue engineering

1.5.1. Bone tissue engineering

The phrase “tissue engineering” was coined by Robert Langer and Joseph P. Vacanti in 1993 and is defined as an “interdisciplinary field that applies the principles of engineering and the life sciences toward the development of biological substitutes that restore, maintain, or improve tissue formation” [8]. William Haseltine coined the term “regenerative medicine” in 2001: “Regenerative medicine is the regeneration and remodelling of tissue *in vivo* for the purpose of repairing, replacing, or enhancing organ function, and the engineering and growing of functional tissue substitutes *in vitro* for implantation *in vivo* as a biological substitute for damaged or diseased tissues and organs” [7] According to Haseltine’s definition, tissue engineering is a subset of regenerative medicine that focuses primarily on the in vitro synthesis of tissues for implantation using biocompatible materials, signalling molecules, and human cells. Indeed, tissue engineering is a kind of regenerative medicine therapy alongside organ transplantation and reconstructive surgery. However, transplantation and surgery are the primary clinical therapies.

Three components of tissue engineering, including isolated cells, external stimuli, and matrices or scaffolds, were included in the

definitions of tissue engineering (**Figure 1-9**). In tissue engineering therapies, matrices/scaffolds facilitate cell growth and differentiation by providing a 3D porous environment that is friendly to cells. The primary source of neo-tissue creation is the cells of endogenous progenitor cells or seeded cells. Exogenous physical and pharmacological stimuli activate the precise genes required to regulate the growth and synthesis of neo-tissues [7, 8].

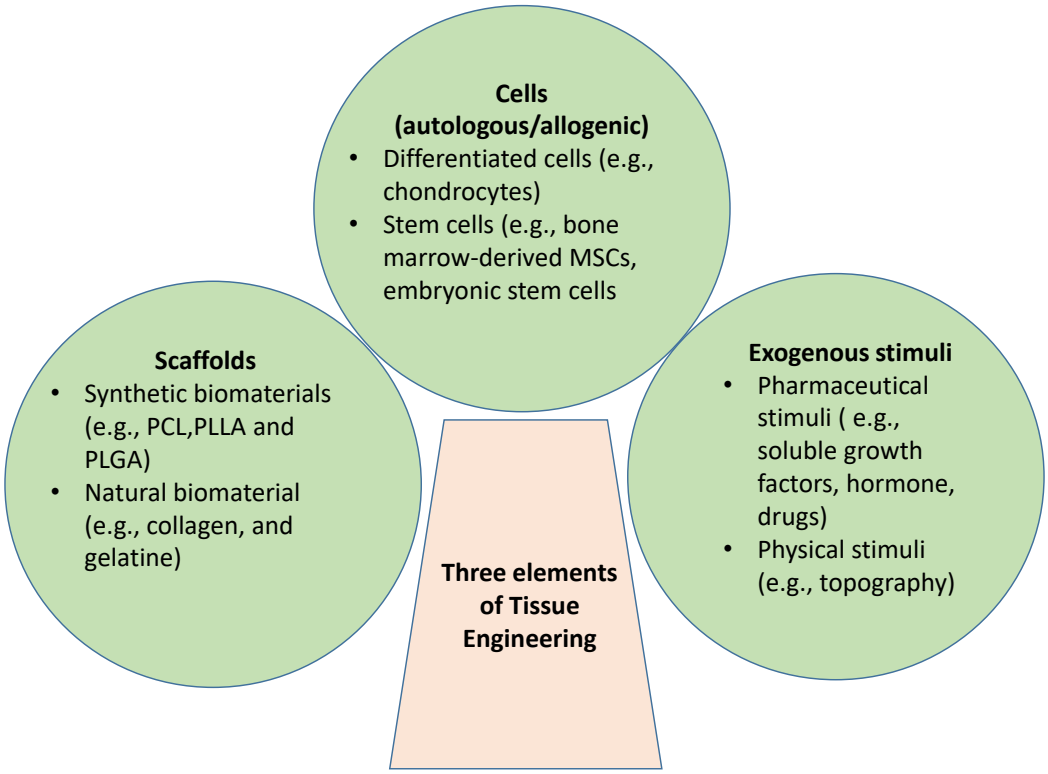


Figure 1-9: Three tissue engineering components for in vitro tissue substitute fabrication: cells, scaffolds, and exogenous stimuli.

It is acknowledged that bone has a self-healing property [2]. However, this feature cannot be achieved when substantial damage affects the bone, such as a large fracture [89, 90]. Thus, bone transplants

are often required to restore the normal function and natural biomechanical properties of the damaged bone. Autologous grafts are still the clinical gold standard for enhancing osteoinductive, osteoconductive, and completely histocompatible bone, thereby lowering the danger of immunogenic responses and disease transmission. Despite these advantages, autografts have limits owing to the limited quantity of tissue available for grafting, the morbidity at the donor site, and the necessity for subsequent surgery, all of which might result in implant failure. On the other hand, allogenic bone grafts are used as an alternative approach due to the unavailability of autologous grafts. However, disease transmission and immune rejection are still important issues to solve [91].

Bone tissue engineering mainly focuses on regenerating the bone to restore and maintain its function *in vivo* [92]. In contrast to most conventional techniques, bone tissue engineering (BTE) considers the use of a porous scaffold that guides cell adhesion, differentiation, proliferation, and molecular signals that stimulate progenitor cell differentiation into the osteoblastic phenotype (**Figure 1-10**) [93]. This field of research has become more popular, aiming to evade the challenge of bone grafts; however, understanding the biological behaviour of cells, ECM, and materials is critical in tissue engineering [91].

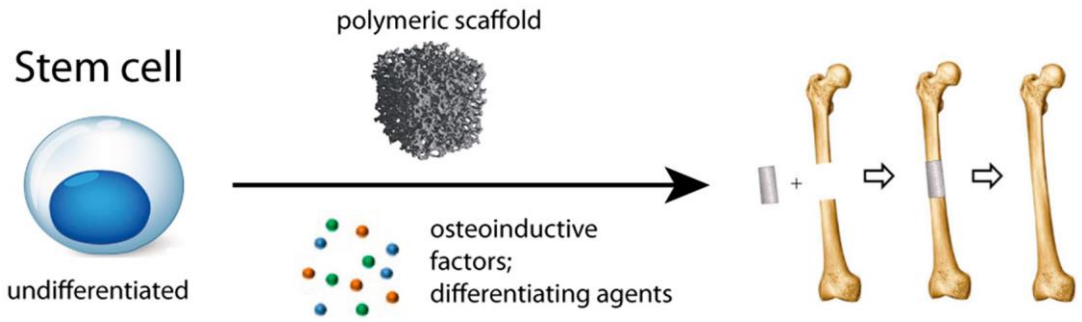


Figure 1-10: The basic elements of bone tissue engineering. Adapted from [93].

1.5.2. Scaffolds

The scaffold is defined as a 3D structure and is considered the main part of tissue engineering. The purpose of using a scaffold is to offer a template for the cells to attach to. Moreover, the scaffold's structure can be designed to mimic the ECM properties of the organ, which in turn gives it mechanical support and stimulates bone tissue *in vivo* [90-92]. A scaffold's performance can be defined in terms of biocompatibility, biodegradability, porosity, and mechanical strength. These parameters are critical when considering bone tissue regeneration [89]. Interconnected pores within the scaffold are essential for the continued growth of bone tissue. The purpose of pores is to allow nutrients and molecules to be transported into the inner part of scaffolds and enable the cell to grow and dispose of waste. It has been shown that the formation of bone tissue on scaffolds begins at the outside edge and progresses inward [89, 92, 94]. A high-porous scaffold means increasing surface area per volume, which can influence biodegradation kinetics and be varied by the change in porosity of the scaffold. The

biodegradation of the scaffold through chemical dissolution or cell-mediated degradation is crucial and an indicator for tissue repair and replacement of the scaffold with new tissue with no residues [94]. It has been reported that a pore size ranging from 100 to 150 μm is the minimum pore size for bone tissue growth in scaffolds [89, 95].

On the other hand, pores with more than 300 μm enhance bone formation and vascularization [95]. Furthermore, the pore size can influence ECM production and organisation. Also, for optimum bone healing, the scaffold's mechanical properties should match the original host tissue [96]. However, many factors affect the strength and degradation kinetics of porous scaffolds, including pore size, strut orientation, and geometry [97]. Moreover, surface chemistry, charge, controlling the hydrophilicity of the scaffold surface, and topography influence the cell interaction with the scaffold material [98-100].

The position and direction of struts lead to control of the geometrical features of the scaffold, including porosity, pore size and shape, and mechanical properties [101-105]. These are considered essential factors for a tissue engineering scaffold. Notably, several studies have revealed the effect of scaffold geometry on cell attachment, proliferation, and tissue formation [102, 105-107]. Scaffold geometry, on the other hand, impacts various factors in tissue engineering. For illustration, porosity, mechanical properties, and biology, including cell seeding and expansion, may all be influenced by the design of the scaffold [105, 108, 109]. Interestingly, printing speed and extrusion rate are also considered

factors affecting the scaffold's porosity since these directly influence the strut size.

Scaffolds for tissue engineering are still in progress of being developed by researchers to serve as a 3D microenvironment matrix [110]. Improper distribution of cells, seepage of cells out of the scaffold, cell death, inadequate cell differentiation, and insufficient integration into the host tissue are common obstacles in scaffold design for tissue engineering [111]. Consequently, enhancing the physical, mechanical, and chemical features of the scaffold may improve cell survival and differentiation. Ideal scaffolds should be biodegradable since this allows for the formation of new tissue and should not provoke an inflammatory reaction. Furthermore, several important factors should be considered, such as elasticity, surface chemical functionality, sensitivity to pH or temperature, micro- and nano-topography of the surface, and capacity to be metabolised in the body when biodegraded [112]. Moreover, the scaffold should promote cell migration and match the mechanical properties of native tissue *in-vivo* [113]. So far, many materials with some of these features have been researched for use in BTE, but constructing a scaffold that meets all of the aforementioned parameters remains difficult. Recent research has focused on using scaffolds for delivering targeted therapeutics to the bone to give molecules such as growth factors (e.g., bone morphogenic protein 2 (BMP2)), small molecules (e.g., dexamethasone), which are essential for bone regeneration, or medicines and small molecules that may treat bone problems locally. A

number of studies on the subject demonstrate the vital and promising control release techniques in treating skeletal illnesses [114, 115].

1.6. Biomaterial selection for 3D scaffolds

The biomaterial is an essential part of the scaffold used in bone tissue engineering. It should meet many requirements, including not being toxic, surface chemistry, stiffness, enhancing cell migration and attachment, and being osteogenic [116-118]. Also, the degradation rate is crucial and should be degraded simultaneously with the newly formed bone [119].

Ceramic-based scaffolds such as hydroxyapatite (HA), β-tricalcium phosphate (β-TCP), and calcium sulphate have been extensively used to replace the bone graft. These materials are used because of their chemical similarity with those in bones, biocompatibility, osteoconductivity, and mechanical robustness [120, 121]. It can be used alone or as a supplementary substance to confer variable mechanical properties to the material used in bone tissue engineering. Its osteoconductive features make it useful for scaffold fabrication for bone tissue regeneration purposes [122]. Many investigations have shown the direct effect of ceramic particle morphology on inducing osteoinduction and osteoconduction. Moreover, it has been demonstrated that the size of hydroxyapatite particles can influence the degradation rate and the scaffold's ability to promote the growth of bone tissue [114, 123, 124]. For hydroxyapatite microparticles, it has been reported that this size decreases the scaffold resorbability; conversely, nano-sized particles can be degraded by macrophages, osteoclasts, and even osteoblasts

and can be utilised by osteoblasts to produce new bone tissue *in situ* [125].

Furthermore, these materials are available in terms of production and supply, are uncomplicated in sterilisation and storage, and have a low risk of disease transmission and immunogenicity [121, 126-128]. It has been noticed that the degradation rate for these composites has not been optimal so far. Calcium sulphate takes a week, and TCP requires months to be resorbed; however, HA may take years [126, 129]. Different biomaterials have been investigated to match the biomechanical and structural requirements for bone tissue formation. Titanium alloys are widely used clinically due to their corrosion resistance, thermal stability, osteointegration properties, and biocompatibility. However, the high cost and high mechanical moduli limit their widespread development and usage as scaffolds. Ti6Al4V is an excellent example of a metallic biomaterial. The Young's modulus of Ti6Al4V material is approximately 110 Giga Pascals (GPa), which is higher than that of natural bone. This mismatch in moduli can result in stress shielding between the implant and host tissue, ultimately leading to implant failure and bone tissue resorption [130]. Adding a hydroxyapatite coating to the surface can significantly increase the osteogenesis of the bone [131]. Metal matrix composites, such as Ti6Al4V, have numerous remarkable advantages; nonetheless, their inability to biodegrade fundamentally limits their potential as ideal materials [130].

Polyester-based materials include poly (ε-caprolactone) (PCL), poly (lactide-co-caprolactone) (PLCL), polylactic acid (PLA), and poly (lactic-

co-glycolic acid) (PLGA). These materials are characterised as inert materials with proper mechanical and physical properties, which render them suitable for use as scaffolds for tissue engineering or carriers for drug delivery. In addition, polyester modification easily enhances cell adhesion and modulates the immune response. Most aliphatic polyester polymers are hydrophobic and have distinguished mechanical behaviour and biodegradability [132].

PCL has grabbed the attention of researchers because of its biocompatibility, mechanical features, and bioresorbable. Many articles have been published using PCL for spinal fusion surgery. Fortifying PCL with HA and TPC compounds appears vital to achieving effective fusion [133-135]. Reichert *et al*. utilised a PCL-TCP composite material for the 3D printing of a highly porous scaffold with high elasticity (22.2 MPa), demonstrating bone formation with improved mechanical stability *in vivo* [136]. Moreover, Kao *et al*. fabricated a 3D surface with poly (lactic acid) and modified it with poly (dopamine). This modification rendered the surface of the scaffold hydrophilic and enhanced cell migration, adhesion, and differentiation compared to poly (lactic acid) alone [137].

Developing completely functioning bone scaffolds with adequate mechanical strength to repair massive bone lesions still faces significant hurdles. Various material categories, including ceramics, polymers, and hydrogels, have proven unable to duplicate the characteristics of bone when used alone. When combining groups of materials in composite 3D scaffolds, favourable material properties and bioactivity can be enhanced. Consequently, improved performance of the individual

biomaterials is necessary for their positive interactions with host tissues. Therefore, with the utilisation of innovative biomaterials and new tactics, particularly the integration of stem cells, nanotechnology, pharmaceutics, material sciences, and other fields, the approaches for bone regeneration will make significant progress [138-140].

A new innovative solution with a new biomaterial composition is being searched for to illustrate solid proof for osteogenesis, cost, and safety. HA and TCP remain active and are essential mineral components of osteoconductive scaffolds. Biodegradable polyester scaffolds made of PCL or PLA are used in research on bone tissue engineering. It is possible to modify their properties to achieve the required mechanical properties, degradation rates, or biological responses [141].

1.7. Scaffolds fabrication

1.7.1. Conventional methods

Solvent casting/particulate leaching is a conventional process for manufacturing scaffolds that begins with dissolving the polymer in an organic solvent (**Figure 1-11A**). Then, the polymer solution is combined with porogen to form a polymer-porogen mixture. Afterwards, the solvent is evaporated, which hardens the polymer. Finally, water is used to dissolve the porogen, which is often a salt, e.g., sodium chloride. This method yields a polymer scaffold with a porous network; however, it is challenging to regulate the pore geometry and pore interconnectivity of the scaffolds [142].

Gas foaming removes the need for solvents in solvent casting and particle leaching method (**Figure 1-11B**). This method generates a porous structure by nucleating and expanding gas bubbles scattered throughout a polymer. In the beginning, heated compression moulding is utilised to create solid discs of a polymeric material, such as PLGA poly (lactic-co-glycolic acid). Following this, the discs are saturated with carbon dioxide by exposing them to high-pressure CO_2 gas (5.5 MPa) at room temperature for 72 hours. Afterwards, the pressure is decreased to ambient levels (P^0CO_2). This produces thermodynamic instability in the gaseous phase. Thus, the CO_2 gas starts to phase separate from the polymer, and in order to reduce free energy, the gas molecules begin to cluster, resulting in the creation of pores. This method can achieve porosities of up to 93% and pore diameters of up to 100 mm. Nevertheless, managing pore connections and pore size is difficult [143].

Also, scaffolds can be fabricated using the freeze-drying technique. Freeze-drying begins with the freezing of a polymer solution, which results in solvent ice crystals surrounded by polymer aggregates (**Figure 1-11C**). The surrounding pressure is then reduced using a vacuum below the equilibrium vapour pressure of the frozen organic solvent (P^0). Thus, the solvent sublimates directly from the solid state to the gaseous state. After the complete evaporation of the solvent, a porous, interconnected polymer scaffold remains [144].

Phase separation depends on variations in heat energy to cause the de-mixing of a homogeneous polymer/solvent solution. When a polymer like PLLA is dissolved in an organic solvent, it can become

thermodynamically unstable and dynamically split into a polymer-rich phase and a solvent-rich phase at low temperatures. This method begins with dissolving a polymer in a high-boiling, low-molecular-weight solvent at a high temperature, often around the polymer's melting point, allowing for the formation of a homogenous melt blend. The polymer solution is then cast into the desired scaffold shape and refrigerated to induce phase separation and precipitation of the polymer solution into a polymer-rich phase and a solvent-rich phase, resulting in the formation of porous scaffolds (**Figure 1-11D**). Extraction, evaporation, or sublimation are then used to remove the solvent from the solvent-rich phase. This results in a porous scaffold since the solvent removal leaves holes in the polymer matrix [144].

Electrospinning is a prominent scaffold production technology that can build interconnected nanofibrous porous scaffolds (**Figure 1-11E**). This approach draws charged filaments of polymer solutions or polymer melts as thin jets from a syringe attached to a metallic needle towards a collection plate using an externally generated electric field. Micro- and nanoscale fibres may be successfully produced and deposited to form a scaffold that can include composite materials and biomolecules[145].

Table 1-1: Conventional methods for 3D scaffold fabrication for bone tissue engineering. Adapted from [140].

Manufacturing Method	Benefits	Potential Limitations
Solvent casting/ particulate leaching	• Relatively simple technique that allows the creation of scaffolds with regular porosity, controlled composition and pore size.	• Use of organic solvents precludes cells and biomolecules being included directly in scaffolds. • Can be difficult to control pore shape and interconnectivity • Limited thickness of structures and mechanical properties achievable

Gas Foaming	• Eliminates the use of chemical solvents	• High pressures involved prohibit the inclusion of cells and bioactive molecules directly into scaffolds. • Temperature labile materials may be denatured during the compression moulding step. • Difficult to control pore sizes and ensure interconnectivity
Emulsification Freeze-Drying	• Does not require the use of solid porogen	• Requires use of organic solvents • Small pore size and • Porosity often irregular • Long processing time

Phase Separation	• Eliminates leaching step of porogen • Can be combined with other techniques easily	• Small pore sizes limit the use • Use of organic solvents inhibits the use of bioactive molecules or cells during scaffold fabrication.
Electrospinning	• Creates scaffold with large surface area for cell attachment • Simple and inexpensive technique	• Organic solvents may be required, which can be harmful to cells • Limited mechanical properties • Difficult to incorporate precise microarchitecture into constructs

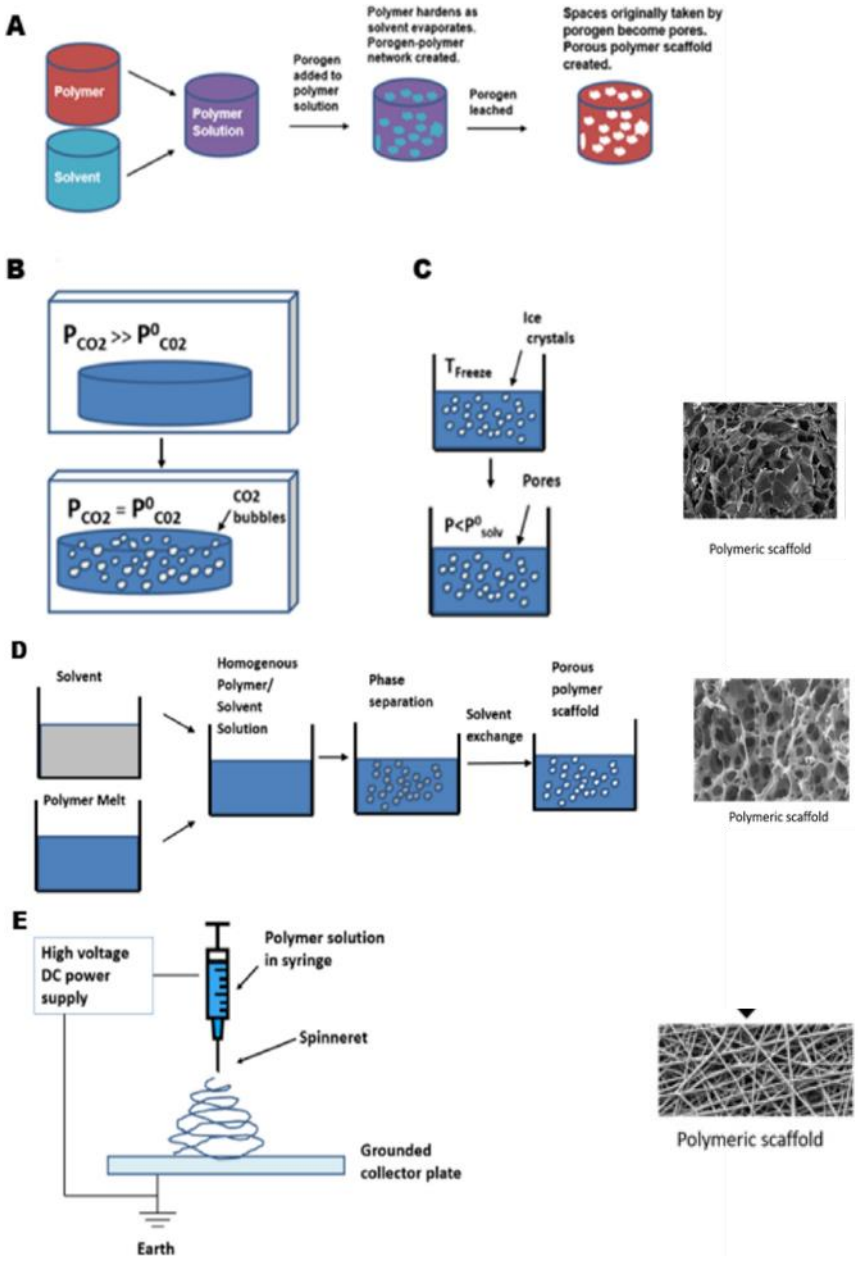


Figure 1-11: Common methodologies employed in the fabrication of scaffolds. (**A**) Solvent casting-particle leaching process (**B**) Gas foaming (C) Freeze-drying (**D**) Phase separation (**E**) Electrospinning. Adapted from [140].

1.7.2. 3D printing techniques

Conventional scaffold fabrication techniques often allow minimal pore size, shape, and interconnectivity control. With the advent of 3D

printing technology, scientists now have a better handle on scaffolds' microarchitecture and spatial content. With 3D printing technology, scaffolds are created by building up successive layers of a selected material. Starting from the base and working upwards, each layer is stuck together, forming a 3D structure. A 3D printer takes its structural instructions from a computer-aided design (CAD) model uploaded to it. The CAD models depict three-dimensional objects in a succession of cross-sectional layers, enabling 3D printers to produce models physically via an additive process [140].

The fabrication of scaffolds starts with a 3D image, which can be obtained from clinical imaging modalities such as computed tomography (CT) or magnetic resonance imaging (MRI) or can be drawn by computer-aided design (CAD). Then, additional software is needed to slice CAD models into G-code, which encodes 3D CAD models in a format that 3D printers can read. G-code allows for modifying and optimising printing parameters, including print speed, layer height, print head temperature, and pressure [140].

3D printing is progressively applied to tissue engineering due to its advantages in the manufacturing of intricate structures that are inconceivable or challenging for conventional manufacturing techniques [146, 147]. The capability to accurately control and reproduce 3D structures has made 3D printing a valuable tool for creating scaffolds for tissue engineering [148]. Numerous 3D printing techniques have been used to manufacture scaffolds. Extrusion-based 3D printing is supposedly the most widely used procedure in tissue engineering due to

its comparatively low cost. Various materials, including polymers, ceramics, and hydrogels with or without incorporated cells, can be 3D printed [103, 147, 149, 150].

Furthermore, there are other widely used 3D printing techniques, including fused deposition modelling (FDM), selective laser sintering (SLS), stereolithography (SLA), and numerous forms of direct writing (**Figure 1-12a-e**) [151]. All these techniques print 3D scaffolds layer by layer without any additional tools. **Table 1-2** summarises 3D printing techniques used in bone tissue engineering.

Extrusion printing is an attractive approach to creating complex 3D scaffolds, which involves the computer-controlled deposition of a thick slurry of polymer ink layer by layer at room temperature to create three-dimensional objects. This technique has been used to print polymeric inks in which 3D object consolidation is accomplished by a fluid-to-gel or gel-to-solid transition during printing. Developing precise and reproducible inks or suspensions for printing materials with a greater variety of chemistries is one of the obstacles [152].

Many factors need to be considered to achieve a reasonable resolution of the printed object, such as needle diameter and rheological properties of the polymer solution, printing speed, pressure, and other material properties [153-155]. Numerous extrusion printers can print various materials with autonomous printing instructions, effortlessly making composite structures. Extrusion 3D printing is valuable for scaffold fabrication for heterogeneous tissue, such as osteochondral tissue, due

to its capability to co-print different materials and control the polymer dispensing layer-by-layer [155, 156].

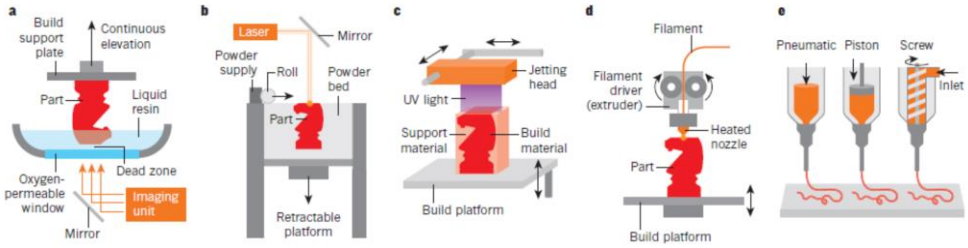


Figure 1-12: Common 3D printing methods. (**a**) The light-based 3D printing method is known as continuous liquid interface production. (**b**), Light-based selective laser sintering of powders (SLS). (**c**), Light- and ink-based photocurable inkjet printing of photopolymerizable resins (SLA). (**d**), Ink-based fused deposition modelling of thermoplastic filaments (FDM). (**e**), Direct ink writing using viscoelastic inks. Adapted from [157].

Table 1-2: AM techniques being used in bone tissue engineering. Adapted from [11].

AM Technique	Process	Materials used	Pros and cons
Extrusion/Robocasting	• Materials dissolved in the organic solvent to prepare a viscous solution • Printing of material layer by layer from a nozzle at a specific rate under constant pressure	• PCL • HA/PCL • PLA • HA/PLA • Bioactive glass • PLA/G5 glass	+ • Ability to incorporate drugs, small molecules, and cells in a printed scaffold – • Materials restriction (not soluble in organic solvents)

Fused deposition modelling (FDM)	• Thermally heated polymers extruded through a nozzle	• PCL • PCL/TCP • TCP/polypropylene (PP) • Tricalcium Phosphate	+ • No need for a platform to support the construct – • Restricted to thermoplastic polymers • Not capable of incorporating cells and proteins due to high temperature
Selective laser sintering (SLS)	• Powder bed preparation • Powder added layer by layer • Sintering each layer by laser	• PCL • Nano HA • Calcium phosphate (CaP)/poly (hydroxybutyratecohydroxyvalerate)(PHBV) • Carbonated hydroxyapatite	+ • No need for support for the construct • No need for Post printing processing – • The resolution depends on the laser

		(CHAp)/poly(L-lactic acid) (PLLA) • PLLA • β-TCP • PHBV	beam diameter.
Stereolithography (SLA)	• platform immersed in photopolymer liquid (resin) • focused light exposed according to the desired design • Polymer solidifying at the focal point, the non-exposed polymer remains liquid, • Construct fabricated Layer by layer by platform moving downward	• Poly(propylene fumarate) • (PPF)/diethyl fumarate (DEF) • PPF/DEF-HA • PDLLA/HA • β-TCP	+ • The complex internal structure can be achieved • Growth factors, proteins, and the cell can be incorporated – • Only restricted to photopolymers.

1.8. Immunological response of biomaterials

The immune system is continuously monitoring the body for pathogen invasion, foreign substances, and tissue damage [158]. To eradicate the hazard, the immune system employs an intricate cascade of immune modulators comprised of different soluble cytokines, cell types, and cellular interactions [159]. The interplay between the host tissue and the implanted material initiates a series of events that start with the interaction with blood components, which leads to the deposition of a protein layer on the surface of the biomaterial, forming a provisional matrix. The immune cells are recruited, leading to an acute or chronic inflammation; this inflammation leads to the development of granulation tissue, a foreign body reaction, fibrosis, and ends with a fibrous capsule formation [160]. This reaction, known as the "foreign body response" (FBR), can be deleterious to both the host and the implanted device's function [160]. Implanted biomaterial usually activates the innate (neutrophils, macrophages, dendritic cells, and natural killer cells) and adaptive (T and B-cells) immune cells in the body [161]. Also, immune cells can migrate large distances to reach the location of damaged tissue. After recognising the implanted material, the innate immune system generates a non-specific inflammatory reaction. On the other hand, the adaptive immune system produces a highly specific response and a long-term memory [162].

The immune cells can recognise injured tissue by identifying the damage-associated molecular patterns (DAMPs) generated by dying cells, damaged cells, or stressed cells. Likewise, pathogen-associated

molecular patterns (PAMPs), molecules derived from the invading pathogens, indicate the presence of a foreign substance. Pattern recognition receptors (PRRs) are present on the membranes of both immune cells and certain stromal cells. Notably, antigen-presenting cells (APCs), such as macrophages, possess these receptors and have the capacity to recognize and interact with Damage-Associated Molecular Patterns (DAMPs) and Pathogen-Associated Molecular Patterns (PAMPs), thus initiating the immune response [158]. To elucidate the process, antigen-presenting cells (APCs) such as macrophages, dendritic cells (DCs), and B cells bind to PAMPS or DAMPs via their PRRs, thereby triggering inflammatory signalling pathways and promoting innate immunity. Additionally, dendritic cells (DCs) play a vital role in initiating an immune response specific to antigens and facilitating a targeted immunological reaction by provoking particular immune responses. During their immature stage, these immature DCs survey the peripheral tissues to detect self-antigens or pathogens, particularly in regions where the invasion of pathogens is expected, such as the epidermis, respiratory epithelium, and gastrointestinal tract [163, 164].

Due to the invasive nature of biomaterial implantation in normal tissue homeostasis and structure, it leads to the occurrence of oedema and bleeding at the implantation site. Oedema formation involves the accumulation of plasma proteins in the damaged tissue. Upon the introduction of a biomaterial into the body, it comes into direct contact with the host's bloodstream. Consequently, serum proteins, including albumin, fibronectin, fibrinogen, vitronectin, complement, and other

immunomodulatory proteins, adhere to the surface of the implant. Concurrently, in response to tissue injury, neutrophils are the first immune cells to appear. Neutrophils primarily function to eliminate foreign substances through processes like phagocytosis, degranulation, and the release of neutrophil extracellular traps (NETs), which are a network of extracellular DNA threads that capture and bind pathogenic microorganisms [165].

Moreover, neutrophils have been demonstrated to produce cytokines (e.g., IFN-γ and IL-10) that control the activities of adjacent cells and assist in the resolution of inflammation [166]. Several investigations have shown that macrophages are the primary mediators of the FBR in biomaterials [167, 168]. Macrophages are generally categorised into two phenotypes: M1-like macrophages, also known as traditionally activated macrophages, and M2-like macrophages, also known as alternatively activated macrophages. During the early phases of tissue healing, IFN-γ, lipopolysaccharide (LPS), and tissue necrosis factor (TNF-α) activate macrophages into M1-like macrophages, which have a pro-inflammatory phenotype [169]. However, M2-like macrophages display activation in response to IL-4 and IL-13, both of which possess anti-inflammatory properties [169]. Upon reaching the implantation site, monocytes undergo migration and differentiation, transforming into M1 macrophages and carrying out phagocytosis, which represents their primary function. Consequently, adherent M1 macrophages endeavour to eliminate the biomaterial by releasing degradative enzymes and reactive oxygen species (ROS). In situations where the biomaterial's size

prevents internalization, macrophages enter a process termed "frustrated phagocytosis," leading to the fusion of macrophages into foreign body giant cells (FBGCs) on the biomaterial's surface to enhance their phagocytic capabilities [170]. In the initial stages of Foreign Body Response (FBR) and wound healing, the macrophage phenotype is predominantly M1, displaying pro-inflammatory characteristics. Nevertheless, the amalgamation of macrophages into Foreign Body Giant Cells (FBGCs) frequently triggers a phenotypic shift towards alternatively activated M2 macrophages, which exhibit anti-inflammatory properties (**Figure 1-13**) [171]. Extended IL-4 production from activated T cells, mast cells, and basophils often induces this transition [172]. In response to cues from their milieu, macrophages can adopt various functional phenotypes [171]. At the interface between the tissue and the material, foreign body giant cells (FBGCs) secrete substances that act as chemoattractants for fibroblasts. This, in turn, stimulates the synthesis of matrix collagens, resulting in the formation of a collagen-rich, avascular fibrotic capsule [173]. Fibroblasts are stromal cells which play a critical regulatory role in the process of wound healing. Tissue fibrosis is characterized by the excessive deposition of collagen-rich extracellular matrix, leading to the replacement of functional connective tissue. This condition arises due to uncontrolled fibroblast activity [174]. However, it is important to note that biomaterial-mediated fibrosis does not always have negative effects. In certain cases, fibrotic growth into surgical meshes is essential for effectively sealing internal incisions [175]. On the other hand, the formation of a collagenous fibrotic capsule can have

adverse consequences, such as the detachment of the implanted medical device from the surrounding host tissue. This, in turn, impedes device-tissue integration, leading to device failure [173].

Inflammation linked to implants remains a serious barrier to developing biomaterials for medical devices. Thus, biomaterial design aims to create biomaterials that can utilise the body's defence and pro-healing mechanisms to promote healing and integration while minimising the deleterious effects of the immune system.

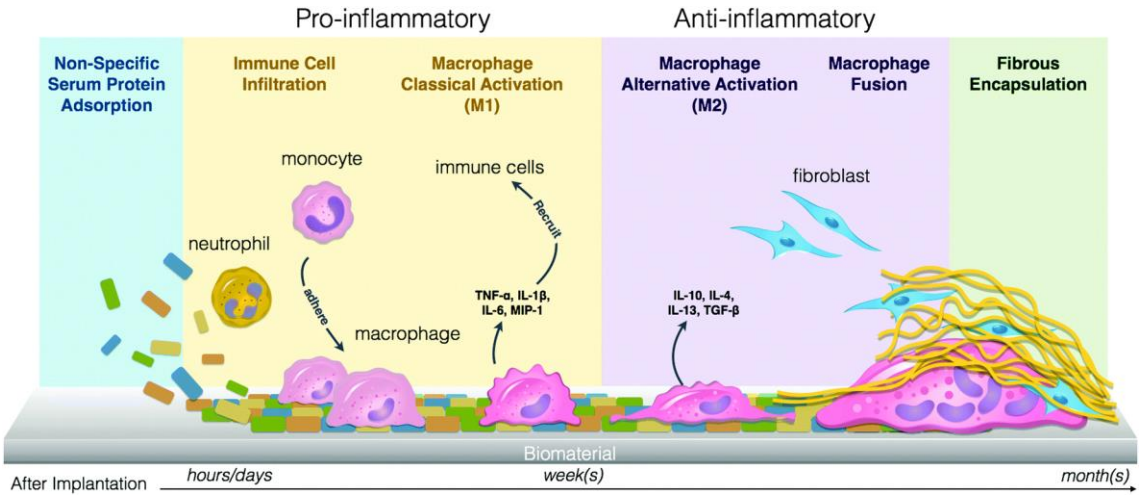


Figure 1-13: Foreign-body reaction timeline. Proteins on biomaterial surfaces start the foreign body response. The adsorbed protein layer attracts monocytes, which develop into classically activated (M1) macrophages that release pro-inflammatory cytokines TNF-α, IL-1β, IL-6, and MIP-1. M1 macrophages become alternatively activated (M2) macrophages that produce IL-10, IL-4, IL-13, and TGF-β. These cytokines induce macrophage fusion, FBGC development, fibroblast adhesion/proliferation, collagen deposition, and a mostly avascular fibrotic capsule. Adapted from [161].

1.9. Scaffold-based techniques for regulating the bone-regeneration immune microenvironment

Until now, the majority of interest in bone tissue engineering has centred on how biomaterials directly influence the destiny of exogenous or endogenous stem cells that contribute to the repair of injured bone tissues [176, 177]. The ultimate objective of utilising biomaterials in bone tissue engineering is to serve as a scaffold to provide physical support and biological signals to support tissue repair. However, implanting a biomaterial scaffold often elicits an unfavourable immune response, leading to its failure to integrate with host tissue [178].

It is crucial to regulate the activation of macrophages after implantation. This process is critical to removing microbes and debris, material biodegradation, tissue regeneration, vascularization, and the organisation of ECM after tissue damage [171]. Consequently, macrophages can modulate chronic inflammation and wound healing balance after the implantation of biomaterials [179]. Modulating the interaction between macrophages and biomaterial scaffolds is being searched for [79, 180]. Biomaterial surface chemistry can influence the cellular response [181], and the amount and type of adsorbed proteins on the biomaterial surface also affect cell behaviour [182].

It has been reported that scaffold microstructure and topology influence macrophage attachment, infiltration, and polarisation to M1 and M2 [169, 183, 184]. Furthermore, incorporating a control release system to release anti-inflammatory drugs or cytokines has impacted the immune response

to implants [185, 186]. The following are the strategies used to modulate macrophage interaction (**31**):

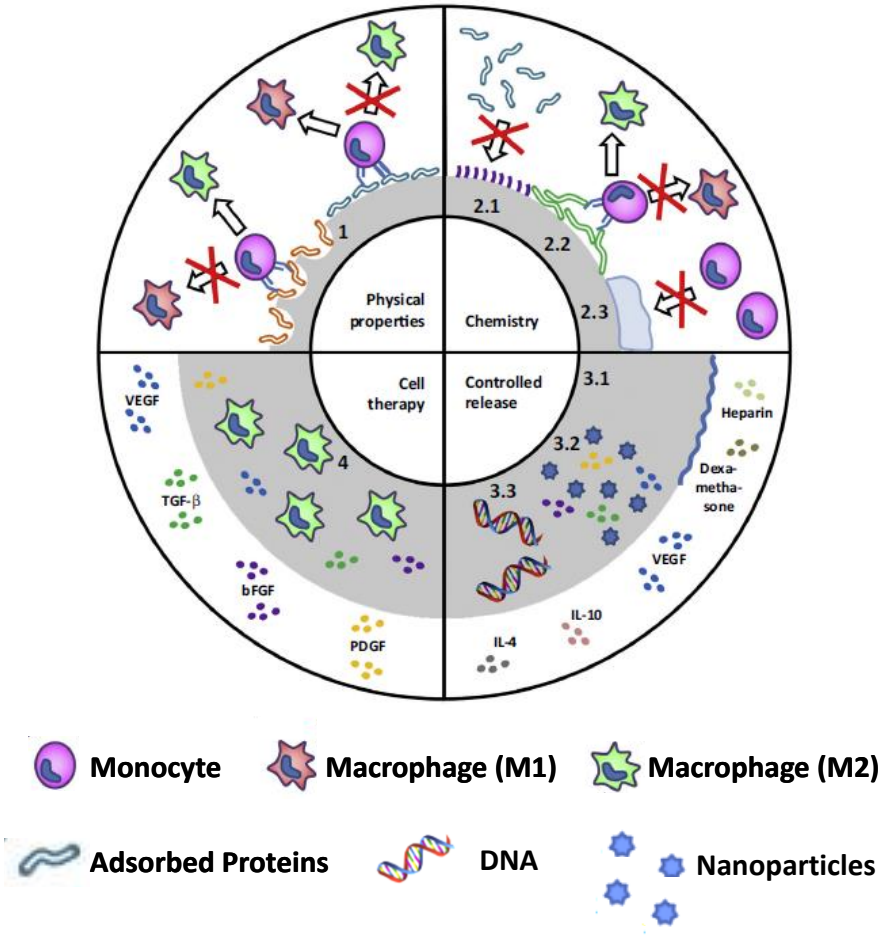


Figure 1-14: Various strategies to modulate macrophages include: (**1**) biomaterial physical properties. (**2**) Using chemistry such as (**2.1**) non-biofouling, (**2-2**) biomimetic ECM, and (**2.3**) hydrogels to isolate implants from immune cells, thus limiting an inflammatory response. (**3**) Using control release systems, to deliver anti-inflammatory agents from the surface (**3.1**), or from embedded nanoparticles (**3.2**), and gene delivery systems to induce/supress cells to secrets anti-inflammatory agents. (**4**) Embedded immune cells secrete pro-angiogenic and pro-regenerative cytokines. Adapted from [187].

1.9.1. Physical and chemical properties

Numerous investigations have shown that biomaterials' surface and biochemical aspects modulate macrophage polarisation [188]. The regulatory impact of biomaterials on immune cells is mostly determined by their surface properties, potentially because they influence protein adsorption [189]. Soon after the implantation of the biomaterial into the body, proteins (such as fibronectin, fibrinogen, albumin, vitronectin, and complement proteins) rapidly bind to its surface. Various aspects of protein adsorption are heavily influenced by the biomaterial's inherent features (e.g., topography and surface chemistry). Adsorption of a protein onto a biomaterial might result in conformational changes that expose previously hidden regions or epitopes of the adsorbed protein to the immune system [190]. Thus, specific biological responses to the surface structure of the biomaterial are activated when the immune cells detect and attach to the surface of the implanted biomaterial. For instance, fibrinogen denatures when bound to a biomaterial's surface, presenting two epitopes (190-202, P1, and 377-395, P2) [191]. These epitopes bind with the phagocyte integrin Mac-1 (CD11b/CD18), promoting an inflammatory response. Therefore, the intensity of the inflammatory reaction increases as more epitopes are revealed [191].

The biomaterial's surface topography is frequently used to influence macrophage adhesion and polarisation [192]. Changes in cell adherence, alignment, morphology (cytoskeletal structure), proliferation, viability, gene expression, and differentiation have been seen on patterned surfaces [193]. Innovative micro and nano-manufacturing

techniques and other technologies have enabled the construction of sophisticated surface features with a tunable pattern [194].

Several techniques have been utilised effectively to create micro and nanoscale-structured topography on the biomaterial surface, such as chemical etching, chemical vapour deposition, photolithography, scanning probe lithography, electron beam lithography, nanoimprinting, thin film deposition, phase separation, and self-assembly [195-197]. Groove topography is the most commonly employed pattern to study cell behaviour. Various biomaterials have been fabricated with nano- and micro-grooves to modulate cell interaction with biomaterial surfaces [198, 199]. McWhorter *et al*. demonstrated that a high proportion of macrophages align along the grooves' principal axis. Their alignment and orientation tend to improve with decreasing groove width and rising groove depth close to the cell’s dimensions. To manipulate cell morphology and direct the polarisation of macrophages, surfaces with 20 and 50 µm grooves were created. It was discovered that the elongation of cells increased macrophage polarisation toward an M2-like phenotype and the production of M2-like cytokines (IL-4, IL-13), indicating that cell shape impacts and modulates the phenotypic polarisation of macrophages [200]. In a separate investigation, titanium surfaces with micro- and nanopatterned grooves increased macrophage elongation, with substrates with 400–500 nm-wide grooves exhibiting the greatest effect. Interestingly, the surface grooves have induced anti-inflammatory and pro-healing phenotypes in macrophages, indicating the potential of surface modification to control macrophage function [201].

Also, in terms of geometry and its role in affecting macrophage phenotype, several studies have shown the influence of the size and shape of the implant in controlling FBR. It has been reported by Salthouse *et al*. that the biocompatibility effect of rods with different shapes (circular, triangular and pentagonal) demonstrated that rods with circular shapes have a minimum FBR comparable to triangular and pentagonal shapes. These results confirmed the importance of implant shape in manipulating macrophage interaction [202].

Increasing the diameter of the struts in the micro range (5–6 μm) for electrospun scaffolds has induced cultured macrophages to express M2 phenotype markers, whereas macrophages cultured on thinner struts (0.69 μm) have expressed M1 phenotype markers *in vitro* [169, 184]. The mechanism behind how the scaffold microstructure induces macrophage polarisation is unclear. On the other hand, pore size and porosity are also crucial parameters in determining the efficacy of biomaterials since they affect the transport of oxygen and nutrients as well as macrophage polarisation. It has been found that increasing the pore sizes and porosity of an electrospun scaffold has resulted in elevating the expression of M2 marker Arginase 1 while decreasing the expression of M1 marker Inducible nitric oxide synthase (iNOS), indicating that they encouraged the polarisation of macrophages towards the pro-regenerative M2 phenotype rather than the pro-inflammatory M1 phenotype [203]. Furthermore, the chemical characteristics of the material surface, e.g., surface charge and hydrophilicity, have a substantial effect on the adherence of macrophages and the release of pro-inflammatory

cytokines and chemokines. Hydrophilic surfaces did not elicit activated monocyte adherence, but hydrophobic surfaces boosted monocyte attachment, resulting in a local inflammatory response [204]. Hotchkiss et al. discovered that rough titanium surfaces with greater hydrophilicity favoured M2 macrophage polarisation [204].

Immune, epithelial, and endothelial cells use projections known as pseudopodia or lamellipodia to perceive their surroundings. At the tips of these protrusions, there are structures resembling hair called filopodia. These filopodia are constituted of bundles of actin filaments that function by sensing the surfaces of the substrate. Once filopodia locate an appropriate binding site, cells localise on the substrate by activating many signalling pathways [205]. The surface significantly impacts these signalling cascades and bulk characteristics of biomaterials, such as hydrophilicity, hydrophobicity, roughness, charge, chemistry, and stiffness, and plays a critical role in cell-material interactions [206].

Integrins are a widely expressed family of transmembrane receptors that govern the first contact between cells and surfaces. Cellular processes such as growth, motility, shape, differentiation, and adhesion are regulated by integrins through interactions with the surface-adsorbed proteins on the material, such as fibrinogen and fibronectin. Also, integrins can convey signals from the cell's exterior to its interior or vice versa, and cell-substrate adhesion is dependent on this signalling [207]. A mechanistic study revealed that surface hydrophilicity can mediate fibronectin and fibrinogen adsorption and conformation and activate the PI3K and NFk-B signalling pathways via the selective expression of

integrin β1 or β2, thereby tailoring the macrophage response to generate a favourable immune microenvironment for osteogenesis and bone formation [208].

Additionally, the surface charge has a profound influence on the immunological response. Inflammation is more likely to be triggered by positively charged (cationic) than negatively charged (anionic) or neutral surfaces [209, 210]. The surface of the majority of mammalian cells, including immune cells, is negatively charged [211]. Positively charged particles can typically induce greater cellular internalisation by macrophages than negatively charged particles. Miller et al. used liposome nanoparticles composed of 1,2-dioleolyl-sn-glycero-3-phosphatidylcholine (neutrally charged), 1,2-dioleoyl-3-dimethylammonium propanediol (positively charged), and 1,2-dioleolyl-sn-glycero-3-phosphatidylserine (negatively charged), and found that J774 macrophages endocytosed positively and negatively charged liposomes to a greater extent than uncharged liposomes, according to in vitro data.

Additionally, positively charged liposomes were taken up by macrophages to a greater extent than negatively charged liposomes [212]. Moreover, cationic polymers such as polyethylenimine (PEI), cationic gelatin, dextran, and polylysine can activate M1 macrophages via the toll-like receptor-4 (TLR-4) pathway and induce the secretion of IL-12 to stimulate the Th1 response by activating M1 macrophages [213]. Also, THP-1 monocytes were cultured on nanofibrillated cellulose films with surface charges of cationic, anionic, and neutral charges. The

results showed that THP-1 cultured on anionic films is activated towards the pro-inflammatory phenotype M1, whereas neutral surfaces promote moderate activation. Interestingly, the cationic surface did not induce the activation of the cell toward the M1 phenotype, and none of the surfaces activated the macrophages toward the M2 phenotype. This was justified by the fact that the surface chemistry of the functionalized films affected the adsorbed proteins, which resulted in distinct protein compositions and/or conformations that promoted both cell adhesion and activation [214].

Moreover, structures mimicking the ECM can modulate the body's immune response. Hyaluronan (HA) has been extensively used for coating biomaterials and nanoparticles. This material is naturally present in joints. It was illustrated that HA could suppress MCP-1, IFN-γ, and IL-6, which mediated the stimulation of M1 macrophages and induced IL-10, a cytokine related to the M2 phenotype. This effect depends on the degree of sulfation of HA. The purpose of using ECM coating is to reduce inflammation by preventing chronic M1 activation, which is a critical factor in implant rejection [215].

1.9.2. Immunomodulatory drugs released from scaffolds

Modulating the immune system response toward biomaterials by anti-inflammatory agents is a potential technique to enhance biomaterial performance [186, 216]. However, using these drugs should be carefully evaluated in each case, considering the risks and benefits of treatment [187]. Several classes of anti-inflammatory medications exist, including non-steroidal anti-inflammatory drugs (NSAIDs), corticosteroids, and

biological agents. Glucocorticoids and nonsteroidal anti-inflammatory drugs (NSAIDs) are commonly used to treat inflammation and pain. However, their mechanisms of action and effects on the immune system are distinct [187].

NSAIDs, including ibuprofen and aspirin, inhibit the cyclooxygenase (COX) enzymes responsible for prostaglandin production. Prostaglandins are chemical mediators that cause inflammation, pain, and fever as part of the immune response. NSAIDs reduce pain and inflammation by inhibiting prostaglandin production [217]. However, NSAIDs do not directly affect the immune system. NSAIDs have a relatively narrow range of effects on the immune system, primarily reducing inflammation symptoms and pain. Hence, they do not have a significant impact on the overall function of the immune system [217].

On the other hand, glucocorticoids, such as prednisone and dexamethasone, are synthetic glucocorticoids that mimic the effects of the body's natural steroid hormones. These drugs have potent anti-inflammatory and immunosuppressive properties [218]. Glucocorticoids exert their therapeutic effects by binding to glucocorticoid receptors (GR) in the cytoplasm of immune cells. This binding initiates a cascade of events that modulates the expression of the cytokines involved in inflammation and immune responses, resulting in the suppression of the immune response [219].

Although NSAIDs and glucocorticoids have anti-inflammatory properties, they differ in their effects on the immune system. NSAIDs do not directly

affect the immune system but reduce inflammation by inhibiting prostaglandin production. Conversely, glucocorticoids have potent immunosuppressive effects, suppressing the immune response by inhibiting the cytokine produced by immune cells [217] [218]. It has been demonstrated that glucocorticoids modulate macrophages by inhibiting pro-inflammatory cytokine production, including TNF-α, IL-6, and IL-1β [220], and stimulating the production of anti-inflammatory mediators such as IL-10 and TGF-β and enhancing the expression of surface markers CD163 and CD206 [221].

There are several implications for these differences in the effects of NSAIDs and glucocorticoids on the immune system. For example, glucocorticoids may be more effective than NSAIDs in treating autoimmune diseases, such as rheumatoid arthritis, where the immune system is overactive and causing damage to the body's tissues. However, the immunosuppressive effects of glucocorticoids may increase the risk of infections, making them less suitable for treating infections or other conditions where the immune response is needed to fight the infection [222].

Dexamethasone has gained popularity as a bone growth promoter due to its ability to stimulate the proliferation and differentiation of mesenchymal stem cells into osteoblasts. However, the concentration and duration of treatment are crucial issues to consider when administering dexamethasone [223]. It has been reported that prolonged treatment with dexamethasone has been linked to significant bone loss and osteoporosis [224-226].

Although the role of physical and chemical characteristics of biomaterials in the regulation of macrophage polarisation has been conclusively demonstrated [188], the delicate regulation of macrophage phenotypes, such as how to regulate the degree of polarisation and the precise time point of regulation, remains mainly unknown. In contrast, biomaterials that control the release of anti-inflammatory drugs, cytokines, and genes can provide more control over the time and magnitude of macrophage polarisation [190]. Diverse biomaterial-based drug delivery techniques for progressively regulating macrophage polarisation have been developed recently, which is advantageous for advancing our knowledge of the regulation of macrophage behaviour and precise control of polarisation degree [190, 227].

Cytokines can alter the microenvironment of the tissue by controlling the phenotype of recruited immune cells. Therefore, certain cytokines might modulate macrophage phenotypes into M1 and/or M2 phenotypes and *vice versa* at the inflammation site [185]. The direct administration of anti-inflammatory cytokines, such as IL-10 and IL-4, enhances the polarisation of M2 macrophages, while INF-γ polarises the macrophages into the M1 phenotype [228]. Spiller *et al*. developed a decellularized bone scaffold with IFN-γ physically adsorbed for rapid release (24 h) and IL-4 attached through biotin-streptavidin binding for sustained release (6 days). The results showed that the early fast release of IFN-γ boosted M1 polarisation in macrophages and improved scaffold vascularization. Their scaffold did not generate strong M1 and M2 activation at early or late stages but resulted in a heterogeneous macrophage M1/M2

phenotype [229]. Different activation periods are required to prevent phase overlap when designing delivery systems to influence the sequential polarisation of macrophages. Chen et al. devised a titania nanotube (TNT) scaffold with two hydrogel layers. IL-4 was loaded into the hydrogel on the TNT scaffold, and IFN-γ was positioned between the two hydrogel layers. IFN-γ was quickly released within three days, promoting the polarisation of macrophages towards the M1 phenotype. In contrast, IL-4 was continually released throughout the course of the first week. Interestingly, after four days, the controlled release stimulated the transition of macrophages from the M1 to M2 phenotype by sequential release of IFN-γ and lL-4 [230].

In recent years, significant progress has been made in developing delivery systems for the local release of glucocorticoids such as dexamethasone, heparin, superoxide dismutase, and indomethacin, which, when loaded into scaffolds, can reduce inflammation and fibrous encapsulation around the scaffold [231, 232]. Dexamethasone has grabbed attention due to its anti-inflammatory properties and the ability to stimulate osteogenic differentiation and chondrogenesis in MSCs [233, 234]. Haynesworth and colleagues discovered in 1996 that exposing cells to dexamethasone reduced the production of pro-inflammatory cytokines such as IL-11 and IL-6 [235].

Also, Feng *et al.* have demonstrated that treating immune thrombocytopenia patients with a high dose of dexamethasone has restored the balance of macrophages toward M2-like phenotypes [216]. Following this, there has been an increase in reports on the

immunomodulatory effects of dexamethasone. For example, dexamethasone suppresses IL-12-induced IFN-γ secretion and IFN regulatory factor-1 expression in T cells and natural killer (NK) cells [236]. However, dexamethasone has the practical disadvantage of inhibiting angiogenesis and delaying tissue healing in the tissues surrounding the implant [237]. To address this issue, Patil *et al*. studied the combination of dexamethasone and vascular endothelial growth factor (VEGF) as an anti-inflammatory and neovascularization treatment loaded in PLGA/poly (vinyl alcohol) (PLGA/PVA) hydrogel scaffolds. According to the findings, the combination has counteracted the anti-angiogenic action of dexamethasone by improving the maturation of blood vessels at the implantation site [237].

These findings demonstrated the significance of defining the release patterns in vivo and adapting them to the intended use. As stated before, macrophages perform various functions throughout the regeneration processes, and each macrophage phenotype may arise and stay active multiple times. Therefore, there is a need to design a delivery system with an adjusted release kinetic according to the tissue specification and choose the effective modulatory time to prevent a mixed phenotype [190]. In addition, excessive polarisation of a particular macrophage phenotype might result in unfavourable outcomes [238]. Due to the heterogeneity of the *in vivo* environment, few studies have investigated the relationship between required drug concentrations and the extent of macrophage polarisation. It has been demonstrated that macrophages derived from aged mice are insensitive to IFN-γ, indicating that higher

doses are required to induce M1 polarisation [239]. Therefore, determining the precise dose required for macrophage polarisation in vivo requires further study in the future, which is critical for designing an effective drug delivery system. Also, due to the remarkable outcomes obtained in regulating macrophage phenotypes by biomaterials and the close link between distinct phenotypes of macrophages and the tissue regeneration process, I believe that immunomodulating biomaterials can enhance tissue repair outcomes, and this is a promising direction for the future design of biomaterials for bone tissue regeneration.

1.10. Aims and objectives of the thesis

The classic approach to bone tissue engineering mainly focuses on biomaterials, stem cells, and releasing growth factors to control and drive the osteogenesis of MSCs. However, the cross-talk between bone cells and immune cells is still being explored. Moreover, the role of macrophages in bone development is being explored in bone tissue engineering, specifically stimulating M2 polarisation to enhance bone tissue regeneration, which has gained much attention from investigators.

Utilisation of anti-inflammatory drugs is considered one of the methods of modulating the immune response. Dexamethasone is a steroidal drug with anti-inflammatory and osteogenic properties and has been utilised in various control release systems to study the anti-inflammatory effect or osteogenic capability separately. However, to my knowledge, the interplay between macrophage polarisation and osteogenic differentiation of MSCs under controlled release of dexamethasone has not been studied. Moreover, several challenges impact the development

of a control release system, including fine-tuning of drug release, rapid bursts of the drug, drug properties, drug loading, synthesis and manufacturing conditions of the release system, biocompatibility, and the material properties used for control release construction.

This thesis aims to investigate the effect of released dexamethasone from 3D printed scaffolds on modulating the immune response and enhancing MSC osteogenesis. The objectives of this project are:

- To formulate 3D printing PCL dexamethasone inks composed of different surfactants, including Pluronic® F-127, Pluronic® F-68, sucrose acetate isobutyrate (SAIB), Pluronic® L-31, and sorbitan monooleate (Span80), and assess the printability.
- Assessment of the effect of surfactants on the release behaviour and kinetics of dexamethasone from 3D printed scaffolds.
- Investigate the biocompatibility and immunomodulation of the released dexamethasone on M1 pro-inflammatory macrophages.
- Assessment of the effect of released dexamethasone on the immunomodulation of M1 pro-inflammatory macrophages and enhancement of the osteogenesis of MSC in a direct co-culture system.

2. Chapter two: General Material and methods

2.1 Extrusion-based 3D printing

This technique is widely used in tissue engineering to fabricate scaffolds. In this method, a 3D model can be manufactured from a range of viscoelastic materials such as thermoplastic materials, pastes, polymers, and hydrogels, which can be extruded using a syringe tool (metallic or organic solvent-resistant plastic) and then dispensed via a screw-driven force or pneumatic piston-driven on a building platform at room temperature layer by layer to build the 3D structures. These materials can solidify through solvent evaporation, UV polymerisation, sintering, coagulation, or gelation [240].

2.2 Scanning Electron microscope (SEM)

A scanning electron microscope is a powerful tool that enables the analysis and examination of the morphology, chemical composition, and crystalline structure of the material's surface. In addition, SEM uses an electron beam instead of visible light to produce high-resolution images. Therefore, SEM images can be produced by interacting an electron beam with an atom at various depths within the sample. This interaction produced various signals with various energies, including secondary electrons (SE), backscattered electrons (BSE), X-rays, and cathodoluminescence [241].

Moreover, secondary electrons (SE) escape from the top few nanometers of the material’s surface. It is characterised as a low-energy (3-5 eV) signal that tends to be highly localized, making it possible to use it to produce a high-resolution image. On the other hand, BSE has more

energy from SE greater than 50 eV and is often used in analytical SEM along with the spectra made from X-rays. BSE can give information about elemental distribution as this signal is emitted from a deeper location in the sample. Moreover, X-rays can provide information about elements' identities [241].

The SEM comprises an electron source, an anode, an electromagnetic lens, a scanning coil, a sample stage, a screen, and different detectors. The detectors can include a secondary scatter electron detector (SED), a backscatter electron detector (BSED), and X-ray detectors (**Figure 2-1**) [241].

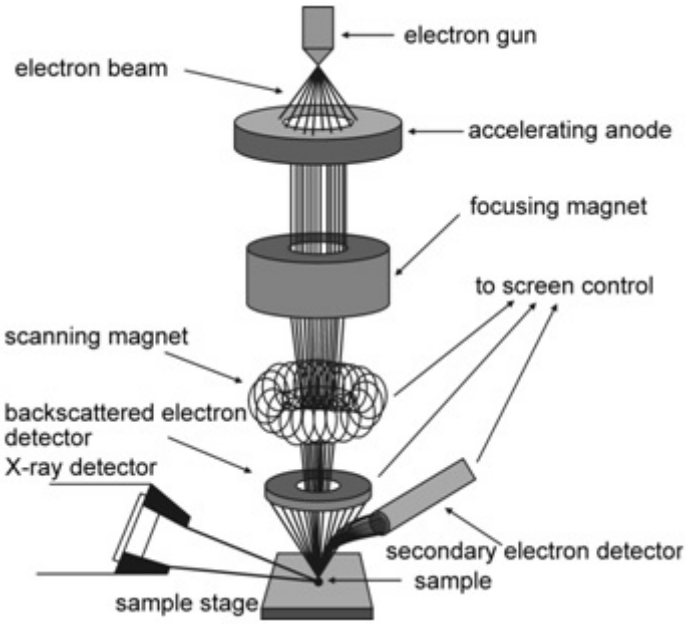


Figure 2-1: Schematic diagram of the SEM component. Image from https://www.technoorg.hu/news-and-events/articles/high-resolution-scanning-electron-microscopy-1/#

2.3 Differential scanning calorimetry (DSC)

DSC is a widely used technique for the characterisation of various materials. It measures the thermal changes of the material as a function of time and temperature. During DSC analysis, both the sample and reference are subjected to the same temperature. As a result, the thermal change in the material can be determined by measuring the difference in the heat flow of the sample relative to the heat flow of the reference sample (**Figure 2-2**). During the analysis, materials can show an endothermic event, which means that the sample absorbs heat; thus, the heat flow to the reference is lower than the sample. On the other hand, exothermic events can take place, which means that the sample releases energy. This event occurs when the heat flow to the reference is higher than the sample [242].

The DSC can also be utilised to monitor the thermal changes in a sample when it is subjected to controlled temperatures. The thermal changes (enthalpy changes) that occur to the sample during the analysis may be due to a chemical reaction or a physical transformation that can be detected. This method can provide useful information regarding the degree of crystallinity of the material. Furthermore, it can be used to investigate the changes in heat capacity that happen during solid-state transformation by measuring the heat flow when the sample is heated or cooled in a controlled manner. Consequently, it is a useful thermal technique to determine amorphous materials' glass transition temperature (T_g) and melting temperature (T_m).[242].

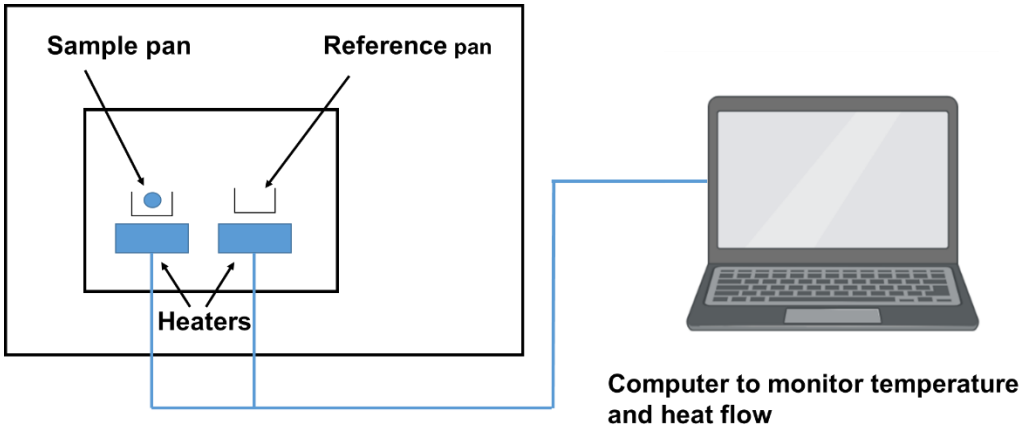


Figure 2-2: Schematic diagram representation of the DSC.

2.4 Attenuated Total Reflectance-Fourier Transformed Infrared Spectroscopy (ATR-FTIR)

ATR-FTIR spectroscopy is a non-destructive rapid absorption technique commonly used to analyse liquid, semisolid, and solid samples with minimal sample preparation. FTIR is typically used to examine the middle infrared spectrum between 400 and 4000 cm^{1}. FTIR spectra provide information regarding rotational and vibrational changes within the analysed molecules. There are two main regions where various FTIR vibrational bands are found: a) the fingerprint region and b) the group frequency region. For the fingerprint region, the infrared spectrum is located between 1450 and 600 cm^{1}. This region is typically complex, and assigning all absorption peaks to the studied material is difficult.

In contrast, the infrared spectrum can be found in the 4000–1450 cm^{1} region for the group frequency region. Bands in the group frequency region typically have a reasonable separation and are associated with the stretching vibrations of diatomic units. This region is useful for structure elucidation and identifying organic compounds [243].

In ATR-FTIR, an infrared beam is directed onto an optically dense crystal with a high refractive index at an angle greater than the critical angle, inducing total internal reflection. Then, this internal reflection produces an evanescent wave that propagates beyond the surface of the crystal and into the sample that is in contact with the crystal. This evanescent wave penetrates the sample under analysis by a few microns (0.5 µm - 5 µm). When the sample subsequently absorbs energy in the infrared spectrum, the evanescent wave will be altered or attenuated (**Figure 2-3**) [244].

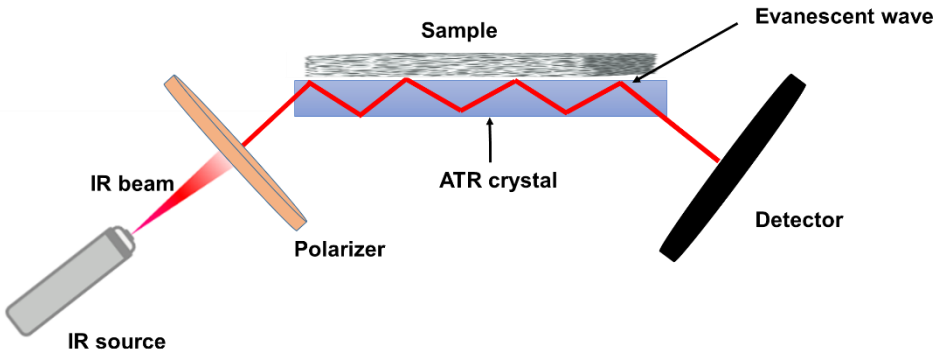


Figure 2-3: An ATR-FTIR system is depicted in a schematic representation. The infrared beam traverses the ATR crystal, which is overlaid by the sample on its upper surface. The evanescent wave penetrates the sample and undergoes absorption by the sample material. The system's polariser generates incident beams that are polarised in parallel and perpendicular orientations. Graph prepared by Biorender.

2.5 Time of Flight Secondary Ion Mass Spectroscopy (ToF-SIMS)

Time-of-Flight Secondary Ion Mass Spectroscopy (ToF-SIMS) is an advanced surface characterization technique used to analyze the composition of various materials, typically at the atomic or molecular

level. It is particularly sensitive, capable of detecting elements and compounds on the surface of a material down to the parts per million or even parts per billion in some cases [245]. The fundamental principle behind ToF-SIMS is the bombardment of a target material with a primary ion beam (often composed of ions like $Bi3^+$, Au^+, Ga^+, etc.). These ions have sufficient energy to cause the ejection of atoms or molecules (secondary ions) from the very outermost layers of the surface. The impact of the primary ions results in the ejection of secondary ions from the surface. These secondary ions are molecules, molecular fragments, or atoms from the surface of the sample, and they carry a positive or negative charge. The nature and behaviour of these ions depend on the sample's surface conditions and the characteristics of the primary ion beam (**Figure 2-4**).

After the secondary ions are ejected, they are subjected to an electric field that accelerates them into a flight tube. Since all ions are given the same kinetic energy, the speed of each ion is determined by its mass-to-charge ratio. Lighter ions will travel faster than heavier ones. The ions' "time of flight" through this tube (i.e., the time they take to reach the detector) is carefully measured and is used to determine each ion's mass-to-charge ratio. The ions eventually strike a detector after passing through the flight tube. The time from when they were ejected (due to the primary ion impact) to when they hit the detector is precisely measured. This time measurement is used to calculate the ions' mass-to-charge ratios, as it is directly related to this parameter. A spectrum representing the counts of ions (intensity) versus the mass-to-charge ratio is

generated. The analyst can then identify the presence of specific elements or compounds by interpreting this spectrum [246].

Moreover, ToF-SIMS can also create high-resolution images by rastering the primary ion beam across the surface and recording the intensity of specific secondary ions emitted from each spot. This process forms an image showing the distribution of elements or compounds across the area of the sample that was analysed.

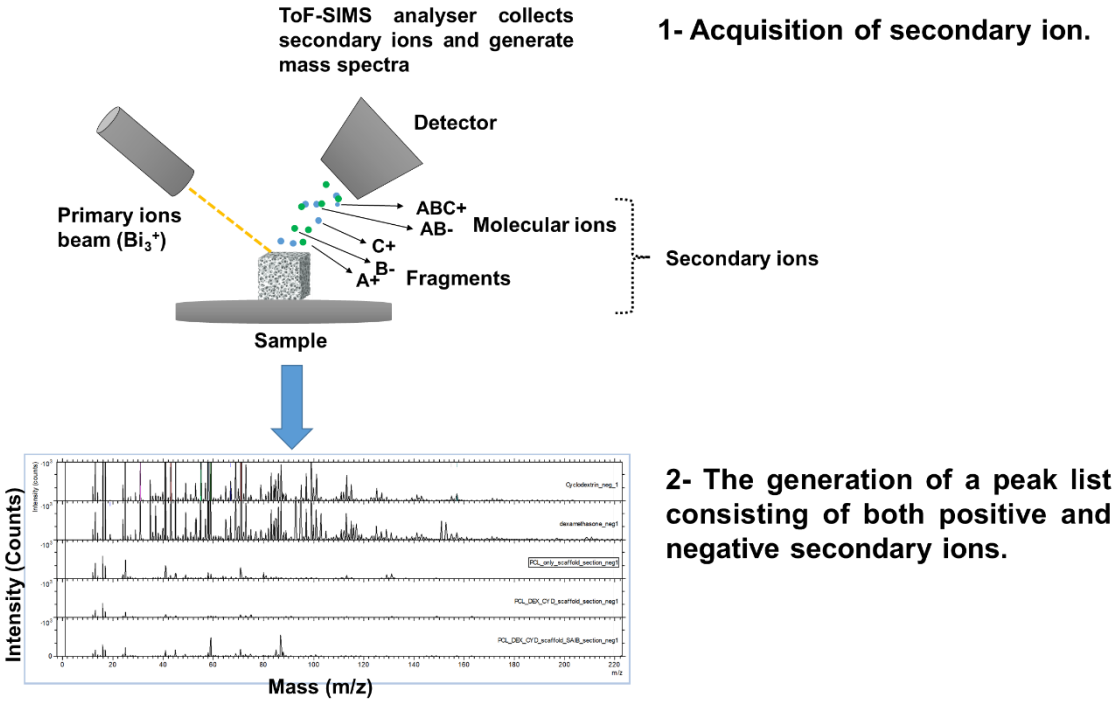


Figure 2-4: Data acquisition was performed utilizing Time-of-Flight Secondary Ion Mass Spectrometry (ToF-SIMS), and a representative spectrum was subsequently generated. The graphical representation was prepared by Biorender.

2.6 Mesenchymal stem cells (MSCs) culturing.

The osteogenesis study in this thesis was performed using immortalised human mesenchymal stem cells (MSCs). Primary MSCs derived from

human bone marrow (provided by TCS Cellworks, Buckingham, UK, catalogue number SC-7500) were immortalised by retrovirus-mediated transduction of the cells with human telomerase reverse transcriptase and the human papillomavirus E6 and E7 genes. This process was carried out by Dr Hassan Rashidi and Dr James Dixon (University of Nottingham, Nottingham, UK) and generously donated. MSCs were clonally selected due to the variation in differentiation potential among clones after immortalization and maintained in the lab according to the previous protocol [247]. Immortalised MSCs were evaluated on a regular basis to ensure that they could expand without losing their tri-lineage differentiation potential, which is the chondrogenic, osteogenic, or adipogenic lineage, in response to adequate differentiation stimuli. All cell culture experiments were conducted with aseptic techniques in a Class II biosafety cabinet. Cell cultures were maintained in a 37°C humidified atmosphere containing 5% CO_2 in the incubator.

2.7 Immunofluorescence assay

Immunofluorescence assay techniques are utilised to evaluate biomolecules' qualitative and quantitative distribution and expression levels in biological samples. The technique employs fluorescently labelled antibodies and fluorescence imaging techniques to detect and visualise target biomolecules in cells and/or tissue samples [248]. Methods of immunofluorescence utilised in this project are described in the following subsections.

2.7.1 Immunocytochemistry

Antigens of interest, such as proteins in cells or tissue samples, are targeted for detection or visualization. The target antigens can be detected using direct or indirect immunofluorescence, respectively (**Figure 2–5**). Both procedures utilise antigen-specific primary antibodies. The primary antibody in direct immunofluorescence is chemically bound to a fluorophore. Thus, the straightforward immunofluorescence technique involves a single incubation step with the target antigen.

On the other hand, indirect immunofluorescence uses two antibodies (two steps). In the first step, the unlabeled primary antibody is bound specifically to the target antigens. In the second step, the fluorophore-labelled secondary antibody is bound to the unlabeled primary antibody. In the indirect immunofluorescence method, several secondary antibodies can bind to a single primary antibody, allowing for greater SNR (signal-to-noise ratio) and fluorophore flexibility. The antigen-target-bound fluorophore can be visualised using a fluorescent microscope [249].

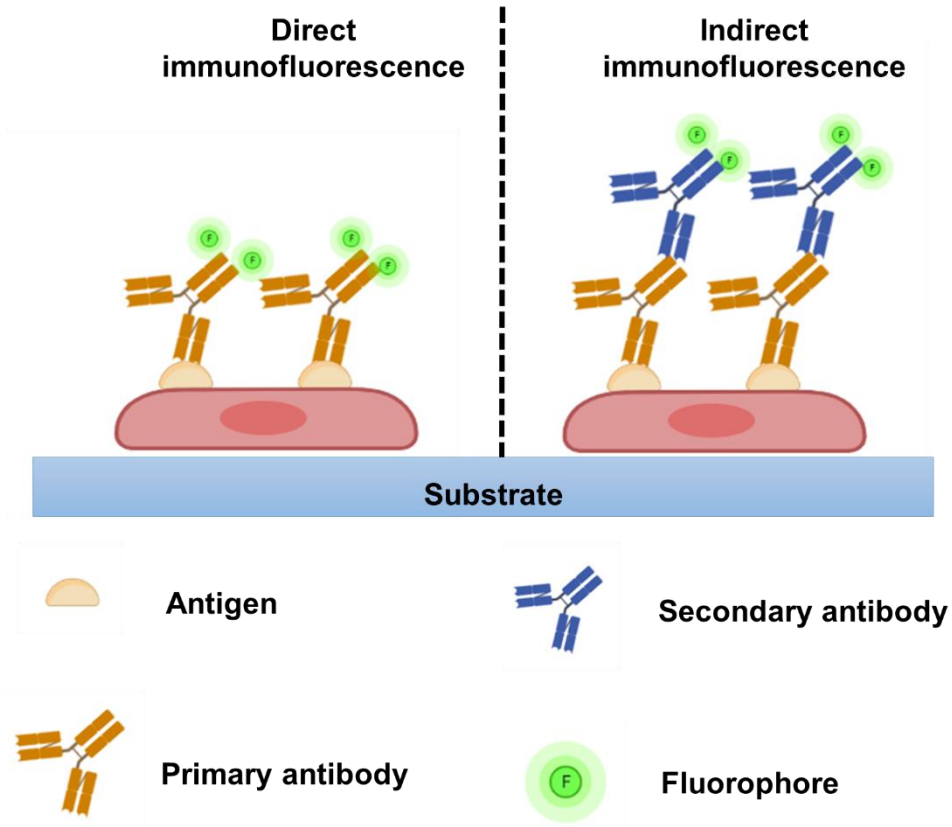


Figure 2-5: Direct and indirect immunofluorescent procedures. Figure made in Biorender.

2.7.2 Fluorescence microscopy

Fluorescence microscopy is used to visualise targeted antigens after immunocytochemistry procedures. Fluorescence imaging instruments consist of laser-scanning confocal microscopes, two-photon excitation microscopes, and wide-field microscopes. Sample type and imaging requirements determine the choice of the imaging instrument. Most of these microscopes are known as epifluorescence microscopes because the excitation and emission of light pass through the same objective [249].

A light source, excitation filter, dichroic, objective lens, emission filter, eyepiece, and CCD camera are the components of an epifluorescence microscope. Briefly, the light source produces a broad spectrum of light transmitted through the excitation filter. The excitation filter transmits the required light wavelength for this fluorophore while reflecting others. The transmitted light is then reflected onto the sample by the dichroic mirror, and the objective focuses on the sample. The fluorophores bound to the antibody absorb this excitation light, elevating the electrons' energy from the ground to the excited state. Afterwards, when the energy returns to its ground state, the fluorophore emits light with a longer wavelength than the excitation light, known as the "emitted light." The role of the objective lens is to collect the emitted light and transmit it through the dichroic to the emission filter; next, the emission filter transmits the appropriate wavelength of light to the eyepiece or CCD camera for sample visualisation. **Figure 2-6** shows a schematic representation of this

process.

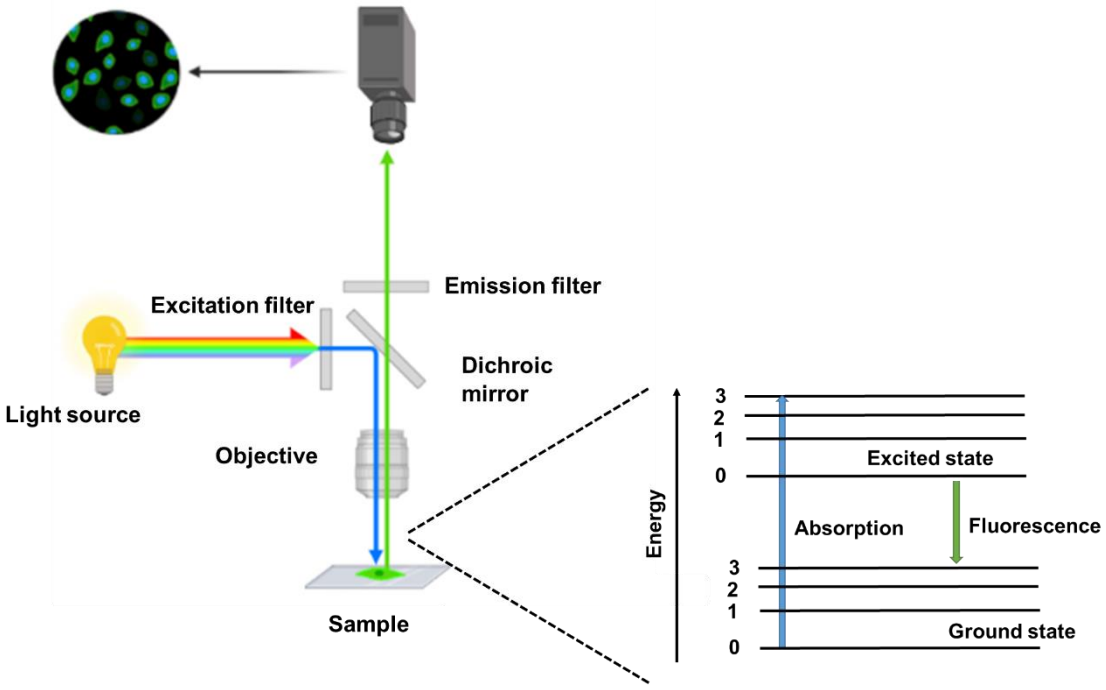


Figure 2-6: Schematic diagram visually represents the epifluorescence microscope. The Jablonski diagram illustrates the process of energy absorption and subsequent fluorescence emission. The figure generated by Biorender.

2.7.3 Enzyme-linked immunosorbent assay (ELISA)

ELISA is an immunological technique which considered highly sensitive and specific for detecting and quantifying antibodies, proteins, and peptides [250]. The antigen is first immobilised on a microplate surface and then complexed with an antibody conjugated to a reporter enzyme. The test is accomplished by measuring the activity of the reporter enzyme through incubation with an appropriate substrate to produce a measurable product that enables detection. Several ELISA methods are available, including sandwich, direct, and indirect methods (**Figure 2–7**).

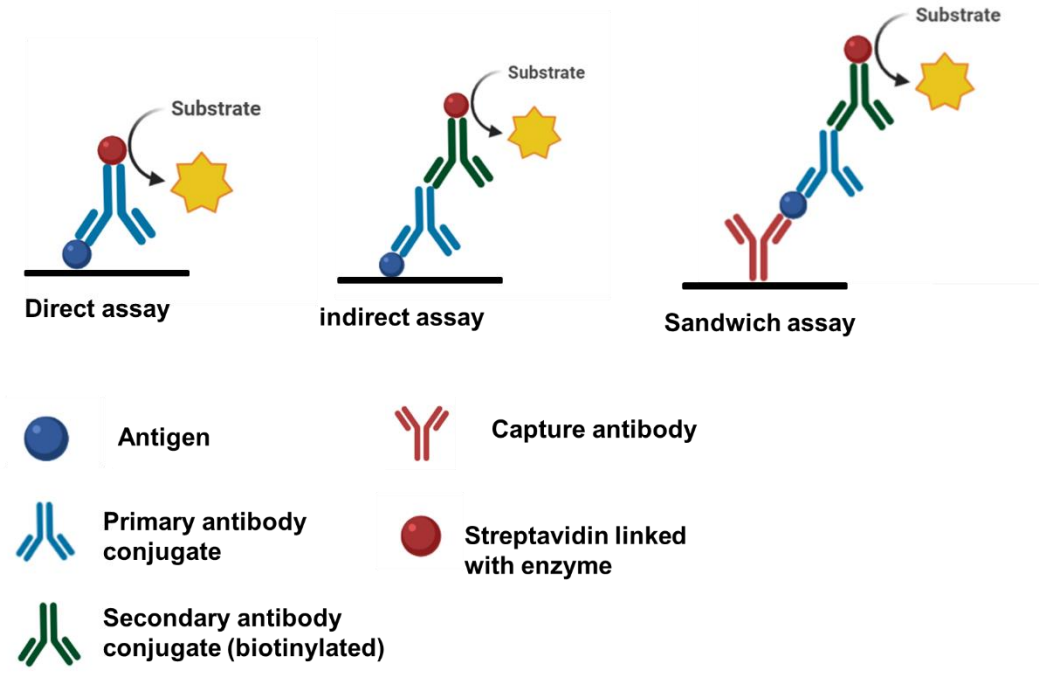


Figure 2-7: Various enzyme-linked immunosorbent assay (ELISA) techniques encompass direct, indirect, and sandwich assays. The schematic representation was created by Biorender.

The sandwich ELISA method is the most frequently employed ELISA technique and has been used in this thesis. This technique involves coating a microplate well with a capture antibody, upon which the antigen or analyte is captured. Then, a second antibody, the detection antibody, with a distinct epitope, is added to the wells. Thus, the analyte is sandwiched between two antibodies, each detecting a distinct antigen epitope. The antibody for detection is conjugated to a protein or coenzyme, such as biotin. After the antibodies have been incubated, a detection reagent is added. The detection reagent is streptavidin-horse radish peroxidase (HRP), which binds to the biotin-conjugated detection antibody due to its high affinity for biotin. With the assistance of HRP,

adding a colourless substrate reagent (tetramethylbenzidine or peroxide) produces a coloured product. The colour change is proportional to the concentration of the analyte. Then, a spectrophotometer can quantify this colourimetric change [250].

2.8 Polymerase Chain Reaction (PCR)

PCR is a biochemical technique used to duplicate a single DNA molecule into millions of copies. The process relies on the DNA polymerase's ability to synthesise complementary DNA from single-stranded DNA templates. The method of amplification consists of the following three steps: i) the denaturation step, in which double-stranded DNA is denatured by heat to produce single-stranded DNA. ii) The annealing step, in which primers, which are short DNA fragments aligned with single DNA strands, iii) The extension step, in which DNA polymerase extends the primers, producing two copies of the original DNA strand. These three actions form a cycle [251]. Reverse transcription-quantitative PCR (RT-qPCR) is a subset of methods employing this principle.

RT-qPCR is the most common technique for quantifying gene expression in biological samples. The extracted RNA must be reverse transcribed into complementary DNA (cDNA) using the enzyme reverse transcriptase in this approach. The resulting cDNA is then used as a template for the subsequent qPCR. qPCR is similar to PCR, with the addition of a fluorescent label that enables real-time quantification of amplification. The two most common fluorescent systems used in RT-qPCR are SYBER Green dyes for DNA binding and TaqMan probes for

hydrolysis. This research utilised DNA-binding SYBER Green dyes. These perform their function by emitting fluorescence when intercalated with dsDNA during the extension phase of the PCR. Each RT-qPCR run consists of 30 to 40 cycles, during which the emitted fluorescence is measured. The amount of target dsDNA present is proportional to the amount of fluorescence detected [252]. **Figure 2-8** illustrates a summary of the method.

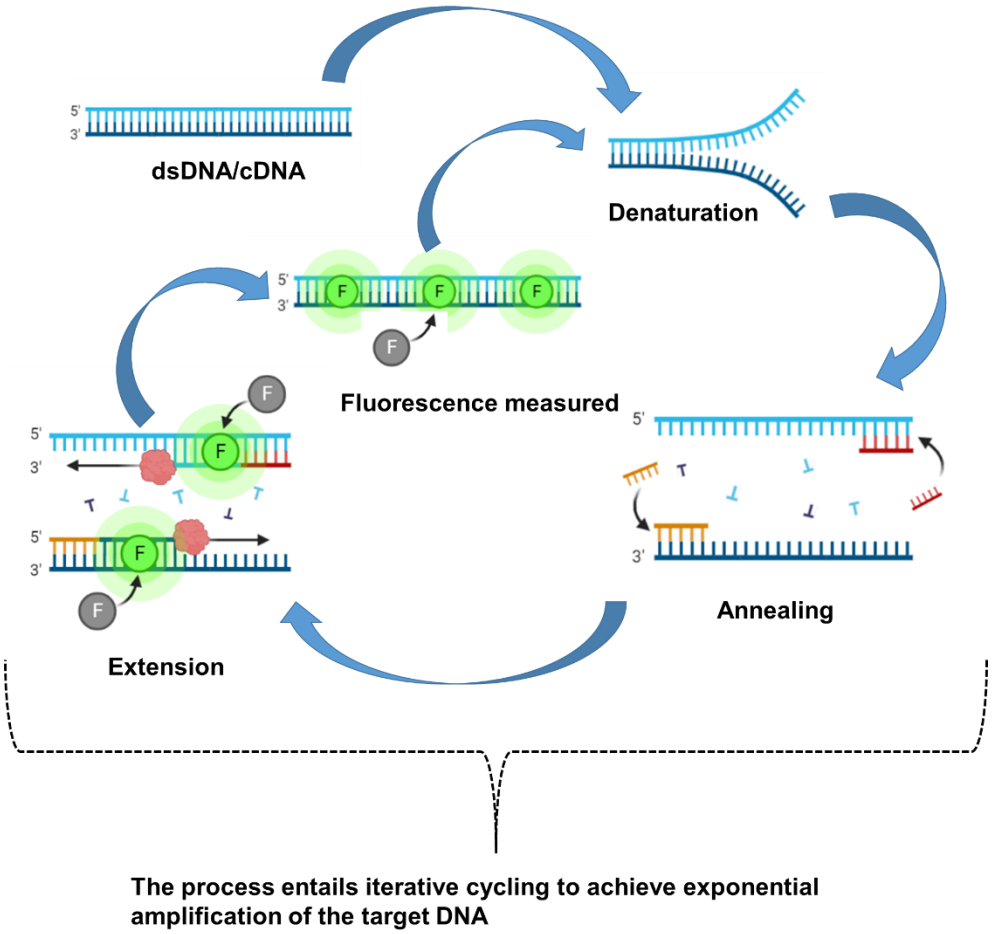


Figure 2-8 Depiction of the steps involved in reverse transcription-quantitative polymerase chain reaction (RT qPCR). The RT-qPCR process encompasses denaturation, annealing, and extension stages. Subsequently, fluorescence intensity is assessed, and the cycle is reiterated. The accompanying figure was generated by Biorender.

3. Chapter Three: Developing 3D printed scaffolds for the controlled release of dexamethasone

3.1 Introduction

Additive manufacturing (3D printing) is progressively utilised in tissue engineering applications due to its advantages in fabricating delicate structures that are challenging to manufacture using conventional fabrication processes [146, 147]. The capacity to precisely manipulate and recreate three-dimensional structures has made 3D printing an effective tool for fabricating scaffolds for tissue engineering purposes [148]. Various 3D printing techniques have been utilised to produce scaffolds for tissue engineering purposes, including fused deposition modelling (FDM), stereolithography (SL), selective laser sintering (SLS), and extrusion-based. Extrusion-based 3D printing is reportedly the most widely employed technique in the tissue engineering industry to fabricate scaffolds due to its relatively low cost and use of a wide range of materials, including polymers, ceramics, and hydrogels with or without cells [103, 147, 149, 150].

3D printed scaffolds, living cells, and bioactive drugs are the pillars of tissue engineering [8]. These scaffolds can be designed to mimic the natural extracellular matrix (ECM) of the tissue being engineered, allowing an ideal environment for cell attachment, infiltration, and angiogenesis [7]. Furthermore, these scaffolds can be tailored to the precise requirements of the regenerating tissue, including its size, shape, and mechanical properties [90-92]. Researchers are becoming

increasingly aware of the need for improved outcomes from scaffolds through control over the release of drugs that directly or indirectly influence cellular signalling or tissue regeneration. Therefore, there is an increasing desire to emulate the inherent complexity of natural tissue by delivering numerous bioactive molecules simultaneously, sequentially, or in multiphasic patterns. Researchers anticipate that precisely controlling the delivery of various stimuli across time will improve the rate, amount, and quality of tissue regeneration [253].

Moreover, besides the structural support, 3D printed scaffolds can be fabricated to encapsulate and release various therapeutic molecules, such as growth factors, cytokines, nucleic acids, antibiotics, and anti-inflammatory drugs [254], thus enabling the localised delivery of these molecules to promote tissue regeneration. Also, they can result in an enhanced biological response while avoiding the adverse effects of systemic delivery [255]. Various materials, such as natural materials, synthetic polymers, and composite materials (natural and synthetic), have been used to deliver therapeutic drugs in a controlled manner [256]. Currently, PLLA, polyglycolic acid (PGA), PLGA, and polycaprolactone (PCL) are the most frequently used synthetic polymers to fabricate drug delivery systems for tissue engineering [257].

Drugs can be incorporated within these polymers through three methods: the drug is mixed directly with the polymer and then 3D printed; the drug is impregnated into the 3D printed scaffold in drug solution; or the scaffold’s surface is coated with a layer of polymer, hydrogel, or nanoparticles containing drug [258, 259]. The drug is then released

through diffusion, erosion, or both. The amount and the period of drug release can be adjusted by altering the material's composition or the drug loading percentage [253, 260].

Although technological advancements in the area of controlled release still exist, several challenges affect the development of a control release system, including the difficulty of fine-tuning drug release without compromising the properties of the scaffold, fast burst release of the drug, drug properties such as solubility and biocompatibility, drug loading, synthesis, and manufacturing conditions of the release system, and the material properties used for control release construction [261-263]. However, the burst release is common and can be attributed to synthesis and manufacturing processes, the heterogeneity between drug and polymer properties (hydrophilicity and/or hydrophobicity), and the limited homogeneity of the drug within the polymer used in 3D printing [264].

It would be ideal to fabricate a control release system with high drug loading and reduced burst release. Therefore, several techniques have been developed to mitigate the burst release, such as the utilisation of cross-linkable polymeric coatings [265], increasing the density of crosslinking in the hydrogel and surface extraction [265], developing hybrid polymer composites [266], increasing the layer thickness of the coating in micro-encapsulation [267], and varying the composition of drugs and polymers. Moreover, chemical and covalent conjugation are considered an additional effective method for mitigating the burst release effect [268]. Unfortunately, many proposed methods for preventing burst

release include extra costly steps of fabrication or steps that reduce the percentages of drug loading or add new components.

Dexamethasone, a synthetic glucocorticoid anti-inflammatory drug, has gained popularity in bone tissue engineering research due to its ability to enhance osteogenic differentiation, inexpensive cost, and high stability [223]. At optimal concentrations between 10 and 100 nM, dexamethasone stimulates bone growth by boosting the development and maturation of mesenchymal stem cells into osteoblasts [223]. However, it is critical to consider the concentration when administering dexamethasone, as it has been observed that concentrations above 1000 nM demonstrate toxic effects, and prolonged treatment with dexamethasone has also been linked to osteoporosis [224-226].

Previous studies have used polymers with added surfactants to assess drug-release behaviour from various 3D printed delivery systems. These systems were fabricated using fused deposition modelling (FDM) 3D printing. In FDM printing, the polymer, drug, and surfactant combinations are first hot-melt extruded to manufacture the filament. The filament is then loaded into the printer to be printed [115, 269, 270]. While FDM has many advantages, there are several drawbacks when it comes to fabricating drug-loaded scaffolds, including polymer oxidation due to high temperatures. Also, some drugs are sensitive to high temperatures and can be degraded during printing [271]. However, the controlled release of dexamethasone with reduced burst release from PCL has not been reported from 3D printed scaffolds prepared by direct ink writing (DIW) at the time of thesis writing.

This chapter aimed to develop a novel ink material that could be readily employed in direct ink writing to fabricate 3D printed scaffolds and be capable of controlling dexamethasone release. Thus, it has been hypothesised that surfactants could play an important role in controlling the release of dexamethasone from the 3D printed PCL scaffolds, reducing the initial burst release and achieving a more sustained therapeutic effect. In particular, the surfactants used in this study exhibit various degrees of hydrophilicity and hydrophobicity. Therefore, different hydration levels can be anticipated, which could affect the release of dexamethasone from 3D printed scaffolds.

To achieve that, PCL was blended with a series of FDA-approved non-ionic surfactants, Pluronics F127, F68, and L31. These surfactants are triblock (ABA type) copolymers composed of poly-ethylene oxide (PEO)/poly-propylene oxide (PPO)/poly-ethylene oxide (PEO) and exhibit a wide range of hydrophilicity and hydrophobicity due to the ratio of PEO/PPO [272]. Moreover, PCL was blended with sorbitan monooleate (Span80) and sucrose acetate isobutyrate (SAIB). Both Span 80 and SAIB are water-insoluble and were used in drug delivery to modify the release behaviour [272, 273].

3.2 Materials and Methods

3.2.1 Chemicals

Polycaprolactone (PCL) (440744-250G) (Mn 80,000) , dexamethasone-cyclodextrin (DEX-CYD) (D2915-100MG), methanol (439193), dichloromethane (DCM) (560463), dexamethasone (D1756-100MG), sucrose acetate isobutyrate (SAIB) (W518107-1KG-K), sorbitan monooleate (Span80) (S6760-250ML), and poloxamers F127 (P2443-250G), and L31 (435406-250ML) were purchased from Sigma-Aldrich, UK. F68 (A1288,0100) was purchased from ITW reagents, UK.

3.2.2 Ink preparation and 3D printing of scaffolds loaded with DEX-CYD

To prepare PCL/DEX-CYD scaffolds. DEX-CYD complex was added to DCM at three different concentrations (0.77%, 1.54%, and 3.85% wt/wt, corresponding to 0.05%, 0.1%, and 0.25% wt/wt of dexamethasone). PCL was then added to the drug solutions at a concentration of 57% wt/vol (PCL/DCM). On the other hand, different formulations of PCL with nonionic surfactants of poloxamers (F127, F68, and L31), Span80, and sucrose acetate isobutyrate (SAIB) were added to PCL at two mass ratios (70:30 and 60:40, PCL: excipient) to reach a final concentration of 57% wt/vol in DCM. DEX-CYD was added at a concentration of 2.63% wt/wt (equivalent to 0.17% wt/wt dexamethasone). Afterwards, all inks were left on the roller overnight to completely dissolve before printing. Lattice scaffolds with a dimension of 10 x 10 x 5 mm^3 were designed by BioCAD^{TM} software (regenHU, Switzerland). PCL solutions were printed by a 3D Discovery printer (regenHU, Switzerland) through a tapered tip

(31G, 160 μm internal diameter, Integrated Dispensing Solutions) with the following parameters: strut spacing of 0.52 mm edge-to-edge, a speed rate of 10 mm/s, a layer thickness of 0.12 mm, and 6 bar of pressure.

3.2.3 Dexamethasone Microcrystals preparation

Dexamethasone microcrystals were prepared by the standard precipitation method. Dexamethasone was dissolved in 0.3 ml of methanol (30 mg/ml), injected into 2.7 ml of deionized water containing 0.5% (w/v) or 1% (w/v) F127, and left on a magnetic stirrer with an agitation speed of 1000 RPM in a fume hood at room temperature. The solution was kept for 6h to allow for methanol evaporation. After that, suspended dexamethasone crystals were freeze-dried for 48h [274].

3.2.4 Dexamethasone Microcrystal Characterisation.

The particle size was confirmed by using a scanning electron microscope (JEOL JSM-6490LV, U.K.) operated at an accelerating voltage of 15 kV with varying magnification (50-1,300x). Sample preparation involved depositing a single drop of the dexamethasone particle suspension onto conductive carbon tape (double-adhesive) fixed on the surface of the sample stub, followed by drying at ambient temperature. The samples were placed in a vacuum sputter coater chamber (Leica EM SCD005 sputter coater) and coated with gold for 90 seconds using an accelerating voltage of 25 mA.

3.2.5 Surface characterisation of 3D printed scaffolds

The topographies, diameters of printed struts, and pore interconnectivity of the 3D printed scaffolds were visualised by a scanning electron microscope (JEOL JSM-6490LV, U.K.) operated at an accelerating voltage of 15 kV with varying magnification (50-1,300x). Firstly, a conductive carbon tape (double-adhesive) was fixed to the surface of the sample stub. After that, all scaffolds were cut and mounted on the stubs. Then, samples were placed in a vacuum sputter coater chamber (Leica EM SCD005 sputter coater) and coated with gold for 90 seconds using an accelerating voltage of 25 mA.

3.2.6 SEM Images analysis

The Struts, and pore sizes of 3D printed scaffolds, and dexamethasone microcrystals sizes were analysed from SEM images by ImageJ (FIJI virsion) (NIH,USA). SEM images of 3D printed scaffolds (50x, and n=8 images), and dexamethasone microcrystal (1,300x, and n=8 images). Images were imported into ImageJ, the scale was calibrated by drawing a straight line over the known scale bar of the imported image. Afterwards, the "set scale" function from the analyze menu was used to set the scale. Subsequently, the area of interest were selected by drawing a straight line on the strut diameter, or the pore from edge to edge. These measurements were obtained by executing the 'Measure' functions within ImageJ. The recorded data is then analyzed by calculating the mean diameter and standard deviation of struts and pores (**Appendix Figure 7-1**).

3.2.7 Differential Scanning Calorimetry

The melting point (T_m) and glass transition (T_g) of pure PCL, Dexamethasone-Cyclodextrin, and all 3D printed PCL scaffolds were obtained using the TA Discovery Q 2000 differential scanning calorimetry (DSC) instrument with a refrigerated cooling unit (TA Instruments, New Castle, Delaware). Samples were weighed within the 5–10 mg range, loaded into Tzero Hermetic pans, and sealed with lids. The samples were then heated from 25 to 200 °C at 5 °C/min with a flow rate of nitrogen gas of 50 ml/min. The thermogram of each sample was recorded using TRIOS data analysis software and plotted by OriginPro 2022 (OriginLab Corporation, Northampton, MA, USA). The crystallinity (X_c) value was calculated according to [275].

$$\boldsymbol{Xc = \left(\frac{\Delta Hm}{\Delta Hm\ (crys)}\right) X100} \qquad \textbf{(3.1)}$$

Where ΔH_m is the enthalpy of melting, and $\Delta H_{m\ (crys)}$ is the endothermic enthalpy of perfect crystalline PCL, which is 139.6 J/g [275].

3.2.8 Attenuated Total Reflectance- Fourier Transform Infra-Red Spectroscopy (ATR-FTIR)

The spectra of 3D printed scaffolds were obtained using an ATR-FTIR spectrometer (Agilent Technologies FTIR, Cary 360, Santa Clara, CA, USA). A small amount of each sample, about 5–10 mg, was used and placed on the FTIR crystal diamond plate. After that, the spectra of the samples were obtained in absorbance mode in the spectral region of 600 to 4000 cm^{-1}, utilising a scanning resolution of 8 cm^{-1} [29].

3.2.9 Time of Flight Secondary Ion Mass Spectroscopy (ToF-SIMS)

Analysis was conducted using a ToF-SIMS IV instrument (IONTOF, GmbH) using monoisobic Bi_3^+ primary ion source operated at 25 keV (High current bunched mode), and a pulsed target current of ~0.3 pA were employed for surface analysis. Dual-beam dynamic SIMS was conducted using a 20 keV Ar_{1900} gas cluster ion beam (GCIB) with a target current of 10 nA as a sputter beam and a 25 keV Bi_3^+ analysis beam with a pulsed target current of ~0.3 pA. Non-interlaced depth profiling was employed, whereby the sputter and analysis ion beams operate at alternating intervals with 5 frames of sputtering per 1 analysis frame and a 0.5 s pause between the sputtering and analysis. A region of 500 µm × 500 µm was sputtered, and a 200 µm × 200 µm region was analysed with pixel density 128 × 128. The polarity used was negative, and the total ion dose was 5.38 x 10^{16} ions/cm^2. The static limit of the primary ion is ≤10^{12} ions/cm^2. The current of the electron flood gun for charge neutralisation approximately 10uA. Data analysis of the measurements were carried out with the IonToF software SurfaceLab7 (IONTOF GmbH). Positive ion spectra were mass calibrated to the $CH3^+$, $C2H5^+$, $C5H6^+$ and $C7H7^+$ peaks, while the negative spectra were calibrated to $C2^-$, OH^-, $C4H^-$ and $C6H^-$ peaks prior to further analysis. Peak lists (mass list) comprising of all detected secondary ions, with molecular mass (m/z) from 10 to 550 were compiled. Subsequently, peak (or ion) intensities for each spectrum were normalised to total ion intensity counts, to correct for differences in the total secondary ion yields between different spectra [276].

3.2.10 *In vitro* release of dexamethasone

All 3D printed PCL scaffolds loaded with DEX-CYD were incubated in 10 mL of PBS (pH 7.4) or RPMI basal media at 37 °C, shaking for intervals. At each interval, 10 mL of incubation medium was withdrawn and replaced with 10 mL of PBS at 2, 4, 6, 12, 24 h, and every 2 days. Dexamethasone concentration was measured using a UV-vis spectrophotometer with dual light source and spectral bandwidth of 1.5 nm (Agilent Technologies, UK) by measuring the absorption at 241 nm. The measurements were conducted at room temperature. PBS alone or RPMI alone were used as a blank. The unknown concentrations were quantified based on the calibration curve of known concentrations of dexamethasone. The limit of detection (LOD) and limit of quantification (LOQ) were determined based on the blank (PBS) [277].

$$\textbf{Amount of drug loaded(mg)} = \textbf{weight of scaffold x ratio of drug loaded} \quad \textbf{(3.2)}$$

Where the ratio of drug: polymer = 1:570 (0.17% wt/wt) or 4:570 (0.7% wt/wt)

$$\textbf{Drug release } (\%) = \left(\frac{\textbf{Amount of drug released in medium}}{\textbf{Weight of loaded drug in scaffold}}\right)\textbf{X100} \quad \textbf{(3.3)}$$

$$\text{LOD} = X_b + 3S_b \qquad \text{LOQ} = X_b + 10S_b \quad \textbf{(3.4)}$$

Where X_b is mean, and S_b is the standard deviation of the blank.

3.2.11 Drug release kinetics

A zero-order equation, a first-order equation, the Higuchi equation, and the Krosmeyer-Peppas equation were used to fit the release profiles of dexamethasone according to the following equations [278]:

- **Zero-Order**

$$f_i = k_o \cdot t \qquad (3.5)$$

Where f_i indicates the fraction of drug dissolved in time t, with the zero-order release rate constant k_0. The data generated form the zero-order model is plotted as cumulative % of drug released vs time.

- **First-Order**

$$log\ C = \log Co - kt/2.303 \qquad (3.6)$$

In which Co is the initial concentration of the drug, **k** is the first-order release rate constant, and **t** is the time. The data generated form the first-order model is plotted as log cumulative % of drug remaining vs time which would produce a straight line with a slope of -K/2.303.

- **Higuchi model**

$$F = k_H \cdot t^{1/2} \qquad (3.7)$$

k_H represents the Higuchi release rate constant. The data obtained from the Higuchi model is typically plotted as cumulative % drug release versus the square root of time.

❖ **Krosmeyer–Peppas Model**

$$M_t / M_\infty = kt^n \qquad \textbf{(3.8)}$$

Where M_t / M_∞ represents the fraction of drug released at time **t**, **k** is the Korsmeyer-Peppas release rate constant, and **n** describes the release mechanism. In the Korsmeyer-Peppas model, the value of n describes the drug's release mechanism. When n ≤ 0.43, it suggests that the drug release is controlled by Fickian diffusion, whereas when n ≥ 0.85, the drug release is governed by an erosion. In addition, for n values between 0.85 and 0.43, drug release is governed by two mechanisms: diffusion and erosion. In this model, data gained from *in vitro* drug release studies is usually plotted as log cumulative % drug release versus log time.

3.3 Results

3.3.1 Ink preparation and 3D printed scaffold characterisation

Figure 3-1 depicts a schematic overview of the steps of PCL inks used for scaffold preparation. We implemented a one-step fabrication method to ensure a uniform composition and distribution of dexamethasone within the ink and the resultant 3D printed scaffolds. Initially, we prepared PCL with different concentrations of dexamethasone-cyclodextrin (DEX-CYD) scaffolds to assess the effect of concentration on the release behaviour. A calculated amount of dexamethasone-cyclodextrin corresponding to 0.05, 0.1, and 0.25% of dexamethasone (wt/wt drug/polymer weight) was dissolved in DCM. Then PCL was added at a final concentration of 57% wt/vol (PCL/DCM). The concentration of PCL

in this study was chosen based on a previous study [197]. The polymer ink was viscous and able to hold its shape in static conditions; it was also able to be transferred to the printing cartridge and solidify after printing immediately after DCM evaporation. The addition of dexamethasone at 0.05, 0.1, and 0.25% wt/wt to PCL was shown to be soluble in PCL ink with no visible precipitation of the drug (**Figure 3-2**).

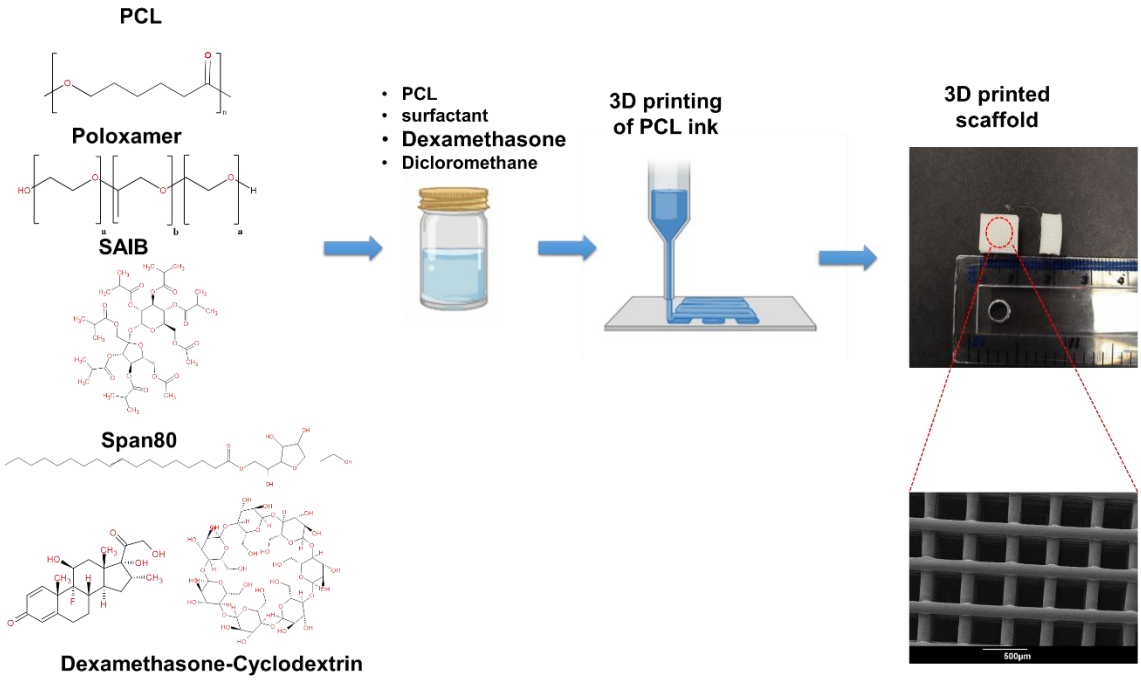


Figure 3-1: Schematic diagram showing PCL ink preparation, 3D printing.

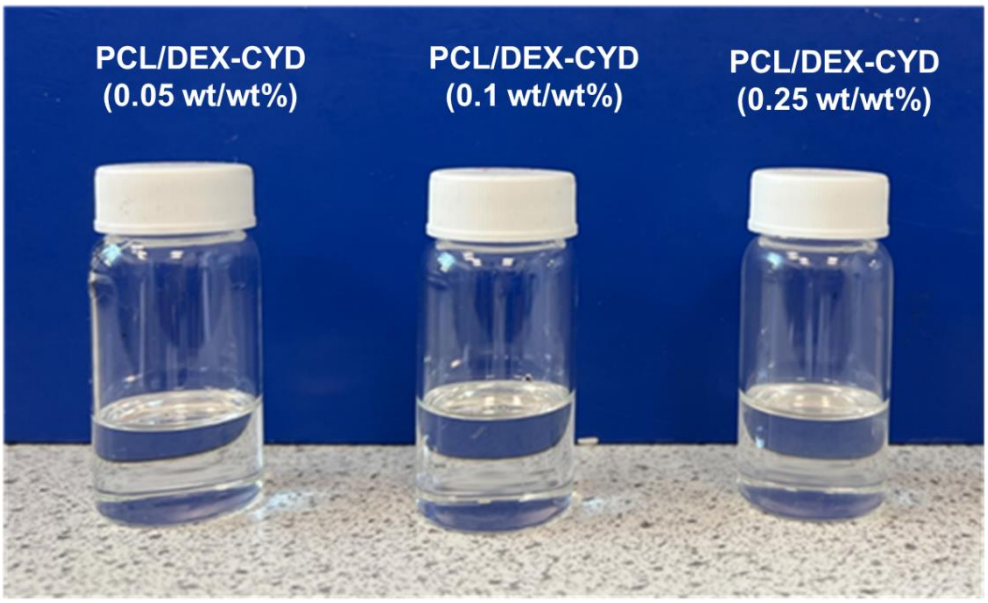


Figure 3-2: Images of different concentrations of dexamethasone-cyclodextrin dissolved with PCL in DCM.

PCL inks composed of 0.05% and 0.1% dexamethasone (wt/wt drug/polymer weight) were successfully 3D printed by direct ink writing. **Figure 3-3A-B** shows the success of 3D printing PCL/DEX-CYD 0.1% wt/wt scaffold, also demonstrating the maintained lattice shape and interconnected pores of the 3D printed structure. However, the ink containing 0.25% wt/wt of dexamethasone clogged the nozzle during printing (**Figure 3-4**). This clogging could be attributed to drug aggregation in the polymer due to the decreased drug solubility in the PCL polymer. When these aggregated particles reach the nozzle, they obstruct the ink flow and block the nozzle.

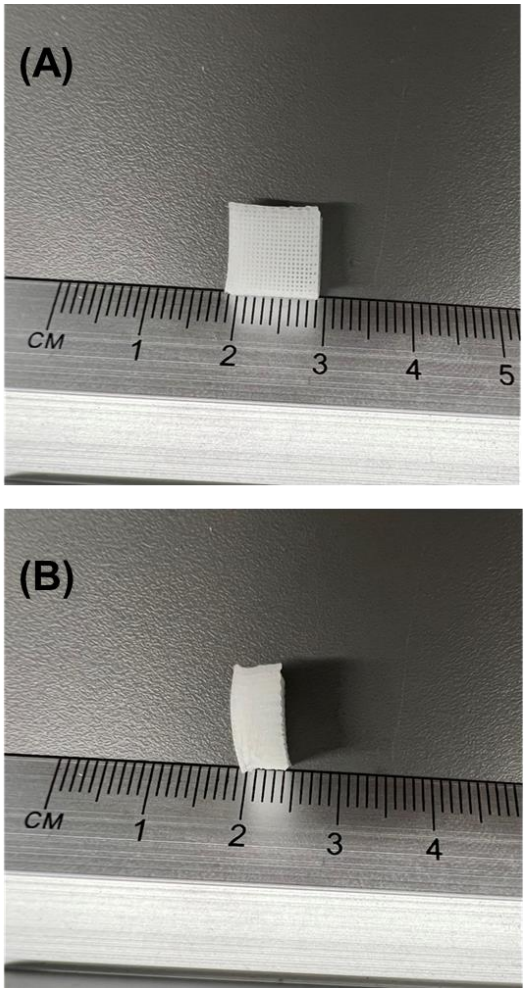


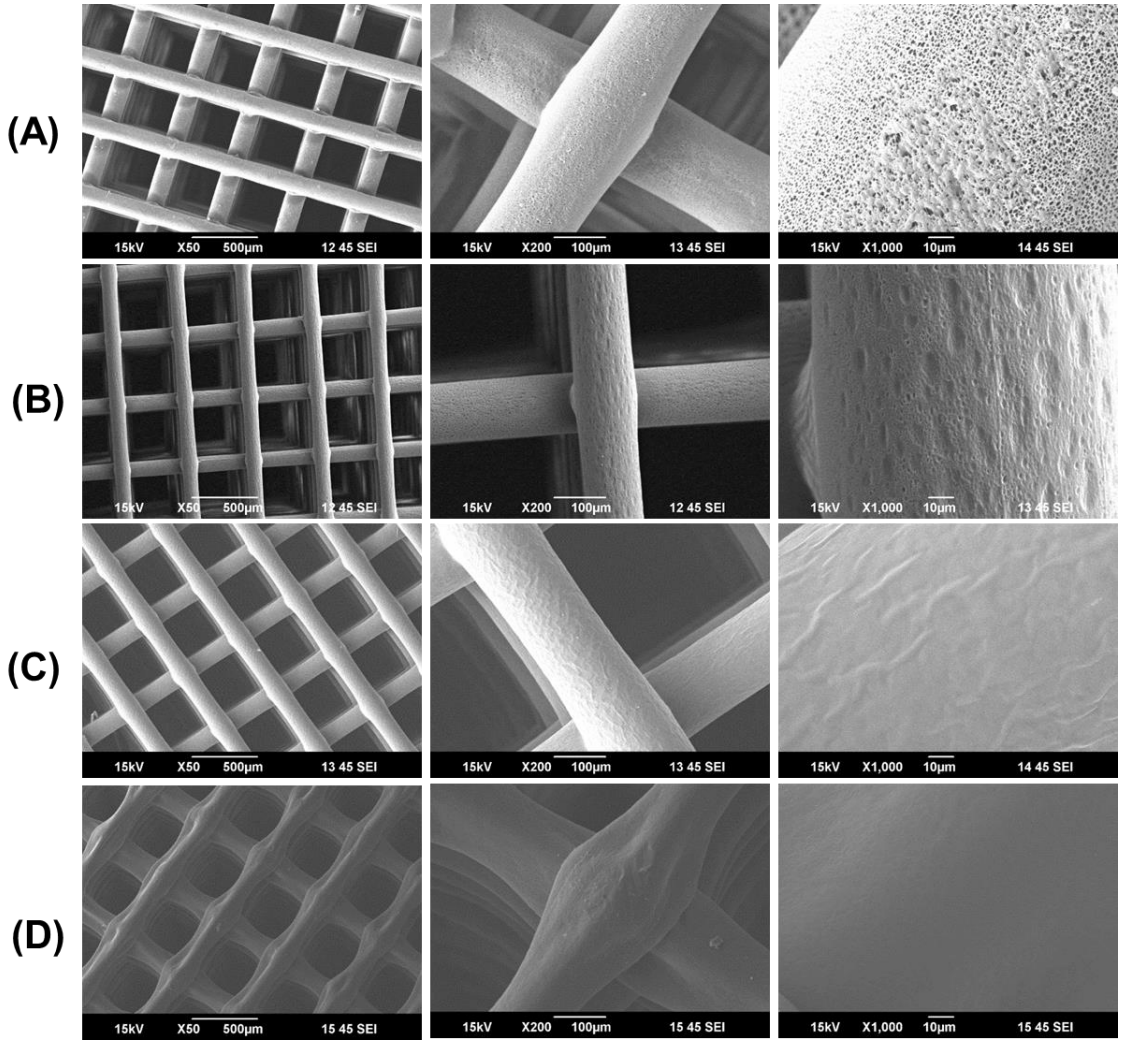
Figure 3-3: 3D printed lattice PCL scaffold composed of 0.1% wt/wt of dexamethasone, showing the top view (**A**) and side view (**B**).

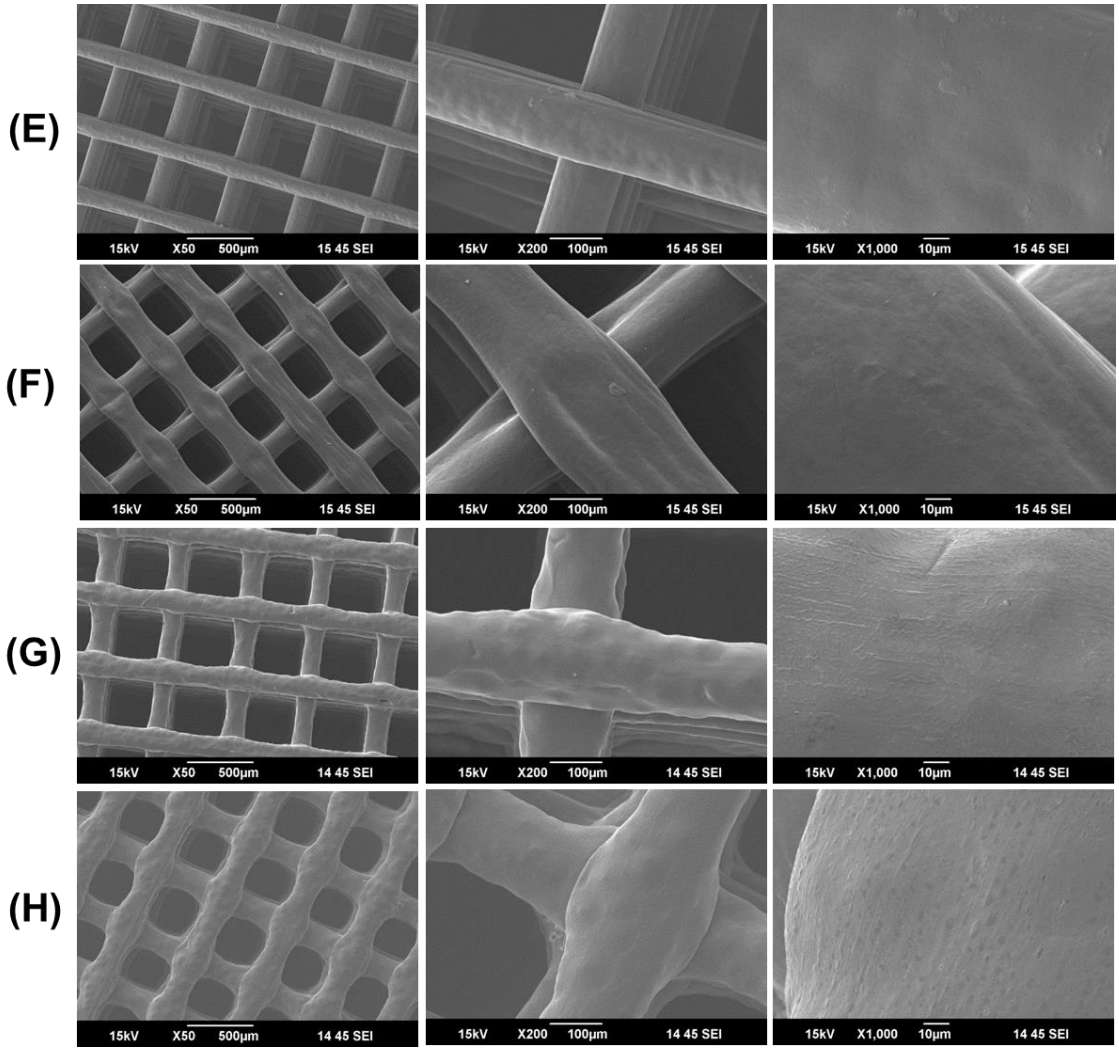


Figure 3-4: Nozzle clogged during printing with PCL ink contained 3.85% wt/wt of dexamethasone-cyclodextrin, corresponding to 0.25% wt/wt of dexamethasone.

The objective of the study was to investigate the impact of surfactants on the release profile. For this purpose, a concentration of dexamethasone below 0.25% wt/wt was selected to prevent potential nozzle blockage. To achieve this, a precise quantity of dexamethasone-cyclodextrin, corresponding to 0.17% dexamethasone (wt/wt drug/polymer weight), was dissolved in DCM, equivalent to 1 mg/ml in DCM before the addition of PCL. Several formulations with varying concentrations of F127, F68, L31, Span80, and SAIB (30 and 40%) (wt/wt surfactant/polymer weight) were then combined with the PCL polymer to reach a final concentration of 57% wt/vol in DCM. The resulting inks exhibited homogeneity without any drug precipitation.

SEM micrographs of 3D printed scaffolds with varying concentrations of F127, F68, L31, Span80, and SAIB captured by scanning electron microscopy (SEM) demonstrate the struts and pore sizes. The top view shown in **Figures 3-5 A–L** demonstrates the success of the struts' deposition during printing and the pore sizes across the different scaffolds. Noticeably, PCL and PCL/DEX-CYD scaffolds showed micropore formation on the struts' surface (**Figures 3-5A and B**). This may be due to the rapid evaporation of the organic solvent and the consequent evaporation-induced phase separation [279]. Meanwhile, these pores have no appearance at the junctions of struts. This may be attributed to the relatively slower evaporation of the organic solvent in these areas [279, 280]. On the other hand, these micropores were not seen on the surface of the scaffolds containing F127, F68, L31, Span80, and SAIB (**Figures 3-5K and L**). Adding surfactants to the PCL is believed to slow organic solvent evaporation and reduce phase separation [266, 281]


(A)
15kV X50 500µm 12 45 SEI
15kV X200 100µm 13 45 SEI
15kV X1,000 10µm 14 45 SEI
(B)
15kV X50 500µm 12 45 SEI
15kV X200 100µm 12 45 SEI
15kV X1,000 10µm 13 45 SEI
(C)
15kV X50 500µm 13 45 SEI
15kV X200 100µm 13 45 SEI
15kV X1,000 10µm 14 45 SEI
(D)
15kV X50 500µm 15 45 SEI
15kV X200 100µm 15 45 SEI
15kV X1,000 10µm 15 45 SEI


(E)
15kV X50 500µm 15 45 SEI
15kV X200 100µm 15 45 SEI
15kV X1,000 10µm 15 45 SEI
(F)
15kV X50 500µm 15 45 SEI
15kV X200 100µm 15 45 SEI
15kV X1,000 10µm 15 45 SEI
(G)
15kV X50 500µm 14 45 SEI
15kV X200 100µm 14 45 SEI
15kV X1,000 10µm 14 45 SEI
(H)
15kV X50 500µm 14 45 SEI
15kV X200 100µm 14 45 SEI
15kV X1,000 10µm 14 45 SEI

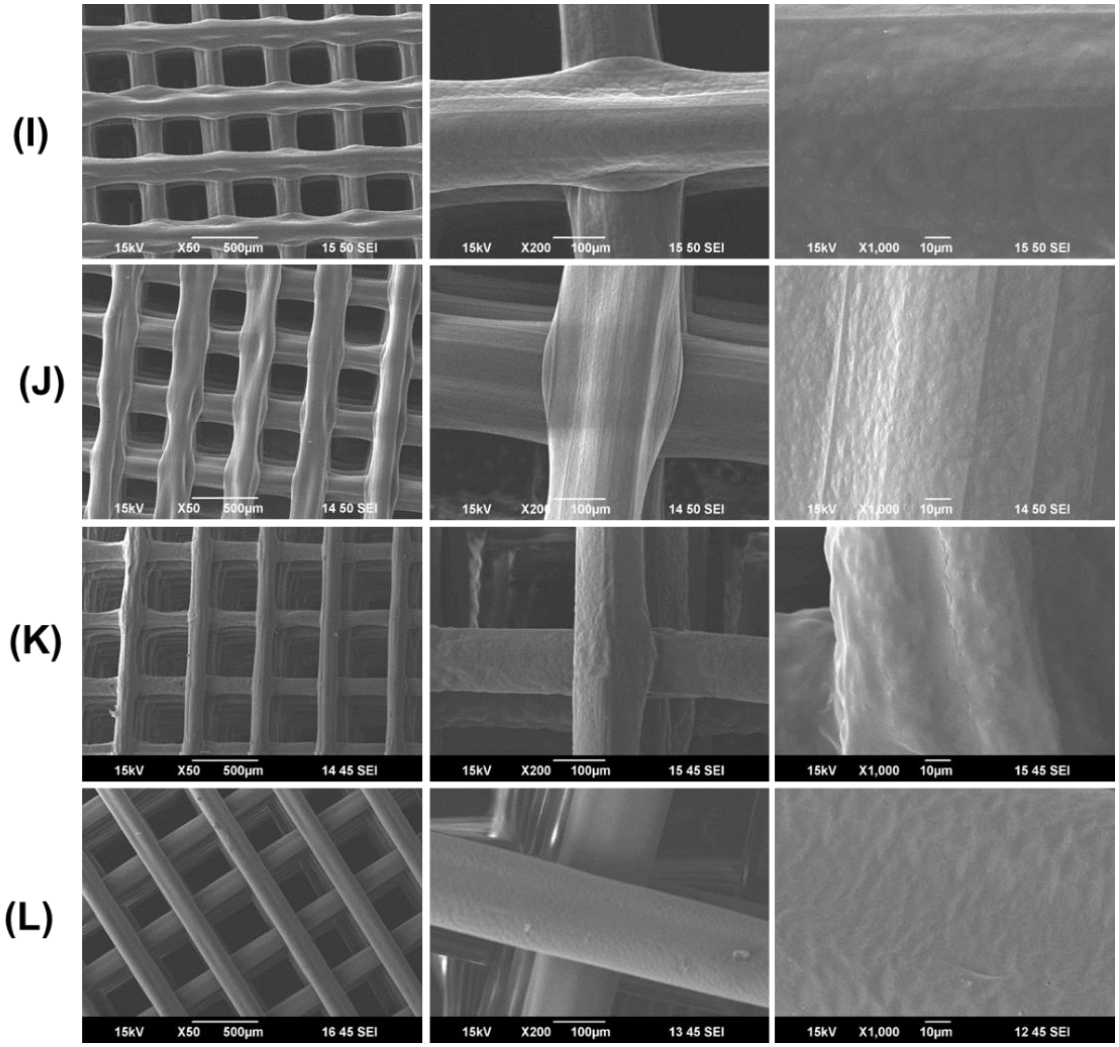


Figure 3-5: SEM micrographs for 3D printed PCL scaffolds loaded with 0.17% wt/wt DEX-CYD under different magnifications (X50, X200, and X1000) show the struts' morphology, strut sizes (edge-to-edge) of the strut, and pore shape (square). (**A**) PCL ONLY; (**B**) PCL/DEX-CYD (**C**) PCL/F127 (70:30). (**D**) PCL/F127 (60:40). (**E**) PCL/F68 (70:30). (**F**) PCL/F68 (60:40). (**G**) PCL/Span80 (70:30). (**H**) PCL/Span80 (60:40). (**I**) PCL/L31 (70:30). (**J**) PCL/L31 (60:40). (**K**) PCL/SAIB (70:30). (**L**) PCL/SAIB (60:40).

As shown in **Figure 3-6A**, scaffolds containing 40% wt/wt of F127, F68, Span 80, and L31 showed strut diameters higher than the internal diameter of the nozzle, which is 160 µm. This may be attributed to the die-swell effect [282]. This effect was not seen in scaffolds containing SAIB, which showed a diameter smaller than the ID of the nozzle. On the other hand, the porosity of scaffolds is essential for directing cells and the development of new tissue growth [92]. It has been found that a minimum pore size of 100 to 150 µm is required for bone tissue formation in scaffolds [89, 95]. The images showed pores larger than 300 µm (**Figure 3-6B**). This size is believed to promote bone growth and vascularization, according to [95].

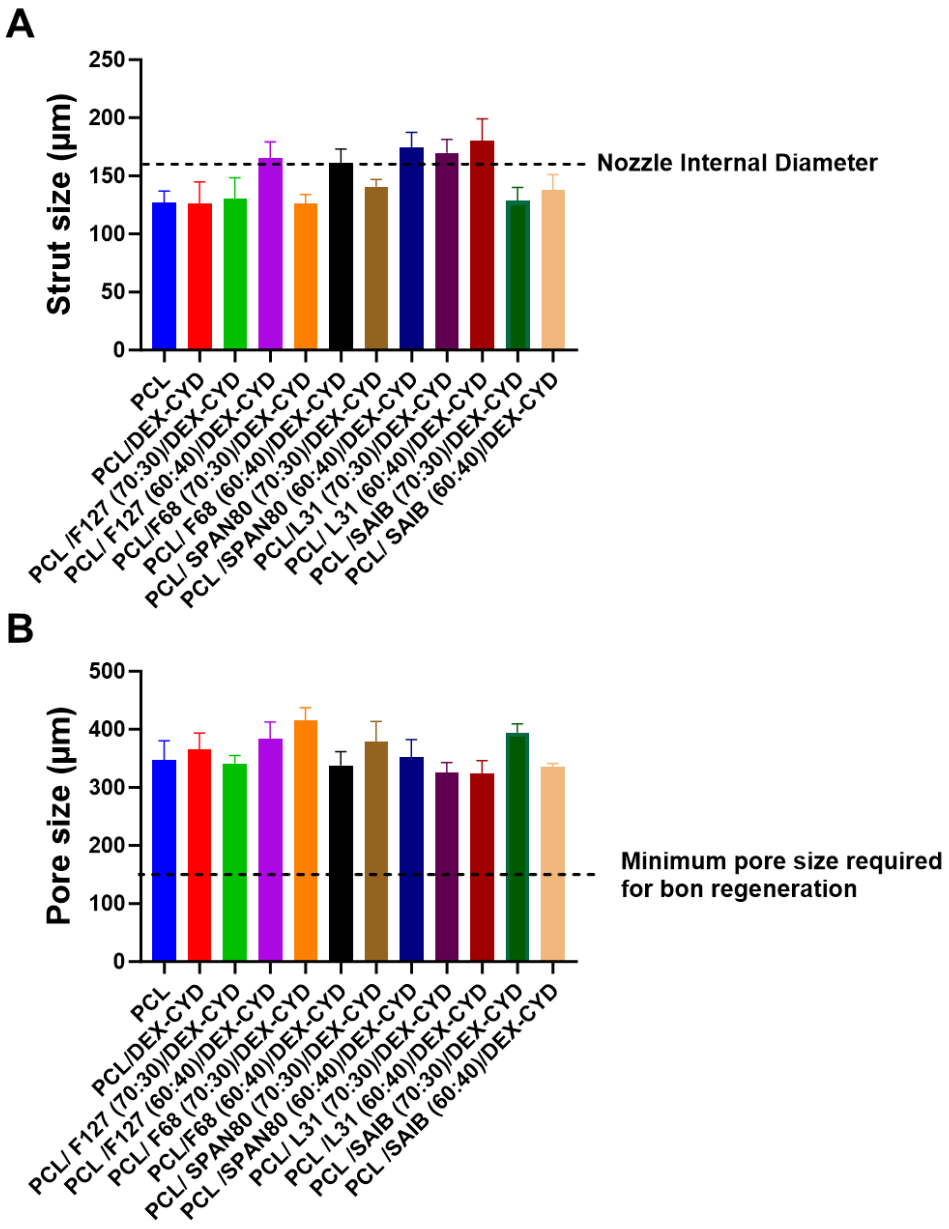


Figure 3-6: Strut diameter measurements and pore sizes from edge to edge of 3D printed scaffolds were calculated using ImageJ. (**A**) The measured pore sizes for all 3D printed scaffolds (**B**) The measured strut sizes for all 3D printed scaffolds Results are represented as mean ±SD (n = 8).

3.3.2 Fabrication of 3D printed PCL scaffolds with high drug loading using dexamethasone microcrystal (DEX-MC)

In the previous **section 3.3.1** of PCL ink preparation, we increased the DEX-CYD concentration to 3.85% wt/wt (corresponding to 0.25% wt/wt of dexamethasone) and tried to print with it. This concentration blocked the nozzle during printing due to drug aggregation in polymer due to the decreased drug solubility in PCL polymer. When these aggregated particles reach the nozzle, they obstruct the flow of the ink and block the nozzle. Therefore, I used dexamethasone microcrystals to fabricate a high drug loading 3D printed PCL scaffold. Printing PCL scaffolds with high drug loading can maintain the therapeutic efficacy of the released drug over an extended period of time. Moreover, to avoid the possibility of nozzle blockage during printing, I have reduced the drug particle size by utilising the basic anti-solvent precipitation method to prepare dexamethasone microcrystals.

3.3.2.1 Characterisation of dexamethasone microcrystal (DEX-MC)

Using a basic antisolvent precipitation procedure shown in (**Figure 3-7**), dexamethasone was dissolved in methanol and subsequently injected into a vial containing the anti-solvent. The anti-solvent contained deionized water and poloxamer F127 as a stabilizer. The purpose of adding F127 as stabilizer because surfactants can inhibit the coagulation or flocculation of particles by forming a protective layer around them. This electrostatic or steric stabilization prevents particles from coming into close contact, thereby maintaining their small size and preventing

aggregation. F127 was added as 05, and 1% (wt/vol) to assess the effect of concentration on the size of dexamethasone microcrystal size. Furthermore, the utilization of stirring speeds at 600 and 1000 RPM was undertaken with the objective of evaluating the impact of agitation on the dexamethasone microcrystal size (**Table 3-1**). 1% wt/vol Poloxamer F127 with 1000 RPMI yielded a particle size of (3.5 ± 1.47 µm) smaller than the other prepared particles, which is confirmed by SEM images (**Figure 3-8**).

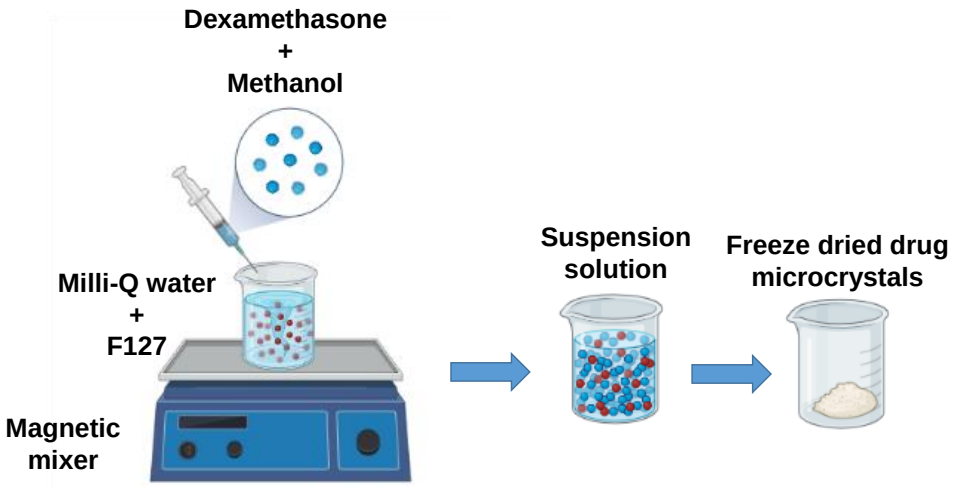


Figure 3-7: Schematic diagram of microcrystal preparation.

Table 3-1: Dexamethasone microcrystal preparation method and the resultant size. The sizes were measured by using ImageJ ±SD (n=8 SEM images).

Drug (Conc.)	**Stabilizer (Conc.)**	**Agitation speed**	**Size**
DEX (30 mg/ml) in 0.3 ml Methanol	F-127 0.5% (w/v)	600 RPM	7.81 ± 4.6 μm
	F-127 1% (w/v)	600 RPM	7.86 ± 5.48 μm
	F-127 0.5% (w/v)	1000 RPM	9.7± 5.42 μm
	F-127 1% (w/v)	1000 RPM	3.5 ± 1.47 μm

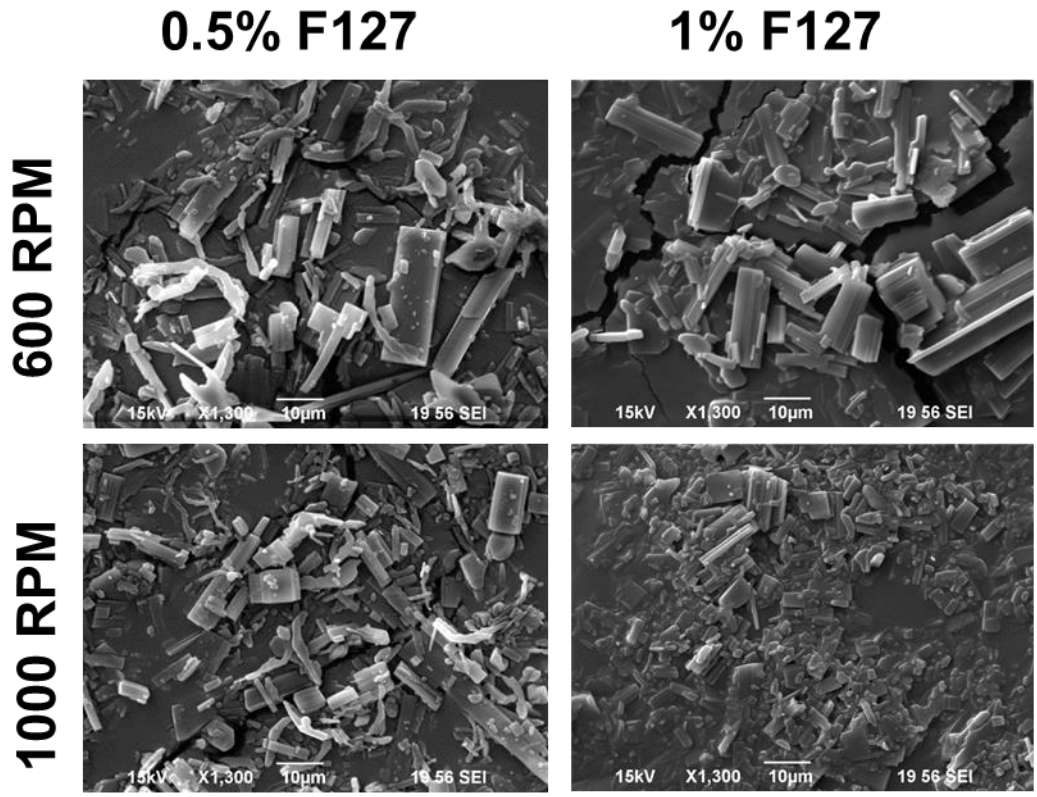


Figure 3-8: SEM micrographs of dexamethasone microcrystals prepared with different F127 concentrations (0.5% and 1% wt/vol) and agitation speeds (600 and 1000 RPM).

3.3.3 Ink preparation and 3D printing of PCL/DEX-MC

Dexamethasone microcrystals were added to 57% wt/vol PCL ink at 0.17 and 0.7% wt/wt, respectively. Both concentrations of dexamethasone microcrystals showed turbid suspensions when mixed with DCM due to the insolubility of dexamethasone in DCM. Conversely, 0.17% wt/wt DEX-CYD appeared clearer (**Figure 3-9**). This is due to the presence of cyclodextrin, which has been shown to enhance the solubility of low-soluble drugs such as dexamethasone in water and aprotic polar solvents such as DCM [283, 284]. Interestingly, when PCL was added to drug suspensions, the ink that contained 0.17% wt/wt DEX-MC appeared

clearer after mixing with PCL, which suggests that the polymer enhanced the drug's solubility. On the other hand, the suspension containing 0.7% wt/wt DEX-MC appeared cloudy. However, after adding PCL, the polymer ink became much clearer but still had apparently dispersed particles in it (**Figure 3-10**). A 3D printed scaffold was successfully printed directly from the viscous solutions of PCL/DEX-MC (0.17% wt/wt) and PCL/DEX-MC (0.7% wt/wt) through a nozzle (160 μm diameter) without any blockage of the nozzle. In contrast, PCL ink composed of dexamethasone-cyclodextrin at a concentration of 3.85% wt/wt corresponds to 0.25% wt/wt dexamethasone and has blocked the nozzle. This could be attributed to the fact that PCL did not increase the solubility of DEX-CYD at this concentration, leading to drug precipitation that clogged the nozzle orifice during printing.

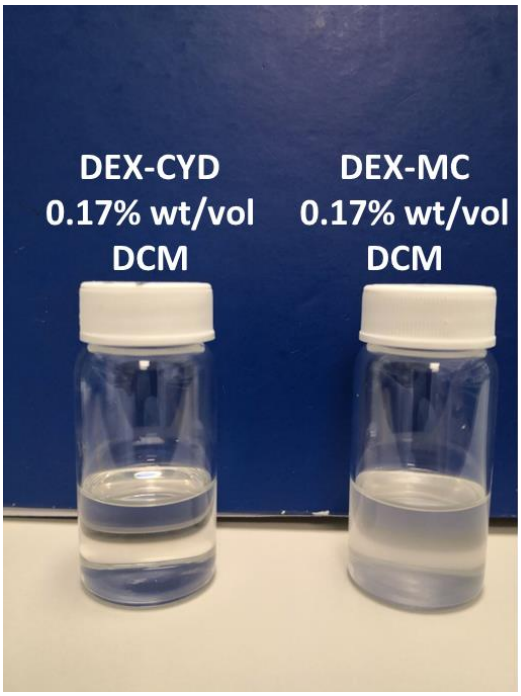


Figure 3-9: Solubility of DEX-CYD and DEX-MC in dichloromethane (DCM).

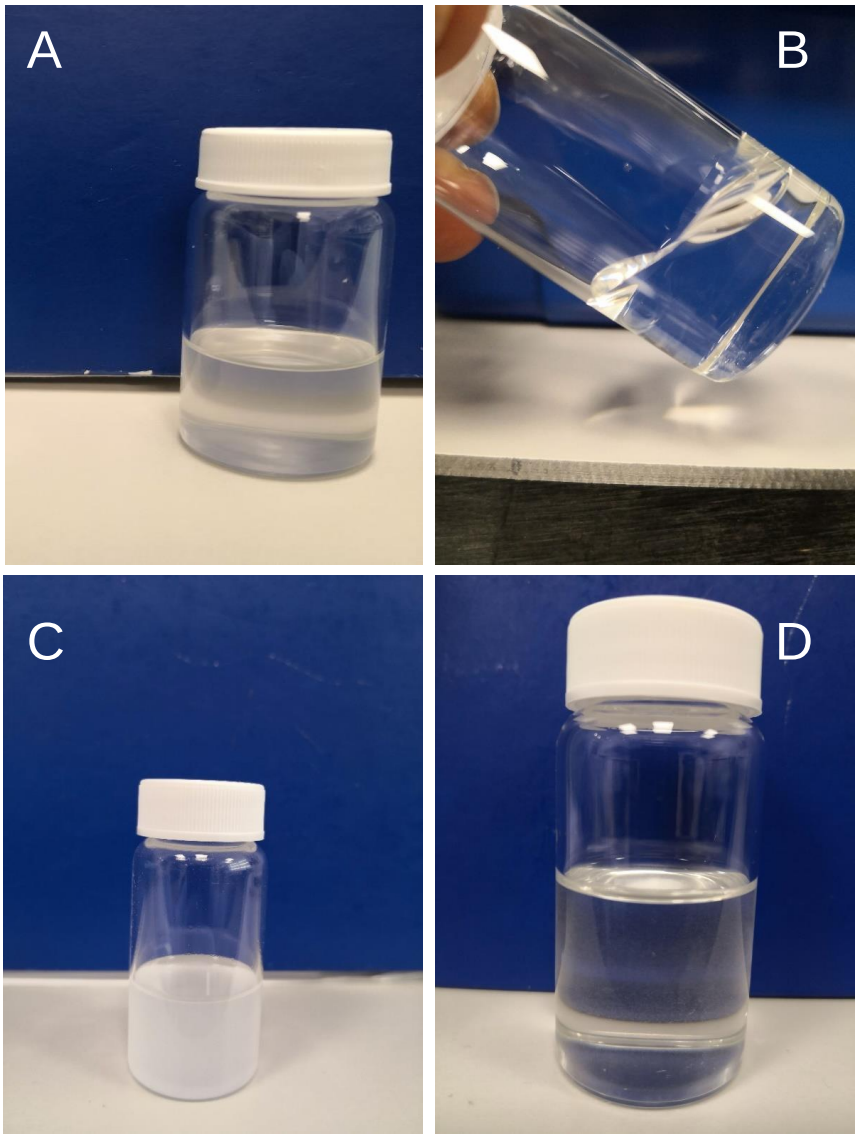


Figure 3-10: Effect of PCL on DEX-MC solubility (**A&B**) 0.17% wt/wt DEX-MC solubility in 57% wt/vol PCL (**C&D**) 0.7% wt/wt DEX-MC solubility in 57% wt/vol PCL.

3.3.4 Characterisation of 3D printed PCL/ DEX-MC scaffolds

Figure 3-11A-C illustrates the SEM micrographs of the 3D printed PCL scaffolds (0.17 and 0.7% wt/wt DEX-MC) and PCL/SAIB (60:40) with 0.7% wt/wt DEX-MC, respectively. The top view illustrates the surface

morphology of the struts after the printing process across all scaffolds. PCL/DEX-MC 0.7% wt/wt scaffolds exhibited an apparent rough surface on the struts compared to PCL/ DEX-MC 0.17% wt/wt scaffolds (**Figure 3-11B**). This morphology was not observed on the surface of PCL/SAIB (60:40)/DEX-MC 0.7% wt/wt scaffolds (**Figure 3-11C**). Furthermore, the diameter of the struts produced by 3D printing is smaller than the nozzle's internal diameter (160 μm) (**Figure 3-12A**). Also, they show interconnected pores larger than 300 μm (**Figure 3-12B**).

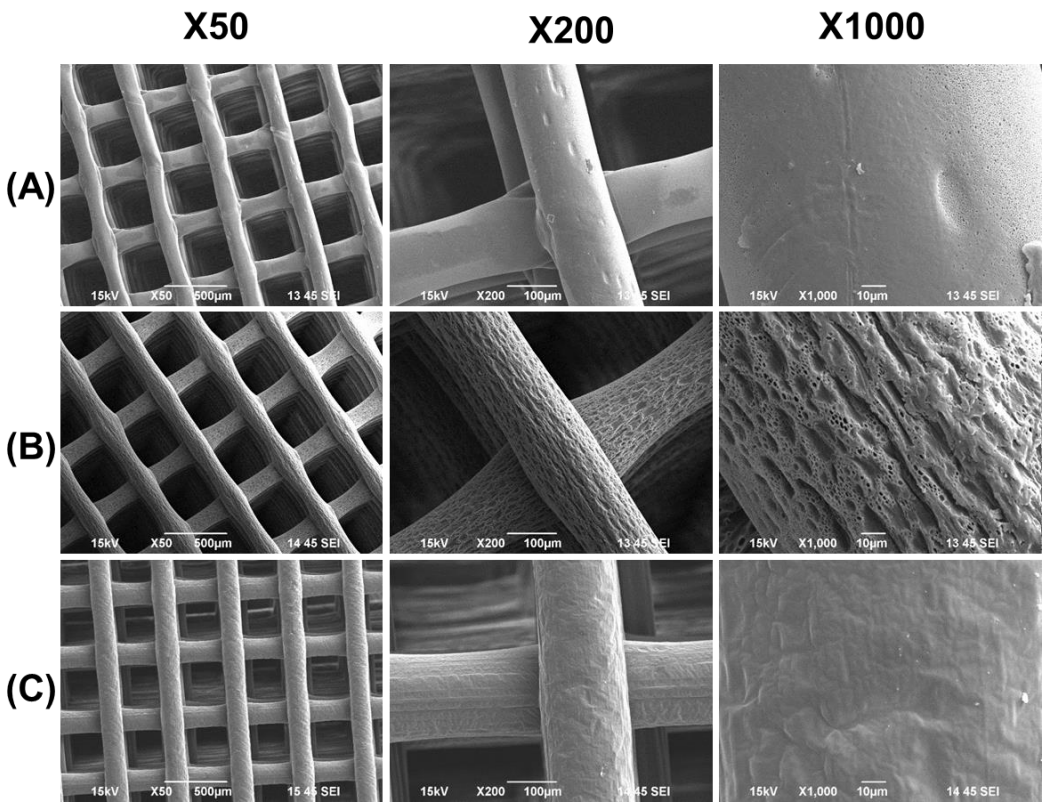


Figure 3-11: SEM micrographs for 3D printed PCL scaffolds in different magnification sizes (X50, X200, and X1000) composed of DEX-MC (**A**) PCL/DEX-MC 0.17% wt/wt; (**B**) PCL/DEX-MC 0.7% wt/wt. (**C**) PCL/SAIB (60:40)/DEX-MC 0.7% wt/wt.

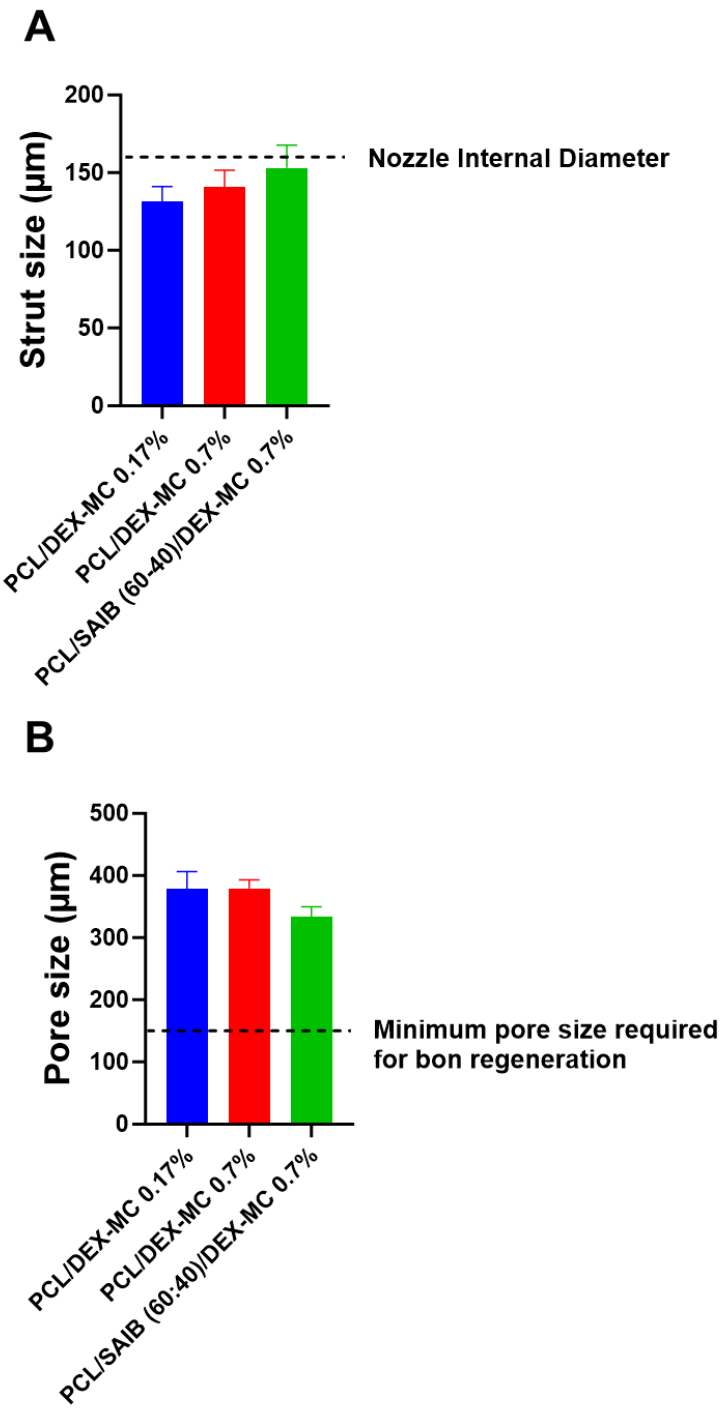


Figure 3-12: Strut diameters and pore sizes, edge-to-edge values of the 3D printed scaffolds, were calculated using ImageJ. (**A**) The measured pore sizes for all 3D printed scaffolds (**B**) The measured strut sizes for all 3D printed scaffolds Results are represented as mean ±SD (n = 8).

3.3.5 Thermal Characterisation

To investigate the interaction between DEX-CYD, surfactants, and PCL, differential scanning calorimetry (DSC) was utilized to examine the thermal properties of the 3D printed scaffolds. Initially, DEX-CYD was incorporated alone within the PCL at 0.17% wt/wt. The endothermic melting peak of DEX-CYD was detected at ~152 °C (**Figure 3-13**). Both PCL and PCL/DEX-CYD showed no dramatic changes in melting point (T_m), nearly 57 and 56 °C, respectively (**Table 3-2**). On the other hand, the 3D printed scaffolds of PCL/F127, PCL/F68, PCL/L31, PCL/Span80, and PCL/SAIB loaded with 0.17% wt/wt of DEX-CYD exhibited different thermal behaviour (**Figure 3-13**). The results showed that mixing PCL with DEX-CYD and surfactants affected the melting temperature (T_m) of PCL. **Table 3-2** shows the calculation of the enthalpy of fusion (ΔH_m), the melting temperature (T_m), and the relative crystallinity of the 3D printed scaffolds. ΔH_m of PCL increased when the DEX-CYD was added at 0.17% wt/wt to 84.36 J/g, compared to PCL alone, which was 65.45 J/g. On the other hand, this value decreased when surfactants were added to PCL compared to pure PCL **Table 3-2**. This is attributed to the plasticizing effect of the surfactants. This plasticizing effect disrupts the intermolecular forces between the polymer chains, making polymers flexible and easy to process. Interestingly, PCL inks made of hydrophilic F127 and F68 showed a high (ΔH_m) compared to PCL scaffolds made of hydrophobic L31, Span80, and SAIB. These reduced values of the enthalpy of fusion shown in **Table 3-2** suggest the impact of surfactant on the decrease of PCL crystallinity compared to PCL with DEX-CYD.

Moreover, **Table 3-2** shows that the addition of DEX-CYD at 0.17% wt/wt to PCL exhibited a high crystallinity value of 60.47% compared to the pure PCL which was 46.92%. Dexamethasone here acted as a nucleating agent, which induced the crystallisation of PCL. Moreover, the degree of crystallinity of PCL decreased when surfactants were added compared to PCL/DEX-CYD 0.17% wt/wt. Interestingly, the addition of hydrophilic F127 and F68 to PCL containing 0.17% wt/wt DEX-CYD showed reduced crystallinity compared to PCL/DEX-CYD 0.17% wt/wt scaffolds and was higher than their counterpart scaffolds containing hydrophobic L31, Span80, and SAIB. On the other hand, the degree of crystallinity for PCL containing hydrophobic L31, Span80, and SAIB was low compared to scaffolds containing hydrophilic F127 and F68 and PCL/DEX-CYD 0.17% wt/wt, respectively. More interestingly, the addition of SAIB at 40% wt/wt to PCL has reduced the polymer crystallinity to 25.94%. These results suggest the capability of surfactants to inhibit crystal growth in PCL, which is apparently more evident in hydrophobic surfactants L31, Span80, and SAIB.

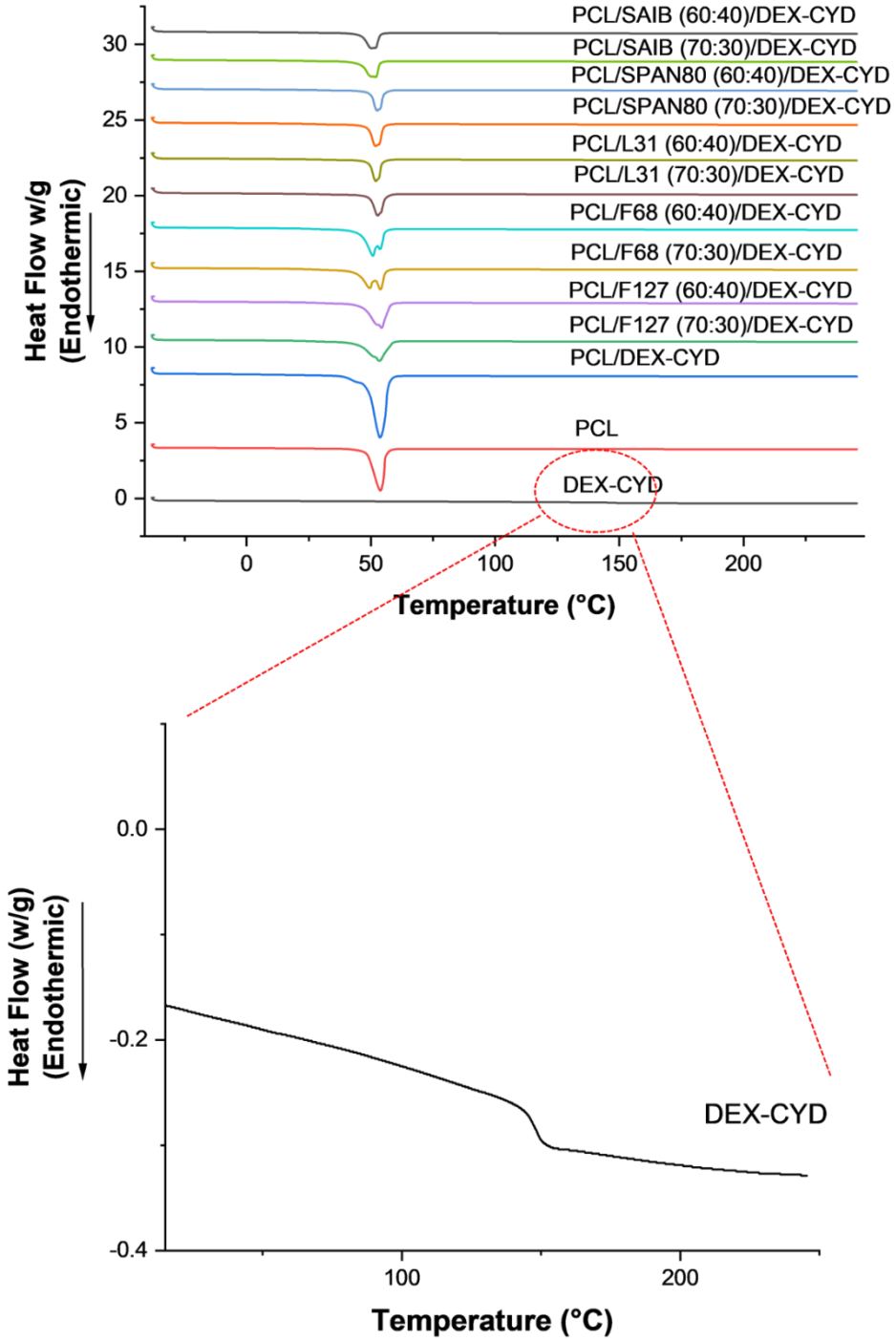


Figure 3-13: DSC thermograph for 3D printed PCL, PCL/F127, PCL/F68, PCL/L31, PCL/Span80, and PCL/SAIB scaffolds with 0.17% wt/wt DEX-CYD.

Table 3-2: Thermal properties of 3D printed composite scaffolds. T_m: Melting temperature; ΔH_m: the enthalpy of melting; X_c: the degree of crystallinity; ND: Not Detected. (n=1).

Sample	T_g (°C)	T_m (°C)	ΔH_m (J/g)	X_c (%)
PCL	45.89	57.53	65.450	46.92
PCL/DEX-CYD (0.17% wt/wt)	44.01	56.08	84.36	60.47
PCL/F127 (70:30)/DEX-CYD	41.73	53.57	59.21	42.44
PCL/F127 (60:40)/DEX-CYD	42.4	54.17	67.56	48.43
PCL/F68 (70:30)/DEX-CYD	ND	54.06	58.89	42.22
PCL/F68 (60:40)/DEX-CYD	42.03	52.38	69.29	49.67
PCL/L31 (70:30)/DEX-CYD	42.84	52.67	39.78	28.52
PCL/L31 (60:40)/DEX-CYD	43.84	51.87	36.35	26.06
PCL/Span80 (70:30)/DEX-CYD	42.51	51.12	39.96	28.85
PCL/Span80 (60:40)/DEX-CYD	42.57	50.04	37.46	26.85
PCL/SAIB (70:30)/DEX-CYD	42.28	51.98	39.17	28.08
PCL/SAIB (60:40)/DEX-CYD	42.61	49.71	36.19	25.94

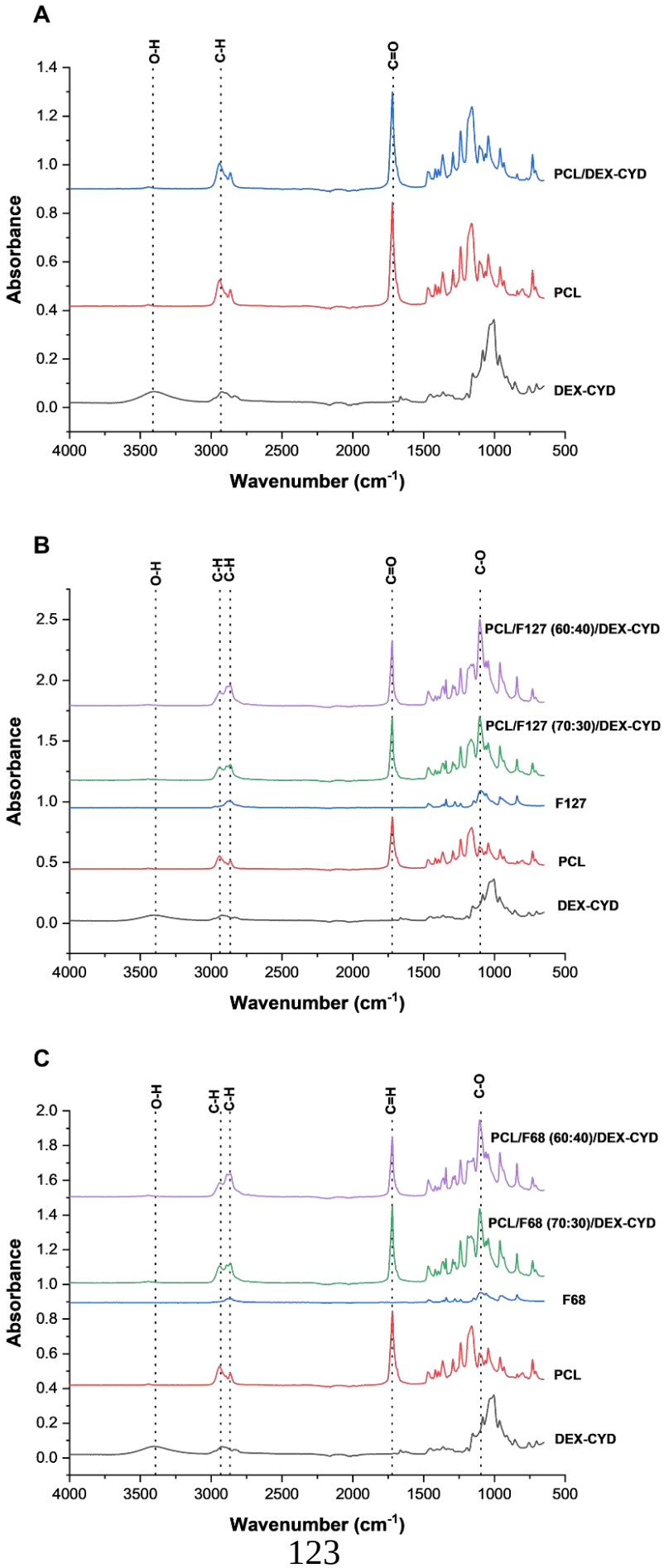
3.3.6 Chemical Characterisation by FTIR

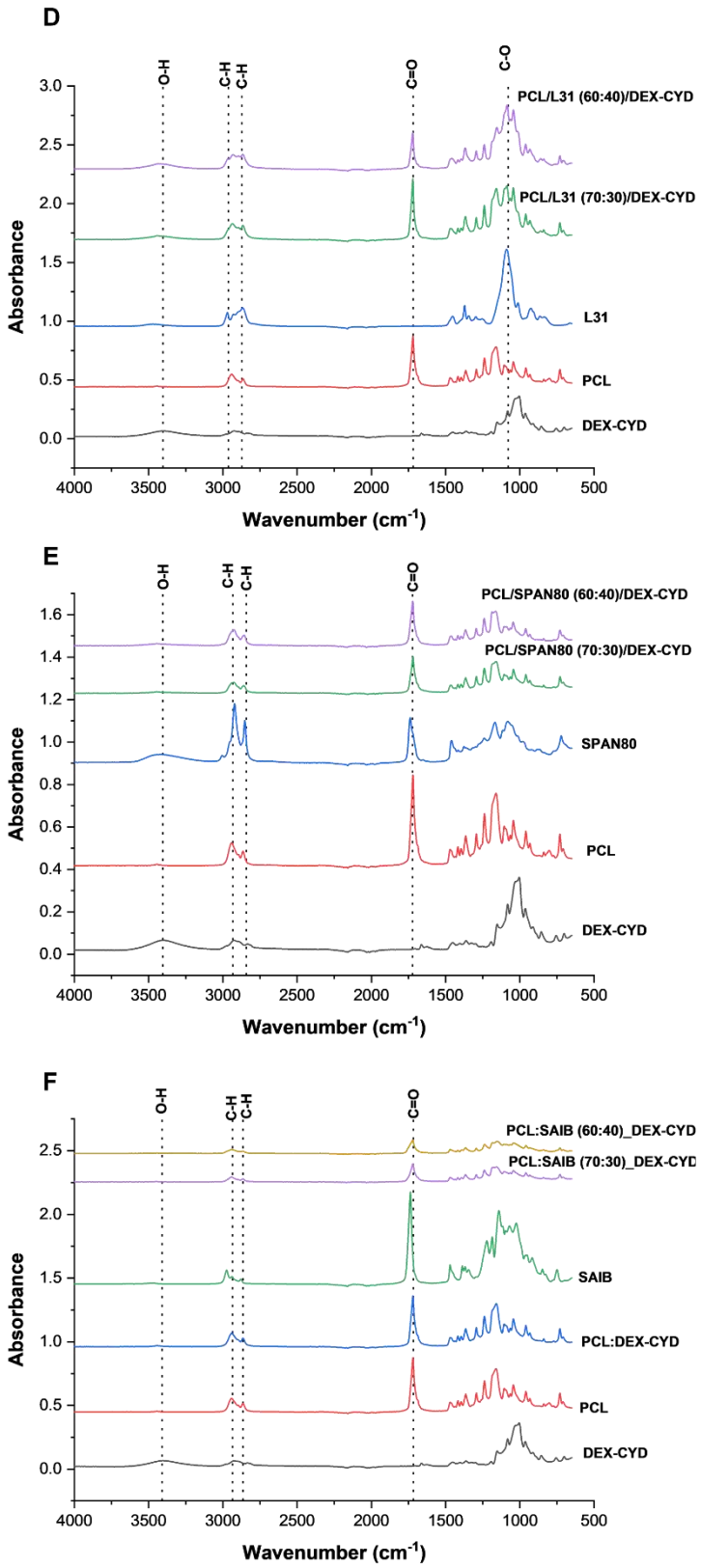
FTIR spectroscopy was performed to determine the chemical interactions between DEX-CYD, PCL, and surfactants. FTIR spectrum of pure PCL scaffold (**Figure 3-14 A**) demonstrated characteristic peaks at 2940 cm^{-1} and 2861 $cm^{-1,}$ which are correlated with the symmetric and asymmetric stretching of the Methyl -CH group, respectively. Moreover, the stretching vibration of the carbonyl group C=O could be assigned to the peak at 1721 cm^{-1} [285]. Additionally, a peak at 3409 cm^{-1}

corresponds to the stretching of the O-H functional group in DEX-CYD [283]. Pluronic F127 has absorption peaks at 2889 cm^{-1} and 1111 $cm^{-1,}$ corresponding to C–H stretching vibrations and C–O stretching vibrations, respectively (**Figure 3-14B**) [286]. Pluronic F68 showed a peak at 2870 cm^{-1} due to the C-H stretching and a peculiar peak at 1111 cm^{-1} caused by the stretching vibrations of C-O (**Figure 3-14C**) [287]. Moreover, L31 showed a broad peak at 3464 cm^{-1} corresponding to O-H vibration, and peaks at 2970 and 2860 attributed to C–H asymmetric and symmetric vibrations, respectively. As well as a strong peak at 1088 cm^{-1} is attributed to C-O stretching (**Figure 3-14D**) [288]. SPAN80, on the other hand, exhibited a board spectrum at 3426 cm^{-1}, indicating O-H stretching. The absorption at 2918 and 2850 cm^{-1} is attributed to C-H stretching, while the strong peak at 1736 cm^{-1} is attributed to C=O stretching (**Figure 3-14E**) [289]. The two peaks, at 2976 cm^{-1} and 1739 cm^{-1}, were detected in SAIB and were assigned to C-H stretching vibrations, and C=O stretching vibrations, respectively (**Figure 3-14F**) [290].

The combination of the characteristic peaks of DEX-MC and PCL was also observed (**Figure 3-14G**). FTIR peaks in PCL/DEX-MC scaffolds were similar to pure PCL peaks. We observed the typical weak absorption peaks at 2940- 2860 cm^{-1} related to C–H asymmetric and C–H symmetric vibrations, respectively. At 1724 cm^{-1}, a stretching vibration peak appears, consistent with the C=O bond, representative of PCL polymer [283]. These results suggest no significant chemical changes were observed due to the addition of DEX-CYD or DEX-MC and the

surfactants to PCL, such as new chemical bond formation between PCL, dexamethasone and the surfactants.


A
O-H
C-H
C=O
PCL/DEX-CYD
PCL
DEX-CYD
Absorbance
Wavenumber (cm-1)
B
O-H
C-H
C-H
C=O
C-O
PCL/F127 (60:40)/DEX-CYD
PCL/F127 (70:30)/DEX-CYD
F127
PCL
DEX-CYD
Absorbance
Wavenumber (cm-1)
C
O-H
C-H
C-H
C=H
C-O
PCL/F68 (60:40)/DEX-CYD
PCL/F68 (70:30)/DEX-CYD
F68
PCL
DEX-CYD
Absorbance
Wavenumber (cm-1)


D
O-H
C-H
C-H
C=O
C-O
PCL/L31 (60:40)/DEX-CYD
PCL/L31 (70:30)/DEX-CYD
L31
PCL
DEX-CYD
Absorbance
Wavenumber (cm-1)
E
O-H
C-H
C-H
C=O
PCL/SPAN80 (60:40)/DEX-CYD
PCL/SPAN80 (70:30)/DEX-CYD
SPAN80
PCL
DEX-CYD
Absorbance
Wavenumber (cm-1)
F
O-H
C-H
C-H
C=O
PCL:SAIB (60:40)_DEX-CYD
PCL:SAIB (70:30)_DEX-CYD
SAIB
PCL:DEX-CYD
PCL
DEX-CYD
Absorbance
Wavenumber (cm-1)

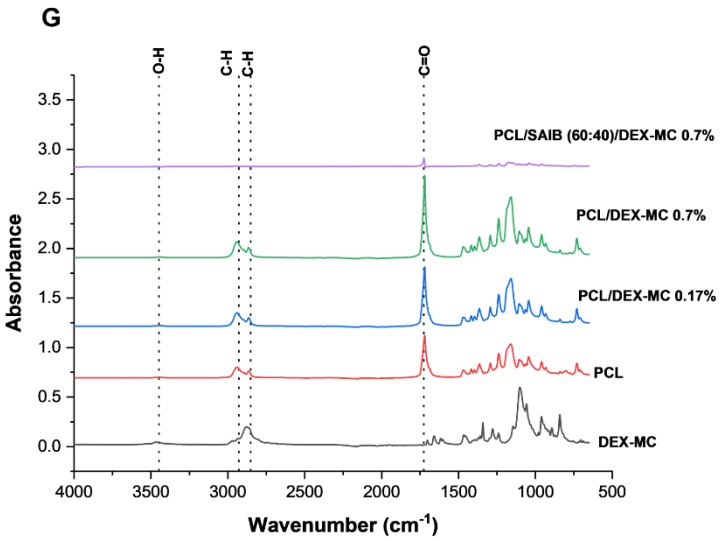


Figure 3-14: FTIR graphs representing absorbance of 3D printed scaffolds containing 0.17% wt/wt DEX-CYD. (**A**) PCL/DEX-CYD. (**B**) PCL/F127/DEX-CYD. (**C**) PCL/F68/DEX-CYD. (**D**) PCL/L31/DEX-CYD. (**E**) PCL/SAIB/DEX-CYD. (**F**) PCL/Span80/DEX-CYD. (**G**) PCL/DEX-MC, and PCL/SAIB/DEX-MC.

3.3.7 *In vitro* release of dexamethasone from 3D printed scaffolds

The accumulative release and release at each collection time point of dexamethasone from all 3D printed scaffolds were examined by using UV-vis at 241 nm. The unknown concentrations were quantified based on the calibration curve of known dexamethasone concentrations (**Appendix Figure 7-2**). Drug loading in scaffolds was calculated and shown in (**Appendix Table 7-1**). **Figure 3-15A** shows the amount released from all PCL/DEX-CYD 3D printed scaffolds over different periods. 0.05, and 0.1% wt/wt PCL/DEX-CYD scaffolds showed the fastest dexamethasone release over 7 days, with an initial burst release of over 50% in the first 12h. They reached nearly 100% cumulative release on day 7 (**Figure 3-15 B**). In contrast, scaffolds containing 0.17%

wt/wt showed a fairly sustained release over 15 days. By comparing the actual release between scaffolds, a greater amount of DEX was released from scaffolds containing 0.17% wt/wt of DEX-CYD. This amount of released DEX-CYD was above the LOQ until day 12 compared to scaffolds containing 0.1 and 0.05% wt/wt DEX-CYD, which showed a quantifiable amount on day 3, respectively (**Figure 3-15C**).

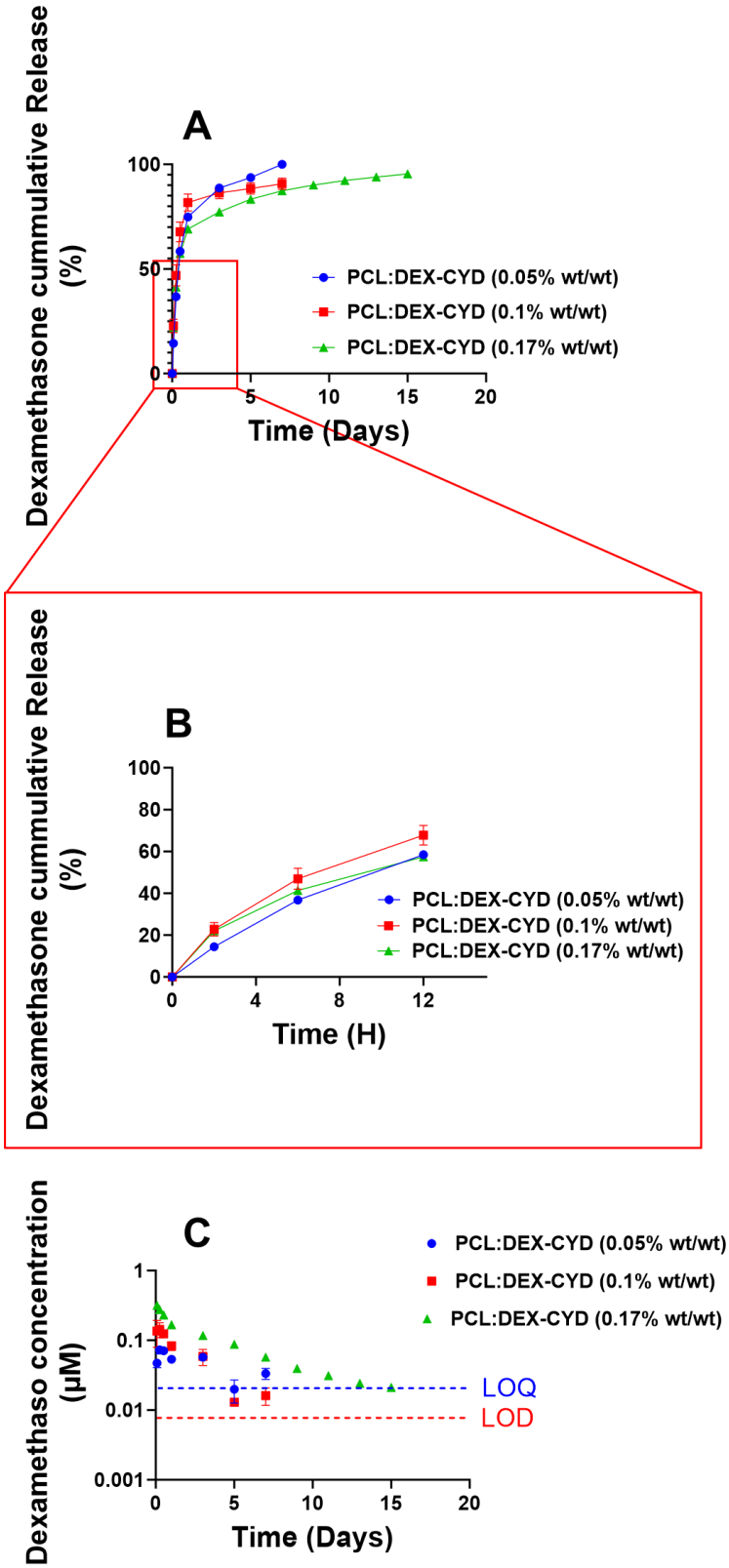


Figure 3-15: cumulative and actual release of dexamethasone from 3D printed PCL scaffolds incubated in 10 ml PBS. (**A**) Cumulative release

percentage of 3D printed PCL scaffolds loaded with 0.05%, 0.1%, and 0.17% wt/wt of dexamethasone-cyclodextrin over 15 days. PBS was collected at 2, 4, 6, 12, 24 h, and every 2 days. (**B**) cumulative release percentage over 12 h. (**C**) Actual release in μM showing the limit of detection (LOD) and limit of quantification (LOQ) of the released dexamethasone. All data represent the mean ± SD (n = 3).

To reduce the burst effect and prolong the release of dexamethasone. Pluronic F127, Pluronic F68, Pluronic L31, Span80, and SAIB, which all have surfactant properties, were added to PCL to test their ability to prolong drug release. Furthermore, the surfactants were added to PCL in different mass ratios (wt/wt), keeping the same drug concentration of 0.17% wt/wt. Our results showed that both scaffolds that contained F127 and F68 showed fast release of dexamethasone over 1 day, with initial burst release over 50% at 2 h, respectively (**Figure 3-16A and B** and **Figure 3-17A and B**). On the other hand, scaffolds containing L31 showed prolonged release of dexamethasone over 7 days (**Figure 3-18A**), with an initial burst release of over 50% at 12 h (**Figure 3-18B**). As noticed in Figure 3-18 C, the amount of released dexamethasone was above the LOQ until day 3.

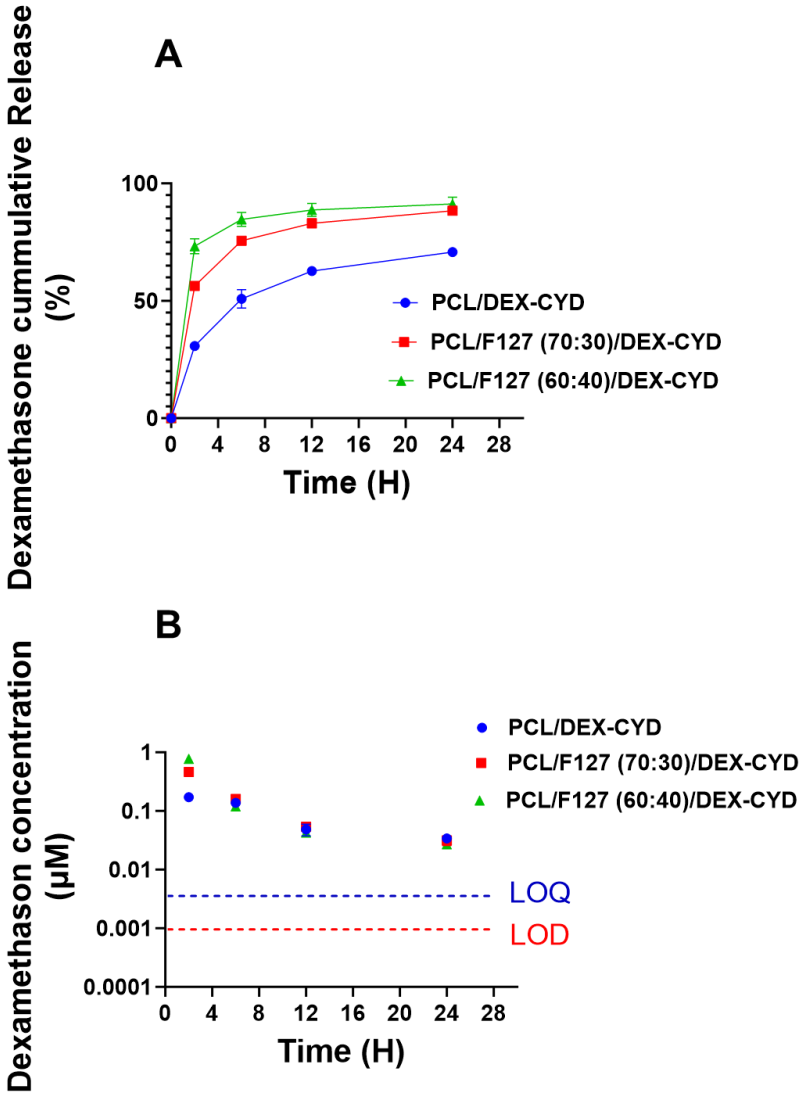


Figure 3-16: Cumulative and actual release of dexamethasone from 3D printed PCL scaffolds incubated in 10 ml PBS. (**A**) Cumulative release percentage of 3D printed scaffolds of PCL, PCL/F127 (70:30), and PCL/F127 (60:40) loaded with 0.17% wt/wt of DEX-CYD. (**B**) Actual release in µM showing the limit of detection (LOD) and limit of quantification (LOQ) of the released dexamethasone. PBS was collected at 2, 4, 6, 12, 24 h, and every 2 days. All data represent mean ± SD (n=3).

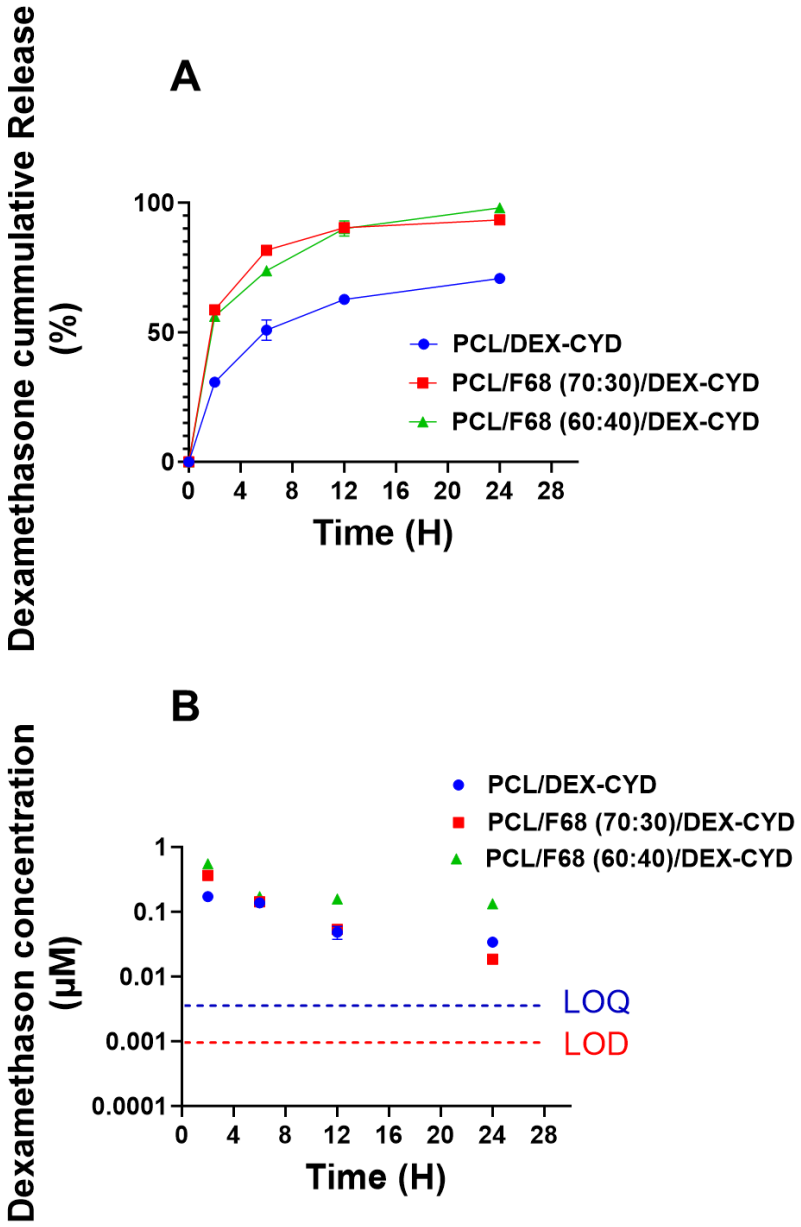


Figure 3-17: Cumulative and actual release of dexamethasone from 3D printed PCL scaffolds incubated in 10 ml PBS. (**A**) Cumulative release percentage of 3D printed scaffolds of PCL/F68 (70:30) and PCL/F68 (60:40) loaded with 0.17% wt/wt of DEX-CYD. (**B**) Actual release in µM showing the limit of detection (LOD) and limit of quantification (LOQ) of

the released dexamethasone. PBS was collected at 2, 4, 6, 12, 24 h, and every 2 days. All data represent mean ± SD (n=3).

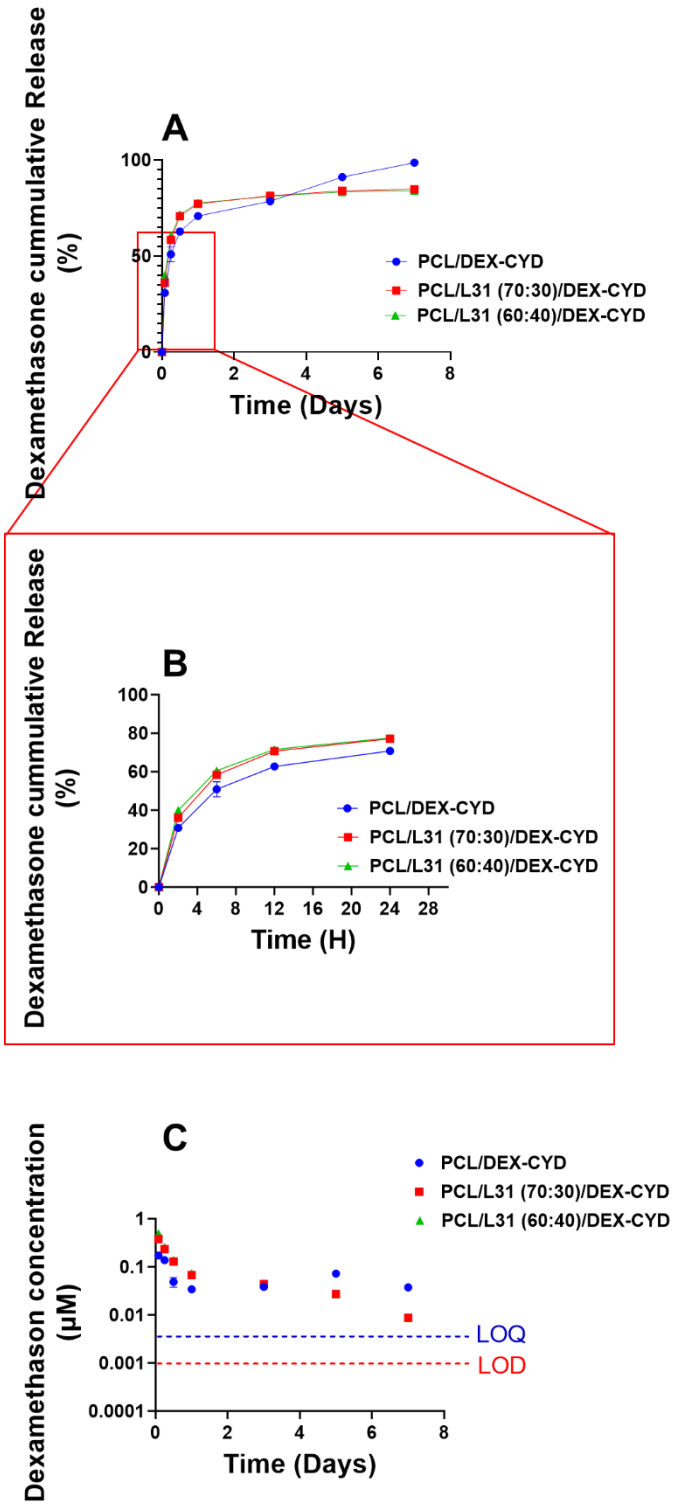


Figure 3-18: Cumulative and actual release of dexamethasone from 3D printed PCL scaffolds incubated in 10 ml PBS. (**A**) Cumulative release percentage of 3D printed scaffolds of PCL, PCL/L31 (70:30), and PCL/L31 (60:40) loaded with 0.17% wt/wt of DEX-CYD. (**B**) cumulative

release percentage over 1 day (**C**) Actual release in μM showing the limit of detection (LOD) and limit of quantification (LOQ) of the released dexamethasone. PBS was collected at 2, 4, 6, 12, 24 h, and every 2 days. All data represent mean ± SD (n=3).

On the other hand, the 3D printed PCL scaffolds composed of Span80 showed prolonged release of dexamethasone over 7 days with an initial burst release reaching 50% and 38% for PCL/Span80 (70:30)/DEX-CYD and PCL/Span80 (60:40)/DEX-CYD, respectively (**Figure 3-19A and B**). As shown in (**Figure 3-19C**), the released amounts of dexamethasone were above the LOQ at days 3 and 9 for PCL/Span80 (70:30)/DEX-CYD and PCL/Span80 (60:40)/DEX-CYD respectively, compared to day 11 for PCL/DEX-CYD.

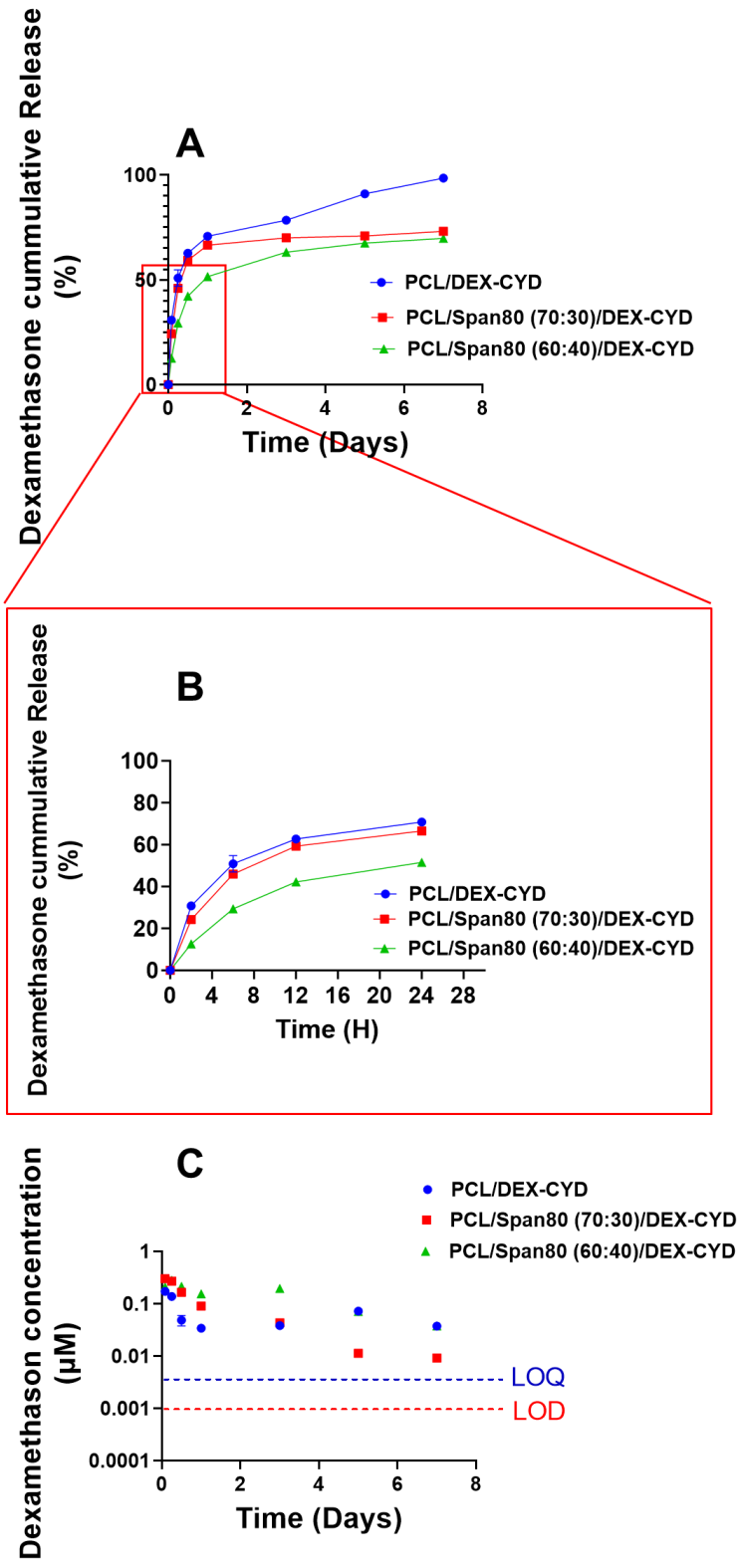


Figure 3-19: Cumulative and actual release of dexamethasone from 3D printed PCL scaffolds. (***A***) Cumulative release percentage of 3D printed scaffolds of PCL, PCL/Span80 (70:30), and PCL/Span80 (60:40) loaded

with 0.17% wt/wt of DEX-CYD. (**B**) Cumulative release percentage over 1 day. (**C**) Actual release in μM showing the limit of detection (LOD) and limit of quantification (LOQ) of the released dexamethasone. PBS was collected at 2, 4, 6, 12, 24 h, and every 2 days. All data represent mean ± SD (n=3).

The release of dexamethasone is prolonged as the SAIB percentage is increased in the formulation. PCL/SAIB (70:30)/DEX-CYD and PCL/SAIB (60:40)/DEX-CYD showed a sustained release reaching 100% and 90% of cumulative release, respectively, up to 35 days compared to PCL/DEX-CYD alone (**Figure 3-20A**). Both PCL/SAIB (70:30)/DEX-CYD and PCL/SAIB (60:40)/DEX-CYD showed nearly 30% and 19% burst release, respectively, in the first 12 hrs, compared to PCL/DEX-CYD without SAIB, which exhibited almost 60% at the same time (**Figure 3-20B**). Moreover, PCL/SAIB (60:40)/DEX-CYD showed a released amount of dexamethasone above the LOQ till day 35, compared to PCL/SAIB (70:30)/DEX-CYD which showed a released amount of dexamethasone above the LOQ till day 20 (**Figure 3-20C**)

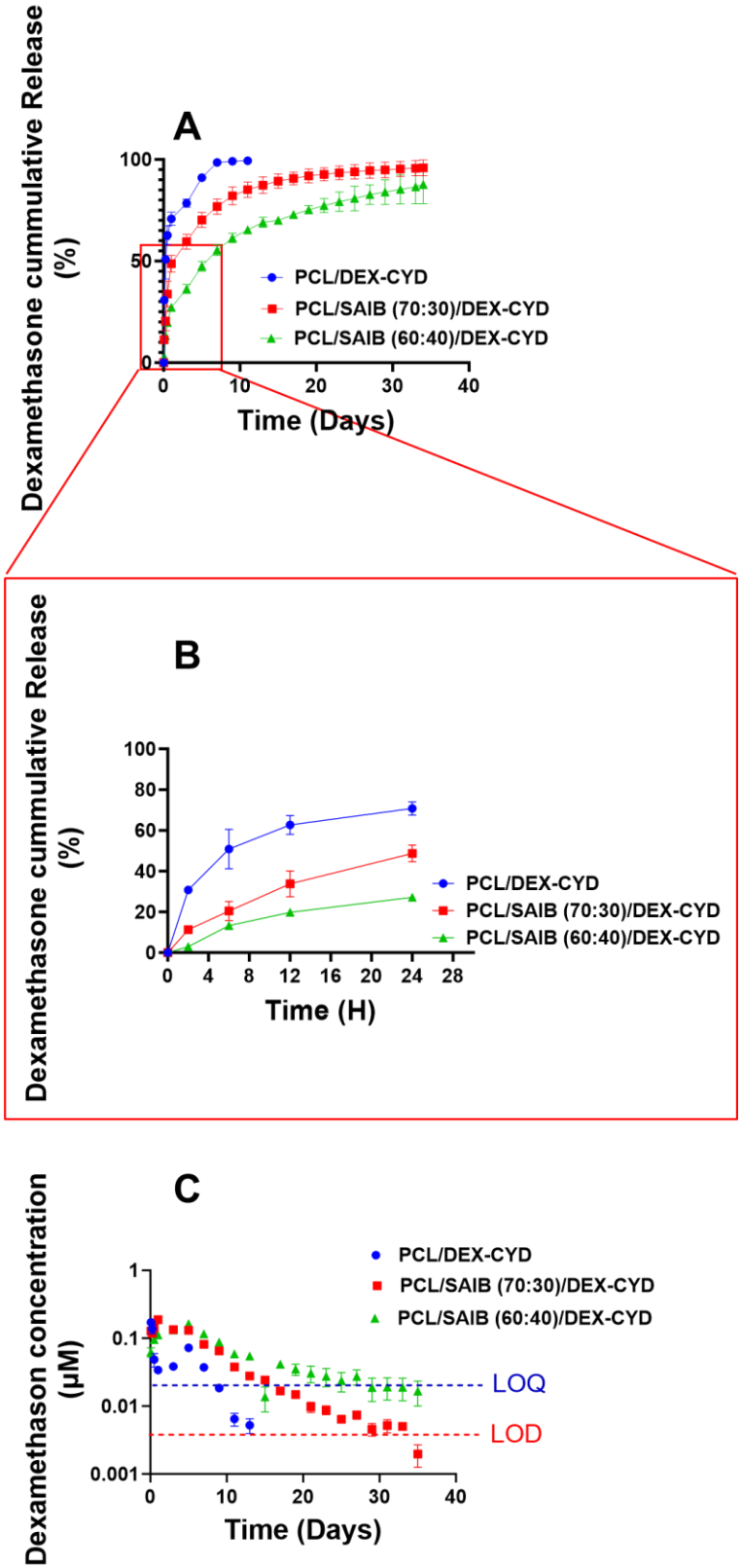


Figure 3-20: Cumulative and actual release of Dexamethasone from 3D printed PCL scaffolds. (**A**) Cumulative release percentage of 3D printed

scaffolds of PCL/SAIB (70:30)/DEX-CYD and PCL/SAIB (60:40)/DEX-CYD. (**B**) Cumulative release percentage over 1 day. (**C**) Actual release in μM showing the limit of detection (LOD) and limit of quantification (LOQ) of the released dexamethasone. PBS was collected at 2, 4, 6, 12, 24 h, and every 2 days. All data represent mean ± SD (n=3).

Previously, DEX-CYD concentration was increased to 3.85% wt/wt (corresponding to 0.25% wt/wt of dexamethasone) and printed with it. Unfortunately, this concentration blocked the nozzle during printing. It is anticipated that the drug solubility at this concentration was decreased in PCL polymer and led to precipitated and aggregated. When these aggregated particles reach the nozzle, they obstruct the ink flow and block the nozzle. Therefore, a concentration of 2.63% wt/wt of DEX-CYD complex (equivalent to 0.17% wt/wt dexamethasone) was chosen to fabricate all scaffolds and study the control release.

Printing PCL scaffolds with high drug loading can maintain the therapeutic efficacy of the released drug over an extended period of time. Moreover, to avoid the possibility of nozzle blockage during printing, the dexamethasone particles were reduced by utilising the basic anti-solvent precipitation method to prepare dexamethasone microcrystals. Dexamethasone microcrystals (DEX-MC) were prepared and incorporated into PCL. Afterwards, 3D printed scaffolds were fabricated with two different ratios: 0.17% wt/wt and 0.7% wt/wt, respectively. Furthermore, SAIB was added to prepare PCL/SAIB (60:40)/DEX-MC (0.7% wt/wt). As shown in (**Figure 3-21A**), PCL/DEX-MC (0.17% wt/wt) exhibited fast release within 1 day. On the other hand, PCL/DEX-MC

(0.7% wt/wt) showed prolonged release over 13 days. Interestingly, PCL/SAIB (60:40)/DEX-MC (0.7% wt/wt) scaffolds prolonged the release of dexamethasone for nearly 30 days. As shown in (**Figure 3-21B**), both PCL/DEX-MC (0.17% wt/wt) and PCL/DEX-MC (0.7% wt/wt) exhibited initial burst releases of 50% and 66%, respectively, in the first 12 h. whereas, PCL/SAIB (60:40)/DEX-MC (0.7% wt/wt) showed a burst release of approximately 30% in the first 12 h. Both PCL/DEX-MC (0.17% wt/wt) and PCL/DEX-MC (0.7% wt/wt), in addition to PCL/SAIB (60:40)/DEX-MC (0.7% wt/wt), showed dexamethasone concentrations above the LOQ at all collection time points (**Figure 3-21C**). These results show the role of SAIB in reducing the early burst release and prolonging the release of dexamethasone over a period of time.

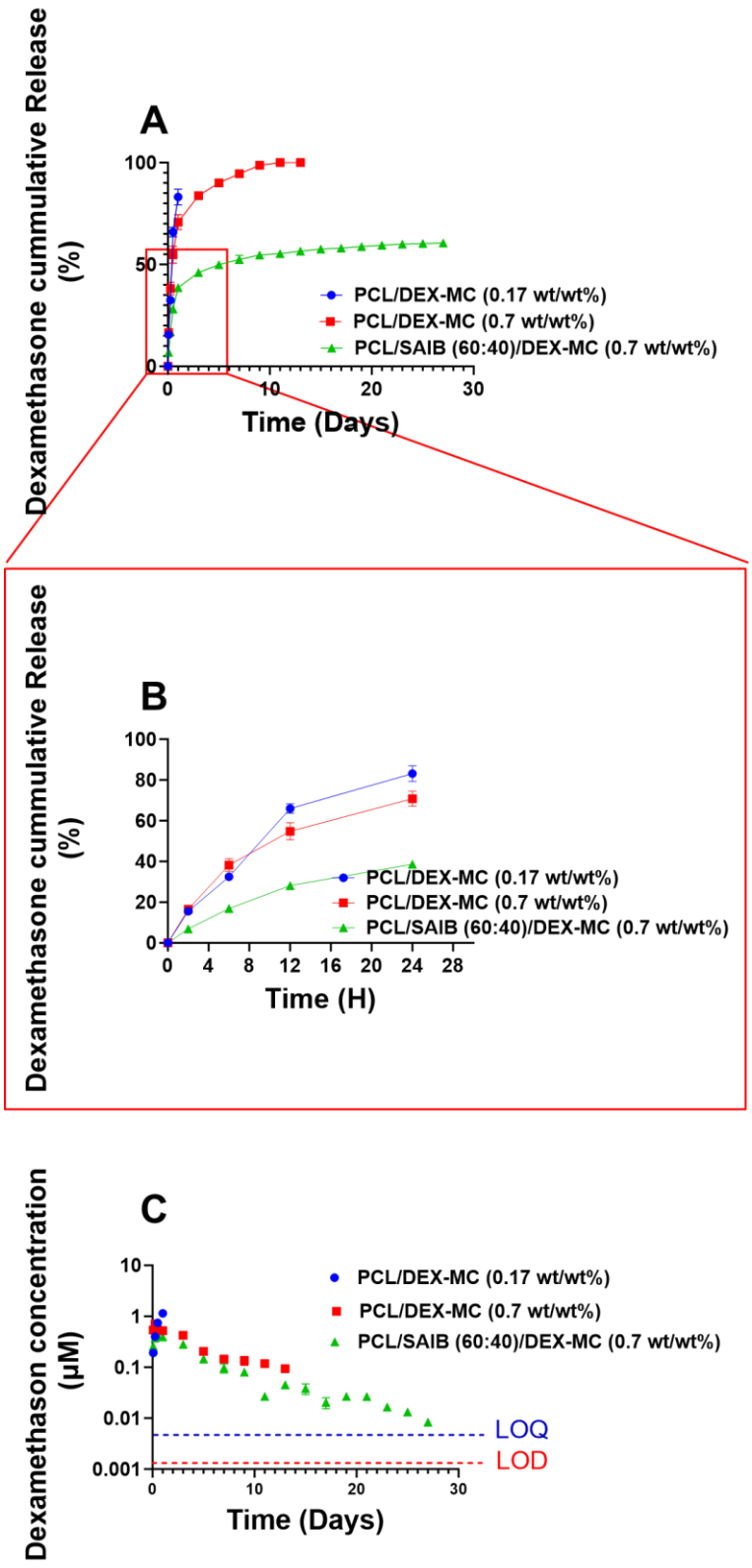


Figure 3-21: Cumulative and actual release of Dexamethasone from 3D printed PCL scaffolds incubated in 10 ml PBS. (**A**) Cumulative release percentage of 3D printed scaffolds of PCL/DEX-MC (0.17% wt/wt),

PCL/DEX-MC (0.7% wt/wt) and PCL/SAIB (60:40)/DEX-MC (0.7% wt/wt). (**B**) Cumulative release percentage over 1 day. (**C**) Actual release in μM showing the limit of detection (LOD) and limit of quantification (LOQ) of the released dexamethasone. PBS was collected at 2, 4, 6, 12, 24 h, and every 2 days. All data represent mean ± SD (n=3).

3.3.8 Drug release Kinetics

The release of drugs from different formulations can be modelled mathematically with a high degree of accuracy. This information can be used to make clinical decisions about dosing regimens. In general, the release of drugs can be plotted against time to produce graphs that indicate the types of processes that are taking place. Dexamethasone release kinetics were obtained using different mathematical models, i.e., first-order, zero-order, Higuchi model, and Krosmeyer-Peppas model (KPM). The parameters of the several kinetic models to which the release data were fitted are shown in (**Figures 3-22 to 3-28**). The R^2 and n values obtained for all 3D printed scaffolds prepared in the present chapter are summarised in **Table 3-3**. PCL/DEX-CYD 0.17% wt/wt is the best-fitting first-order model with R^2 0.94 (**Figure 3-22**), which means that the rate of drug release is predominantly governed by the drug concentration gradient (diffusion). In other words, as the drug concentration decreases within the formulation, the rate of drug release also decreases over time [291]. On the other hand, the addition of the excipients in various ratios has impacted the release mechanism. As shown in (**Figures 3-23D, 3-24D, and 3-25D**) the Korsmeyer-Peppas model best fits scaffolds PCL/F127 (70:30)/DEX-CYD, PCL/F127 (60:40)/DEX-CYD, PCL/F68

(70:30)/DEX-CYD, PCL/F68 (60:40)/DEX-CYD, PCL/L31 (70:30)/DEX-CYD, and PCL/L31(60:40)/DEX-CYD with regression values R^2 of 0.91, 0.96, 0.91, 0.93, 0.95, and 0.98, respectively, and n values higher than 0.85, respectively (**Table 3-3**). According to the Korsmeyer-Peppas kinetic model, when n (the exponent of release) is ≤ 0.43, drug release is controlled by Fickian diffusion. In contrast, when n is ≥ 0.85, drug release is controlled by erosion. Furthermore, for n values between 0.85 and 0.43, drug release is governed by two mechanisms, diffusion and erosion [292]. Moreover, PCL/F127 (70:30)/DEX-CYD, PCL/F127 (60:40)/DEX-CYD, PCL/F68 (70:30)/DEX-CYD, PCL/F68 (60:40)/DEX-CYD, PCL/L31 (70:30)/DEX-CYD, and PCL/L31(60:40)/DEX-CYD fit the first-order model (**Figures 3-23B, 3-24B, and 3-25B**), which implies that the release of dexamethasone from these scaffolds is governed by two mechanisms: erosion and diffusion due to hydration, which result in the fast leaching of F127, F68, and L31 from PCL. The release of dexamethasone from PCL/Span80 scaffolds did not fit any model (**Figures 3-26A to D**). On the other hand, the release of dexamethasone from PCL/SAIB (70:30)/DEX-CYD and PCL/SAIB (60:40)/DEX-CYD fits the first-order with R^2 of 0.97, and 0.98; and fits Higuchi mechanisms with R^2 of 0.94,and 0.96, respectively (**Figures 3-27B and C**), which implies that the release was due to diffusion [293]. The release mechanism of PCL/DEX-MC 0.17% wt/wt exhibited multiple mechanisms: zero order, first order, and Higuchi (**Figures 3-28A, B, and C**). On the other hand, the release of dexamethasone from PCL/DEX-MC at 0.7% wt/wt fits the

first-order model (**Figure 3-28B**). It could be possible that changing the drug concentration is the reason for multiple drug release mechanisms.

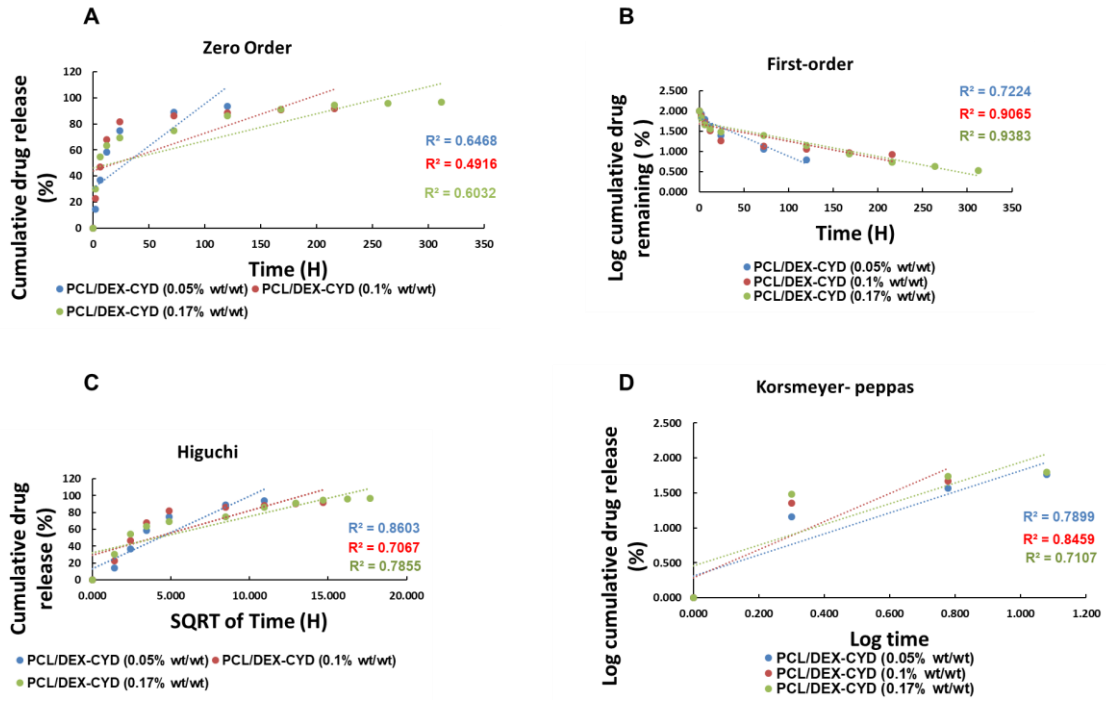


Figure 3-22: Dexamethasone release kinetics of 3D printed PCL scaffolds loaded with 0.05% wt/wt (blue), 0.1% wt/wt (Red), and 0.17% wt/wt (Green) of dexamethasone cyclodextrin respectively fitted to various models: **A**) Zero-order, **B**) First-order, **C**) Higuchi model, and **D**) Korsmeyer-Peppas.

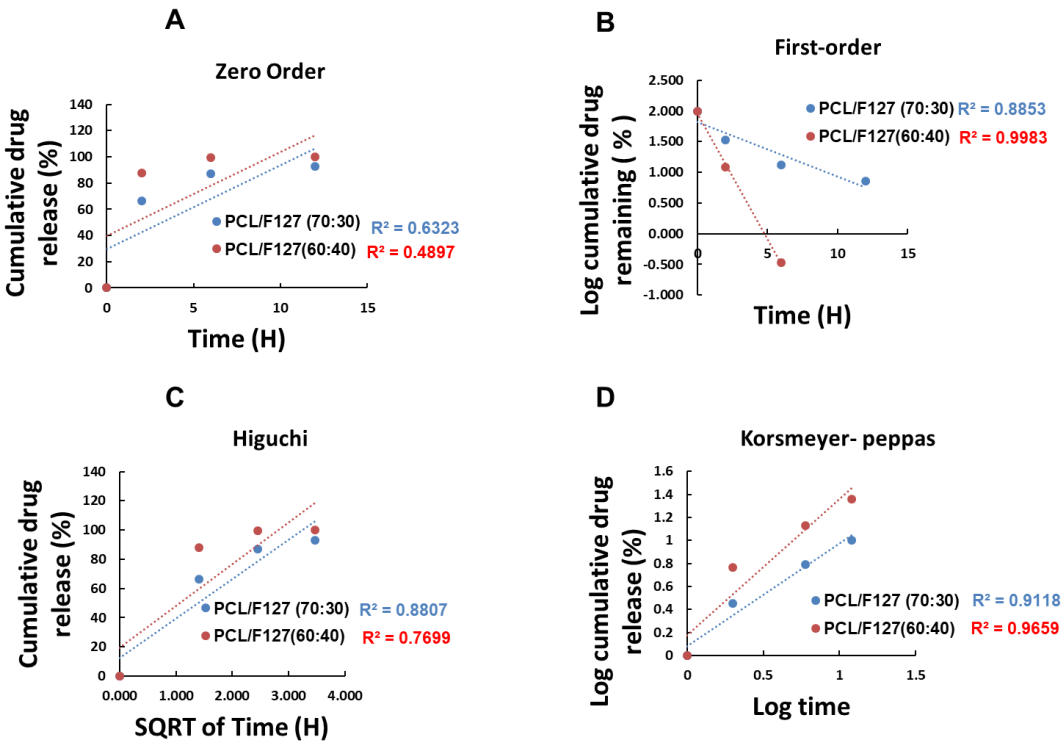


Figure 3-23: Dexamethasone release kinetics of 3D printed PCL scaffolds loaded with 0.17% wt/wt of dexamethasone cyclodextrin. PCL/F127 (70:30) (blue) and PCL/F127 (60:40) (red), fitted to various models: **A**) Zero-order, **B**) First-order, **C**) Higuchi model, and **D**) Korsmeyer-Peppas.

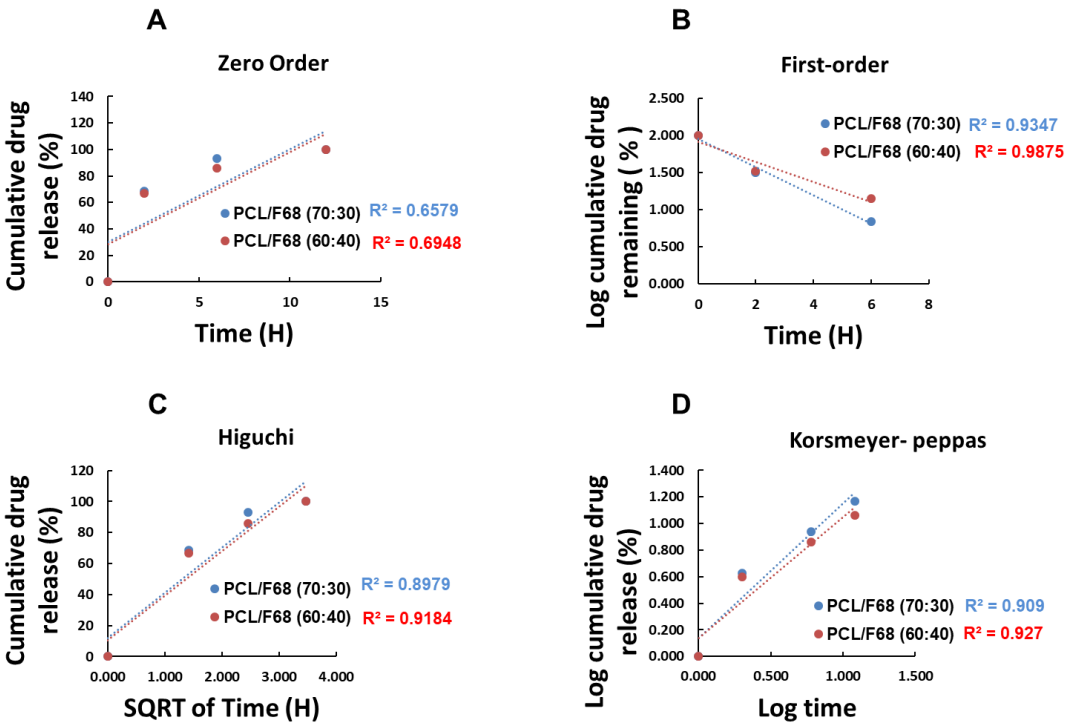


Figure 3-24: Dexamethasone release kinetics of 3D printed PCL scaffolds loaded with 0.17% wt/wt of dexamethasone cyclodextrin. PCL/F68 (70:30) (blue) and PCL/F68 (60:40) (red), fitted to various models: **A**) Zero-order, **B**) First-order, **C**) Higuchi model, and **D**) Korsmeyer-Peppas.

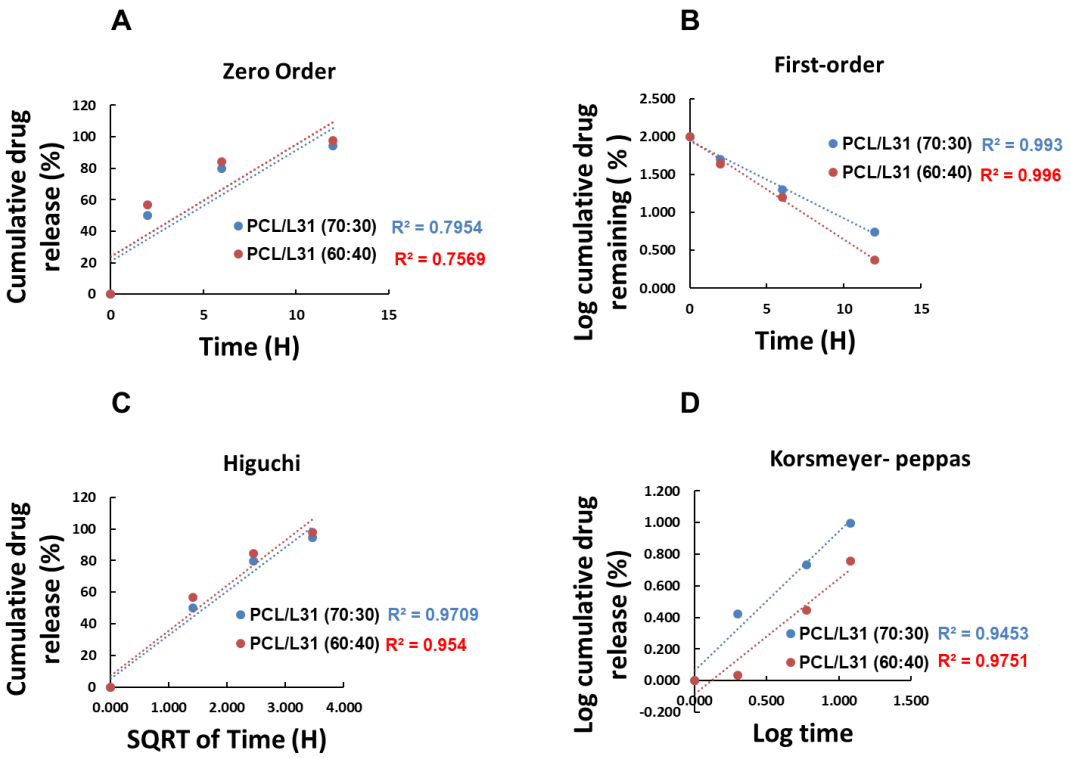


Figure 3-25: Dexamethasone release kinetics of 3D printed PCL scaffolds loaded with 0.17% wt/wt of dexamethasone cyclodextrin. PCL/L31 (70:30) (blue) and PCL/L31 (60:40) (red), fitted to various models: **A**) Zero-order, **B**) First-order, **C**) Higuchi model, and **D**) Korsmeyer-Peppas.

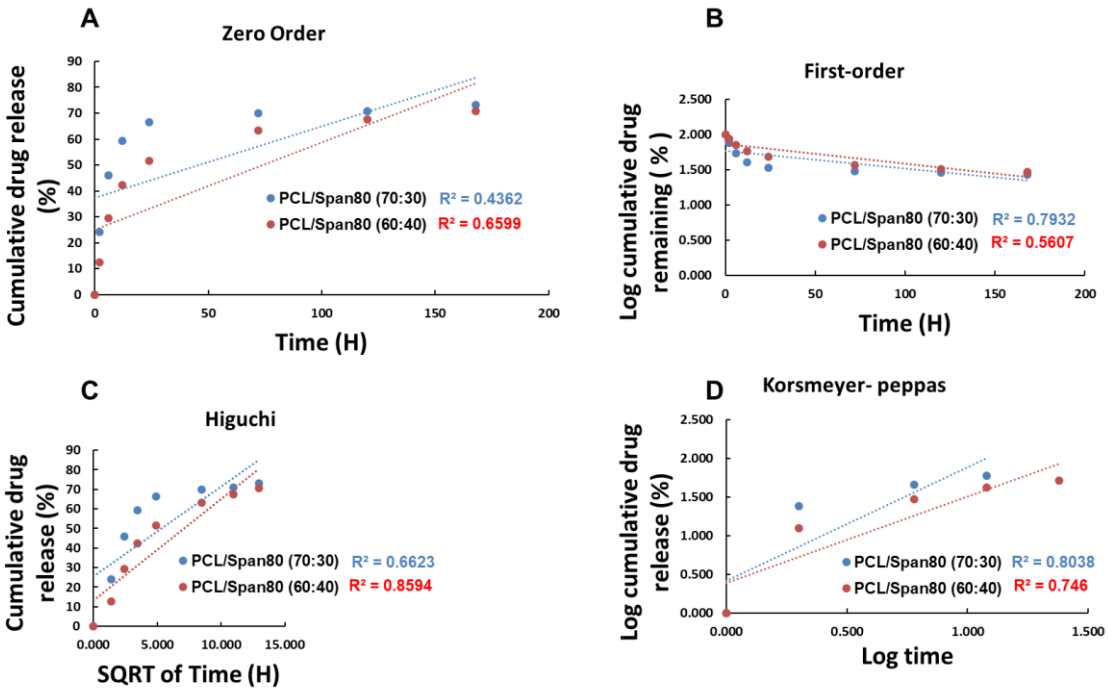


Figure 3-26: Dexamethasone release kinetics of 3D printed PCL scaffolds loaded with 0.17% wt/wt of dexamethasone cyclodextrin. PCL/Span80 (70:30) (blue) and PCL/Span80 (60:40) (red), fitted to various models: **A**) Zero-order, B) First-order, **C**) Higuchi model, and **D**) Korsmeyer-Peppas.

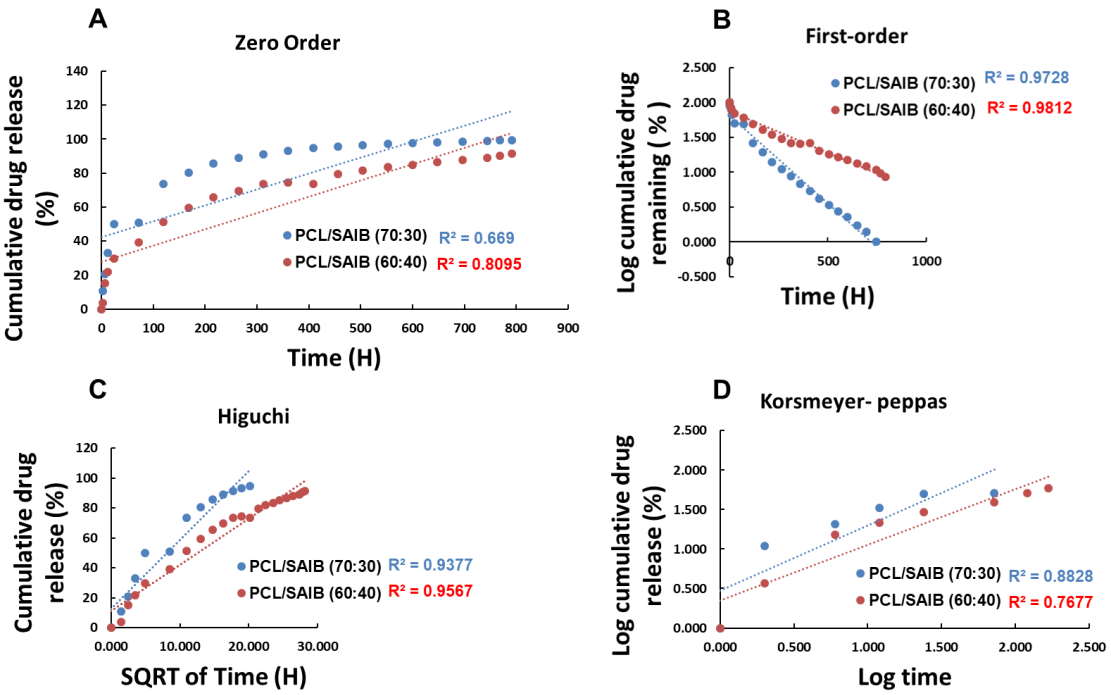


Figure 3-27: Dexamethasone release kinetics of 3D printed PCL scaffolds loaded with 0.17% wt/wt of dexamethasone cyclodextrin. PCL/SAIB (70:30) (blue) and PCL/SAIB (60:40) (red), fitted to various models: **A**) Zero-order, **B**) First-order, **C**) Higuchi model, and **D**) Korsmeyer-Peppas.

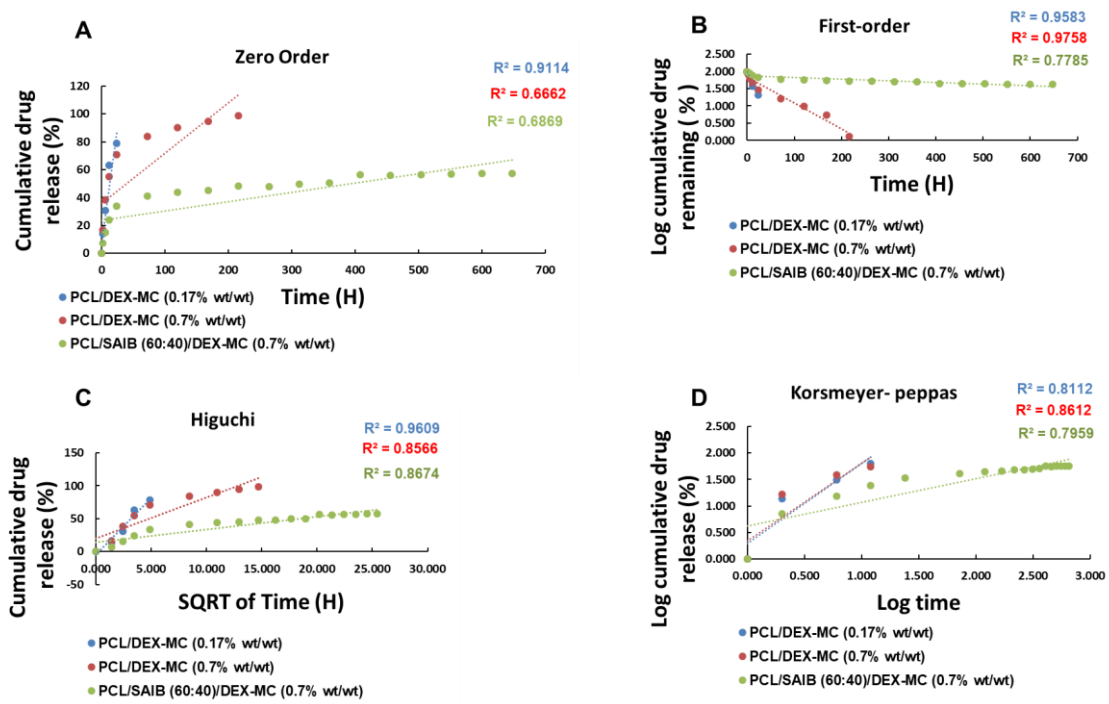


Figure 3-28: Dexamethasone release kinetics of 3D printed PCL scaffolds loaded with various concentrations of dexamethasone microcrystal (DEX-MC) 0.17% wt/wt (blue), 0.7% wt/wt (green), and PCL/SAIB (60:40) loaded with 0.7% wt/wt DEX-MC (red), fitted to various models: **A**) Zero-order, **B**) First-order, **C**) Higuchi model, and **D**) Korsmeyer-Peppas.

Table 3-3: R^2 drug release kinetics values for all 3D printed scaffolds.

3D printed scaffolds	Zero order	First order	Higuchi	KMP	n value KPM
PCL/DEX-CYD (0.05 wt/wt%)	0.65	0.72	0.86	0.79	1.51
PCL/DEX-CYD (0.1 wt/wt%)	0.49	0.91	0.8	0.85	2.01
PCL/DEX-CYD (0.25 wt/wt%)	0.6	0.96	0.71	0.76	1.46
PCL/DEX-CYD (0.17 wt/wt%)	0.6	0.94	0.79	0.76	2.08
PCL/F127 (70:30)/DEX-CYD	0.63	0.89	0.88	0.91	1.03
PCL/F127 (60:40)/DEX-CYD	0.49	0.99	0.77	0.96	0.69
PCL/F68 (70:30)/DEX-CYD	0.66	0.93	0.89	0.91	1.01
PCL/F68 (60:40)/DEX-CYD	0.69	0.99	0.92	0.93	0.91
PCL/L31 (70:30)/DEX-CYD	0.8	0.99	0.97	0.95	0.88

PCL/L31(60:40)/DEX-CYD	0.76	0.99	0.95	0.98	0.73
PCL/Span80 (70:30)/DEX-CYD	0.44	0.79	0.66	0.8	1.47
PCL/Span80 (60:40)/DEX-CYD	0.66	0.56	0.86	0.75	1.12
PCL/SAIB (70:30)/DEX-CYD	0.67	0.97	0.87	0.88	0.82
PCL/SAIB (60:40)/DEX-CYD	0.81	0.99	0.96	0.77	0.71
PCL/DEX-MC (0.17 wt/wt%)	0.91	0.98	0.96	0.81	1.8
PCL/DEX-MC (0.7 wt/wt%)	0.67	0.96	0.86	0.86	1.47
PCL/SAIB (60:40)/DEX-MC (0.7 wt/wt%)	0.69	0.78	0.85	0.8	0.44

3.3.9 Distribution of drugs in 3D printed scaffolds

To explain the reason for improved release after adding SAIB, we analysed the distribution of dexamethasone within different polymer matrices by using ToF-SIMS depth profiling. Two ions from dexamethasone ([M-H]-$C_{22}H_{27}FO_5^-$ and fragment $C_{21}H_{26}FO_4^-$) were detected in the spectra of all dexamethasone-containing scaffolds but not in the PCL/SAIB (60:40) reference scaffold, as shown in **Figure 3-29A and B**. A whole strut was sputtered in the analysis of each sample, as exemplified in **Figure 3-29C**. Dexamethasone was homogeneously distributed on the surface of the PCL/SAIB (60:40)/DEX-CYD (0.17% wt/wt) scaffolds, and the PCL/DEX-CYD (0.17% wt/wt) scaffolds (**Figure 3-29D**). Dexamethasone was demonstrated to be concentrated on the strut surface of the PCL/DEX-CYD (0.17% wt/wt) scaffolds according to the depth profiling, which showed high dexamethasone ion intensity at the strut surface with a rapid signal intensity reduction into the inside of the strut, evidenced by the flatness of the lines of the two dexamethasone ions (**Figure 3-30A**). In contrast, more dexamethasone ions were detected in PCL/SAIB (60:40)/DEX-CYD (0.17% wt/wt) scaffolds (**Figure**

3-30B). Interestingly, the intensities of these dexamethasone ions were much higher in the inside of the SAIB-containing scaffolds (non-flat signal with variations) than those in the PCL/DEX-CYD (0.17% wt/wt) (**Figure 3-30A**). These results demonstrated the advantage of SAIB in enhancing drug distribution within the strut. However, the high signal intensity in PCL/SAIB (60:40)/DEX-CYD (0.17% wt/wt) scaffolds (**Figure 3-30B**) could be attributed to the fact that SAIB influences the signal intensity of dexamethasone a phenomenon known as the matrix effect.

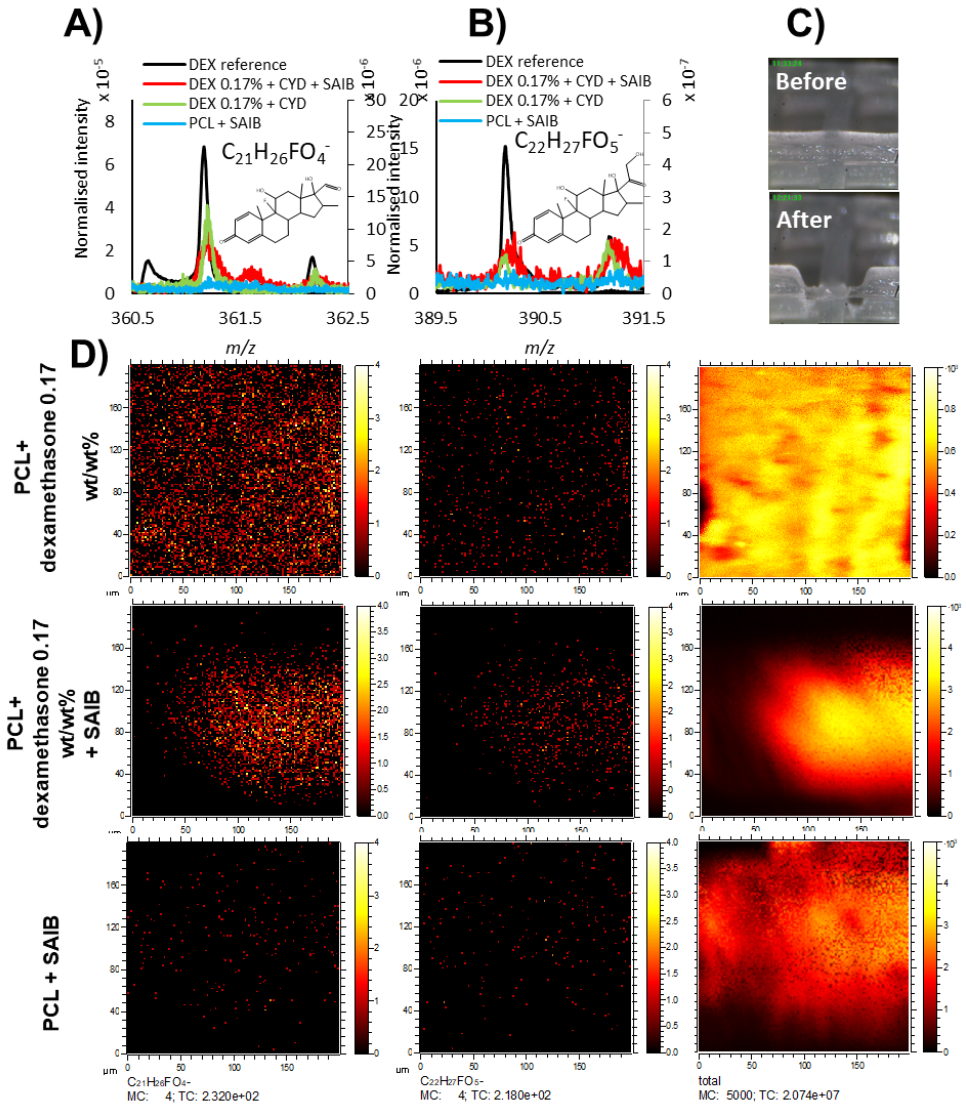


Figure 3-29: Dexamethasone distribution within polymer struts was analysed by using ToF SIMS. **A** and **B**) the two dexamethasone ion peaks. **C**) Image of a strut before and after depth profiling. **D**) Image of ions from different 3D printed scaffolds: PCL+dexamethasone 0.17% wt/wt with SAIB, PCL+dexamethasone 0.17% wt/wt, and PCL with SAIB.

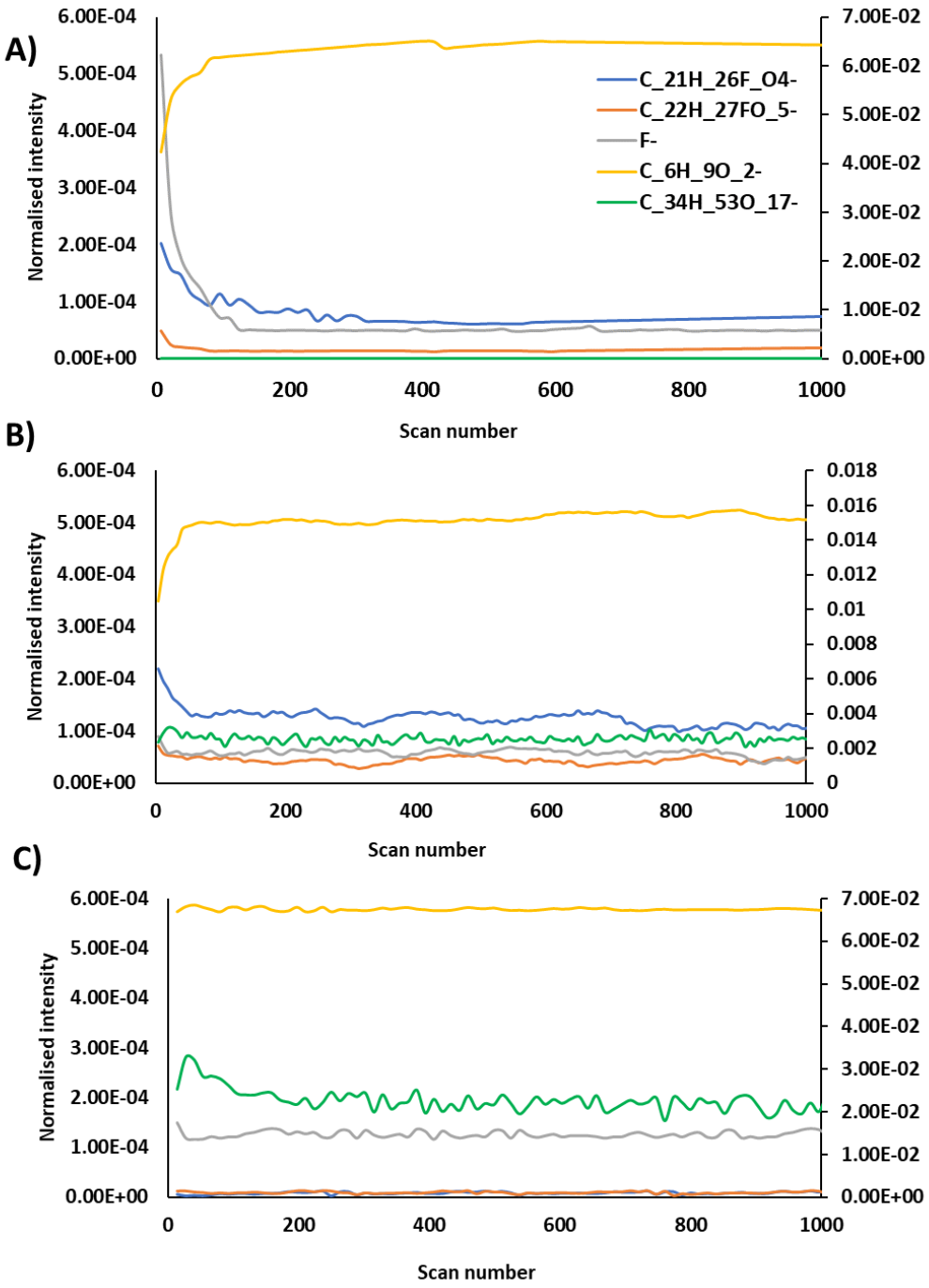


Figure 3-30: Depth profiles of dexamethasone molecular ion $C22H27FO5^-$ (orange) and fragment $C21H26FO4^-$ (blue), F^- (grey), PCL marker $C6H9O2^-$ (yellow), and SAIB marker $C34H53O17^-$ (green) in **A**) PCL + dexamethasone 0.17% wt/wt **B**) PCL+dexamethasone 0.17% wt/wt + SAIB, and **C**) PCL + SAIB scaffolds.

3.4 Discussion

Dexamethasone is a steroidal anti-inflammatory drug used to reduce inflammation and as an osteogenic agent *in vitro* to stimulate the differentiation of mesenchymal stem cells into osteogenic lineages [233, 234]. Although it has been shown that long-term treatment with dexamethasone reduces tissue responsiveness, it is essential to restrict the body's exposure to high glucocorticoid concentrations due to their severe side effects [294]. Therefore, Localised drug delivery systems will deliver the therapeutic medication to the affected area, providing the optimal drug concentration and avoiding the drug toxicity and unwanted side effects that result from systematic drug administration [255].

In this chapter, all 3D printing inks were prepared by blending PCL with different mass ratios of surfactant to reach a final concentration of 57% (w/v) in DCM, which was selected from a previous study where PCL concentration was increased in DCM to reach 57% (w/v) [197]. This concentration of polymer mixtures exhibited a gel form and eased the transfer into printer cartridges, allowing the strut dispensing and construction of the 3D scaffolds by direct ink writing [197, 295]. The printability of inks was mainly affected by their viscosity, which could be modified by the evaporation or addition of DCM solvent to the gel [197]. Moreover, the quality of printing increases with the increasing viscosity of the printing materials, as materials with higher viscosity are more likely to retain their strut shape after deposition [296]. However, increasing the viscosity can reduce the printing resolution, and lead nozzles are more likely to clog when used with these materials [297].

Another point to consider is that the quality of prints produced by direct ink writing depends on the size of the nozzle and the "extrudate swell phenomenon," where the diameter of the material increases after it exits the nozzle [298]. The SEM results showed that the diameter of the struts in the 3D printed scaffolds made of PCL, PCL/DEX-CYD, PCL/DEX-MC, and PCL/SAIB was smaller than the internal diameter of the nozzle. After printing scaffolds using DIW, the polymer structure solidified rapidly as the highly volatile DCM solvent evaporated, resulting in an overall structure that shrank after the DCM solvent evaporated. Furthermore, it has been demonstrated in another study that the nozzle can print a strut much thinner than the nozzle's internal diameter. This is attributed to the interplay between the printing speed and dispensing rate of the ink through the nozzle, which led to the stretching of the strut, which was higher than the dispensing rate used in our study, which is 10 mm/s [197, 299, 300].

On the other hand, scaffolds containing 40% wt/wt of F127, F68, Span 80, and L31 showed strut diameters larger than the internal diameter of the nozzle (160 µm). This phenomenon is known as "die swell," which occurs during the extrusion of the polymer ink, where the polymer swells as it exits the nozzle orifice [299]. Several factors could lead to this phenomenon, including polymer molecular weight, viscoelasticity, the presence of plasticizers, and the printing parameters [282, 299, 301, 302]. Zhong *et al*. illustrated that die swell was decreased after adding two kinds of cationic surfactants to polystyrene. This material showed

different characteristics, including strong shear thinning behaviour, which was attributed to the reduced die swell [282].

PCL and PCL/DEX-CYD scaffolds showed micropore formation on the struts' surface, possibly due to the rapid organic solvent evaporation [280]. In contrast, these micropores were not seen on the surface of the scaffolds containing F127, F68, L31, Span80, and SAIB. It is believed that adding surfactants to the polymer slowed the organic solvent evaporation rate and reduced PCL phase separation [303]. Surfactants can improve the miscibility of immiscible polymer components by reducing interfacial tension and promoting intermolecular interactions. As a result, this can lead to a finer dispersion of polymer phases and the formation of more homogeneous mixtures [303].

Polymers have several uses in pharmaceutical and biomedical applications. Current efforts in drug delivery have focused on the use of polymer mixtures with surfactants to enhance drug release, early burst reduction, and improve bioavailability [279, 302, 304]. It is crucial to have a thorough knowledge of polymer compatibility in the presence of drugs and surfactants. In this chapter, PCL with dexamethasone was blended with the surfactants F127, F68, L31, Span80, and SAIB to evaluate the effect of these additives on prolonging the release of dexamethasone. DSC studies were conducted to investigate phase separation and calculate the degree of crystallinity. A change in glass transition temperature (T_g) is a direct evidence of the miscibility of polymers. The calculated T_g for the mixtures were lower than PCL scaffolds (**Table 3-**

2), indicating that the addition of dexamethasone, Pluronics, Span80 and SAIB functioned as plasticizers [305].

Furthermore, the melting temperature (T_m) was also used to assess the degree of phase separation in the blends. When two polymers are compatible in the amorphous state, the disturbed order in the crystalline phase reduces the T_m [306, 307]. As shown in (**Table 3-2**), the (T_m) of PCL was lowered when blended with a more hydrophobic SAIB. Suggesting the phase mixing of SAIB with PCL. In contrast, the T_m remained unchanged when combined with hydrophilic F127 and F68. These results indicated a phase separation, supported by the double melting peaks, which was more noticeable in PCL/F68 scaffolds (**Figure 3-11**).

The crystalline melting enthalpy (ΔH) results indicated that PCL/F127 and PCL/F68 have greater crystallinity values than PCL/L31, PCL/Span80 and PCL/SAIB. T_m is related to the structure and size of crystals, whereas ΔH relates to crystallinity (X_c). The addition of dexamethasone increased the crystallinity (X_c) of PCL compared to PCL alone, as shown in (**Table 3-2**). Moreover, I noticed that increasing dexamethasone concentration up to 1% wt/wt in 2D films of PCL resulted in increased crystallinity (X_c) of PCL and the enthalpy of fusion (ΔH) (**Appendix Figure 7-3**) & (**Appendix Table 7-2**). Here, dexamethasone may act as a nucleating agent and accelerate PCL crystallization [308].

Furthermore, findings in my project suggested that the hydrophilicity/hydrophobicity of surfactants influences the nucleation and

development of crystalline spherulites by altering the interfacial free energy between the amorphous and crystalline phase in PCL [309]. The degree of crystallinity (X_c) for hydrophobic PCL/L31, PCL/Span80, and PCL/SAIB scaffolds was much lower than that of the PCL/F127 and PCL/F68 scaffolds and the PCL alone. The drop in ΔH in the blends with increasing amounts of surfactants is more apparent for the PCL/L31, PCL/Span80, and PCL/SAIB blends than for the PCL/F127 and PCL/F68 blends. This suggested that the hydrophobic L31, Span80, and SAIB may mix more easily with the PCL polymer chains in the amorphous phase [307].

The release of dexamethasone from polymeric matrices has been the subject of extensive research. Variable release profiles can be attained by selecting suitable polymeric matrices, geometries, preparation methods, drug doses, and particle sizes [186, 294, 310]. However, prolonged release of dexamethasone from 3D printed PCL prepared by direct ink writing method with reduced early burst release has not been achieved. Initially, we prepared PCL/DEX-CYD inks with different concentrations of 0.2%, 0.7%, and 1% wt/wt. These results showed a prolonged release was achieved from all 2D films with variable cumulative releases behaviour and mechanisms (**Appendix Figure 7-4 and Appendix Figure 7-5**) and (**Appendix Table 7-3**).Moreover, these results showed that increased drug loading had increased the degree of crystallinity of PCL (**Appendix Table 7-2**), which could be attributed to the prolonged release of dexamethasone from 2D film. The effect of polymer crystallinity on release behaviour was investigated in the

literature, illustrating how it affects the rate of drug release [311-313]. This is not the scope of the current thesis.

On the other hand, all PCL/DEX-CYD (0.05%, 0.1%, and 0.17% wt/wt) 3D printed scaffolds similarly showed early burst release, which could be attributed to the drug's presence on the struts' surface. This was proven by ToF-SIMS depth profiling for the 3D printed scaffold PCL/DEX-CYD 0.17% wt/wt, which showed a high signal of dexamethasone on the surface, which then became undetected in the internal of the struts (**Figures 3-20 and 3-21 A**). This work investigated the possibility of decreasing dexamethasone burst release and extending the release time by combining PCL with F127, F68, L31, Span80, and SAIB. Based on findings in my project, blends of PCL and surfactants produced 3D scaffolds with smooth-surface struts. However, SAIB was more effective than Pluronics F127, F68, and L31 at reducing the initial drug burst release and extending the overall release period. Furthermore, these results validated the observation that the relatively hydrophilic Pluronic F127 and F68 rapidly leached out during the incubation period, resulting in a rapid dexamethasone release. The weight loss measurements support this observation (**Appendix Figure 7-6**).

On the other hand, the hydrophobic L31 has reduced the burst release and prolonged the release of dexamethasone compared to F127 and F68. PCL/L31 blend scaffolds, in which L31 chains were intertwined with the amorphous PCL chains, effectively sustained dexamethasone release. Pluronics are synthetic surfactants made up of three blocks: two blocks of ethylene oxide (EO) and one block of propylene oxide (PO).

The EO blocks are hydrophilic, meaning they are attracted to water, while the PO blocks are hydrophobic and repelled by water. The ratio of EO to PO blocks in pluronic can be varied, which gives them a wide range of hydrophilic and hydrophobic properties [314]. These results agree with what was published by Park *et al*. [300]. They demonstrated the effect of blending hydrophilic F108, P104, and hydrophobic L101 pluronics with PLA on controlling the release of proteins. They found that when matrices were incubated in an aqueous solution, water first hydrated the amorphous region by penetrating the matrices. Consequently, the PLA/L101 blend scaffolds exhibited liquid-crystalline phase transitions, suggesting the formation of a gel-like structure that fills the pores on the PLA surface. This phase maintains the protein molecules within the pores, preventing their rapid release.

Moreover, 40% wt/wt of SAIB blended with PCL prolonged the release of dexamethasone from 3D printed scaffolds for more than 30 days, whereas mixing 40% wt/wt of F127 and F68 in the 3D printed PCL scaffolds showed that more than 95% of dexamethasone was released after one day of incubation in PBS (**Figure 3-20**). This effect was attributed to the hydrophobicity of SAIB, which slows the diffusion of dexamethasone from a 3D printed scaffold when incubated in PBS. Sucrose acetate isobutyrate (SAIB) is a food additive. It is frequently employed as a weighting agent in beverages and as a stabilizer for flavour emulsions to prevent the separation of citrus oils in beverages. SAIB is also utilized as a fragrance fixative and to confer transfer-resistant properties to lipstick. This compound is a colorless, tasteless,

and viscous liquid that is insoluble in water and exhibits a strong affinity for lipids [315]. Numerous studies have documented SAIB's effectiveness as a material for regulating the burst release of drugs from control release systems [272, 273]. In this thesis the impact of adding SAIB as 30%, and 40% (w/w) to PCL has reduced the initial burst release from 60% to 30% and 19% at the first 12h and prolonged dexamethasone release over 35 days, respectively (**Figure 3-20**). This finding agrees with what has been reported on the impact of mixing SAIB on the controlled release of therapeutic agents. It has been shown that SAIB/PLGA hybrid electrospuns significantly prolonged the release and reduced the initial burst of the Minocycline hydrochloride antibiotic from 66.18% to 2.92%, and the initial release of Naringin from 63.20% to 0.00%, respectively [316, 317].

Furthermore, the effect of hydrophobic and hydrophilic additives on the release profile of drugs has been reported. Zare M. *et al*. showed that the addition of ethyl heptanoate and glycerol at different ratios (1, 3, and 5% w/w) reduced the burst release and prolonged the release of leuprolide acetate loaded in poly(D, L-lactide-co-glycolide)hydroxylated (PLGA-H). Ethyl heptanoate has a greater effect than glycerol. To explain this phenomenon, it appears that because glycerol is a hydrophilic additive, its presence in polymer formulations increases the water exchange rate, resulting in rapid drug release. Adding ethyl heptanoate as a hydrophobic additive, on the other hand, decreases the water exchange rate and controls the release [279].

Furthermore, DEX-CYD concentration in PCL ink was increased to 3.85% wt/wt, equivalent to (0.25% wt/wt of dexamethasone). Unfortunately, this percentage blocked the nozzle during the printing. It seems that PCL did not increase the solubility of the drug complex at this concentration, leading to drug precipitation which blocked the nozzle orifice during printing. Nozzle clogging during printing with high drug concentrations can occur due to several reasons: Higher drug concentrations in the ink can lead to an increase in ink viscosity. The increased viscosity can make it difficult for the ink to flow smoothly through the printing nozzle, resulting in clogging. The drug particles or additives may contribute to the increased viscosity, causing the ink to become more resistant to flow [318]. Some drugs or additives may have a tendency to aggregate or form clusters within the ink. These aggregates can be larger than the nozzle diameter, leading to blockages. Aggregation can occur due to various factors, such as drug-polymer interactions, inadequate mixing, or improper solvent choice. When aggregates reach the nozzle, they can obstruct the flow and cause clogging. On the other hand, the drug or its excipients may not be fully compatible with the ink formulation, including the polymer matrix or other additives. This incompatibility can lead to the formation of precipitates within the ink, which can clog the nozzle [319, 320].

As a result, dexamethasone was prepared as a microcrystal in order to overcome the nozzle blockage during printing and examine the effect of high drug loading on the release behaviour of 3D printed scaffolds. We successfully printed a PCL scaffold with a high drug loading of DEX-MC

without nozzle blockage. This may be attributed to the fact that PCL polymer has enhanced dexamethasone microcrystals' solubility in the amorphous phase [270, 321]. As this is not the scope of the current thesis, further investigation is required to understand the interaction between drug and polymer and the effect of this on the nozzle blockage mechanism.

Both scaffolds loaded with 0.17% and 0.7% wt/wt showed an initial burst release greater than 60% in the first 24h. Vacanti *et al*. studied the release of dexamethasone from a PCL electrospun scaffold loaded with dexamethasone. They also found a burst release of dexamethasone from PCL and attributed the fast release to the low intermolecular interaction between PCL and dexamethasone [186]. The current work has proven no covalent bonds were formed between them, but it could be physical ones such as hydrogen bonding or hydrophobic interactions between PCL, dexamethasone, and SAIB, which cannot be detected by FTIR and require highly sensitive instrumentation such as Raman spectroscopy.

Adding SAIB to the scaffolds loaded with 0.7% wt/wt of DEX-MC has reduced the burst release to around 40% in the first 24h and sustained the release of dexamethasone for nearly 30 days. During the prolonged release, we noticed that PCL/SAIB/DEX-MC 0.7% wt/wt almost achieved 50% over 30 days. This may be due to the heterogeneity of dexamethasone microcrystal size (**Figure 3-8**) which may affect drug leaching from scaffold during the release compared to the dexamethasone-cyclodextrin complex, which has a higher solubility due

to the presence of cyclodextrin [283, 322]. This scaffolds required further study to examine dexamethasone release behaviour and effect for several months.

For decades, drug release has been an essential topic in the field of drug delivery. With the advancement of material design and engineering, complex and multifunctional novel materials have been incorporated into the creation of drug-delivery devices and systems. The term "drug release" refers to the migration of drugs from their initial position in a polymer matrix to the release medium [264]. The release mechanism of drugs is an important consideration, particularly in the context of formulating a delivery system that can administer the medication gradually throughout a designated timeframe [323]. Drugs incorporated in polymeric carriers are usually released by diffusion, degradation, or a combination of both mechanisms [323]. Moreover, it has been reported that the release mechanism can be altered by changing the composition of the polymer used in designing the release system [324].

In this chapter, DEX-CYD was incorporated into PCL as 0.05, 0.1, and 0.17% wt/wt. It is evident from (**Table 3-3**) that the release mechanism of PCL scaffolds loaded with 0.1% and 0.17% wt/wt fits the first-order mechanism. In porous matrices, the amount of drug released is directly proportional to the amount of drug remaining in the matrix. This means that as the amount of drug released increases, the amount of remaining drug in the matrix decreases. As a result, the amounts of released drugs tend to decrease over time [278]. Moreover, due to the slow degradation

of PCL, diffusion through the scaffold is the only feasible drug release mechanism [323].

The findings presented in this chapter provide a comprehensive view of the release mechanisms for various formulations of dexamethasone-loaded scaffolds, specifically highlighting the efficiency of certain combinations and the versatility in release dynamics. Each of the models Korsmeyer-Peppas, first-order, Higuchi, and zero-order elucidates different aspects of the drug release process, often related to the diffusion mechanism or the erosion involved in the release from the scaffolds.

Notably from (**Figures 3-23D, 3-24D, and 3-25D**) several PCL (polycaprolactone) formulations with different poloxamer ratios (PCL/F127, PCL/F68, PCL/L31) showed a high degree of compliance with the Korsmeyer-Peppas model, evidenced by the robust R^2 values ranging from 0.91 to 0.98 (**Table 3-3**). This suggests that the release mechanism of dexamethasone from these particular scaffolds is more complex, governed by a combination of diffusion and erosion processes. According to the Korsmeyer-Peppas kinetic model, when ‘n’ (the exponent of release) is less than 0.43, drug release is controlled by Fickian diffusion. In contrast, when n is greater than 0.85, drug release is controlled by erosion. Furthermore, for n values between 0.85 and 0.43, drug release is governed by two mechanisms: diffusion and erosion [292]. The ‘n’ values for PCL/F127 (70:30)/DEX-CYD, PCL/F127 (60:40)/DEX-CYD, PCL/F68 (70:30)/DEX-CYD, PCL/F68 (60:40)/DEX-CYD, PCL/L31 (70:30)/DEX-CYD, and PCL/L31(60:40)/DEX-CYD

greater than 0.85 (**Table 3-3**), which imply that the release of dexamethasone is caused by the erosion, this could potentially be due to the swelling of the polymers, altering the network structure for drug diffusion, and the simultaneous degradation of the scaffold by leaching of poloxamers F127, F68, and L31 out of PCL scaffolds by hydration. It has been reported that the release of strontium ranelate (SrR) from polyvinyl alcohol (PVA)–strontium ranelate (SrR)–Polycaprolactone (PCL) electro spun scaffolds fitting Krosmeyer-peppas model with a release governed by Fickian diffusion and it was assumed as fast as possible in the samples with higher SrR content [325]. In another report, electrospun polycaprolactone (PCL)–gelatin blends were investigated to understand the release mechanism of Rhodamine B dye. The results indicated that diffusion was a dominant mechanism for PCL–gelatin electrospun fibres. As gelatin is highly soluble in water and tends to gelate, it affects the diffusion of release media in and out of the scaffold [324]. Moreover, drug release from polymer blends is a complex process. One or more mechanisms can dominate drug release from polymer. Wu *et al*. studied the release mechanism of ciprofloxacin hydrochloride from electrospun PLGA scaffolds. The study identifies three stages of drug release: Stage I involves fibre swelling and diffusion; Stage II involves diffusion through a fused membrane structure resulting in slow release; and Stage III involves polymer degradation and release of the remaining drug [291].

The inability of PCL/Span80 scaffolds (**Figure 3-26A-D**) to fit any tested models is intriguing. This irregularity might be attributed to the instability

or inconsistency in the formulation or possibly due to a more complex release mechanism that doesn't adhere to common kinetic models. Further investigation into the physical properties of these scaffolds and the interaction between Span80 and PCL could elucidate the underlying reasons for this observation.

On the other hand, the release of dexamethasone from PCL/SAIB fits the first order and Higuchi mechanism (**Figure 3-27B-C**). Drug release from polymer blends is considered a complex process and can be dominated by one or more mechanisms, whether diffusion or erosion [324]. Higuchi's mechanism assumes that drug release is primarily driven by diffusion and that the drug's solubility or dissolution rate is not the limiting factor. The model is commonly applied to solid dosage forms, such as matrices or reservoir-based systems, where the drug is dispersed within a polymer or matrix material. Furthermore, in the Higuchi mechanism, the drug release profile typically shows an initial burst release, followed by a slower and sustained release as diffusion becomes the dominant mechanism [293]. Interestingly, no burst release was noticed at the first 24 h, and the drug release was dominated by a zero-order mechanism (**Appendix Figure 7-7**), which implies that the release of the drug was constant, irrespective of the amount of drug present in the scaffolds, which is attributed to the presence of SAIB, which has an impact on slowing the diffusion of the drug [272, 278]. The dexamethasone release from PCL/SAIB scaffolds followed both first-order and Higuchi models suggests an intricate release mechanism driven by concentration gradients (first-order) and a diffusion process (Higuchi), possibly through

a matrix system. It may indicate a more controlled and sustained release strategy, beneficial for prolonged drug delivery applications.

The release of dexamethasone from PCL/DEX-MC scaffolds at 0.17% wt/wt exhibited multiple release mechanisms: zero order, first order, and Higuchi (**Figures 3-28A, B, and C**). This complexity in release mechanisms suggests that the release of dexamethasone from this scaffold composition is highly dependent on various factors, possibly including the drug loading and the drug microcrystal size. The zero-order release suggests a constant release rate, which is desirable in maintaining a therapeutic drug concentration. However, the concurrent applicability of the first-order and Higuchi models suggests an initial concentration-dependent burst release followed by a diffusion-controlled process (**Figure 3-21**). This complexity might be attributed to the formulation's ability to accommodate different release phases, potentially advantageous for immediate therapeutic effect followed by sustained release.

Lastly, the release of dexamethasone from PCL/DEX-MC at 0.7% wt/wt fits the first-order model (**Figure 3-28B**), suggesting that, in this specific case, the release behaviour is predominantly influenced by the concentration. Higher concentrations might alter the polymer matrix's physical characteristics, affecting the drug's solubility or diffusion coefficients.

3.5 Summary

In this chapter, I have successfully fabricated 3D printed scaffolds prepared from several blends of PCL and surfactants loaded with dexamethasone. I was able to optimise the default printing parameters. SEM has shown that all scaffolds were reproduced with a slightly smaller strut size than the printing nozzle. Moreover, adding F127, F68, L31, Span80, and SAIB resulted in smooth strut surface morphology. On the other hand, scaffolds fabricated from PCL and dexamethasone only exhibited micropores on the strut surface. Different characterisation techniques were utilised, including DSC, FTIR, and ToF-SIMS. All the techniques have revealed that blending PCL with SAIB and dexamethasone has no chemical interaction, and the addition of hydrophobic surfactants like SAIB has reduced PCL crystallinity compared to hydrophilic surfactants F127 and F68. Moreover, the presence of SAIB in the scaffold formulation has improved the drug distribution in the strut compared to the PCL scaffold without SAIB. The release behaviour of dexamethasone from all 3D printed scaffolds was studied, and prolonged release of dexamethasone over 30 days was achieved by using SAIB.

In the next chapter, 3D printed PCL/SAIB/DEX-CYD will be utilised to study the effect of prolonged release of dexamethasone on the immunomodulation of M1 macrophages and to explore the impact of dexamethasone release on macrophage polarisation and osteogenic differentiation of mesenchymal stem cells in macrophage-MSC co-cultures.

4. Chapter Four: Control release of dexamethasone from 3D printed scaffolds promotes M2-like macrophage and enhances osteogenic differentiation of MSCs

4.1 Introduction

Bone tissue engineering commonly utilises biomaterial scaffolds which can accommodate stem cells and/or molecules that promote angiogenesis, stem cell recruitment and osteogenic differentiation [197, 326]. The responses of bone-forming stem/progenitor cells to biomaterial scaffolds have been the focus of this field [327, 328]. Increasingly, the interactions between osteolineage cells and immune cells and the inflammatory response associated with implanted scaffolds have attracted more attention [329, 330]. It is now well-known that immune cells play critical roles in bone healing and homeostasis [9]. Early inflammation is essential for removing debris and dead cells, promoting angiogenesis, and recruiting cells to the fracture site [331]. However, this inflammation needs to subside and resolve to allow proper bone formation. Persistent inflammation without returning to normal homeostasis status is associated with impaired tissue repair and fibrosis [332]. The presence of a biomaterial scaffold increases the complexity of the immunological microenvironment at a bone defect site due to biomaterial-immune cell interactions [173]. On the other hand, biomaterials offer an opportunity to module local immune responses towards a favorable condition for tissue regeneration. The utilisation of biomaterial physical and chemical properties and their ability as drug

carriers have been investigated to modulate immune response that favors tissue regeneration [332, 333].

Bone healing depends on coordinated interactions between inflammatory cells and osteogenic stem/progenitor cells [329]. Macrophages have been demonstrated to be a critical player during fracture repair. In particular, macrophages exhibit different activation statuses and functions depending on the stimuli they are exposed to. Conventionally, two activation statuses of macrophage (classically activated pro-inflammatory M1 and alternatively activated anti-inflammatory M2 have been widely described [76]. Animal studies have shown that fractures do not heal without the direct involvement of macrophages [334]. Moreover, efficient fracture healing relies on the migration of bone marrow-derived monocytes/macrophages to the fracture site [335]. Bone resident osteomacs have also been described as critical mediators of endochondral and intramembranous bone healing [73, 336].

Co-culture of MSCs with macrophages has shown that M0 and M1 macrophages solely stimulated the osteogenic differentiation of MSCs in the early and middle stages (measured by ALP activity and gene expression of early-stage osteogenic markers), whilst M2 induced higher late-stage mineralisation (4 weeks *in vitro*) [87]. However, in another study, both M1 and M2 macrophages were found to promote similar levels of bone mineralisation in MSCs after 4 weeks of co-culture [337]. Subjecting MSCs to a 72- to 96-hour pro-inflammatory environment (M1) before polarising macrophages to M2 by using IL-4 was found to be

critical for optimal matrix mineralisation *in vitro* [338]. Oncostatin M has been identified as a soluble factor which is secreted from M1 macrophages via a COX-2 and PGE2 regulatory loop for promoting osteogenic differentiation of MSCs [9]. Taken together, the literature shows that the initial inflammation and presence of M1 macrophages and subsequent macrophage transition to M2 are important for osteogenic differentiation and mineralisation. Existing conflicting data in the literature also necessitates more investigate on this topic.

However, these studies have only investigated the effects of macrophages on MSCs in vitro by adding cytokines directly to culture media to modulate macrophage polarisation. In the bone tissue engineering context, this switch of macrophage polarisation using soluble factors would need to be achieved *in situ*. To this end, incorporation and sequential release of M1 and M2-promoting molecules (IFN-γ, IL4) from decellularised bovine bone scaffolds were demonstrated to promote initial M1 polarisation and subsequent transition to M2, which enhanced vascularisation within the scaffolds [229]. A similar approach for titania nanotubes showed increased M1 and M2 cytokines at early (3 days) and late time points (7 days), respectively, *in vitro* [230]. PEG-based hydrogels loaded with IL10 and aspirin-triggered resolvin-D1 (both for inflammation resolution) have been shown to polarise macrophages towards an anti-inflammatory M2 phenotype [339]. It is worth noting that these studies all showed relatively quick release of inflammation-modulating soluble factors. Anti-inflammatory drugs, such as dexamethasone, have been loaded in 3D printed or

electrospun polymer scaffolds to modulate inflammation or to promote osteogenic differentiation [115, 308, 333, 340]. Despite its known adverse effect on bone remodelling at supraphysiological concentrations [341], 10-100nM dexamethasone has been widely used to promote osteogenic differentiation of MSCs in vitro [342]. The release profile of loaded dexamethasone is polymer matrix dependent, with PLA delivering a more sustained release compared to burst release from PCL [333]. Moreover, the burst release of dexamethasone from PCL did not reduce inflammatory capsule compared to drug-free PCL electrospun fibres [333], suggesting a controlled release of dexamethasone is necessary for modulating inflammation.

To the best of our knowledge, the interplay between macrophage polarisation and osteogenic differentiation of MSCs under controlled release scaffolds has not been investigated before. Given the potential of immunomodulatory biomaterial scaffolds in orthopaedics and other fields, studies like the one presented here will offer new insight into this important topic of macrophage-MSC crosstalk. Herein, I studied the responses of macrophages and MSCs under the presence of controlled-release PCL scaffolds to mimic the case of bone healing with the presence of an immunomodulatory biomaterial scaffold. I hypothesise that the localised release of dexamethasone from scaffolds not only promotes osteogenic differentiation but also modulates macrophage activation status to favour bone formation. In **chapter 3,** the sustained release of dexamethasone from polycaprolactone (PCL) by adding the excipient-sucrose acetate isobutyrate (SAIB) was achieved. In this

chapter, the polarisation of macrophages and osteogenic differentiation of MSCs were investigated in macrophage-MSC co-cultures in the presence of a control release system.

4.2 Materials and Methods

4.2.1 Materials

Polycaprolactone (PCL, Mn 80,000), fetal bovine serum (FBS), mercaptoethanol, penicillin/ streptomycin, 70% ethanol, T75 tissue culture flask, 24 wells tissue culture plates, 6 wells tissue culture plates, papain, dexamethasone-cyclodextrin (DEX-CYD, mass ratio 65:1000=dex:(dex+cyd), granulocyte-macrophage colony-stimulating factor (GM-CSF), Lipopolysaccharide (LPS) from *E. coli*, macrophage colony-stimulating factor (M-CSF), Interleukin 4 (IL-4), methanol, dichloromethane (DCM), cetylpyridinium chloride (CPC), Alizarin Red, non-essential amino acids, β-glycerophosphate, and ethylenediaminetetraacetic acid (EDTA) were purchased from Sigma-Aldrich, UK. THP1 cell line (ATCC no. TIB-202), Phorbol 12-myristate 13-acetate (PMA), Quanti-iTTM Picogreen® kit, mouse anti-human calprotectin antibody, Rhodamine red goat anti-mouse IgG (H + L) secondary Ab, Alexa flour 488 goat anti-rabbit IgG (H + L) secondary Ab, DAPI and RPMI-1640 were purchased from Fisher Scientific, UK. α-MEM (BE12-169F) and ToxiLight^{TM} non-destructive cytotoxicity bioassay kit were purchased from Lonza, UK, and rabbit anti-human MR Ab from Abcam-UK.

4.2.2 Ink preparation and 3D printing of scaffolds

To prepare PCL/SAIB (60:40) Dexamethasone-Cyclodextrin (DEX-CYD) scaffolds. A 2.63 wt/wt% of Dexamethasone-Cyclodextrin (equivalent to 0.17% wt/wt dexamethasone) was dissolved in DCM. Sucrose acetate isobutyrate (SAIB) was added to PCL at mass ratios (60:40, PCL: excipient) combined with the PCL polymer to reach a final concentration of 57% wt/vol in DCM. The inks were left on the roller overnight to completely dissolve prior to printing. Lattice scaffolds with a dimension of 10 x 10 x 5 mm^3 were designed by BioCAD software. PCL solutions were printed in the air by 3D Discovery printer (regenHU, Switzerland) through a tapered tip (31G, 160 µm internal diameter, Integrated Dispensing Solutions) with the following parameters: strut spacing of 0.52 mm, speed rate of 8 mm/s, 0.12 mm layer thickness, and 6 bar of pressure.

4.2.3 Thermogravimetric (TGA) analysis

TGA was conducted using a TGA thermal analyzer (TA Instruments TGA500, USA). Samples were heated from 25 to 800 °C at a rate of 10 °C min^{-1} under nitrogen flow.

4.2.4 THP1 culturing and Polarisation to macrophage

THP1 monocytes were expanded in THP1 cell culture medium (RPMI-1640 containing 10% heat-inactivated fetal bovine serum (FBS), 1% penicillin/streptomycin (P/S), 10 mM 4-(2-hydroxyethyl)-1 piperazineethanesulfonic acid (HEPES), 1% GlutaMax, 1 mM Sodium Pyruvate, 2.5 g/L Glucose and 0.05 mM Mercaptoethanol. THP-1 cells are supposed to duplicate in 24-48 hrs, and the cell density shouldn't exceed 1,000,000 cells/ml to keep the cells healthy.

Monocytes were stimulated by 50 ng/ml of PMA in an enriched medium for 6 hrs to activate cells to macrophage M0 lineage. After 6 hrs, PMA-enriched medium was decanted and substituted with fresh complete growth media. Macrophages were rested in culture overnight at 37°C and 5% CO_2. For M1 polarisation, M0 cells were exposed to 50 ng/mL GM-CSF and 100 ng/ml LPS and incubated for 72 hrs at 37°C and 5% CO_2. For M2 polarisation, M0 cells were exposed to 50 ng/ml M-SCF and 20 ng/mL IL-4, and all groups were incubated at 37°C and 5% CO_2 for 72 hrs to fully polarised and become ready for further study.

4.2.5 Immunomodulation dexamethasone does on the polarisation of M1 macrophages.

To assess the ability of DEX-CYD to modulate the polarisation of M1 macrophage. $5X10^5$ cells/well of THP-1 monocytes were seeded into 24-well plates and then activated into M0 macrophage by 50 ng/ml PMA for 6 hrs. Afterwards, PMA-enriched medium was substituted with fresh complete growth media and rested overnight at 37°C and 5% CO_2. Next, M0 macrophages were treated with (100, 10, 1, 0.1, and 0.01 µM) of DEX-CYD in the presence of 50 ng/ml GM-CSF and 100 ng/mL LPS. The treated cells were incubated for intervals times 3 and 7 days. Media were collected for cytokines analysis at each time-point, and cells were fixed with 4% paraformaldehyde and used for immunofluorescent staining.

4.2.6 Polarisation of M1 macrophage by released dexamethasone.

To assess the ability of released DEX to modulate the polarisation of M1 macrophage. $2x10^6$ cells/well THP-1 monocytes were seeded into 6-well plates and then activated with 50 ng/ml PMA for 6 hrs. After 6 hrs, PMA-

enriched medium was substituted with fresh complete growth media and rested overnight at 37°C and 5% CO_2. M0 macrophages were incubated with 3D printed scaffolds (PCL/DEX-CYD and PCL/SAIB/DEX-CYD, and PCL) in the presence of 50 ng/mL GM-CSF and 100 ng/mL LPS. Cells were incubated for intervals times 3 and 7 days. Media were collected for cytokines analysis at each time point, and cells were fixed with 4% paraformaldehyde and used for immunofluorescent staining.

4.2.7 Bioactivity of released dexamethasone from PCL/SAIB/DEX-CYD

The bioactivity effect of released dexamethasone from PCL/SAIB (60:40)/DEX-CYD in basal RPMI media has been assessed. Initially, the absorbance of released dexamethasone at days 15, 25, and 35 was measured by UV-vis. On the other hand, the immunomodulatory effect of the released dexamethasone on the M1 macrophage polarisation was assessed too. $5X10^5$ cells/well of THP1 were seeded in 24 well plates and activated to M0 macrophage for 6 hours by 50 ng/ml PMA. After the activation period, PMA media was withdrawn, replaced with complete fresh media, and incubated overnight. M0 macrophages were treated with the released media of 3D printed scaffolds after the addition of 10% heat-inactivated fetal bovine serum (FBS), 1% penicillin/streptomycin (P/S), 10mM 4-(2-hydroxyethyl)-1 piperazineethanesulfonic acid (HEPES), 1% GlutaMax, 1mM Sodium Pyruvate, 2.5 g/L Glucose and 0.05 mM Mercaptoethanol in the presence of 100 ng/ml of LPS and 50 ng/ml of GM-CSF. Then, cells were incubated for 3 and 7 days. At each time point, media were collected and transferred to a new Eppendorf tube

and centrifuged at 13,000 xg 4°C to remove cellular debris. Supernatants were transferred to a new Eppendorf tube and frozen at -80°C. Human tumour necrosis factor-alpha (TNF-α), human lL-6, human IL-10, and human TGF-β1 DuoSet ELISA kit (R&D Systems) were quantified according to manufacturer's guidelines, and normalized to DNA content.

After media collection at each interval times, cells were digested with 1 mL of digestive solution (280 μg/mL papain, 50 mM EDTA, 5 mM L-cysteine in PBS pH 6.5) and incubated at 65°C overnight. Cell lysates were centrifuged at 13,000 *xg* 4°C for 5 min to remove cellular debris, and the supernatant was used to quantify total DNA concentration by using Quanti-iTTM Picogreen® kit according to manufacturer instructions.

4.2.8 MSCs expansion and osteogenic differentiation

Bone-derived human mesenchymal stem cells (MSCs) were immortalised, clonally selected (due to the variation in differentiation potential among clones), and maintained according to previous protocols [247]. The MSCs have been regularly assessed to ensure the capability of expansion without the loss of trilineage differentiation potential. MSCs were incubated in an expansion medium (Dulbecco's modified Eagle's medium (DMEM, high glucose) supplemented with 10% fetal bovine serum (FBS), 1% non-essential amino acids, 1% GlutaMax, and 1% penicillin/streptomycin solution. Osteogenic differentiation was induced using (αMEM containing 10% FBS, 1% 1% GlutaMax, 1% penicillin/streptomycin solution, and 10 mM β-glycerophosphate) with 100 nM dexamethasone.

4.2.9 Macrophages polarisation and co-culture with MSCs

THP1 monocytes were expanded in THP1 cell culture medium (RPMI-1640 containing 10% FBS, 1% Penicillin/Streptomycin, 10 mM 4-(2-hydroxyethyl)-1 piperazineethanesulfonic acid (HEPES), 1 mM Sodium Pyruvate, 1% GlutaMax, 2.5 g/L Glucose and 0.05 mM Mercaptoethanol. Monocytes were stimulated by 50 ng/mL of PMA in an enriched medium for 6 hrs to activate cells to macrophage M0 lineage. After 6 hrs, the PMA-enriched medium was decanted and substituted with fresh complete growth media. Macrophages were rested in culture overnight at 37°C and 5% CO_2. For M1 polarisation, M0 cells were exposed to 50 ng/mL Granulocyte-macrophage colony-stimulating factor (GM-CSF) and 100 ng/mL Lipopolysaccharide (LPS) and incubated for 72 hrs at 37°C and 5% CO_2 to fully polarise and become ready for further study [343].

To evaluate macrophage phenotype's stability in co-culture media composed of (1:1) (α-MEM: RPMI 1640) containing 10% FBS, 1% Penicillin/Streptomycin, and 1% Glutamax. THP-1 monocytes (5 x 10^5 cells/well) were seeded in 24-well plates and activated to M0 macrophages with phorbol-12-myristate-13-acetate (PMA). Then, cells were polarised into M1 and M2 for 3 days. At the end of day 3, polarisation media were removed, replaced with fresh media, and further incubated for 7 days. At the end of each time point, supernatants were collected, and cells were fixed with 4% paraformaldehyde for immunostaining.

Polarised M1 macrophages and MSCs were plated concurrently in a 5:1 ratio (2 x 10^5 macrophages: 4 x 10^4 MSCs) in a 6-well plate, as reported in [87]. The co-culture system utilised a mixed osteogenic-macrophage medium comprised of 50% osteogenic and 50% macrophage medium (α-MEM: RPMI 1640), 10% FBS, 1% antibiotic-antimycotic, 1% Glutamax supplemented with 10 mM β-glycerophosphate, with 100 nM dexamethasone. After plating macrophages and MSC co-cultures, 3D printed PCL/SAIB/DEX-CYD scaffolds were added to co-culture groups and incubated for 21 Days.

4.2.10 Cytotoxicity

The cell viability of THP1 and MSCs was assessed using the ToxiLight™ non-destructive cytotoxicity bioassay kit (Lonza). The assay measures the release of adenylate kinase (AK) from cells with compromised cell membranes. The AK catalyses the conversion of ADP to ATP, which is then detected through bioluminescence. The emitted light intensity is linearly related to the AK concentration and can be detected using a plate reader.

4.2.11 Cell proliferation

Cell proliferation was quantified by using DNA content. THP1 or MSCs cells were digested with 1 mL of digestive solution (280 μg/mL papain, 50 mM EDTA, 5 mM L-cysteine in PBS pH 6.5) and incubated at 65°C overnight. Cell lysates were centrifuged at 13,000 *xg* 4°C for 5 min to remove cellular debris, and the supernatant was used to quantify total DNA concentration by using Quanti-iTTM Picogreen® kit according to manufacturer instructions.

4.2.12 Alkaline phosphatase (ALP) activity

Pierce PNPP (p-nitrophenyl phosphate), a colourimetric and soluble substrate, was used to evaluate the ALP activity according to the manufacturer's recommendations. Cells were washed twice with 1× assay buffer. Then, cells were lysed in 1mL 1% Triton-X-100 diluted in 1× assay buffer. 50 µL supernatant was transferred to a 96-well plate. A 50 µL PNPP was added to the supernatant and then allowed to react for 30 min at room temperature. The absorbance was measured at 405 nm. Total ALP activity was calculated according to manufacturer instructions.

4.2.13 Alizarin red staining (ARS)

Alizarin red staining was used to investigate mineralised nodule formation. Cells were washed 3 × for 15 min at room temperature with PBS and fixed with 4% formaldehyde. Then, cells were washed with deionized (DI) water and stained with 1 mL of 40 mM ARS per well for 30 min. DI water was used to wash the cells prior to imaging and quantification. The images of stained samples images were collected with a Nikon SMZ1500 and Nikon Digital sight DS-Fi2 camera from Nikon, Japan. Subsequently, stained cultures were quantified by following a de-staining procedure for 15 min at room temperature using 10 % (wt/vol) CPC in 10 mM sodium phosphate at pH 7.0. The ARS concentration was measured by absorbance at 562 nm.

4.2.14 RUNX2 gene expression

RNA was extracted from cells using the RNeasy Plus Minikit (Qiagen) according to the manufacturer's instructions. cDNA was synthesized from 1 microgram of total RNA using cDNA synthesis using a qPCRBIO

cDNA synthesis kit (PCR Biosystems) according to the manufacturer's instructions. qRT-PCR was performed on QuantStudio™ 3 Real-Time PCR System SYBR chemistry. The primers used for qRT-PCR are listed in **Table 4-1**. Data were analyzed using Design and Analysis Software v2.6.0, QuantStudio 3. Relative expression of genes of interest was calculated by normalizing against the housekeeping gene glyceraldehyde 3-phosphate dehydrogenase (GAPDH) using the ΔΔCT Method.

Table 4-1: Table of primers used to study osteogenesis using an RT-PCR.

Genes	**Primers**	**Sequence (5' –3')**
RUNX2	Forward	GGAGTGGACGAGGCAAGAGTTT
	Revers	AGCTTCTGTCTGTGCCTTCTGG
GAPDH	Forward	CTCTGCTCCTCCTGTTCGACA
	Revers	ACGACCAAATCCGTTGACTC

4.2.15 Cytokines release analysis

The release of pro and anti-inflammatory cytokines and the osteogenic markers from culture media was quantified using the enzyme-linked immunosorbent assay (ELISA) at the end of each interval time. Incubation media were transferred to a new Eppendorf tube and centrifuged at 13,000 *xg* 4°C to remove cellular debris. Supernatants were transferred to a new Eppendorf tube and frozen at -80°C. Human tumour necrosis factor-alpha (TNF-α), human IL-1β, human IL-6, human IL-10, human TGF-β1, and human bone morphogenic protein 2 (BMP-2)

DuoSet ELISA kit (R&D Systems) were quantified according to manufacturer's guidelines.

4.2.16 Immunofluorescent staining of macrophages

Macrophages treated with dexamethasone were investigated to assess the drug's ability to switch macrophage polarisation to M1 or M2 lineage. At the end of each interval time 3,7,14, and 21 days, the cells were fixed with 4% paraformaldehyde. Tow blocking steps were performed: 1) 3% BSA and 1% glycine (Fisher Scientific) in PBS, 2) 5% goat serum in PBS. Cells were stained with 2 ug/ml mouse anti-human calprotectin antibody and 1 μg/ml rabbit anti-human MR Ab for 1 h, then stained with 8 μg/ml Rhodamine red goat anti-mouse IgG (H + L) secondary Ab and 8 μg/ml Alexa flour 488 goat anti-rabbit IgG (H + L) secondary Ab for 1 h. Cells were counterstained with 250 ng/ml DAPI, and then cells were imaged with ZOE™ Fluorescent Cell Imager (Bio-Rad) with a 20x air objective.

4.2.17 Fluorescent intensity measurement

Fluorescence intensity was quantified by measuring the integrated density of calprotectin and mannose receptors positive cells, this was normalized against the total number of cells (DAPI). Images were analysed using ImageJ software (Fiji version) (NIH,USA). Analysis routines are presented in (**Appendix Figure 7-8**).

4.2.18 Statistical Analysis

All values in this study were reported as the mean or mean ± standard deviation (SD). Statistically significant differences were analysed using a one-way analysis of variance with Tukey’s post hoc test. *, **, ***, or ****

indicated statistical differences with $p < 0.05$, $p < 0.01$, $p < 0.001$, and $p < 0.0001$, respectively.

4.3 Results

4.3.1 Thermogravimetric (TGA) analysis

Thermogravimetric analysis (TGA) was used to assess the thermal stability of the 3D printed scaffolds and the amount of DCM, as the residual amount of it is biologically toxic and must be removed to render scaffold biocompatibility. The TGA curves of all scaffolds are shown in (**Figure 4-1**). No weight alterations were observed within the anticipated temperature range for DCM evaporation (40 °C to 100 °C), indicating the lack of any remaining DCM solvent in the 3D printed scaffolds following their fabrication. It could be seen that all scaffolds decomposed completely after 450°C. The addition of DEX-CYD had lowered the decomposition temperature. Noticeably, the addition of SAIB has decreased the decomposition of PCL from the region (250 °C to 450 °C), which could be due to the plasticising effect of SAIB.

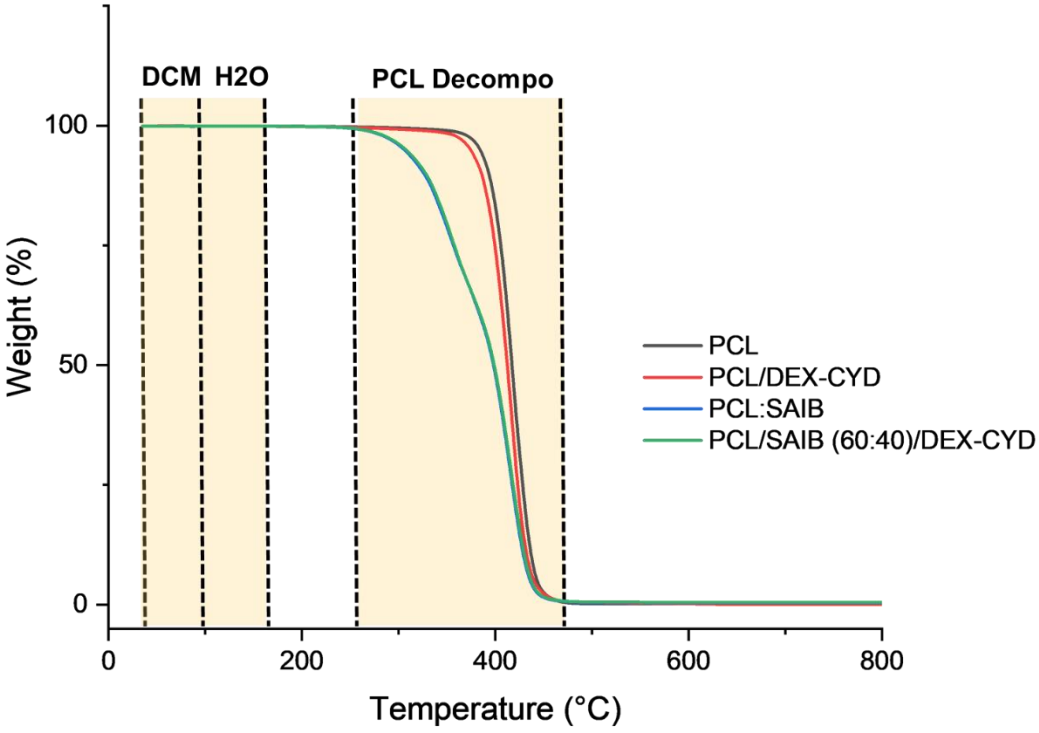


Figure 4-1: Thermogravimetric analysis (TGA) spectra of 3D printed scaffolds, PCL, PCL/DEX-CYD (0.17% wt/wt), PCL/SAIB (60:40) and, PCL/SAIB (60:40)/DEX-CYD (0.17% wt/wt) 3D printed scaffolds.

4.3.2 Polarisation of macrophages in RPMI single media, and co-culture mix media

This project was designed to model bone regeneration in inflammatory conditions and the potential of adding a sustained release system to immunomodulate macrophage activation status that benefits osteogenesis in macrophage-MSC co-cultures. THP-1 monocytes were used as a model cell type of human monocytes, and their ability to polarise to the M1 and M2 phenotypes in RPMI single media and mixed media (50:50 RPMI:α-MEM) was shown in (**Figure 4-2A & 4-3A**) respectively. The M1 maker (calprotectin) was significantly higher on day 3 and day 7 compared to M0 in single media. Furthermore, the M2 marker (mannose) was significantly higher on day 3 and day 7, respectively, compared to M0 (**Figure 4-2B**). On the other hand, in mixed media M1 marker was significantly higher on day 3 compared to M0, whereas M2 was significantly higher on day 3 and 7, respectively, compared to M1 (**Figure 4-3B**). In addition, two M1 markers (IL-6 and TNF-α) and an M2 marker (IL-10) were quantified by ELISA for macrophages polarized in single and mixed media. IL-6 and TNF-α cytokines were significantly elevated in M1 macrophages on days 3 and 7, respectively, while IL-10 was high on days 3 and 7 compared to M1 (**Figure 4-2C**). At mixed media, both M1 markers (IL-6 & TNF-α) and M2 marker (IL-10) were significantly higher on days 3 and 7, respectively (**Figure 4-3C**). These results suggest that co-culture media did not affect the differentiation of THP-1 monocytes to M0, M1 and M2 phenotypes compared to RPMI media [87].

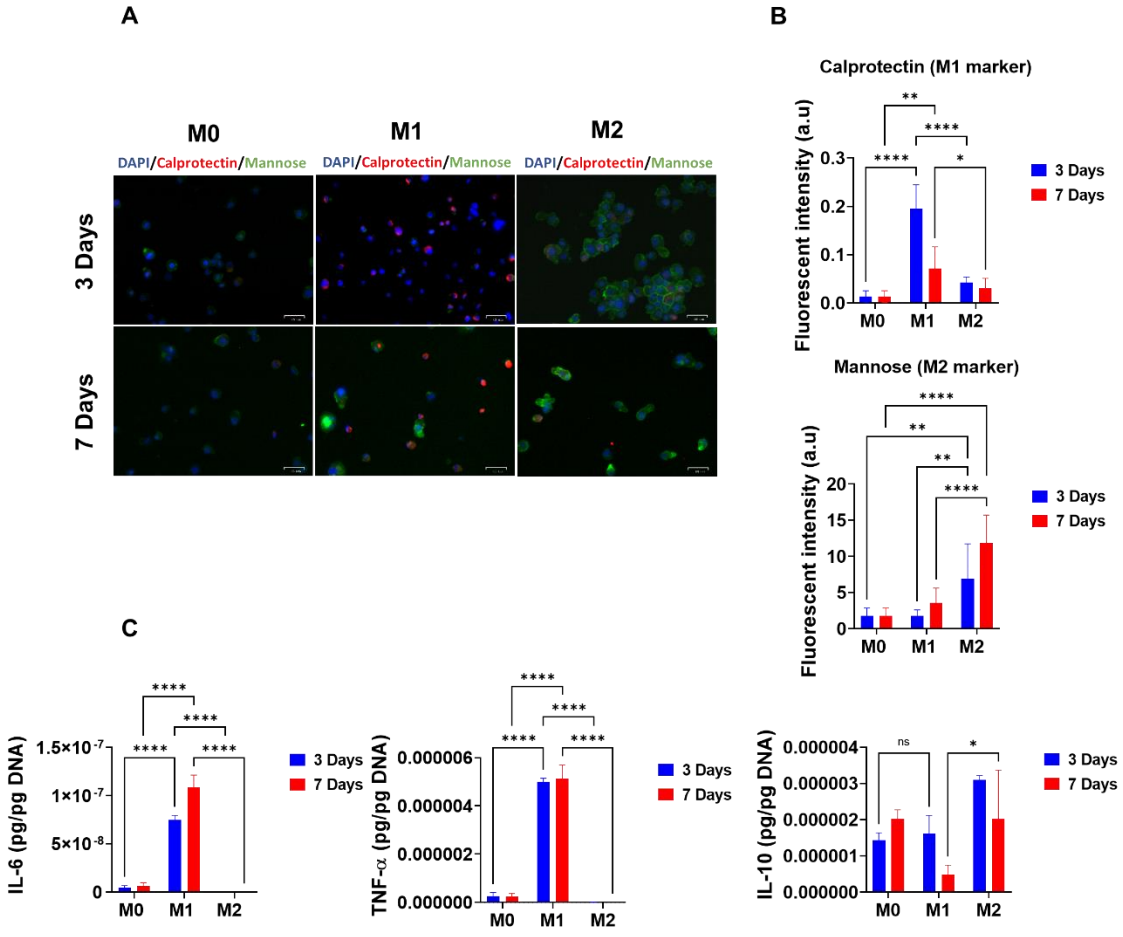


Figure 4-2: The polarisation of M0, M1 and M2 macrophages derived from THP-1 monocytes and M0, M1, and M2 cytokine expression. **A**) Immunostaining of macrophages polarised at days 3 and 7 in RPMI single-media. The scale bar is 40 µm, respectively. **B**) Fluorescence intensity was quantified by measuring the integrated density of Calprotectin (M1) and Mannose (M2) positive cells; this was normalized against the total number of cells (DAPI) by ImageJ. **C**) pro-inflammatory cytokines TNF-α, IL-6, and anti-inflammatory IL-10 quantification of macrophages polarised in RPMI single media were quantified by ELISA and normalized to DNA content. All data represent mean ± SD (n=3).

Statistical analysis was performed by one-way analysis of variance with Tukey's post hoc test indicated statistical differences with * $p < 0.05$, ** $p < 0.01$, *** $p < 0.001$, and **** $p < 0.0001$, respectively.

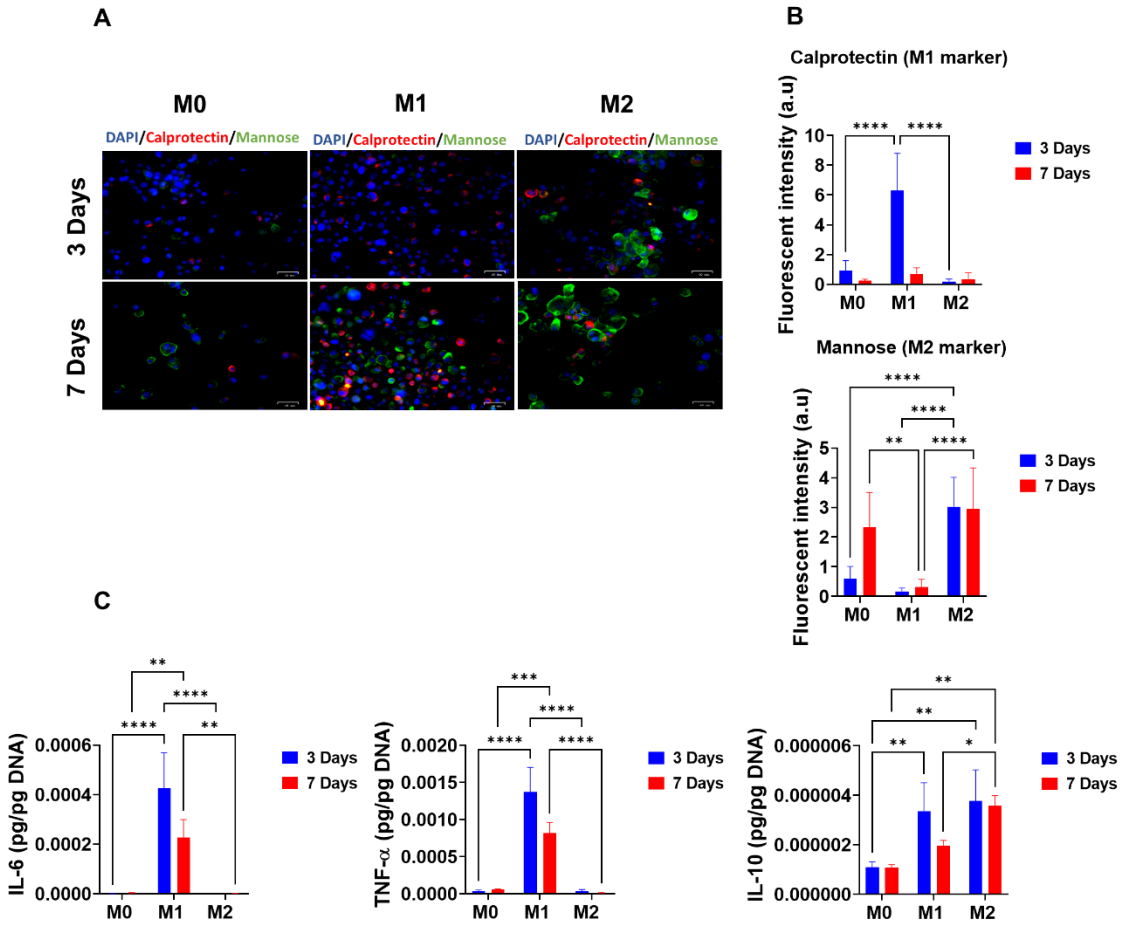


Figure 4-3: The polarisation of M0, M1 and M2 macrophages derived from THP-1 monocytes and M0, M1, and M2 cytokine expression. **A**) Immunostaining of macrophages polarised at days 3 and 7 in a mixed-media (RPMI:α-MEM). The scale bar is 40 µm, respectively. **B**) Fluorescence intensity was quantified by measuring the integrated density of Calprotectin (M1) and Mannose (M2) positive cells; this was normalized against the total number of cells (DAPI) by ImageJ. **C**) pro-

inflammatory cytokines TNF-α, IL-6, and anti-inflammatory IL-10 quantification of macrophages polarised in a mixed-medium (RPMI:α-MEM) were quantified by ELISA and normalized to DNA content. All data represent mean ± SD (n=3). Statistical analysis was performed by one-way analysis of variance with Tukey's post hoc indicated statistical differences with * $p < 0.05$, ** $p < 0.01$, *** $p < 0.001$, and **** $p < 0.0001$, respectively.

4.3.3 Cytotoxicity of controlled release scaffolds

After achieving a more sustained release of dexamethasone by PCL/SAIB/DEX-CYD scaffolds, the cytotoxicity of this drug delivery system on macrophages and MSCs was studied. Cell viability and proliferation were measured by the ToxiLight™ assay and PicoGreen™ assay, respectively. As co-culture will be carried out in a mixture of media (50:50 RPMI: α-MEM), the effect of the composition of culture media on cells was first tested. Cell viability (macrophages and MSCs) was similar between the single media and the co-culture media (50:50 RPMI: α-MEM) (**Figure 4-4A and C**). In addition, there was no difference in cell viability across all sample groups for macrophages. Macrophages also did not proliferate, which was expected as these monocyte-derived macrophages do not proliferate after activation by PMA (**Figure 4-4B and C**) [226].

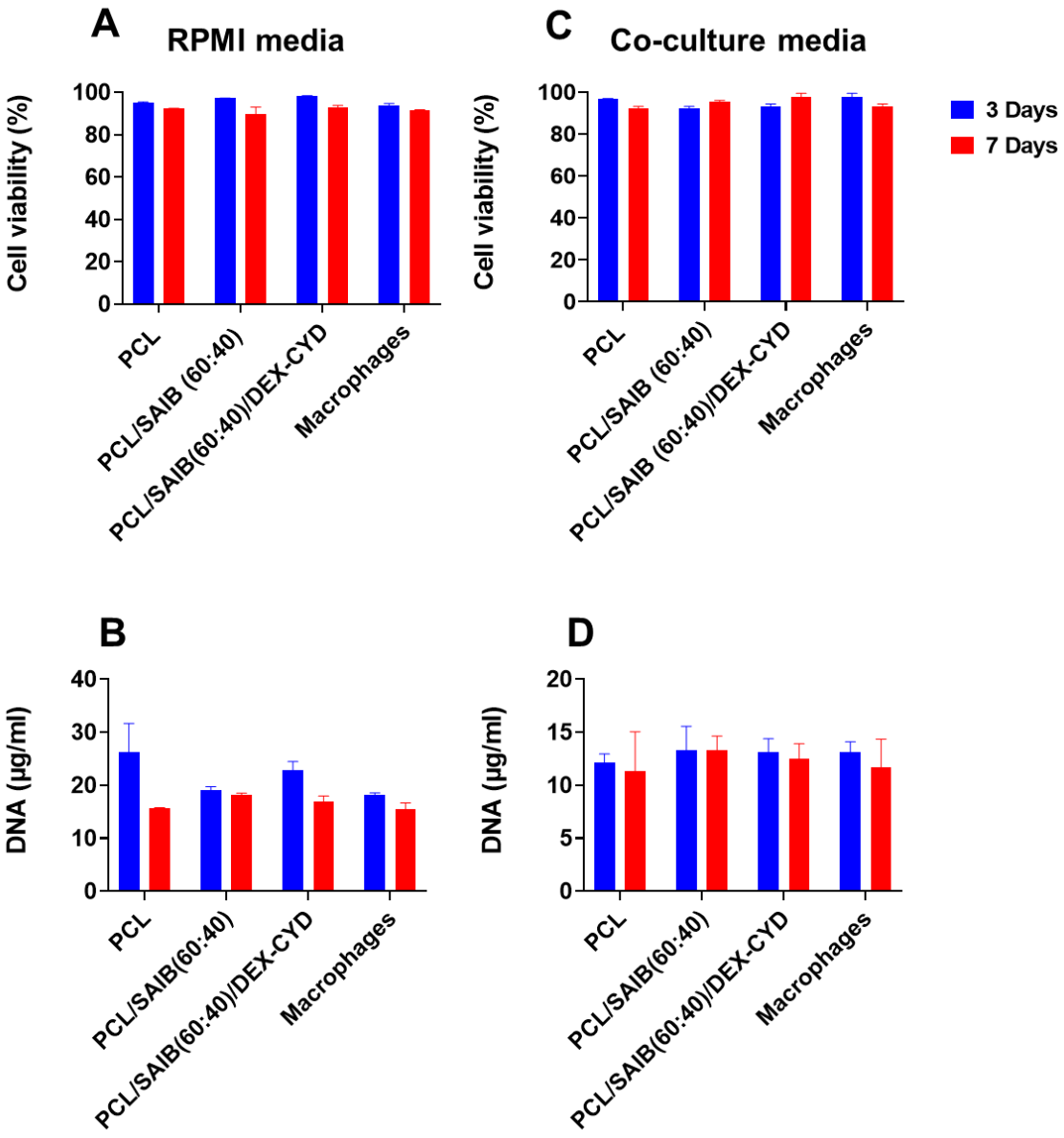


Figure 4-4: THP-1 were cultured in RPMI media or co-culture media separately and differentiated into macrophages in the presence of PMA for 6h and rested overnight. 3D printed scaffolds subsequently were submerged in the presence of LPS and GM-CSF for 3 and 7 days. **A**) and **C**) Cell viability was determined by ToxiLight™ cytotoxicity assay. **B** and **D**) Cell proliferation was determined by Quanti-iTTM Picogreen®. All data represent mean ± SD (n=3). Statistical analysis was performed by one-way analysis of variance with Tukey's post hoc test indicated

statistical differences with * $p < 0.05$, ** $p < 0.01$, *** $p < 0.001$, and **** $p < 0.0001$, respectively.

For the MSCs, the presence of scaffold (PCL+SAIB+dexamethasone) reduced cell proliferation compared to the MSC-only culture (**Figure 4-5A and C**). This is likely caused by the released dexamethasone in the culture, which inhibited the proliferation of MSCs [226]. The co-culture media enhanced the proliferation of MSCs compared to α-MEM media. This could be attributed to the broader range of nutrients in the co-culture media comparable to single media (**Appendix Table 7-4**). The viability of MSCs was not affected by the drug-release scaffold or the medium composition. However, MSC viability decreased slightly at day 21 compared to days 7 and 14 (**Figures 4-5B and D**).

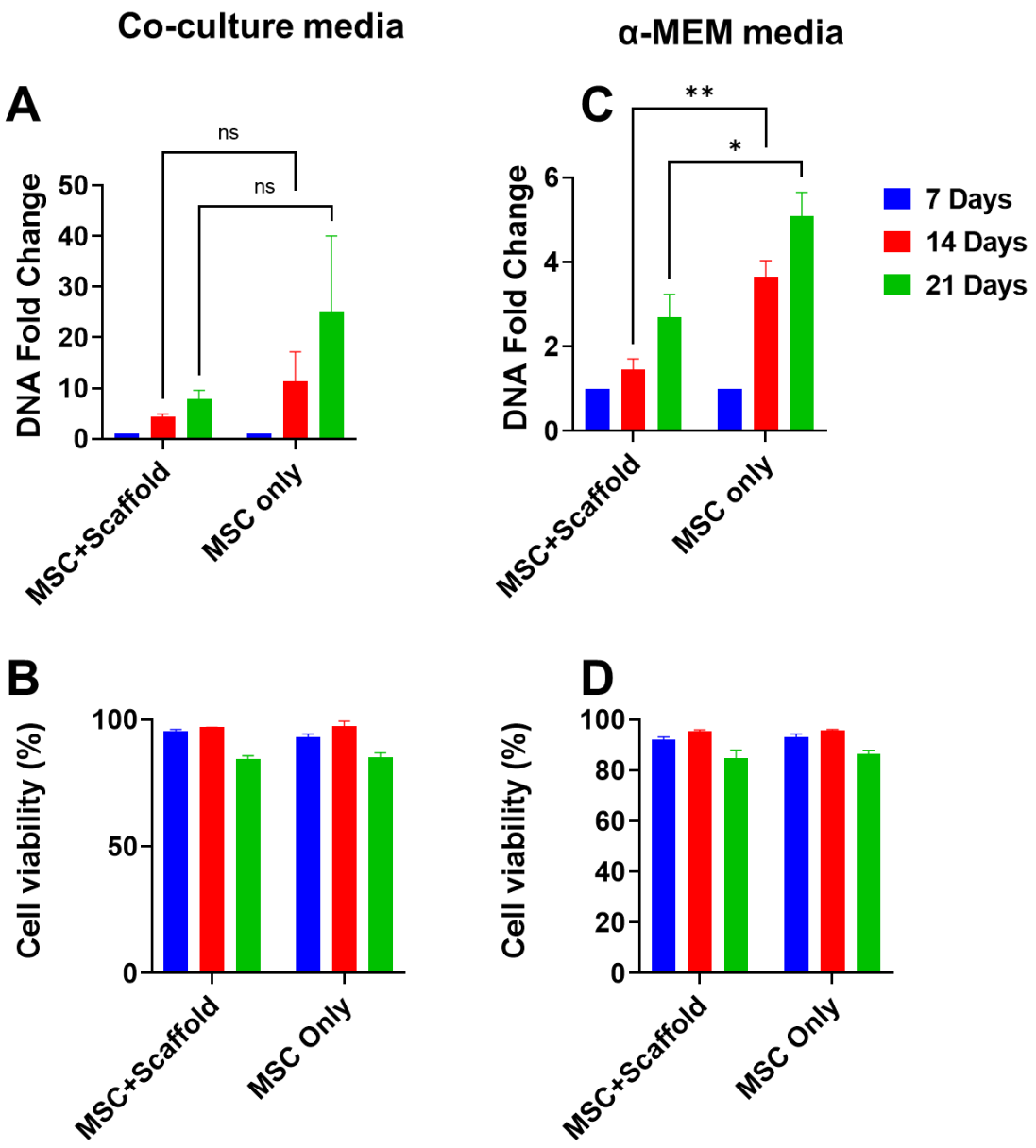


Figure 4-5: Viability and proliferation of MSCs in α-MEM and co-culture media with or without drug-loaded scaffolds PCL/SAIB (60:40)/DEX-CYD (0.17% wt/wt). DNA fold change was normalised to day 7. All data represent mean ± SD (n=3). * $p < 0.05$, ** $p < 0.01$.

4.3.4 Immunomodulation of macrophages by controlled release of dexamethasone

After confirming the cytotoxicity of the dexamethasone-encapsulated scaffolds, before studying the interactions between macrophages and MSCs in co-cultures, the polarisation of macrophages by dexamethasone in single cultures was characterized. Different amounts of dexamethasone were directly added (bolus) to culture media to determine the effective concentrations that can modulate macrophage polarisation. **Figure 4-6** shows that the effective concentration of dexamethasone was approximately in the 10 nM to 100 nM range (depending on the specific M1 cytokine). The M2 markers (IL-10 and TGF-β1) were not noticeably affected by dexamethasone concentrations during the 7-day cultivation. This suggested that the suppressive effect of dexamethasone on the M1 phenotype was relatively quick compared to its effect on switching macrophages to the M2 phenotype.

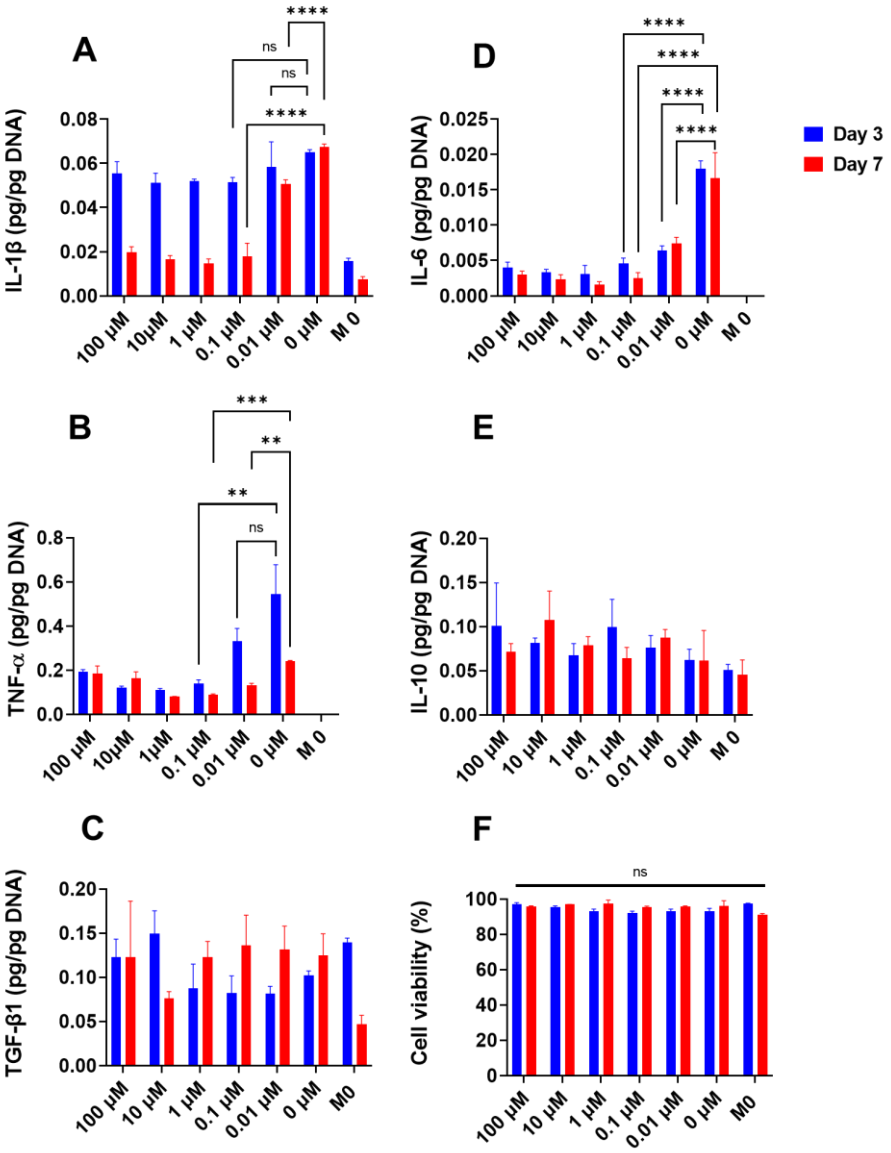


Figure 4-6: Effect of dexamethasone concentration on macrophage polarisation and viability. THP-1 cells were first differentiated into M0 macrophages with PMA. LPS, GM-CSF, and dexamethasone were then added together to the media (except the M0 control). The concentrations of IL-1β, TNF-α, IL-6, IL-10, and TGF-β1 were quantified by ELISA and normalised to cell DNA content. All data represent the mean ± SD (n=3). * $p < 0.05$, ** $p < 0.01$, *** $p < 0.001$, and **** $p < 0.0001$.

After assessing the effect of free doses of dexamethasone on M1 immunomodulation, the effect of scaffold-released dexamethasone on the polarisation of macrophages was subsequently investigated. Dexamethasone-loaded scaffolds were submerged into M0 culture together with LPS and GM-CSF added to the media (except M0 control). Culture with the dexamethasone-loaded scaffolds significantly reduced the M1 cytokine IL-6 at days 3 and 7. TNF-α was also reduced in the dexamethasone-loaded scaffolds on days 3 and 7 compared to their drug-free PCL counterparts (**Figure 4-7A and b**). On the other hand, IL-10 was significantly high at day 7 compared to M0 macrophages. IL-10 was significantly increased at day 3 in scaffolds not containing dexamethasone compared to scaffolds containing dexamethasone; this was attributed to the adaptive mechanism in LPS-stimulated macrophages to downregulate the proinflammatory cytokines IL-6 and TNF-α [344, 345]; meanwhile, TGF-β1 was significantly produced on days 3 and 7 compared to M0 macrophages (**Figure 4-7C and D**). This suggested that the concentration of released dexamethasone was in the effective concentration range. According to the release study, the estimated released concentrations at days 3 and 7 are 13 nM and 11 nM, respectively (**Appendix Table 7-5**), which falls within the effective range demonstrated in the bolus addition experiment **Figure 4-6**.

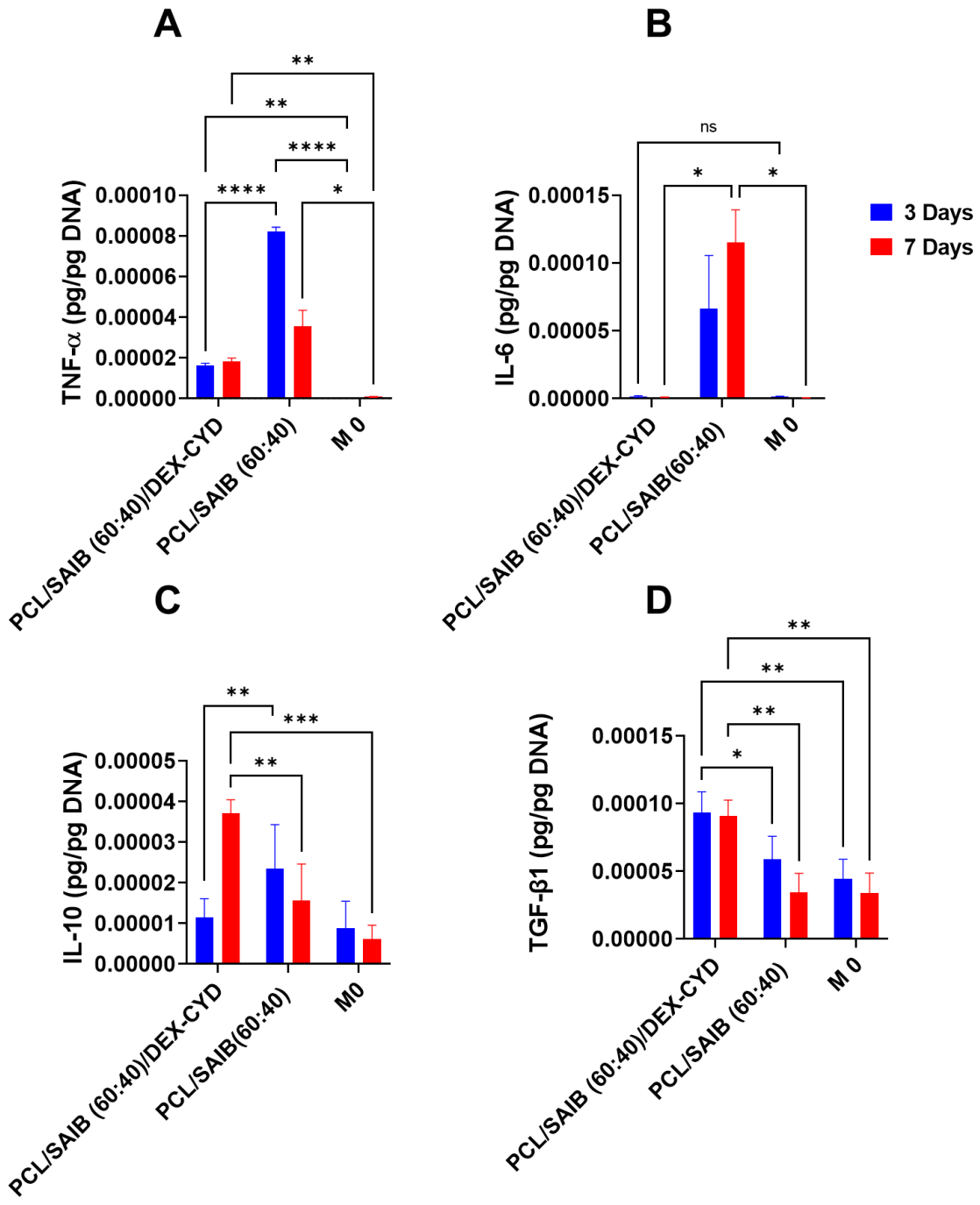


Figure 4-7: Quantification of pro-inflammatory TNF-α and IL-6, and anti-inflammatory cytokines IL-10 and TGF-β1 cytokines in macrophage culture. THP-1 cells were first differentiated into M0 macrophages with PMA. LPS, GM-CSF, PCL/SAIB (60:40) and PCL/SAIB (60:40)/DEX-CYD scaffolds were then added together to the media (except the M0

control) for 3 and 7 days, respectively. The concentrations of TNF-α, IL-6, IL-10, and TGF-β1 were quantified by ELISA and normalised to cell DNA content. All data represent the mean ± SD (n = 3). * $p < 0.05$, ** $p < 0.01$, *** $p < 0.001$, and **** $p < 0.0001$.

Moreover, the bioactivity effect of released dexamethasone from PCL/SAIB (60:40)/DEX-CYD has been assessed. The absorbance of released dexamethasone on days 15, 25, and 35 was detected at 241 by UV-vis (**Figure 4-8**). On the other hand, the immunomodulation of M1 macrophages by the released dexamethasone was also assessed. Interestingly, these doses significantly reduced the pro-inflammatory cytokines IL-6 and TNF-α (**Figure 4-9A and B**) and enhanced the production of anti-inflammatory cytokines IL-10 and TGF-β1 (**Figure 4-9C and D**); these results proved the bioactivity of released dexamethasone after prolonged release. (**Appendix Table 7-5**) shows the corresponding concentration of released dexamethasone from PCL/SAIB (60:40)/DEX-CYD 3D printed scaffolds on each day calculated by UV-vis.

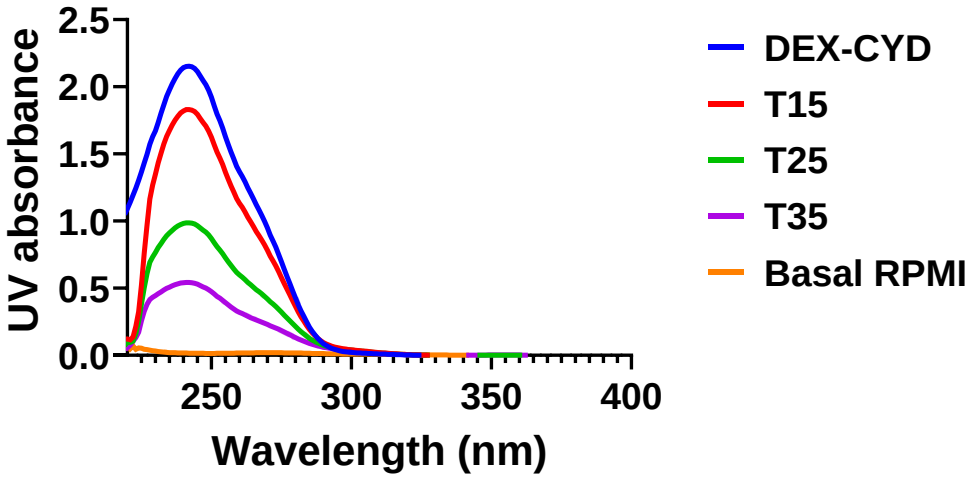


Figure 4-8: UV–vis absorbance of dexamethasone as received and released from 3D printed PCL/SAIB (60:40)/DEX-CYD scaffold at different time points after 15, 25, and 35 days, respectively in basal RPMI media.

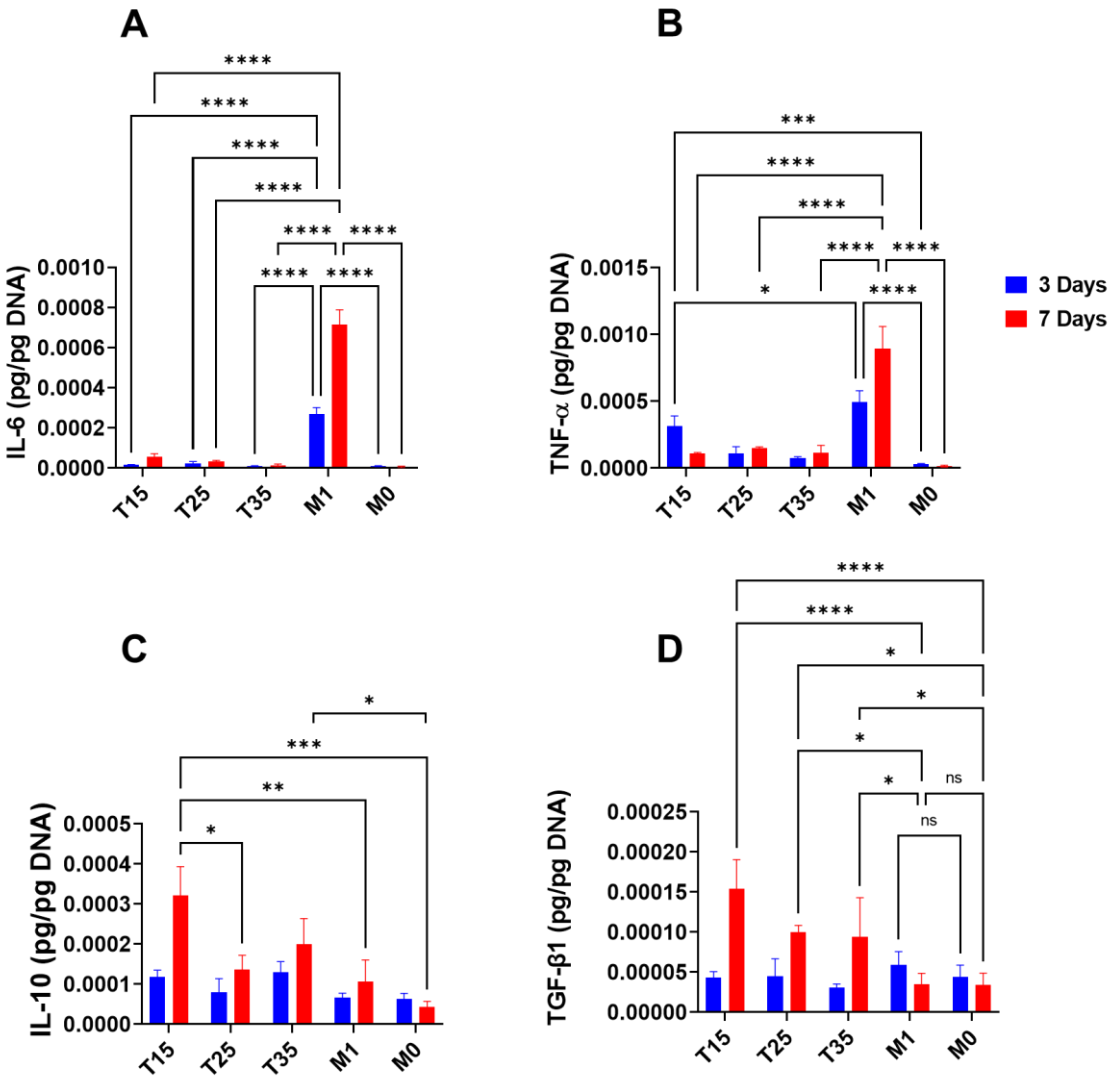


Figure 4-9: Bioactivity assessment of dexamethasone released from PCL/SAIB (60:40)/DEX-CYD. THP-1 cells were first differentiated into M0 macrophages with PMA. Then, LPS, GM-CSF, and dexamethasone released from PCL/SAIB (60:40)/DEX-CYD scaffolds on 15, 25, and 35 dyes were added together to M0 macrophage (except the M0 control). The concentrations of TNF-α, IL-6, IL-10, and TGF-β1 were quantified by ELISA and normalised to cell DNA content. All data represent mean ± SD (n=3). * $p < 0.05$, ** $p < 0.01$, *** $p < 0.001$, and **** $p < 0.0001$.

4.3.5 Osteogenic differentiation and macrophage polarisation in co-cultures

To investigate the interactions between macrophages and the osteogenic differentiation of MSCs, a mixture of two types of cells (5:1-Macrophage: MSC) were co-cultured in the presence of 3D printed scaffolds loaded with dexamethasone over 21 Days. The cell ratio was chosen based on published data on the optimal ratio for maximising osteogenic differentiation of MSCs [87, 338]. The osteogenesis of M1+MSC co-culture in the presence of a 3D printed scaffold was assessed by ALP activity, an early marker of osteogenic differentiation (**Figure 4-10A**). ALP was significantly increased in the cultures with the presence of dexamethasone-loaded scaffolds at day 7 compared to the MSC-only culture. This was likely due to the pro-osteogenic differentiation property of dexamethasone, which is typically added to cultures at 10nM to 100nM range for osteogenic differentiation via inducing Runx2 expression [346]. Compared to MSC only, the co-cultures with M1 or M0 also significantly enhanced the secretion of ALP at day 7. This might be due to the cytokines secreted by M1 and M0 cells that promoted osteogenic differentiation [347, 348]. There was no statistical difference in ALP secretion between the four cultures (excluding the MSC-only culture) on day 7.

ALP was higher in cultures with the presence of scaffolds at day 14 and day 21, suggesting a stronger effect of dexamethasone on osteogenic differentiation compared to M1 macrophages. Between the two cultures with the presence of scaffolds, the inclusion of M1 cells significantly

promoted ALP at day 14, indicating a synergistic effect of M1 and dexamethasone on osteogenic differentiation. However, ALP was at similar levels at day 21 for these two scaffold-included cultures, possibly due to the switching of the M1 to M2 phenotype caused by dexamethasone. M0+MSC showed higher ALP than MSC-only culture at day 7, but no statistical difference at later time points. M1+MSC showed a higher ALP level on day 14 compared to MSC-only culture, but no difference on day 21.

Alizarin staining for measuring calcium content was used to determine the mineralisation level of MSCs co-cultured with macrophages in the presence of dexamethasone-releasing scaffolds (**Figure 4-10B and C**). Matrix mineralisation was significantly increased in cultures with dexamethasone-loaded scaffolds at day 21, which again confirmed the osteogenic property of dexamethasone. At day 7, the mineralisation was higher in the M1+MSC co-culture compared to the MSC-only culture, followed by comparable mineralisation between them on day 14 and day 21. This result correlated with the ALP data, where the MSC+M1 coculture showed a higher ALP level compared to the MSC-only culture at day 7. When the two cultures with scaffolds were compared, mineralisation was higher at day 7 for the M1+MSC+scaffold culture. Mineralisation was comparable (not statistically different) at day 14 and day 21 between these two cultures. These data demonstrated that the inclusion of M1 only promoted early-stage osteogenic differentiation. Late-stage osteogenic differentiation was dominated by the pro-osteogenic property of dexamethasone.

RUNX2 (a master osteogenic differentiation regulator) was higher for cultures with dexamethasone-releasing scaffolds and the M1+MSC culture at day 3 compared to the MSC-only culture (**Figure 4-10D**). The M1+MSC culture exhibited a similar RUNX2 level at day 3 compared to the scaffold-containing cultures. The highest level of RUNX2 was the M1+MSC+scaffold culture at day 7, which suggested a synergistic effect between M1 and dexamethasone on promoting osteogenic differentiation. This synergistic effect was also seen for ALP at a later time point (day 14) for the same culture. At day 21, the two scaffold-containing cultures showed similar levels of RUNX2 but higher than the other cultures.

BMP-2 has been reported as a soluble mediator for enhanced osteogenesis from macrophages [349]. At day 7, M1+MSC+scaffold, MSC+Scaffold and M1+MSC showed a statistically higher level of BMP-2 compared to MSC only culture, suggesting both dexamethasone and M1 macrophages increased the secretion of BMP-2. At day 21, M1+MSC+scaffold, MSC+scaffold and M1+MSC showed a significantly higher BMP2 compared to MSC-only culture (**Figure 4-10E**).

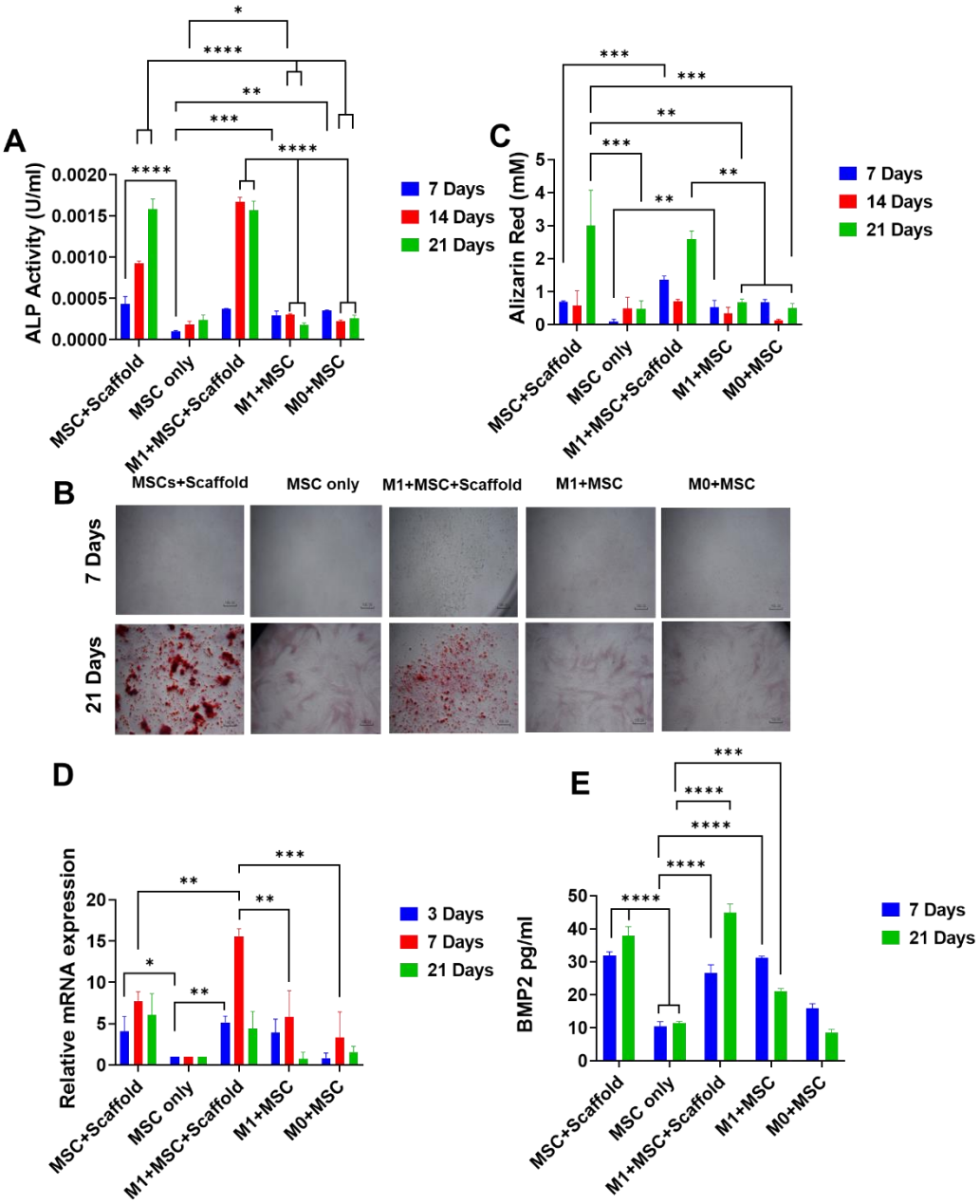


Figure 4-10: (**A**) ALP activity in macrophages-MSc co-cultures over 7, 14 and 21 days (**B**) Alizarin red staining showing the mineralisation in different cultures. Scale bar-100 µm. (**C**) Quantification of Alizarin red staining. (**D**) Gene expression of osteogenic marker RUNX2. (**E**) BMP-2 level in different cultures. All data represent mean ± SD (n=3). * $p < 0.05$, ** $p < 0.01$, *** $p < 0.001$, **** $p < 0.0001$.

Taking the ALP, Alizarin red staining and RUNX2 expression data together, they showed a pro-osteogenesis effect of M1 macrophages at early time points. The osteogenic differentiation was dominated by dexamethasone at later time points. There was some synergistic effect between these two factors at early/mid-time points. The disappearance of the pro-osteogenic property by M1 may be due to the activation status change of the macrophages caused by dexamethasone.

To verify this, the activation status of macrophages in the co-cultures was investigated over time. The results showed the transition of macrophage activation status from M1 to M2 by the sustained release of dexamethasone (**Figure 4-11**). Surface markers for M1 (calprotectin) and M2 (mannose receptor) were fluorescently stained to characterise the different activation statuses of macrophages (**Figure 4-11A**). The M1 maker (calprotectin) was much lower at day 3 for the scaffold-containing media, which suggested a suppression of the M1 phenotype at early time points. At day 21, the expression of the M1 surface marker was still lower in the scaffold-containing medium due to the sustained release of dexamethasone. On the other hand, the biggest difference in the M2 marker was at day 21, with the scaffold-containing media showing the highest mannose receptor level (**Figure 4-11B**). This suggested that the transition from M1 to M2 phenotype took a longer time compared to the relatively quick suppression of the M1 phenotype. MSCs also showed an immunosuppressive effect evidenced by lower calprotectin and higher mannose receptors at days 7 and 14 compared to day 3 for the M1+MSC culture. However, this effect diminished at day 21, evidenced by the

relative increase and decrease of calprotectin and mannose receptors, respectively.

In addition, two anti-inflammatory cytokines (IL-10, TGF-β1) and one pro-inflammation cytokine (IL-6) were measured by ELISA (**Figure 4-11C**). The scaffold culture suppressed IL-6 secretion at all-time points. The M0+MSC culture secreted significantly more IL-6 than the M0 culture, suggesting the source of this cytokine from the MSCs. Both the M1+MSC and M0+MSC showed higher IL-6 than the MSC-only culture at days 3 and 7, suggesting a simulated secretion of this cytokine from the MSCs by the macrophages. In addition, the M1+MSC culture secreted more IL-6 compared to the M0+MSC culture at all four-time points, suggesting an effect of macrophage phenotype on IL-6 from MSCs. It has previously been shown that MSC-produced IL6 skews monocytes towards an anti-inflammatory phenotype [350].

TGF-β1 was higher in the M1+MSC and M0+MSC cultures compared to the scaffold culture at day 14 and day 21 (**Figure 4-11C**). Dexamethasone at supraphysiological concentrations inhibits the proliferation (but not differentiation) of MSCs which also secrete TGF-β1 [226]. Therefore, the relatively lower TGF-β1 secretion in the scaffold culture was possibly attributed to this inhibitory effect. TGF-β1 was similar between the M1+MSC and the M0+MSC culture, suggesting the two macrophage phenotypes had minimal impact on the secretion of this cytokine from MSCs. IL-10 had a significant elevation at day 7 meanwhile no difference amongst the five cultures at day 21.

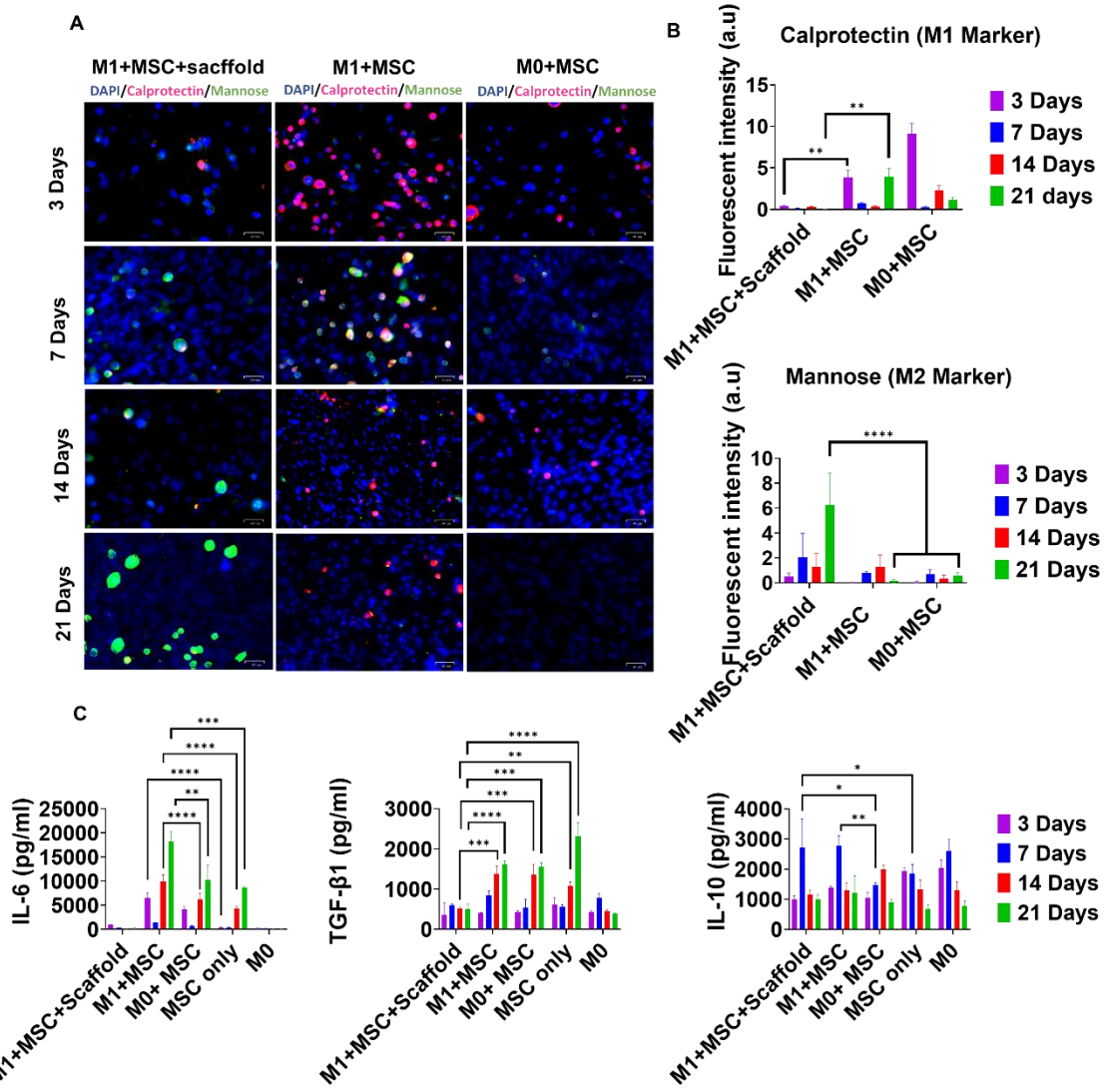


Figure 4-11: Macrophage activation status in co-cultures. (**A**) Immunostaining of M1 marker calprotectin (red) and M2 marker mannose receptor (green) and cell nuclei (blue). Scale bar-100 µm. (**B**) Fluorescence intensity was quantified by measuring the integrated density of Calprotectin (M1) and Mannose (M2) positive cells; this was normalized against the total number of cells (DAPI) by ImageJ. (**C**) Quantifying pro-inflammatory (IL-6) and anti-inflammatory cytokines (TGF-β1 and IL-10). All data represent mean ± SD (n=3). * $p < 0.05$, ** $p < 0.01$, *** $p < 0.001$, **** $p < 0.0001$.

4.4 Discussion

This project reported for the first time the interactions between MSCs and macrophages in co-cultures with the sustained release of an anti-inflammatory and pro-osteogenic differentiation drug. I have achieved a sustained release of dexamethasone from PCL by adding SAIB to the polymer matrix, which only demonstrated burst release in previous studies. The polarisation of macrophages into M1 or M2 in RPMI and co-culture media was then characterized. Prior to co-culture, macrophages were differentiated into different phenotypes, M0, M1, and M2, and their characteristics were analyzed. The secretion patterns of specific cytokines (TNF-α, IL-6, and IL-10) were used to differentiate M0, M1, and M2 macrophages, indicating successful polarisation of distinct macrophage types. In addition, measuring the relative fluorescence intensity of the macrophage surface markers mannose receptor (M2 marker) and calprotectin (M1 marker) provided an additional method for interpreting macrophage subtypes [343, 351]. Following this characterisation, M1 macrophage and MSC (mesenchymal stem cell) co-cultures were initiated in the presence of a control release system.

Dexamethasone was selected due to its dual properties: anti-inflammation and pro-osteogenic differentiation. The prolonged use of systemic corticosteroids, such as dexamethasone, is associated with potentially serious adverse effects. For example, prolonged use of dexamethasone has been shown to induce osteoporosis, possibly due to its ability to inhibit the proliferation of osteogenic precursors [226, 352]. However, this adverse effect was shown to be concentration dependant,

requiring >100 nanomolar concentrations to inhibit the proliferation of osteogenic precursors [226]. I have hypothesised that a locally implanted scaffold can potentially reduce the systemic exposure of this drug while achieving nanomolar therapeutic concentrations at the desired sites. The concentrations tested in this project showed effects on both promoting osteogenic differentiation of MSCs and suppressing the M1 phenotype of macrophages. The dexamethasone released from a 3D printed PCL scaffold reduced proliferation but not the differentiation of human MSCs (**Figure 4-5**). The concentrations of released dexamethasone were slightly lower than the physiological level of cortisol (100nM-700nM) [353]. However, these two glucocorticoids have different potencies, with dexamethasone 17-30 times more potent than cortisol [353], meaning a supraphysiological level of released glucocorticoid from the scaffolds. This possibly explains the proliferation-inhibitory effect observed by the concentration range demonstrated in this study and suggests a possible lower concentration of dexamethasone or less potent glucocorticoid to try in the future. The volume of media (10mL) was fixed in both the release and the co-culture studies, hence affecting the drug concentration. During *in vivo* implantation, the local drug concentration will depend on the volume of the surrounding body fluids, how quickly they are replenished via diffusion and circulation and how quickly the drug is eliminated *in vivo*. The final concentration of a drug in a scaffold may need to be tuned to fit the specific implantation site. Another choice of anti-inflammatory drug is nonsteroidal anti-inflammatory drugs. However, their mechanism of action involves the COX-2/PGE2 process,

which mediates the communication between macrophages and MSCs. Therefore, NSAIDs will compromise bone healing, which has been reported in the literatures [354, 355].

Various studies have confirmed the importance of macrophages in osteogenesis. Depleting macrophages using liposome clodronate or, in genetically modified mice, lacking macrophages led to compromised bone formation [72, 356]. However, the exact macrophage phenotype that stimulates osteogenesis has had some conflicting data. Some studies reported only M1 promoted osteogenic differentiation [337]. Other reports have shown all three phenotypes (M0, M1, and M2) showed enhanced osteogenic differentiation of MSCs [87, 337, 357, 358]. This project showed a pro-osteogenic effect of M1 macrophages at early time points. This agrees with previous *in vitro* and *in vivo* reports showing that macrophages contributed to osteogenesis early during the inflammatory phase of fracture healing. A combination of factors is likely responsible for macrophage-mediated enhanced osteogenesis. OSM and BMP-2 have attracted relatively more attention as the critical soluble mediators for macrophage-mediated enhanced osteogenesis. The data in this study showed that both dexamethasone and M1 increased the level of BMP-2 compared to MSC-only culture. This confirms the role of BMP-2 in enhanced osteogenesis. At the late time point (21 days), the effect of M1 on BMP-2 secretion diminished, possibly due to the immunosuppressive effect of MSCs and dexamethasone on macrophages (**Figure 4-10E**). The cellular source of BMP-2 was not invested in this study. Both MSC and macrophages have been reported

to be able to secret BMP-2 [359]. Future efforts will involve an investigation of the source and timing of BMP-2.

M0 macrophages were also able to promote ALP and matrix mineralization at day 7, but this effect diminished at later time points (**Figure 4-10A and C**). This partially agrees with previous studies [87, 358]. However, these data did not show M0 had a superior effect in enhancing osteogenesis compared to M1, which exhibited a better osteogenesis effect (evidenced by RUNX2 and BMP-2 data). The later stage of osteogenesis (day 21) , ALP activity was the highest in the two scaffold cultures MSC+ scaffolds, and M1+MSC+scaffold, suggesting the mineralisation effect was dominated by the released dexamethasone from the scaffolds (**Figure 4-10A-C**). The released dexamethasone switched the phenotype of macrophages from M1 to M2 over time, evidenced by the increased level of mannose receptor (**Figure 4-11A and B**). As this experiment did not include an M2-MSC culture, the comparison between M2 macrophages and dexamethasone in their effect on enhancing mineralisation was not obtained. The effect of dexamethasone-release scaffold on osteogenic differentiation may come from the combined effect of the drug and the M2 macrophages induced by it. As the initial inflammation and its resolution are both important for successful bone healing, future efforts will be needed to better control the timing of the released drug. For example, the released drug should not inhibit the initial beneficial inflammatory response but to prevent chronic inflammation. However, applying this concept will need careful consideration as surgery and implantation of scaffold could happen over

a range of timings after the formation of bone defects, which requires an assessment of the inflammatory status at the time.

It is also well known that MSCs possess immunosuppressive properties via paracrine signalling or cell-cell contact [360]. For example, MSCs have been shown to switch activated M1 macrophages to an M2 phenotype via prostaglandin E2 [361, 362]. Immuno-regulatory effects of placental MSCs have been found to be mediated by soluble molecules, such as IL10 and TGF-β1, acting partially via glucocorticoid receptors and progesterone receptors [363]. In this study, the immunosuppressive effect of MSCs on M1 macrophages was transitory and to a lesser degree compared to dexamethasone, which showed a dramatic effect on switching macrophage phenotype from M1 to M2 (evidenced by calprotectin and mannose receptor) (**Figure 4-11A and B**). The M1+MSC and M0+MSC co-cultures showed a higher level of IL-6 compared to the scaffold culture (M1+MSC+scaffold) and M0 cultures, suggesting the secretion of IL-6 from MSCs (**Figure 4-11C**). IL-6 is a pleiotropic cytokine and is one of the cytokines associated with M1 macrophages. MSC can also secret IL-6 when they are primed by TLR4 [364]. Interestingly, IL-6 has been found to enhance the polarisation of M2 macrophages but requires the involvement of IL-4 and IL-13 [365]. IL-6 was also found to promote osteogenic differentiation in bone marrow-MSCs via an autocrine/paracrine IL-6/IL-6R/STAT3 signalling pathway [366] and to promote migration of osteogenic stromal cells [367]. The increase in IL-6 secretion in macrophage (M0/M1)+MSC co-cultures (**Figure 4-11C**) suggested the role of this cytokine in macrophage-

mediated enhanced osteogenesis. The dexamethasone scaffold completely blocked the secretion of IL-6 whilst still promoting osteogenesis, suggesting its overriding effect. Future effort will be needed to elucidate how the M0 and M1 macrophages induced the secretion of IL-6 from MSCs, and how dexamethasone supressed it.

4.5 Summary

Enhancing osteogenesis via modulating immune cells is emerging as a new approach to address current challenges in repairing bone defects and fractures. However, much remains unknown about the crosstalk between immune cells and osteolineage cells during bone formation. Moreover, biomaterial scaffold-based approaches to effectively modulate this crosstalk to favour bone healing are also lacking. This study is the first to investigate the interactions between macrophages and mesenchymal stem cells (MSCs) in co-cultures with the sustained release of an anti-inflammatory and pro-osteogenesis drug (dexamethasone) from 3D printed scaffolds. I have successfully achieved the sustained release of dexamethasone from polycaprolactone (PCL) by adding the excipient-sucrose acetate isobutyrate (SAIB). Dexamethasone was released over 35 days in the nM range. The osteogenic differentiation of MSCs was enhanced by M1 macrophages at early time points. The late-stage mineralisation was dominated by dexamethasone, with little contribution from the macrophages. Besides confirming BMP-2, whose secretion was promoted by both dexamethasone and M1 macrophages as a soluble mediator for enhanced osteogenesis, IL-6 was found to be a possible

new soluble factor that mediated osteogenesis in macrophage-MSC co-cultures. The phenotype switching from M1 to M2 was drastically enhanced by the scaffold-released dexamethasone but only marginally by the co-cultured MSCs. These results offer new insight into macrophage-MSC crosstalk and demonstrate the potential of using drug-release scaffolds to both modulate inflammation and enhance bone regeneration.

5. Chapter Five: Conclusion and future works

5.1 Conclusion

Additive manufacturing, commonly known as 3D printing, is increasingly used in tissue engineering applications. This is attributed to its advantages in fabricating intricate structures that are challenging to produce through traditional manufacturing techniques [146, 147]. The ability to accurately manipulate and duplicate three-dimensional objects has made 3D printing a potent tool for producing scaffolds for tissue engineering [148]. Bone tissue engineering predominantly revolves around the restoration and preservation of bone function *in vivo* [92]. This field employs biomimetic scaffolds, osteoinductive molecules, and osteogenic cells to facilitate the regeneration of bone in cases involving pathological conditions and sizable defects [326]. Nevertheless, implanted scaffolds may induce a foreign body reaction in the host, impairing its biological function and delaying wound healing and tissue regeneration [173, 368].

The function of macrophages in bone growth has recently been investigated in bone tissue engineering. Macrophages have a role in fracture healing and biomaterial reaction [369]. M1 polarisation induced by biomaterial implants leads to inflammatory response, granuloma formation, fibrous encapsulation, and implant collapse [370]. On the other hand, M2 reduces fibrous encapsulation, promotes vascularisation, and maintains implant integration [371].

While the influence of physical and chemical cues present in biomaterials on macrophage modulation has been extensively validated [188], the

precise regulation of macrophage phenotypes, encompassing the modulation of polarisation degree and determining the optimal timing for regulation, remains largely elusive. Conversely, biomaterials that facilitate the delivery of anti-inflammatory drugs, cytokines, and genes offer greater control over both the temporal dynamics and intensity of macrophage polarisation [190].

Dexamethasone is a steroidal drug with anti-inflammatory and osteogenic properties and has been utilized in various control release systems to study the anti-inflammatory effect or osteogenic capability [186, 233, 234]. The challenges encountered in the field of controlled drug release arise from the intricacy of precisely regulating drug release, as well as the occurrence of rapid burst release. Factors contributing to burst release include synthesis and manufacturing conditions, the heterogeneous nature of polymer matrices, characteristics of the drug itself, and restricted diffusion of the drug within 3D printed scaffolds [261, 262].

The works in the current thesis aimed to develop novel 3D printed scaffolds that prolong the release of dexamethasone by a single method of fabrication of polymer ink. Indeed, dexamethasone and PCL polymer were blended with various Poloxamers F127, F68, and L31 and Span80 and SAIB, respectively. The cytotoxicity and bioactivity effect of prolonged release of dexamethasone from PCL/SAIB candidate scaffold was investigated on the immunomodulation of M1 to M2 macrophage after addressing the bioactivity of released dexamethasone. We have effectively investigated the impact of dexamethasone release from the

PCL/SAIB composite scaffold on the immunomodulation of M1 macrophages and mesenchymal stem cells (MSCs) osteogenesis in co-cultures of macrophages and MSCs. The current chapters (**chapters 3 and 4**) detail the steps taken to conduct these works.

In **Chapter 3**, in the beginning, we successfully prepared different dexamethasone-loaded PCL, including 0.05%, 0.1%, and 0.17%, and the printing parameters were successfully optimized. The concentration of dexamethasone 0.17% wt/wt was utilized to fabricate novel 3D printed PCL scaffolds blended (30% and 40% wt/wt) of F127, F68, L31, Span80 and SAIB loaded with dexamethasone. I was able to optimize the default printing parameters too. Furthermore, SEM images showed that all scaffolds were reproduced with a nearly smaller strut size than the printing nozzle and large pore size (**Figure 3-6**). Moreover, the addition of surfactants resulted in smoothed strut surface morphology. On the other hand, scaffolds fabricated from PCL and dexamethasone only exhibited a pore formation on their struts' surface (**Figure 3-5**). Different characterizing techniques were utilized, including DSC, FTIR, and ToF-SIMS. All used techniques revealed that blending PCL with dexamethasone and surfactants has no significant chemical interaction. Moreover, the inclusion of dexamethasone, hydrophilic surfactants F127 and F68 has increased the crystallinity of PCL.

In contrast, the presence of the hydrophobic surfactant L31, Span80 and SAB has reduced the degree of crystallinity. Interestingly, the presence of SAIB in scaffold formulation has improved the drug distribution in the strut compared to the PCL scaffold without SAIB (**Figure 3-29 and**

Figure 3-30). Then, I studied the release behaviour of dexamethasone from all 3D printed scaffolds. The results showed different release profiles and mechanisms. PCL scaffolds prepared from F127 and F68 domistrated a burst and fast release were dominated dominated by Korsmeyer-Peppas model which imply that the release was due to the erosion and diffusion (**Figure 3-23 and Figure 3-24**). PCL/L31 scaffolds showed multible release mechanism First order, Higutch, and Korsmeyer-Peppas (**Figure 3-25**). In comparison, PCL/SAIB/DEX-CYD scaffold showed a prolonged release profile dominated by the First ordered and Higuchi mechanism (**Figure 3-27**). The release of dexamethasone from different scaffold compositions exhibits diverse release mechanisms, as evidenced by the fitting of various mathematical models. The choice of scaffold material and composition, as well as the presence of additives like surfactants or microcrystal, can significantly influence the drug release kinetics. These findings are important for the design and optimization of drug delivery systems for specific therapeutic applications, allowing for tailored drug release profiles based on the desired therapeutic effect and duration.

In **Chapter 4**, I utilized the PCL/SAIB (60:40)/DEX-CYD 3D printed scaffolds prepared in **Chapter 3** to study the effect of the released dexamethasone on the immunomodulation of M1 macrophages. I have shown that the released dexamethasone was not affected by the fabrication process and could polarize M1 macrophages into M2 phenotypes by reducing the production of IL-6 and TNF-α (**Figure 4-7**). Then, macrophages were polarized into M1 and co-cultured with MSC to

examine the impact of the controlled release of dexamethasone on the immunomodulation of M1 macrophages and enhance the ontogenesis of MSC in the co-culture system.

For the first time, the interaction between MSCs and macrophages in co-cultures with controlled release of an anti-inflammatory and pro-osteogenic differentiation drug was investigated. The dual-property dexamethasone both promoted osteogenic differentiation and suppressed pro-inflammatory M1 macrophages in MSC-macrophage co-cultures (**Figure 4-11C**). I have found that M1 macrophages contributed to osteogenesis at early time points, and this effect diminished at later time points. M1 macrophages showed a stronger osteogenic effect than M0 macrophages. The late-stage mineralisation was dominated by dexamethasone. Dexamethasone promoted more secretion of BMP-2 compared to macrophages, whilst M1 macrophages had more BMP-2 secretion than M0 macrophages (**Figure 4-10**). IL-6 secretion from MSCs was enhanced by macrophages, particularly M1 macrophages, suggesting the pro-osteogenic property of this cytokine in macrophage-induced osteogenesis (**Figure 4-11C**). These findings highlighted the critical role of inflammatory response in the osteogenic differentiation of osteoprogenitor cells and the importance of studying the interactions between inflammatory and bone-forming cells. In addition, this work highlights the potential of controlled release of drugs from implantable scaffolds to modulate both osteogenic differentiation and macrophage activation status in bone fracture healing.

5.2 Future work

This thesis has addressed an important challenge and provided technological solutions to mitigate the drug burst release and prolong the release of dexamethasone from 3D printed scaffolds. Also, the potential of adding a sustained release system to immunomodulate macrophage activation status that benefits osteogenesis in macrophage-MSC co-cultures *in vitro* to model bone regeneration in inflammatory conditions. Many crucial pieces of research needed to be conducted to advance the controlled drug release from 3D printed scaffolds along the clinical translation routes.

Firstly, the mechanical property of the scaffolds will need to be improved. The addition of surfactant has decreased the mechanical property of the scaffold (**Appendix Figure 7-9**), which renders them low mechanical property make them not suitable for the application when load bearing is considered in the treatment. Developing a core-shell printed scaffold by using fibreglass in the core and the shell made from PCL/SAIB/DEX-CYD would be effective.

Secondly, as all cell experiments throughout the thesis were carried out in vitro using THP1 monocyte cell lines and immortalised human MSCs, it is important to further ensure that primary human MSCs and monocytes respond to the control release system as same as THP1 cell lines and immortalised MSCs. The immortalised MSCs employed in this dissertation were clonally chosen; hence, the cells cannot represent the diversity often seen in primary MSCs from various donors (termed "clonal heterogeneity"). I have reported here the cross-talk between the MSCs

and macrophages in the presence of the controlled release, but the cellular origin of the secretomes, such as bone morphogenetic protein-2 (BMP-2) and IL-6, was not explored in this study. Previous studies have indicated that both mesenchymal stem cells (MSCs) and macrophages possess the capability to secrete BMP-2 and IL-6. Subsequent investigations will be directed towards elucidating the specific cellular source and temporal dynamics of BMP-2 and IL-6 production. Conducting the co-culture experiments in a trans-well system and monitoring the gene expression at an early time point in MSCs and macrophages would answer these questions.

Lastly, the effectiveness of the scaffolds created for this thesis should be assessed in vivo using models of bone defects. To show if the controlled release of dexamethasone from PCL/SAIB (60:40)/DEX-MC (0.7% wt/wt) may result in excellent integration with the native tissue and the neo-formation of bone tissues, in addition to immunomodulating the inflammation. Long-term research (e.g., 6-month studies) would be needed. The rabbit model may be mostly used because its healing response resembles humans'. Also, it is apparent that big animal models, such as goats and sheep, are necessary when assessing the mechanical property effect is required since these animals experience larger loads as closely as humans do.

Moreover, future endeavours will be required to enhance the precise temporal regulation of drug release. It is essential to ensure that the released drug does not impede the initial advantageous inflammatory response while effectively preventing the development of chronic

inflammation. Developing implants with delayed drug release could yield promising results.

6. Chapter Six: References

1. Hadjidakis, D.J. and I.I. Androulakis, *Bone Remodeling.* Annals of the New York Academy of Sciences, 2006. **1092**(1): p. 385-396.
2. Mourino, V. and A.R. Boccaccini, *Bone tissue engineering therapeutics: controlled drug delivery in three-dimensional scaffolds.* J R Soc Interface, 2010. **7**(43): p. 209-27.
3. Li, J.J., et al., *A Novel Bone Substitute with High Bioactivity, Strength, and Porosity for Repairing Large and Load-Bearing Bone Defects.* Advanced Healthcare Materials, 2019. **8**(8): p. 1801298.
4. Dimitriou, R., et al., *Bone regeneration: current concepts and future directions.* BMC Medicine, 2011. **9**(1): p. 66.
5. Amini, A.R., C.T. Laurencin, and S.P. Nukavarapu, *Bone tissue engineering: recent advances and challenges.* Critical Reviews™ in Biomedical Engineering, 2012. **40**(5).
6. Vidal, L., et al., *Reconstruction of Large Skeletal Defects: Current Clinical Therapeutic Strategies and Future Directions Using 3D Printing.* Frontiers in Bioengineering and Biotechnology, 2020. **8**.
7. Haseltine, W.A., *The Emergence of Regenerative Medicine: A New Field and a New Society.* e-biomed: The Journal of Regenerative Medicine, 2001. **2**(4): p. 17-23.
8. Langer, R. and J.P. Vacanti, *Tissue engineering.* Science, 1993. **260**(5110): p. 920-6.
9. Horwood, N.J., *Macrophage Polarization and Bone Formation: A review.* Clinical Reviews in Allergy & Immunology, 2016. **51**(1): p. 79-86.
10. Fratzl, P. and R. Weinkamer, *Nature's hierarchical materials.* Progress in Materials Science, 2007. **52**(8): p. 1263-1334.

11. Bose, S., S. Vahabzadeh, and A. Bandyopadhyay, *Bone tissue engineering using 3D printing.* Materials Today, 2013. **16**(12): p. 496-504.
12. Eliaz, N. and N. Metoki, *Calcium Phosphate Bioceramics: A Review of Their History, Structure, Properties, Coating Technologies and Biomedical Applications.* Materials (Basel), 2017. **10**(4).
13. Rho, J.-Y., L. Kuhn-Spearing, and P. Zioupos, *Mechanical properties and the hierarchical structure of bone.* Medical Engineering & Physics, 1998. **20**(2): p. 92-102.
14. Hassenkam, T., et al., *High-resolution AFM imaging of intact and fractured trabecular bone.* Bone, 2004. **35**(1): p. 4-10.
15. Ke, P., et al., *From macro to micro: structural biomimetic materials by electrospinning.* RSC Advances, 2014. **4**(75): p. 39704-39724.
16. Fratzl, P., et al., *Structure and mechanical quality of the collagen–mineral nano-composite in bone.* Journal of Materials Chemistry, 2004. **14**(14): p. 2115-2123.
17. Bonfield, W., M. Wang, and K.E. Tanner, *Interfaces in analogue biomaterials.* Acta Materialia, 1998. **46**(7): p. 2509-2518.
18. Murugan, R. and S. Ramakrishna, *Development of nanocomposites for bone grafting.* Composites Science and Technology, 2005. **65**(15): p. 2385-2406.
19. Bilgiç, E., et al., *Chapter 6 - Architecture of bone tissue and its adaptation to pathological conditions*, in *Comparative Kinesiology of the Human Body*, S. Angin and I.E. Şimşek, Editors. 2020, Academic Press. p. 71-90.
20. Komori, T., et al., *Targeted disruption of Cbfa1 results in a complete lack of bone formation owing to maturational arrest of osteoblasts.* Cell, 1997. **89**(5): p. 755-64.

21. Hong, J.H., et al., *TAZ, a transcriptional modulator of mesenchymal stem cell differentiation.* Science, 2005. **309**(5737): p. 1074-8.

22. Capulli, M., R. Paone, and N. Rucci, *Osteoblast and osteocyte: games without frontiers.* Arch Biochem Biophys, 2014. **561**: p. 3-12.

23. Florencio-Silva, R., et al., *Biology of Bone Tissue: Structure, Function, and Factors That Influence Bone Cells.* BioMed research international, 2015. **2015**: p. 421746-421746.

24. Fakhry, M., et al., *Molecular mechanisms of mesenchymal stem cell differentiation towards osteoblasts.* World J Stem Cells, 2013. **5**(4): p. 136-48.

25. Ducy, P., et al., *Osf2/Cbfa1: a transcriptional activator of osteoblast differentiation.* Cell, 1997. **89**(5): p. 747-54.

26. Manolagas, S.C., *Birth and death of bone cells: basic regulatory mechanisms and implications for the pathogenesis and treatment of osteoporosis.* Endocr Rev, 2000. **21**(2): p. 115-37.

27. Franz-Odendaal, T.A., B.K. Hall, and P.E. Witten, *Buried alive: how osteoblasts become osteocytes.* Dev Dyn, 2006. **235**(1): p. 176-90.

28. Dallas, S.L., M. Prideaux, and L.F. Bonewald, *The osteocyte: an endocrine cell ... and more.* Endocr Rev, 2013. **34**(5): p. 658-90.

29. Rochefort, G.Y., S. Pallu, and C.L. Benhamou, *Osteocyte: the unrecognized side of bone tissue.* Osteoporos Int, 2010. **21**(9): p. 1457-69.

30. Stains, J.P. and R. Civitelli, *Cell-to-cell interactions in bone.* Biochemical and Biophysical Research Communications, 2005. **328**(3): p. 721-727.

31. Ross, F.P., *Osteoclast Biology and Bone Resorption*, in *Primer on the Metabolic Bone Diseases and Disorders of Mineral Metabolism*. p. 25-33.

32. Katsimbri, P., *The biology of normal bone remodelling.* Eur J Cancer Care (Engl), 2017. **26**(6).

33. Arai, F., et al., *Commitment and differentiation of osteoclast precursor cells by the sequential expression of c-Fms and receptor activator of nuclear factor kappaB (RANK) receptors.* J Exp Med, 1999. **190**(12): p. 1741-54.

34. Boyce, B.F. and L. Xing, *Biology of RANK, RANKL, and osteoprotegerin.* Arthritis Res Ther, 2007. **9 Suppl 1**(Suppl 1): p. S1.

35. Gasser, J.A. and M. Kneissel. *Bone Physiology and Biology*. 2017.

36. Maruyama, M., et al., *Modulation of the Inflammatory Response and Bone Healing.* Frontiers in Endocrinology, 2020. **11**.

37. Loi, F., et al., *Inflammation, fracture and bone repair.* Bone, 2016. **86**: p. 119-130.

38. Harwood, P.J., J.B. Newman, and A.L.R. Michael, *(ii) An update on fracture healing and non-union.* Orthopaedics and Trauma, 2010. **24**(1): p. 9-23.

39. Fazzalari, N.L., *Bone fracture and bone fracture repair.* Osteoporos Int, 2011. **22**(6): p. 2003-6.

40. Shapiro, F., *Bone development and its relation to fracture repair. The role of mesenchymal osteoblasts and surface osteoblasts.* Eur Cell Mater, 2008. **15**: p. 53-76.

41. Walters, G., I. Pountos, and P.V. Giannoudis, *The cytokines and micro-environment of fracture haematoma: Current evidence.* Journal of Tissue Engineering and Regenerative Medicine, 2018. **12**(3): p. e1662-e1677.

42. Bastian, O., et al., *Systemic inflammation and fracture healing.* Journal of Leukocyte Biology, 2011. **89**(5): p. 669-673.

43. Karnes, J.M., S.D. Daffner, and C.M. Watkins, *Multiple roles of tumor necrosis factor-alpha in fracture healing.* Bone, 2015. **78**: p. 87-93.

44. Toosi, S. and J. Behravan, *Osteogenesis and bone remodeling: A focus on growth factors and bioactive peptides.* BioFactors, 2020. **46**(3): p. 326-340.

45. Gerstenfeld, L.C., et al., *Fracture healing as a post-natal developmental process: Molecular, spatial, and temporal aspects of its regulation.* Journal of Cellular Biochemistry, 2003. **88**(5): p. 873-884.

46. Kenkre, J.S. and J. Bassett, *The bone remodelling cycle.* Ann Clin Biochem, 2018. **55**(3): p. 308-327.

47. Marsell, R. and T.A. Einhorn, *The biology of fracture healing.* Injury, 2011. **42**(6): p. 551-5.

48. Miron, R.J. and D.D. Bosshardt, *OsteoMacs: Key players around bone biomaterials.* Biomaterials, 2016. **82**: p. 1-19.

49. Hilborn, J. and L.M. Bjursten, *A new and evolving paradigm for biocompatibility.* J Tissue Eng Regen Med, 2007. **1**(2): p. 110-9.

50. Martin, R.B., *The importance of mechanical loading in bone biology and medicine.* J Musculoskelet Neuronal Interact, 2007. **7**(1): p. 48-53.

51. Rubin, J., C. Rubin, and C.R. Jacobs, *Molecular pathways mediating mechanical signaling in bone.* Gene, 2006. **367**: p. 1-16.

52. Szczesniak, A.M., et al., *Mechanical loading modulates glutamate receptor subunit expression in bone.* Bone, 2005. **37**(1): p. 63-73.

53. Anastasio, A.T., et al., *Nanomaterial Nitric Oxide Delivery in Traumatic Orthopedic Regenerative Medicine.* Frontiers in Bioengineering and Biotechnology, 2021. **8**.

54. Arron, J.R. and Y. Choi, *Bone versus immune system.* Nature, 2000. **408**(6812): p. 535-536.

55. Arboleya, L. and S. Castañeda, *Osteoimmunology: The Study of the Relationship Between the Immune System and Bone Tissue.* Reumatología Clínica (English Edition), 2013. **9**(5): p. 303-315.

56. Takayanagi, H., *Osteoimmunology and the effects of the immune system on bone.* Nat Rev Rheumatol, 2009. **5**(12): p. 667-76.

57. Criscitiello, C., et al., *Crosstalk between bone niche and immune system: Osteoimmunology signaling as a potential target for cancer treatment.* Cancer Treatment Reviews, 2015. **41**(2): p. 61-68.

58. Guder, C., et al., *Osteoimmunology: A Current Update of the Interplay Between Bone and the Immune System.* Frontiers in Immunology, 2020. **11**.

59. Dimitriou, R., E. Tsiridis, and P.V. Giannoudis, *Current concepts of molecular aspects of bone healing.* Injury, 2005. **36**(12): p. 1392-1404.

60. Bastian, O.W., et al., *Neutrophils contribute to fracture healing by synthesizing fibronectin+ extracellular matrix rapidly after injury.* Clinical Immunology, 2016. **164**: p. 78-84.

61. Kovtun, A., et al., *The crucial role of neutrophil granulocytes in bone fracture healing.* Eur Cell Mater, 2016. **32**: p. 152-162.

62. Söderström, K., et al., *Natural killer cells trigger osteoclastogenesis and bone destruction in arthritis.* Proceedings of the National Academy of Sciences, 2010. **107**(29): p. 13028-13033.

63. Almeida, Catarina R., et al., *NAP-2 Secreted by Human NK Cells Can Stimulate Mesenchymal Stem/Stromal Cell Recruitment.* Stem Cell Reports, 2016. **6**(4): p. 466-473.

64. Sun, G., et al., *Regulatory B cell is critical in bone union process through suppressing proinflammatory cytokines and stimulating Foxp3 in Treg cells.* Clinical and Experimental Pharmacology and Physiology, 2017. **44**(4): p. 455-462.

65. Yasuda, H., et al., *Osteoclast differentiation factor is a ligand for osteoprotegerin/osteoclastogenesis-inhibitory factor and is identical to TRANCE/RANKL.* Proceedings of the National Academy of Sciences, 1998. **95**(7): p. 3597-3602.

66. van Tuyl, L.H.D., et al., *Baseline RANKL:OPG ratio and markers of bone and cartilage degradation predict annual radiological progression over 11 years in rheumatoid arthritis.* Annals of the Rheumatic Diseases, 2010. **69**(9): p. 1623.

67. Anton, K., D. Banerjee, and J. Glod, *Macrophage-Associated Mesenchymal Stem Cells Assume an Activated, Migratory, Pro-Inflammatory Phenotype with Increased IL-6 and CXCL10 Secretion.* PLOS ONE, 2012. **7**(4): p. e35036.

68. Croes, M., et al., *Proinflammatory T cells and IL-17 stimulate osteoblast differentiation.* Bone, 2016. **84**: p. 262-270.

69. Takayanagi, H., et al., *T-cell-mediated regulation of osteoclastogenesis by signalling cross-talk between RANKL and IFN-gamma.* Nature, 2000. **408**(6812): p. 600-5.

70. Glass, G.E., et al., *TNF-alpha promotes fracture repair by augmenting the recruitment and differentiation of muscle-derived stromal cells.* Proc Natl Acad Sci U S A, 2011. **108**(4): p. 1585-90.

71. Chang, M.K., et al., *Osteal Tissue Macrophages Are Intercalated throughout Human and Mouse Bone Lining Tissues and Regulate Osteoblast Function In Vitro and In Vivo.* The Journal of Immunology, 2008. **181**(2): p. 1232.

72. Vi, L., et al., *Macrophages Promote Osteoblastic Differentiation In Vivo: Implications in Fracture Repair and Bone Homeostasis.* Journal of Bone and Mineral Research, 2015. **30**(6): p. 1090-1102.

73. Raggatt, L.J., et al., *Fracture Healing via Periosteal Callus Formation Requires Macrophages for Both Initiation and Progression of Early*

Endochondral Ossification. The American Journal of Pathology, 2014. **184**(12): p. 3192-3204.

74. Davies, L.C., et al., *Tissue-resident macrophages.* Nature Immunology, 2013. **14**: p. 986.
75. Wynn, T.A. and K.M. Vannella, *Macrophages in Tissue Repair, Regeneration, and Fibrosis.* Immunity, 2016. **44**(3): p. 450-462.
76. Gordon, S., A. Plüddemann, and F. Martinez Estrada, *Macrophage heterogeneity in tissues: phenotypic diversity and functions.* Immunological Reviews, 2014. **262**(1): p. 36-55.
77. Wu, X.-q., et al., *Emerging role of microRNAs in regulating macrophage activation and polarization in immune response and inflammation.* Immunology, 2016. **148**(3): p. 237-248.
78. Tan, H.-Y., et al., *The Reactive Oxygen Species in Macrophage Polarization: Reflecting Its Dual Role in Progression and Treatment of Human Diseases.* Oxidative Medicine and Cellular Longevity, 2016. **2016**: p. 16.
79. Rostam, H.M., et al., *Impact of surface chemistry and topography on the function of antigen presenting cells.* Biomaterials Science, 2015. **3**(3): p. 424-441.
80. Biswas, S.K. and A. Mantovani, *Macrophage plasticity and interaction with lymphocyte subsets: cancer as a paradigm.* Nature Immunology, 2010. **11**: p. 889.
81. Dey, A., J. Allen, and P.A. Hankey-Giblin, *Ontogeny and Polarization of Macrophages in Inflammation: Blood Monocytes Versus Tissue Macrophages.* Frontiers in Immunology, 2015. **5**(683).
82. Lu, D., et al., *Mesenchymal Stem Cell-Macrophage Crosstalk and Maintenance of Inflammatory Microenvironment Homeostasis.* Frontiers in Cell and Developmental Biology, 2021. **9**.

83. Lee, S.-K. and J. Lorenzo, *Cytokines regulating osteoclast formation and function.* Current Opinion in Rheumatology, 2006. **18**(4).

84. Yang, X., et al., *Callus mineralization and maturation are delayed during fracture healing in interleukin-6 knockout mice.* Bone, 2007. **41**(6): p. 928-936.

85. Guihard, P., et al., *Induction of Osteogenesis in Mesenchymal Stem Cells by Activated Monocytes/Macrophages Depends on Oncostatin M Signaling.* STEM CELLS, 2012. **30**(4): p. 762-772.

86. Hume, D.A., J.F. Loutit, and S. Gordon, *The mononuclear phagocyte system of the mouse defined by immunohistochemical localization of antigen F4/80: macrophages of bone and associated connective tissue.* J Cell Sci, 1984. **66**: p. 189-94.

87. Zhang, Y., et al., *Macrophage type modulates osteogenic differentiation of adipose tissue MSCs.* Cell Tissue Res, 2017. **369**(2): p. 273-286.

88. Wu, X., et al., *TNF-a mediated inflammatory macrophage polarization contributes to the pathogenesis of steroid-induced osteonecrosis in mice.* International Journal of Immunopathology and Pharmacology, 2015. **28**(3): p. 351-361.

89. Jones, A.C., et al., *Assessment of bone ingrowth into porous biomaterials using MICRO-CT.* Biomaterials, 2007. **28**(15): p. 2491-2504.

90. Seitz, H., et al., *Three-dimensional printing of porous ceramic scaffolds for bone tissue engineering.* J Biomed Mater Res B Appl Biomater, 2005. **74**(2): p. 782-8.

91. Salgado, A.J., O.P. Coutinho, and R.L. Reis, *Bone tissue engineering: state of the art and future trends.* Macromol Biosci, 2004. **4**(8): p. 743-65.

92. Rezwan, K., et al., *Biodegradable and bioactive porous polymer/inorganic composite scaffolds for bone tissue engineering.* Biomaterials, 2006. **27**(18): p. 3413-31.

93. Ferracini, R., et al. *Scaffolds as Structural Tools for Bone-Targeted Drug Delivery*. Pharmaceutics, 2018. **10**, DOI: 10.3390/pharmaceutics10030122.

94. Habibovic, P., et al., *Osteoconduction and osteoinduction of low-temperature 3D printed bioceramic implants.* Biomaterials, 2008. **29**(7): p. 944-953.

95. Karageorgiou, V. and D. Kaplan, *Porosity of 3D biomaterial scaffolds and osteogenesis.* Biomaterials, 2005. **26**(27): p. 5474-91.

96. Bandyopadhyay, A., et al., *Calcium Phosphate-Based Resorbable Ceramics: Influence of MgO, ZnO, and SiO2 Dopants.* Journal of the American Ceramic Society, 2006. **89**(9): p. 2675-2688.

97. Banerjee, S.S., et al., *Understanding the influence of MgO and SrO binary doping on the mechanical and biological properties of β-TCP ceramics.* Acta Biomaterialia, 2010. **6**(10): p. 4167-4174.

98. Bodhak, S., S. Bose, and A. Bandyopadhyay, *Role of surface charge and wettability on early stage mineralization and bone cell–materials interactions of polarized hydroxyapatite.* Acta Biomaterialia, 2009. **5**(6): p. 2178-2188.

99. Das, K., S. Bose, and A. Bandyopadhyay, *Surface modifications and cell–materials interactions with anodized Ti.* Acta Biomaterialia, 2007. **3**(4): p. 573-585.

100. Tarafder, S., et al., *Electrically Polarized Biphasic Calcium Phosphates: Adsorption and Release of Bovine Serum Albumin.* Langmuir, 2010. **26**(22): p. 16625-16629.

101. Hutmacher, D.W., *Scaffolds in tissue engineering bone and cartilage.* Biomaterials, 2000. **21**(24): p. 2529-2543.

102. Hutmacher, D.W., et al., *Mechanical properties and cell cultural response of polycaprolactone scaffolds designed and fabricated via fused deposition modeling.* J Biomed Mater Res, 2001. **55**(2): p. 203-16.

103. Ruiz-Cantu, L., et al., *Characterisation of the surface structure of 3D printed scaffolds for cell infiltration and surgical suturing.* Biofabrication, 2016. **8**(1): p. 015016.

104. Shao, H., et al., *Bioactive glass-reinforced bioceramic ink writing scaffolds: sintering, microstructure and mechanical behavior.* Biofabrication, 2015. **7**(3): p. 035010.

105. Sobral, J.M., et al., *Three-dimensional plotted scaffolds with controlled pore size gradients: Effect of scaffold geometry on mechanical performance and cell seeding efficiency.* Acta Biomater, 2011. **7**(3): p. 1009-18.

106. Lee, J.W., et al., *Evaluating cell proliferation based on internal pore size and 3D scaffold architecture fabricated using solid freeform fabrication technology.* J Mater Sci Mater Med, 2010. **21**(12): p. 3195-205.

107. Zhang, Z.Z., et al., *Role of scaffold mean pore size in meniscus regeneration.* Acta Biomater, 2016. **43**: p. 314-326.

108. Domingos, M., *Effect of process parameters on the morphological and mechanical properties of 3D Bioextruded poly(ε - caprolactone) scaffolds.* Rapid Prototyping Journal, 2012. **18**(1): p. 56-67.

109. Domingos, M., et al., *The first systematic analysis of 3D rapid prototyped poly(epsilon-caprolactone) scaffolds manufactured through BioCell printing: the effect of pore size and geometry on compressive mechanical behaviour and in vitro hMSC viability.* Biofabrication, 2013. **5**(4): p. 045004.

110. Ge, Z., et al., *Functional biomaterials for cartilage regeneration.* Journal of Biomedical Materials Research Part A, 2012. **100A**(9): p. 2526-2536.

111. Hunt, N.C. and L.M. Grover, *Cell encapsulation using biopolymer gels for regenerative medicine.* Biotechnol Lett, 2010. **32**(6): p. 733-42.

112. Muzzarelli, R.A., et al., *Chitosan, hyaluronan and chondroitin sulfate in tissue engineering for cartilage regeneration: a review.* Carbohydr Polym, 2012. **89**(3): p. 723-39.

113. Thiem, A., et al., *Gelatin-poly(lactic-co-glycolic acid) scaffolds with oriented pore channel architecture - From in vitro to in vivo testing.* Mater Sci Eng C Mater Biol Appl, 2016. **62**: p. 585-95.

114. Liu, Y., et al., *Segmental bone regeneration using an rhBMP-2-loaded gelatin/nanohydroxyapatite/fibrin scaffold in a rabbit model.* Biomaterials, 2009. **30**(31): p. 6276-6285.

115. Costa, P.F., et al., *Additive manufacturing of scaffolds with dexamethasone controlled release for enhanced bone regeneration.* International Journal of Pharmaceutics, 2015. **496**(2): p. 541-550.

116. Alsousou, J., et al., *The biology of platelet-rich plasma and its application in trauma and orthopaedic surgery: a review of the literature.* J Bone Joint Surg Br, 2009. **91**(8): p. 987-96.

117. Stevens, M.M., *Biomaterials for bone tissue engineering.* Materials Today, 2008. **11**(5): p. 18-25.

118. Yan, L.P., et al., *Bioactive macro/micro porous silk fibroin/nano-sized calcium phosphate scaffolds with potential for bone-tissue-engineering applications.* Nanomedicine (Lond), 2013. **8**(3): p. 359-78.

119. Hannink, G. and J.J. Arts, *Bioresorbability, porosity and mechanical strength of bone substitutes: what is optimal for bone regeneration?* Injury, 2011. **42 Suppl 2**: p. S22-5.

120. Campana, V., et al., *Bone substitutes in orthopaedic surgery: from basic science to clinical practice.* J Mater Sci Mater Med, 2014. **25**(10): p. 2445-61.

121. Gupta, A., et al., *Bone graft substitutes for spine fusion: A brief review.* World J Orthop, 2015. **6**(6): p. 449-56.

122. Jiang, J., et al., *Bioactive Stratified Polymer Ceramic-Hydrogel Scaffold for Integrative Osteochondral Repair.* Annals of Biomedical Engineering, 2010. **38**(6): p. 2183-2196.

123. Cunniffe, G.M., et al., *Content-Dependent Osteogenic Response of Nanohydroxyapatite: An in Vitro and in Vivo Assessment within Collagen-Based Scaffolds.* ACS Applied Materials & Interfaces, 2016. **8**(36): p. 23477-23488.

124. Lewandrowski, K.U., et al., *Enhanced bioactivity of a poly(propylene fumarate) bone graft substitute by augmentation with nano-hydroxyapatite.* Biomed Mater Eng, 2003. **13**(2): p. 115-24.

125. Sheikh, Z., C. Sima, and M. Glogauer, *Bone Replacement Materials and Techniques Used for Achieving Vertical Alveolar Bone Augmentation.* Materials, 2015. **8**(6).

126. Grabowski, G. and C.A. Cornett, *Bone graft and bone graft substitutes in spine surgery: current concepts and controversies.* J Am Acad Orthop Surg, 2013. **21**(1): p. 51-60.

127. Nguyen, L.H., et al., *Progenitor cells: role and usage in bone tissue engineering approaches for spinal fusion.* Adv Exp Med Biol, 2012. **760**: p. 188-210.

128. Park, J.J., S.H. Hershman, and Y.H. Kim, *Updates in the use of bone grafts in the lumbar spine.* Bull Hosp Jt Dis (2013), 2013. **71**(1): p. 39-48.

129. Elder, B.D., et al., *A systematic assessment of the use of platelet-rich plasma in spinal fusion.* Ann Biomed Eng, 2015. **43**(5): p. 1057-70.

130. Zhu, L.-Y., et al. *Mechanical characterization of 3D printed multi-morphology porous Ti6Al4V scaffolds based on triply periodic minimal surface architectures*. American journal of translational research, 2018. **10**, 3443-3454.

131. Li, Y., et al., *Improving Osteointegration and Osteogenesis of Three-Dimensional Porous Ti6Al4V Scaffolds by Polydopamine-Assisted Biomimetic Hydroxyapatite Coating.* ACS Applied Materials & Interfaces, 2015. **7**(10): p. 5715-5724.

132. Manavitehrani, I., et al., *Biomedical Applications of Biodegradable Polyesters.* Polymers, 2016. **8**(1).

133. Abbah, S.A., et al., *Biological performance of a polycaprolactone-based scaffold used as fusion cage device in a large animal model of spinal reconstructive surgery.* Biomaterials, 2009. **30**(28): p. 5086-93.

134. Abbah, S.A., et al., *Fusion performance of low-dose recombinant human bone morphogenetic protein 2 and bone marrow-derived multipotent stromal cells in biodegradable scaffolds: a comparative study in a large animal model of anterior lumbar interbody fusion.* Spine (Phila Pa 1976), 2011. **36**(21): p. 1752-9.

135. Abbah, S.A., et al., *Autogenous bone marrow stromal cell sheets-loaded mPCL/TCP scaffolds induced osteogenesis in a porcine model of spinal interbody fusion.* Tissue Eng Part A, 2011. **17**(5-6): p. 809-17.

136. Reichert, J.C., et al., *Custom-made composite scaffolds for segmental defect repair in long bones.* Int Orthop, 2011. **35**(8): p. 1229-36.

137. Kao, C.-T., et al., *Poly(dopamine) coating of 3D printed poly(lactic acid) scaffolds for bone tissue engineering.* Materials Science and Engineering: C, 2015. **56**: p. 165-173.

138. Qasim, M., D.S. Chae, and N.Y. Lee, *Advancements and frontiers in nano-based 3D and 4D scaffolds for bone and cartilage tissue engineering.* Int J Nanomedicine, 2019. **14**: p. 4333-4351.

139. Qu, H., et al., *Biomaterials for bone tissue engineering scaffolds: a review.* RSC Advances, 2019. **9**(45): p. 26252-26262.

140. Turnbull, G., et al., *3D bioactive composite scaffolds for bone tissue engineering.* Bioactive Materials, 2018. **3**(3): p. 278-314.

141. Duarte, R.M., et al., *Biomaterials and Bioactive Agents in Spinal Fusion.* Tissue Eng Part B Rev, 2017. **23**(6): p. 540-551.

142. Johnson, T., et al., *Fabrication of highly porous tissue-engineering scaffolds using selective spherical porogens.* Bio-Medical Materials and Engineering, 2010. **20**: p. 107-118.

143. Dehghani, F. and N. Annabi, *Engineering porous scaffolds using gas-based techniques.* Current Opinion in Biotechnology, 2011. **22**(5): p. 661-666.

144. Capuana, E., et al., *Solution-Based Processing for Scaffold Fabrication in Tissue Engineering Applications: A Brief Review.* Polymers (Basel), 2021. **13**(13).

145. Matthews, J.A., et al., *Electrospinning of Collagen Nanofibers.* Biomacromolecules, 2002. **3**(2): p. 232-238.

146. Chia, H.N. and B.M. Wu, *Recent advances in 3D printing of biomaterials.* J Biol Eng, 2015. **9**: p. 4.

147. Moroni, L., J.R. de Wijn, and C.A. van Blitterswijk, *3D fiber-deposited scaffolds for tissue engineering: influence of pores geometry and architecture on dynamic mechanical properties.* Biomaterials, 2006. **27**(7): p. 974-85.

148. Murphy, S.V. and A. Atala, *3D bioprinting of tissues and organs.* Nat Biotechnol, 2014. **32**(8): p. 773-85.

149. Mistry, P., et al., *Bioprinting Using Mechanically Robust Core-Shell Cell-Laden Hydrogel Strands.* Macromol Biosci, 2017. **17**(6).

150. Woodfield, T.B., et al., *Design of porous scaffolds for cartilage tissue engineering using a three-dimensional fiber-deposition technique.* Biomaterials, 2004. **25**(18): p. 4149-61.

151. Gibson, I., *Additive manufacturing technologies : 3D printing, rapid prototyping, and direct digital manufacturing / Ian Gibson, David Rosen, Brent Stucker*. 2nd ed. ed, ed. D.W. Rosen and B. Stucker. 2015, New York: New York : Springer.

152. Michna, S., W. Wu, and J.A. Lewis, *Concentrated hydroxyapatite inks for direct-write assembly of 3-D periodic scaffolds.* Biomaterials, 2005. **26**(28): p. 5632-9.

153. Bittner, S.M., et al., *Three-dimensional printing of multilayered tissue engineering scaffolds.* Materials Today, 2018. **21**(8): p. 861-874.

154. Bracaglia, L.G., et al., *3D printing for the design and fabrication of polymer-based gradient scaffolds.* Acta Biomaterialia, 2017. **56**: p. 3-13.

155. Sears, N.A., et al., *A Review of Three-Dimensional Printing in Tissue Engineering.* Tissue Engineering Part B: Reviews, 2016. **22**(4): p. 298-310.

156. Gao, G. and X. Cui, *Three-dimensional bioprinting in tissue engineering and regenerative medicine.* Biotechnology Letters, 2016. **38**(2): p. 203-211.

157. Truby, R.L. and J.A. Lewis, *Printing soft matter in three dimensions.* Nature, 2016. **540**(7633): p. 371-378.

158. Dellacherie, M.O., B.R. Seo, and D.J. Mooney, *Macroscale biomaterials strategies for local immunomodulation.* Nature Reviews Materials, 2019. **4**(6): p. 379-397.

159. Chen, Y., et al., *In vitro enteroid-derived three-dimensional tissue model of human small intestinal epithelium with innate immune responses.* PLOS ONE, 2017. **12**(11): p. e0187880.

160. Brown, B.N. and S.F. Badylak, *Extracellular matrix as an inductive scaffold for functional tissue reconstruction.* Translational Research, 2014. **163**(4): p. 268-285.

161. Kim, Y.K., E.Y. Chen, and W.F. Liu, *Biomolecular strategies to modulate the macrophage response to implanted materials.* Journal of Materials Chemistry B, 2016. **4**(9): p. 1600-1609.

162. Mariani, E., et al. *Biomaterials: Foreign Bodies or Tuners for the Immune Response?* International Journal of Molecular Sciences, 2019. **20**, DOI: 10.3390/ijms20030636.

163. Yatim, N., S. Cullen, and M.L. Albert, *Dying cells actively regulate adaptive immune responses.* Nature Reviews Immunology, 2017. **17**(4): p. 262-275.

164. Niess, J.H. and H.-C. Reinecker, *Dendritic cells in the recognition of intestinal microbiota.* Cellular Microbiology, 2006. **8**(4): p. 558-564.

165. Rosales, C., *Neutrophil: A Cell with Many Roles in Inflammation or Several Cell Types?* Frontiers in Physiology, 2018. **9**.

166. Greenlee-Wacker, M.C., *Clearance of apoptotic neutrophils and resolution of inflammation.* Immunological Reviews, 2016. **273**(1): p. 357-370.

167. Higgins, D.M., et al., *Localized Immunosuppressive Environment in the Foreign Body Response to Implanted Biomaterials.* The American Journal of Pathology, 2009. **175**(1): p. 161-170.

168. Bartoli, C.R. and J.J. Godleski, *Blood Flow in the Foreign-Body Capsules Surrounding Surgically Implanted Subcutaneous Devices.* Journal of Surgical Research, 2010. **158**(1): p. 147-154.

169. Garg, K., et al., *Macrophage functional polarization (M1/M2) in response to varying fiber and pore dimensions of electrospun scaffolds.* Biomaterials, 2013. **34**(18): p. 4439-51.

170. Christo, S.N., et al., *Innate Immunity and Biomaterials at the Nexus: Friends or Foes.* BioMed Research International, 2015. **2015**: p. 342304.

171. Xia, Z. and J.T. Triffitt, *A review on macrophage responses to biomaterials.* Biomed Mater, 2006. **1**(1): p. R1-9.

172. Luzina, I.G., et al., *Regulation of inflammation by interleukin-4: a review of "alternatives".* Journal of Leukocyte Biology, 2012. **92**(4): p. 753-764.

173. Anderson, J.M., A. Rodriguez, and D.T. Chang, *Foreign body reaction to biomaterials.* Seminars in Immunology, 2008. **20**(2): p. 86-100.

174. Griffin, R.S., et al., *Imagined Examples of Painful Experiences Provided by Chronic Low Back Pain Patients and Attributed a Pain Numerical Rating Score.* Frontiers in Neuroscience, 2020. **13**.

175. Witherel, C.E., et al., *Macrophage and Fibroblast Interactions in Biomaterial-Mediated Fibrosis.* Advanced Healthcare Materials, 2019. **8**(4): p. 1801451.

176. Huebsch, N., et al., *Matrix elasticity of void-forming hydrogels controls transplanted-stem-cell-mediated bone formation.* Nature Materials, 2015. **14**(12): p. 1269-1277.

177. Jing, Z., et al., *Carbon Nanotube Reinforced Collagen/Hydroxyapatite Scaffolds Improve Bone Tissue Formation In Vitro and In Vivo.* Ann Biomed Eng, 2017. **45**(9): p. 2075-2087.

178. Sadtler, K., et al., *Design, clinical translation and immunological response of biomaterials in regenerative medicine.* Nature Reviews Materials, 2016. **1**(7): p. 16040.

179. Solheim, E., et al., *Biocompatibility and effect on osteogenesis of poly(ortho ester) compared to poly(DL-lactic acid).* Journal of Biomedical Materials Research, 2000. **49**(2): p. 257-263.

180. Zaveri, T.D., et al., *Contributions of surface topography and cytotoxicity to the macrophage response to zinc oxide nanorods.* Biomaterials, 2010. **31**(11): p. 2999-3007.

181. Unadkat, H.V., et al., *An algorithm-based topographical biomaterials library to instruct cell fate.* Proceedings of the National Academy of Sciences, 2011. **108**(40): p. 16565.

182. Sigal, G.B., M. Mrksich, and G.M. Whitesides, *Effect of Surface Wettability on the Adsorption of Proteins and Detergents.* Journal of the American Chemical Society, 1998. **120**(14): p. 3464-3473.

183. Kurpinski, K.T., et al., *The effect of fiber alignment and heparin coating on cell infiltration into nanofibrous PLLA scaffolds.* Biomaterials, 2010. **31**(13): p. 3536-42.

184. Wang, Z., et al., *The effect of thick fibers and large pores of electrospun poly(epsilon-caprolactone) vascular grafts on macrophage polarization and arterial regeneration.* Biomaterials, 2014. **35**(22): p. 5700-10.

185. Reeves, A.R.D., et al., *Controlled release of cytokines using silk-biomaterials for macrophage polarization.* Biomaterials, 2015. **73**: p. 272-283.

186. Vacanti, N.M., et al., *Localized delivery of dexamethasone from electrospun fibers reduces the foreign body response.* Biomacromolecules, 2012. **13**(10): p. 3031-8.

187. Vishwakarma, A., et al., *Engineering Immunomodulatory Biomaterials To Tune the Inflammatory Response.* Trends Biotechnol, 2016. **34**(6): p. 470-482.

188. Smith, T.D., et al., *Harnessing macrophage plasticity for tissue regeneration.* Advanced Drug Delivery Reviews, 2017. **114**: p. 193-205.

189. Wilson, C.J., et al., *Mediation of Biomaterial–Cell Interactions by Adsorbed Proteins: A Review.* Tissue Engineering, 2005. **11**(1-2): p. 1-18.

190. Ye, J., et al., *Promoting musculoskeletal system soft tissue regeneration by biomaterial-mediated modulation of macrophage polarization.* Bioactive Materials, 2021. **6**(11): p. 4096-4109.

191. Hu, W.-J., et al., *Molecular basis of biomaterial-mediated foreign body reactions.* Blood, 2001. **98**(4): p. 1231-1238.

192. Vassey, M.J., et al., *Immune Modulation by Design: Using Topography to Control Human Monocyte Attachment and Macrophage Differentiation.* Advanced Science, 2020. **7**(11): p. 1903392.

193. Hasirci, V. and H. Kenar, *Novel surface patterning approaches for tissue engineering and their effect on cell behavior.* Nanomedicine, 2006. **1**(1): p. 73-90.

194. Barthes, J., et al., *Cell Microenvironment Engineering and Monitoring for Tissue Engineering and Regenerative Medicine: The Recent Advances.* BioMed Research International, 2014. **2014**: p. 921905.

195. Ding, H., et al., *Controlled Microstructural Architectures Based on Smart Fabrication Strategies.* Advanced Functional Materials, 2020. **30**(2): p. 1901760.

196. Ermis, M., E. Antmen, and V. Hasirci, *Micro and Nanofabrication methods to control cell-substrate interactions and cell behavior: A*

review from the tissue engineering perspective. Bioact Mater, 2018. **3**(3): p. 355-369.

197. Prasopthum, A., et al., *Three-Dimensional Printed Scaffolds with Controlled Micro-/Nanoporous Surface Topography Direct Chondrogenic and Osteogenic Differentiation of Mesenchymal Stem Cells.* ACS Applied Materials & Interfaces, 2019. **11**(21): p. 18896-18906.
198. Kushiro, K., et al., *Differences in Three-Dimensional Geometric Recognition by Non-Cancerous and Cancerous Epithelial Cells on Microgroove-Based Topography.* Scientific Reports, 2017. **7**(1): p. 4244.
199. Sun, B., et al., *Preferred cell alignment along concave microgrooves.* RSC Advances, 2017. **7**(11): p. 6788-6794.
200. McWhorter, F.Y., et al., *Modulation of macrophage phenotype by cell shape.* Proceedings of the National Academy of Sciences, 2013. **110**(43): p. 17253-17258.
201. Luu, T.U., et al., *Micro- and Nanopatterned Topographical Cues for Regulating Macrophage Cell Shape and Phenotype.* ACS Applied Materials & Interfaces, 2015. **7**(51): p. 28665-28672.
202. Salthouse, T.N., *Some aspects of macrophage behavior at the implant interface.* J Biomed Mater Res, 1984. **18**(4): p. 395-401.
203. Garg, K., et al., *Macrophage functional polarization (M1/M2) in response to varying fiber and pore dimensions of electrospun scaffolds.* Biomaterials, 2013. **34**(18): p. 4439-4451.
204. Hotchkiss, K.M., et al., *Titanium surface characteristics, including topography and wettability, alter macrophage activation.* Acta Biomaterialia, 2016. **31**: p. 425-434.

205. Roach, P., et al., *Modern biomaterials: a review - bulk properties and implications of surface modifications.* J Mater Sci Mater Med, 2007. **18**(7): p. 1263-77.

206. Dhowre, H.S., et al., *Responsive cell–material interfaces.* Nanomedicine, 2015. **10**(5): p. 849-871.

207. Anselme, K., et al., *The interaction of cells and bacteria with surfaces structured at the nanometre scale.* Acta Biomater, 2010. **6**(10): p. 3824-46.

208. Zhu, Y., et al., *Regulation of macrophage polarization through surface topography design to facilitate implant-to-bone osteointegration.* Science Advances. **7**(14): p. eabf6654.

209. Dobrovolskaia, M.A. and S.E. McNeil, *Immunological properties of engineered nanomaterials.* Nat Nanotechnol, 2007. **2**(8): p. 469-78.

210. Li, J., et al., *Tailoring Materials for Modulation of Macrophage Fate.* Advanced Materials, 2021. **33**(12): p. 2004172.

211. Weiss, L., *The Cell Periphery*, in *International Review of Cytology*, G.H. Bourne, J.F. Danielli, and K.W. Jeon, Editors. 1969, Academic Press. p. 63-105.

212. Miller, C.R., et al., *Liposome-cell interactions in vitro: effect of liposome surface charge on the binding and endocytosis of conventional and sterically stabilized liposomes.* Biochemistry, 1998. **37**(37): p. 12875-83.

213. Chen, H., et al., *The promotion of type 1 T helper cell responses to cationic polymers in vivo via toll-like receptor-4 mediated IL-12 secretion.* Biomaterials, 2010. **31**(32): p. 8172-80.

214. Hua, K., et al., *Surface Chemistry of Nanocellulose Fibers Directs Monocyte/Macrophage Response.* Biomacromolecules, 2015. **16**(9): p. 2787-2795.

215. Kajahn, J., et al., *Artificial extracellular matrices composed of collagen I and high sulfated hyaluronan modulate monocyte to macrophage differentiation under conditions of sterile inflammation.* Biomatter, 2012. **2**(4): p. 226-36.

216. Feng, Q., et al., *High - dose dexamethasone or all - trans - retinoic acid restores the balance of macrophages towards M2 in immune thrombocytopenia.* Journal of Thrombosis and Haemostasis, 2017. **15**(9): p. 1845-1858.

217. Cho, J.Y., *Immunomodulatory effect of nonsteroidal anti-inflammatory drugs (NSAIDs) at the clinically available doses.* Archives of Pharmacal Research, 2007. **30**(1): p. 64-74.

218. Barnes, P.J., *How corticosteroids control inflammation: Quintiles Prize Lecture 2005.* British Journal of Pharmacology, 2006. **148**(3): p. 245-254.

219. Xavier, A.M., et al., *Gene Expression Control by Glucocorticoid Receptors during Innate Immune Responses.* Frontiers in Endocrinology, 2016. **7**.

220. Ehrchen, J.M., J. Roth, and K. Barczyk-Kahlert, *More Than Suppression: Glucocorticoid Action on Monocytes and Macrophages.* Frontiers in Immunology, 2019. **10**.

221. Yona, S. and S. Gordon, *Glucocorticoids turn the monocyte switch.* Immunol Cell Biol, 2007. **85**: p. 81-2.

222. Cutolo, M., et al., *Use of glucocorticoids and risk of infections.* Autoimmunity Reviews, 2008. **8**(2): p. 153-155.

223. Lima, A.C., et al., *Free and copolymerized γ-cyclodextrins regulate the performance of dexamethasone-loaded dextran microspheres for bone regeneration.* Journal of Materials Chemistry B, 2014. **2**(30): p. 4943-4956.

224. Jaiswal, N., et al., *Osteogenic differentiation of purified, culture-expanded human mesenchymal stem cells in vitro.* Journal of Cellular Biochemistry, 1997. **64**(2): p. 295-312.

225. Lane, N.E., *An Update on Glucocorticoid-Induced Osteoporosis.* Rheumatic Disease Clinics of North America, 2001. **27**(1): p. 235-253.

226. Walsh, S., et al., *High concentrations of dexamethasone suppress the proliferation but not the differentiation or further maturation of human osteoblast precursors in vitro: relevance to glucocorticoid - induced osteoporosis.* Rheumatology, 2001. **40**(1): p. 74-83.

227. Yu, T., et al., *Temporal and spatial distribution of macrophage phenotype markers in the foreign body response to glutaraldehyde-crosslinked gelatin hydrogels.* Journal of Biomaterials Science, Polymer Edition, 2016. **27**(8): p. 721-742.

228. Mokarram, N., et al., *Effect of modulating macrophage phenotype on peripheral nerve repair.* Biomaterials, 2012. **33**(34): p. 8793-8801.

229. Spiller, K.L., et al., *Sequential delivery of immunomodulatory cytokines to facilitate the M1-to-M2 transition of macrophages and enhance vascularization of bone scaffolds.* Biomaterials, 2015. **37**: p. 194-207.

230. Chen, J., et al., *Macrophage phenotype switch by sequential action of immunomodulatory cytokines from hydrogel layers on titania nanotubes.* Colloids and Surfaces B: Biointerfaces, 2018. **163**: p. 336-345.

231. Udipi, K., et al., *Modification of inflammatory response to implanted biomedical materials in vivo by surface bound superoxide dismutase mimics.* J Biomed Mater Res, 2000. **51**(4): p. 549-60.

232. Zhong, Y. and R.V. Bellamkonda, *Dexamethasone-coated neural probes elicit attenuated inflammatory response and neuronal loss compared to uncoated neural probes.* Brain Research, 2007. **1148**: p. 15-27.

233. Song, I.-H., A.I. Caplan, and J.E. Dennis, *In vitro dexamethasone pretreatment enhances bone formation of human mesenchymal stem cells in vivo.* Journal of Orthopaedic Research, 2009. **27**(7): p. 916-921.

234. Tangtrongsup, S. and J.D. Kisiday, *Effects of Dexamethasone Concentration and Timing of Exposure on Chondrogenesis of Equine Bone Marrow–Derived Mesenchymal Stem Cells.* CARTILAGE, 2015. **7**(1): p. 92-103.

235. Haynesworth, S.E., M.A. Baber, and A.I. Caplan, *Cytokine expression by human marrow-derived mesenchymal progenitor cells in vitro: effects of dexamethasone and IL-1 alpha.* J Cell Physiol, 1996. **166**(3): p. 585-92.

236. Franchimont, D., et al., *Inhibition of Th1 Immune Response by Glucocorticoids: Dexamethasone Selectively Inhibits IL-12-Induced Stat4 Phosphorylation in T Lymphocytes1.* The Journal of Immunology, 2000. **164**(4): p. 1768-1774.

237. Patil, S.D., F. Papadmitrakopoulos, and D.J. Burgess, *Concurrent delivery of dexamethasone and VEGF for localized inflammation control and angiogenesis.* Journal of Controlled Release, 2007. **117**(1): p. 68-79.

238. O'Brien, E.M., G.E. Risser, and K.L. Spiller, *Sequential drug delivery to modulate macrophage behavior and enhance implant integration.* Advanced Drug Delivery Reviews, 2019. **149-150**: p. 85-94.

239. Yoon, P., et al., *Macrophage hypo-responsiveness to interferon-γ in aged mice is associated with impaired signaling through Jak-STAT.* Mechanisms of Ageing and Development, 2004. **125**(2): p. 137-143.

240. Placone, J.K. and A.J. Engler, *Recent Advances in Extrusion-Based 3D Printing for Biomedical Applications.* Advanced Healthcare Materials, 2018. **7**(8): p. 1701161.

241. Zhou, W., et al., *Fundamentals of Scanning Electron Microscopy (SEM)*, in *Scanning Microscopy for Nanotechnology: Techniques and Applications*, W. Zhou and Z.L. Wang, Editors. 2007, Springer New York: New York, NY. p. 1-40.

242. Leyva-Porras, C., et al., *Application of Differential Scanning Calorimetry (DSC) and Modulated Differential Scanning Calorimetry (MDSC) in Food and Drug Industries.* Polymers, 2020. **12**(1): p. 5.

243. *Vibrational Spectroscopy*, in *Solid State Properties of Pharmaceutical Materials*. 2017. p. 159-179.

244. Glassford, S.E., B. Byrne, and S.G. Kazarian, *Recent applications of ATR FTIR spectroscopy and imaging to proteins.* Biochim Biophys Acta, 2013. **1834**(12): p. 2849-58.

245. Fearn, S., *An Introduction to Time-of-Flight Secondary Ion Mass Spectrometry (ToF-SIMS) and its Application to Materials Science*. 2015, Morgan & Claypool Publishers.

246. Mains, J., C.G. Wilson, and A. Urquhart, *ToF-SIMS Analysis of Dexamethasone Distribution in the Isolated Perfused Eye.* Investigative Ophthalmology & Visual Science, 2011. **52**(11): p. 8413-8419.

247. Okamoto, T., et al., *Clonal heterogeneity in differentiation potential of immortalized human mesenchymal stem cells.* Biochemical and Biophysical Research Communications, 2002. **295**(2): p. 354-361.

248. Odell, I.D. and D. Cook, *Immunofluorescence techniques.* J Invest Dermatol, 2013. **133**(1): p. e4.

249. Wolf, D.E., *Fundamentals of fluorescence and fluorescence microscopy.* Methods Cell Biol, 2013. **114**: p. 69-97.

250. Hosseini, S., et al., *Step by Step with ELISA: Mechanism of Operation, Crucial Elements, Different Protocols, and Insights on Immobilization and Detection of Various Biomolecular Entities*, in *Enzyme-linked Immunosorbent Assay (ELISA): From A to Z*, S. Hosseini, et al., Editors. 2018, Springer Singapore: Singapore. p. 31-56.

251. Marmiroli, N. and E. Maestri. *Chapter 6 – Polymerase chain reaction (PCR)*. 2007.

252. Derveaux, S., J. Vandesompele, and J. Hellemans, *How to do successful gene expression analysis using real-time PCR.* Methods, 2010. **50**(4): p. 227-30.

253. Motamedian, S.R., et al., *Smart scaffolds in bone tissue engineering: A systematic review of literature.* World J Stem Cells, 2015. **7**(3): p. 657-68.

254. Hu, J. and P.X. Ma, *Nano-Fibrous Tissue Engineering Scaffolds Capable of Growth Factor Delivery.* Pharmaceutical Research, 2011. **28**(6): p. 1273-1281.

255. Wu, P. and D.W. Grainger, *Drug/device combinations for local drug therapies and infection prophylaxis.* Biomaterials, 2006. **27**(11): p. 2450-2467.

256. Bhatia, S. and S. Bhatia, *Natural polymers vs synthetic polymer.* Natural Polymer Drug Delivery Systems: Nanoparticles, Plants, and Algae, 2016: p. 95-118.

257. Sachlos, E. and J. Czernuszka, *Making tissue engineering scaffolds work. Review: the application of solid freeform fabrication technology*

to the production of tissue engineering scaffolds. Eur Cell Mater, 2003. **5**(29): p. 39-40.

258. Limongi, T., et al., *Drug Delivery Applications of Three-Dimensional Printed (3DP) Mesoporous Scaffolds.* Pharmaceutics, 2020. **12**(9).

259. Shafiee, A., *Design and Fabrication of Three-Dimensional Printed Scaffolds for Cancer Precision Medicine.* Tissue Engineering Part A, 2020. **26**(5-6): p. 305-317.

260. Roberge, C., et al., *BEPO®: Bioresorbable diblock mPEG-PDLLA and triblock PDLLA-PEG-PDLLA based in situ forming depots with flexible drug delivery kinetics modulation.* Journal of Controlled Release, 2020. **319**: p. 416-427.

261. Huang, X. and C.S. Brazel, *On the importance and mechanisms of burst release in matrix-controlled drug delivery systems.* Journal of Controlled Release, 2001. **73**(2): p. 121-136.

262. Zhou, Y. and X.Y. Wu, *Finite element analysis of diffusional drug release from complex matrix systems. I.: Complex geometries and composite structures1Presented in part at the Conference on Advances in Controlled Delivery, Controlled Release Society, Inc. Proceedings, p. 169–170 (August, 1996, Baltimore, USA), and at the Annual Meeting of the American Association of Pharmaceutical Scientists (October, 1996, Seattle, USA).1.* Journal of Controlled Release, 1997. **49**(2): p. 277-288.

263. Ekenseair, A.K., F.K. Kasper, and A.G. Mikos, *Perspectives on the interface of drug delivery and tissue engineering.* Adv Drug Deliv Rev, 2013. **65**(1): p. 89-92.

264. Fu, Y. and W.J. Kao, *Drug release kinetics and transport mechanisms of non-degradable and degradable polymeric delivery systems.* Expert Opin Drug Deliv, 2010. **7**(4): p. 429-44.

265. Mahmoudi, M., et al., *Superparamagnetic Iron Oxide Nanoparticles with Rigid Cross-linked Polyethylene Glycol Fumarate Coating for Application in Imaging and Drug Delivery.* The Journal of Physical Chemistry C, 2009. **113**(19): p. 8124-8131.

266. Zupančič, Š., et al., *Long-Term Sustained Ciprofloxacin Release from PMMA and Hydrophilic Polymer Blended Nanofibers.* Molecular Pharmaceutics, 2016. **13**(1): p. 295-305.

267. Thote, A.J., et al., *Reduction in the Initial-Burst Release by Surface Crosslinking of PLGA Microparticles Containing Hydrophilic or Hydrophobic Drugs.* Drug Development and Industrial Pharmacy, 2005. **31**(1): p. 43-57.

268. Macdonald, M.L., et al., *Tissue integration of growth factor-eluting layer-by-layer polyelectrolyte multilayer coated implants.* Biomaterials, 2011. **32**(5): p. 1446-1453.

269. Tang, T.O., et al., *Extrusion and 3D printing of novel lipid-polymer blends for oral drug applications.* Biomaterials Advances, 2022. **137**: p. 212818.

270. Alhijjaj, M., P. Belton, and S. Qi, *An investigation into the use of polymer blends to improve the printability of and regulate drug release from pharmaceutical solid dispersions prepared via fused deposition modeling (FDM) 3D printing.* European Journal of Pharmaceutics and Biopharmaceutics, 2016. **108**: p. 111-125.

271. Cano-Vicent, A., et al., *Fused deposition modelling: Current status, methodology, applications and future prospects.* Additive Manufacturing, 2021. **47**: p. 102378.

272. Lee, E.S., et al., *In vitro study of lysozyme in poly(lactide-co-glycolide) microspheres with sucrose acetate isobutyrate.* European Journal of Pharmaceutical Sciences, 2006. **29**(5): p. 435-441.

273. Lu, Y., Y. Yu, and X. Tang, *Sucrose acetate isobutyrate as an In Situ forming system for sustained risperidone release.* Journal of Pharmaceutical Sciences, 2007. **96**(12): p. 3252-3262.

274. Khan, S., et al., *Nanocrystal preparation: low-energy precipitation method revisited.* Crystal Growth & Design, 2013. **13**(7): p. 2766-2777.

275. Gupta, B., Geeta, and A.R. Ray, *Preparation of poly(ε-caprolactone)/poly(ε-caprolactone-co-lactide) (PCL/PLCL) blend filament by melt spinning.* Journal of Applied Polymer Science, 2012. **123**(4): p. 1944-1950.

276. Scoutaris, N., et al., *ToF-SIMS analysis of chemical heterogenities in inkjet micro-array printed drug/polymer formulations.* Journal of Materials Science: Materials in Medicine, 2012. **23**: p. 385-391.

277. Shrivastava, A. and V.B. Gupta, *Methods for the determination of limit of detection and limit of quantitation of the analytical methods.* Chron. Young Sci, 2011. **2**(1): p. 21-25.

278. *5 - Mathematical models of drug release*, in *Strategies to Modify the Drug Release from Pharmaceutical Systems*, M.L. Bruschi, Editor. 2015, Woodhead Publishing. p. 63-86.

279. Zare, M., et al., *Effect of additives on release profile of leuprolide acetate in an in situ forming controlled-release system: In vitro study.* Journal of Applied Polymer Science, 2008. **107**(6): p. 3781-3787.

280. Xue, L., J. Zhang, and Y. Han, *Phase separation induced ordered patterns in thin polymer blend films.* Progress in Polymer Science, 2012. **37**(4): p. 564-594.

281. Ahmad Khairi, M.H., et al., *The field-dependent complex modulus of magnetorheological elastomers consisting of sucrose acetate*

isobutyrate ester. Journal of Intelligent Material Systems and Structures, 2017. **28**(14): p. 1993-2004.

282. Zhong, Y., Z. Zhu, and S.-Q. Wang, *Synthesis and rheological properties of polystyrene/layered silicate nanocomposite.* Polymer, 2005. **46**(9): p. 3006-3013.

283. Daghrery, A., et al., *Electrospinning of dexamethasone/cyclodextrin inclusion complex polymer fibers for dental pulp therapy.* Colloids and Surfaces B: Biointerfaces, 2020. **191**: p. 111011.

284. Yang, J.Y., B.T. Jung, and D.H. Suh, *A simple attempt to change the solubility of polyimide by physical inclusion with β-cyclodextrin and its derivatives.* Polymer, 2001. **42**(20): p. 8349-8354.

285. Pérez-González, G.L., et al., *Development, characterization, and in vitro assessment of multilayer mucoadhesive system containing dexamethasone sodium phosphate.* International Journal of Polymeric Materials and Polymeric Biomaterials, 2021. **70**(18): p. 1316-1328.

286. Karolewicz, B., et al., *Thermal, spectroscopic, and dissolution studies of ketoconazole–Pluronic F127 system.* Journal of Thermal Analysis and Calorimetry, 2014. **115**(3): p. 2487-2493.

287. Seema, S. and M. Datta, *Organoclay Pluronic F68–montmorillonite, as a sustained release drug delivery vehicle for propranolol hydrochloride.* Eur. Chem. Bull, 2014. **3**(6): p. 593-604.

288. Song, H.-M. and J.I. Zink, *Ag (i)-mediated self-assembly of anisotropic rods and plates in the surfactant mixture of CTAB and Pluronics.* RSC advances, 2019. **9**(8): p. 4380-4389.

289. Roy Choudhury, S., et al., *Evaluation of physicochemical properties, and antimicrobial efficacy of monoclinic sulfur-nanocolloid.* Journal of nanoparticle research, 2013. **15**: p. 1-11.

290. Gonçalves, C., et al., *Ionic liquid-mediated processing of SAIB-Chitin scaffolds.* ACS Sustainable Chemistry & Engineering, 2020. **8**(9): p. 3986-3994.

291. Wu, J., et al., *Mechanism of a long-term controlled drug release system based on simple blended electrospun fibers.* Journal of Controlled Release, 2020. **320**: p. 337-346.

292. Gao, Y., et al., *In Vitro Release Kinetics of Antituberculosis Drugs from Nanoparticles Assessed Using a Modified Dissolution Apparatus.* BioMed Research International, 2013. **2013**: p. 136590.

293. Mirzaeei, S., et al. *Metronidazole- and Amoxicillin-Loaded PLGA and PCL Nanofibers as Potential Drug Delivery Systems for the Treatment of Periodontitis: In Vitro and In Vivo Evaluations*. Biomedicines, 2021. **9**, DOI: 10.3390/biomedicines9080975.

294. Kim, D.H. and D.C. Martin, *Sustained release of dexamethasone from hydrophilic matrices using PLGA nanoparticles for neural drug delivery.* Biomaterials, 2006. **27**(15): p. 3031-7.

295. Rogovina, L.Z., V.G. Vasil'ev, and E.E. Braudo, *Definition of the concept of polymer gel.* Polymer Science Series C, 2008. **50**(1): p. 85-92.

296. Malda, J., et al., *25th Anniversary Article: Engineering Hydrogels for Biofabrication.* Advanced Materials, 2013. **25**(36): p. 5011-5028.

297. Melchels, F.P.W., et al., *Additive manufacturing of tissues and organs.* Progress in Polymer Science, 2012. **37**(8): p. 1079-1104.

298. Jungst, T., et al., *Strategies and Molecular Design Criteria for 3D Printable Hydrogels.* Chemical Reviews, 2016. **116**(3): p. 1496-1539.

299. Yuk, H. and X. Zhao, *A New 3D Printing Strategy by Harnessing Deformation, Instability, and Fracture of Viscoelastic Inks.* Advanced Materials, 2018. **30**(6): p. 1704028.

300. Guo, S.-Z., et al., *Solvent-Cast Three-Dimensional Printing of Multifunctional Microsystems.* Small, 2013. **9**(24): p. 4118-4122.

301. Zhu, Z. and S.Q. Wang, *Experimental characterization of extrudate swell behavior of linear polybutadiene.* Journal of Rheology, 2004. **48**(3): p. 571-589.

302. Okor, R.S., *Influence of hydrophilic character of plasticizer and polymer on certain film properties.* International Journal of Pharmaceutics, 1982. **11**(1): p. 1-9.

303. Park, T.G., S. Cohen, and R. Langer, *Poly (L-lactic acid)/pluronic blends: characterization of phase separation behavior, degradation, and morphology and use as protein-releasing matrixes.* Macromolecules, 1992. **25**(1): p. 116-122.

304. Tipduangta, P., et al., *Electrospun Polymer Blend Nanofibers for Tunable Drug Delivery: The Role of Transformative Phase Separation on Controlling the Release Rate.* Molecular Pharmaceutics, 2016. **13**(1): p. 25-39.

305. Chi, M.-S., *Compatibility of cross-linked polymers with plasticizers by glass transition temperature measurement and swelling tests.* Journal of Polymer Science: Polymer Chemistry Edition, 1981. **19**(7): p. 1767-1779.

306. Olabisi, O., L. Robeson, and M. Shaw, *Polymer-Polymer Miscibility Acad.* Press, NY, 1979: p. 126.

307. Martuscelli, E., *Polymer Blends: Processing, Morphology, and Properties*. 2012: Springer Science & Business Media.

308. Li, X., et al., *Composite PLA/PEG/nHA/Dexamethasone Scaffold Prepared by 3D Printing for Bone Regeneration.* Macromolecular Bioscience, 2018. **18**(6): p. 1800068.

309. Van Krevelen, D.W. and K. Te Nijenhuis, *Properties of polymers: their correlation with chemical structure; their numerical estimation and prediction from additive group contributions*. 2009: Elsevier.

310. Yoon, J.J., J.H. Kim, and T.G. Park, *Dexamethasone-releasing biodegradable polymer scaffolds fabricated by a gas-foaming/salt-leaching method.* Biomaterials, 2003. **24**(13): p. 2323-2329.

311. Zilberman, M., *Dexamethasone loaded bioresorbable films used in medical support devices: Structure, degradation, crystallinity and drug release.* Acta Biomaterialia, 2005. **1**(6): p. 615-624.

312. Karavelidis, V., et al., *Evaluating the effects of crystallinity in new biocompatible polyester nanocarriers on drug release behavior.* Int J Nanomedicine, 2011. **6**: p. 3021-32.

313. Jeong, J.-C., J. Lee, and K. Cho, *Effects of crystalline microstructure on drug release behavior of poly(ε-caprolactone) microspheres.* Journal of Controlled Release, 2003. **92**(3): p. 249-258.

314. de Castro, K.C., et al., *Pluronic® triblock copolymer-based nanoformulations for cancer therapy: A 10-year overview.* Journal of Controlled Release, 2023. **353**: p. 802-822.

315. Barakh Ali, S.F., et al., *Development of Abuse-Deterrent Formulations Using Sucrose Acetate Isobutyrate.* AAPS PharmSciTech, 2020. **21**(3): p. 99.

316. Zhang, T., et al., *Electrosprayed minocycline hydrochloride-loaded microsphere/SAIB hybrid depot for periodontitis treatment.* Drug Deliv, 2021. **28**(1): p. 620-633.

317. Zhang, D., et al., *Effect of microsphere size on the drug release and experimental characterization of an electrospun naringin loaded microsphere/sucrose acetate isobutyrate (SAIB) depot.* Polymers for Advanced Technologies, 2020. **31**: p. 1110-1121.

318. Wickström, H., et al., *Inkjet Printing of Drug-Loaded Mesoporous Silica Nanoparticles-A Platform for Drug Development.* Molecules, 2017. **22**(11).

319. Beran, T., et al., *Nozzle clogging factors during fused filament fabrication of spherical particle filled polymers.* Additive Manufacturing, 2018. **23**: p. 206-214.

320. Croom, B.P., et al., *Mechanics of nozzle clogging during direct ink writing of fiber-reinforced composites.* Additive Manufacturing, 2021. **37**: p. 101701.

321. Luebbert, C., F. Huxoll, and G. Sadowski *Amorphous-Amorphous Phase Separation in API/Polymer Formulations*. Molecules, 2017. **22**, DOI: 10.3390/molecules22020296.

322. Aytac, Z. and T. Uyar, *Core-shell nanofibers of curcumin/cyclodextrin inclusion complex and polylactic acid: Enhanced water solubility and slow release of curcumin.* International Journal of Pharmaceutics, 2017. **518**(1): p. 177-184.

323. Rai, B., et al., *Novel PCL-based honeycomb scaffolds as drug delivery systems for rhBMP-2.* Biomaterials, 2005. **26**(17): p. 3739-3748.

324. Munj, H.R., J.J. Lannutti, and D.L. Tomasko, *Understanding drug release from PCL/gelatin electrospun blends.* Journal of Biomaterials Applications, 2016. **31**(6): p. 933-949.

325. Abdollahi Boraei, S.B., et al., *Capability of core-sheath polyvinyl alcohol–polycaprolactone emulsion electrospun nanofibrous scaffolds in releasing strontium ranelate for bone regeneration.* Biomedical Materials, 2021. **16**(2): p. 025009.

326. Bose, S., M. Roy, and A. Bandyopadhyay, *Recent advances in bone tissue engineering scaffolds.* Trends in Biotechnology, 2012. **30**(10): p. 546-554.

327. Prasopthum, A., et al., *Three dimensional printed degradable and conductive polymer scaffolds promote chondrogenic differentiation of chondroprogenitor cells.* Biomaterials Science, 2020. **8**(15): p. 4287-4298.

328. Prasopthum, A., K.M. Shakesheff, and J. Yang, *Direct three-dimensional printing of polymeric scaffolds with nanofibrous topography.* Biofabrication, 2018. **10**(2): p. 025002.

329. Pajarinen, J., et al., *Mesenchymal stem cell-macrophage crosstalk and bone healing.* Biomaterials, 2019. **196**: p. 80-89.

330. Shin, R.L.-Y., et al., *The crosstalk between mesenchymal stem cells and macrophages in bone regeneration: a systematic review.* Stem cells international, 2021. **2021**.

331. Schell, H., et al., *The haematoma and its role in bone healing.* J Exp Orthop, 2017. **4**(1): p. 5.

332. Bridges, A.W., et al., *Chronic inflammatory responses to microgel-based implant coatings.* Journal of Biomedical Materials Research Part A, 2010. **94A**(1): p. 252-258.

333. Vacanti, N.M., et al., *Localized Delivery of Dexamethasone from Electrospun Fibers Reduces the Foreign Body Response.* Biomacromolecules, 2012. **13**(10): p. 3031-3038.

334. Zhou, W., et al., *Dual-Targeted Nanoplatform Regulating the Bone Immune Microenvironment Enhances Fracture Healing.* ACS Applied Materials & Interfaces, 2021. **13**(48): p. 56944-56960.

335. Chan, J.K., et al., *Low-dose TNF augments fracture healing in normal and osteoporotic bone by up-regulating the innate immune response.* EMBO Molecular Medicine, 2015. **7**(5): p. 547-561.

336. Alexander, K.A., et al., *Osteal macrophages promote in vivo intramembranous bone healing in a mouse tibial injury model.* Journal of Bone and Mineral Research, 2011. **26**(7): p. 1517-1532.

337. Lu, L.Y., et al., *Pro-inflammatory M1 macrophages promote Osteogenesis by mesenchymal stem cells via the COX-2-prostaglandin E2 pathway.* Journal of Orthopaedic Research, 2017. **35**(11): p. 2378-2385.

338. Nathan, K., et al., *Precise immunomodulation of the M1 to M2 macrophage transition enhances mesenchymal stem cell osteogenesis and differs by sex.* Bone & Joint Research, 2019. **8**(10): p. 481-488.

339. Sok, M.C.P., et al., *Dual delivery of IL-10 and AT-RvD1 from PEG hydrogels polarize immune cells towards pro-regenerative phenotypes.* Biomaterials, 2021. **268**: p. 120475.

340. Farto-Vaamonde, X., et al., *Post-manufacture loading of filaments and 3D printed PLA scaffolds with prednisolone and dexamethasone for tissue regeneration applications.* European Journal of Pharmaceutics and Biopharmaceutics, 2019. **141**: p. 100-110.

341. Kósa, J.P., et al., *The protective role of bone morphogenetic protein-8 in the glucocorticoid-induced apoptosis on bone cells.* Bone, 2011. **48**(5): p. 1052-1057.

342. Lima, A., et al., *Free and copolymerized γ-cyclodextrins regulate the performance of dexamethasone-loaded dextran microspheres for bone regeneration.* Journal of Materials Chemistry B, 2014. **2**(30): p. 4943-4956.

343. Abuawad, A., et al., *Metabolic characterisation of THP-1 macrophage polarisation using LC–MS-based metabolite profiling.* Metabolomics, 2020. **16**(3): p. 33.

344. Wu, C.-H., et al., *Nitric Oxide Modulates Pro- and Anti-inflammatory Cytokines in Lipopolysaccharide-Activated Macrophages.* Journal of Trauma and Acute Care Surgery, 2003. **55**(3).

345. Oswald, I.P., et al., *Interleukin 10 inhibits macrophage microbicidal activity by blocking the endogenous production of tumor necrosis factor alpha required as a costimulatory factor for interferon gamma-induced activation.* Proceedings of the National Academy of Sciences, 1992. **89**(18): p. 8676-8680.

346. Langenbach, F. and J. Handschel, *Effects of dexamethasone, ascorbic acid and β-glycerophosphate on the osteogenic differentiation of stem cells in vitro.* Stem Cell Research & Therapy, 2013. **4**(5): p. 117.

347. Osta, B., G. Benedetti, and P. Miossec, *Classical and Paradoxical Effects of TNF-α on Bone Homeostasis.* Front Immunol, 2014. **5**: p. 48.

348. Li, C., et al., *Paracrine effect of inflammatory cytokine-activated bone marrow mesenchymal stem cells and its role in osteoblast function.* J Biosci Bioeng, 2016. **121**(2): p. 213-9.

349. Chen, Z., et al., *Osteogenic differentiation of bone marrow MSCs by β-tricalcium phosphate stimulating macrophages via BMP2 signalling pathway.* Biomaterials, 2014. **35**(5): p. 1507-1518.

350. Deng, Y., et al., *Umbilical cord-derived mesenchymal stem cells instruct monocytes towards an IL10-producing phenotype by secreting IL6 and HGF.* Scientific reports, 2016. **6**(1): p. 1-9.

351. Rostam, H.M., et al., *The impact of surface chemistry modification on macrophage polarisation.* Immunobiology, 2016. **221**(11): p. 1237-1246.

352. Wu, Z., et al., *Overexpression of fucosyltransferase 8 reverses the inhibitory effect of high-dose dexamethasone on osteogenic response of MC3T3-E1 preosteoblasts.* PeerJ, 2021. **9**: p. e12380.

353. Ishida, Y. and J.N.M. Heersche, *Glucocorticoid-Induced Osteoporosis: Both In Vivo and In Vitro Concentrations of Glucocorticoids Higher*

Than Physiological Levels Attenuate Osteoblast Differentiation. Journal of Bone and Mineral Research, 1998. **13**(12): p. 1822-1826.

354. Pountos, I., et al., *NSAIDs inhibit bone healing through the downregulation of TGF-β3 expression during endochondral ossification.* Injury, 2021. **52**(6): p. 1294-1299.

355. O'Connor, J.P., et al., *A comparison of the effects of ibuprofen and rofecoxib on rabbit fibula osteotomy healing.* Acta orthopaedica, 2009. **80**(5): p. 597-605.

356. Barrera, P., et al., *Synovial macrophage depletion with clodronate-containing liposomes in rheumatoid arthritis.* Arthritis & Rheumatism, 2000. **43**(9): p. 1951-1959.

357. Wang, J., et al., *M2 macrophages contribute to osteogenesis and angiogenesis on nanotubular TiO2 surfaces.* Journal of Materials Chemistry B, 2017. **5**(18): p. 3364-3376.

358. Loi, F., et al., *The effects of immunomodulation by macrophage subsets on osteogenesis in vitro.* Stem Cell Research & Therapy, 2016. **7**(1): p. 15.

359. Champagne, C.M., et al., *Macrophage cell lines produce osteoinductive signals that include bone morphogenetic protein-2.* Bone, 2002. **30**(1): p. 26-31.

360. Song, N., M. Scholtemeijer, and K. Shah, *Mesenchymal Stem Cell Immunomodulation: Mechanisms and Therapeutic Potential.* Trends Pharmacol Sci, 2020. **41**(9): p. 653-664.

361. Manferdini, C., et al., *Adipose stromal cells mediated switching of the pro-inflammatory profile of M1-like macrophages is facilitated by PGE2: in vitro evaluation.* Osteoarthritis Cartilage, 2017. **25**(7): p. 1161-1171.

362. Németh, K., et al., *Bone marrow stromal cells attenuate sepsis via prostaglandin E(2)-dependent reprogramming of host macrophages*

to increase their interleukin-10 production. Nat Med, 2009. **15**(1): p. 42-9.

363. Abumaree, M.H., et al., *Human Placental Mesenchymal Stem Cells (pMSCs) Play a Role as Immune Suppressive Cells by Shifting Macrophage Differentiation from Inflammatory M1 to Anti-inflammatory M2 Macrophages.* Stem Cell Reviews and Reports, 2013. **9**(5): p. 620-641.

364. Waterman, R.S., et al., *A New Mesenchymal Stem Cell (MSC) Paradigm: Polarization into a Pro-Inflammatory MSC1 or an Immunosuppressive MSC2 Phenotype.* PLOS ONE, 2010. **5**(4): p. e10088.

365. Fernando, M.R., et al., *The Pro-Inflammatory Cytokine, Interleukin-6, Enhances the Polarization of Alternatively Activated Macrophages.* PLOS ONE, 2014. **9**(4): p. e94188.

366. Xie, Z., et al., *Interleukin-6/interleukin-6 receptor complex promotes osteogenic differentiation of bone marrow-derived mesenchymal stem cells.* Stem Cell Res Ther, 2018. **9**(1): p. 13.

367. Glass, G.E., et al., *TNF-α promotes fracture repair by augmenting the recruitment and differentiation of muscle-derived stromal cells.* Proceedings of the National Academy of Sciences, 2011. **108**(4): p. 1585-1590.

368. Bryers, J.D., C.M. Giachelli, and B.D. Ratner, *Engineering biomaterials to integrate and heal: The biocompatibility paradigm shifts.* Biotechnology and Bioengineering, 2012. **109**(8): p. 1898-1911.

369. Ma, Q.-L., et al., *Improved implant osseointegration of a nanostructured titanium surface via mediation of macrophage polarization.* Biomaterials, 2014. **35**(37): p. 9853-9867.

370. Graney, P.L., et al., *In vitro response of macrophages to ceramic scaffolds used for bone regeneration.* Journal of The Royal Society Interface, 2016. **13**(120): p. 20160346.

371. Chen, Z., et al., *The effect of osteoimmunomodulation on the osteogenic effects of cobalt incorporated β-tricalcium phosphate.* Biomaterials, 2015. **61**: p. 126-138.

7. Chapter Seven: Appendices

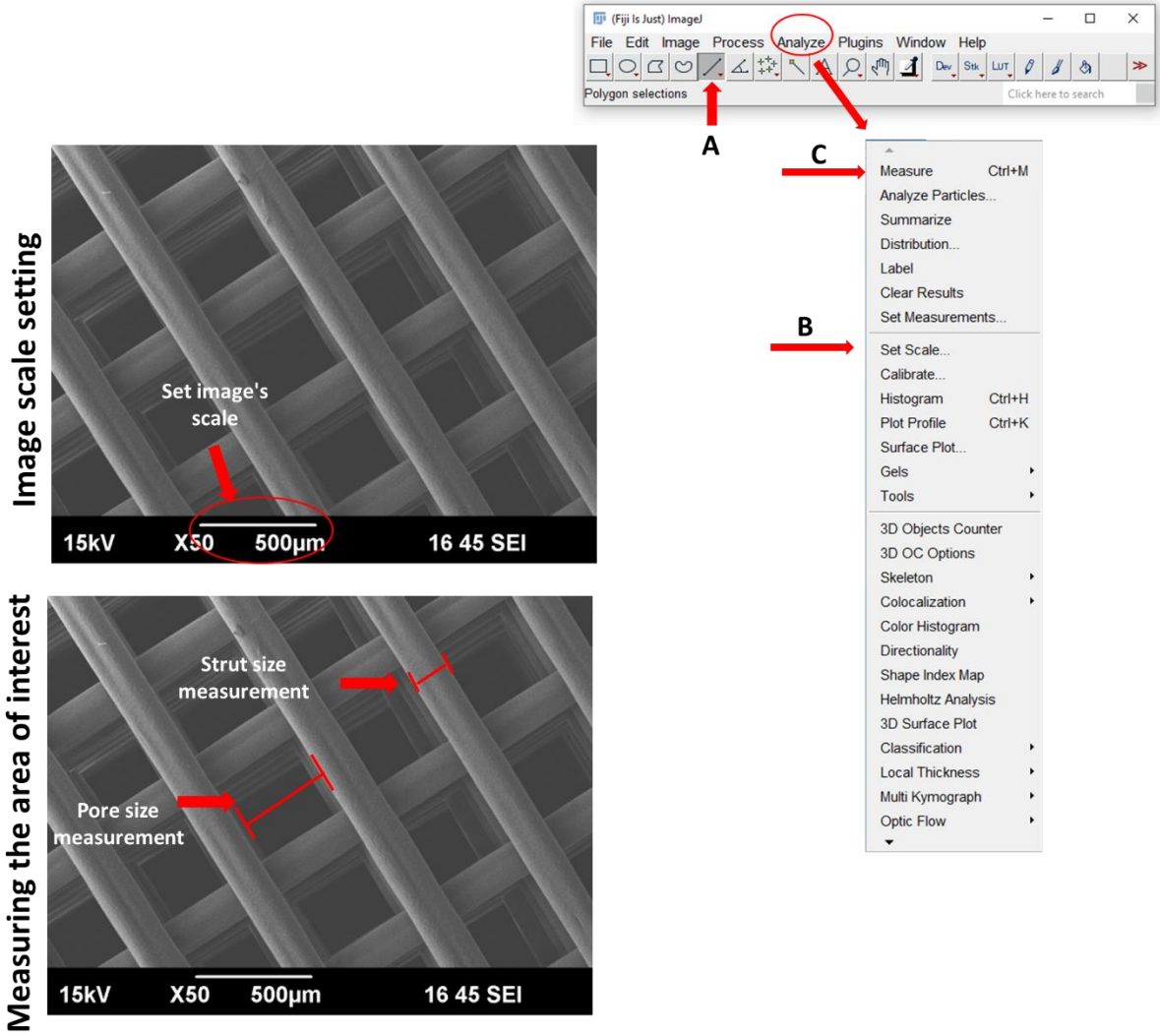


Figure 7-1: Example of image analysis by imageJ. (A) Straight line drawing function to draw a line on the selected area. (B) set scale function to set image scale. (C) Measure function to execute measurement for the selected area.

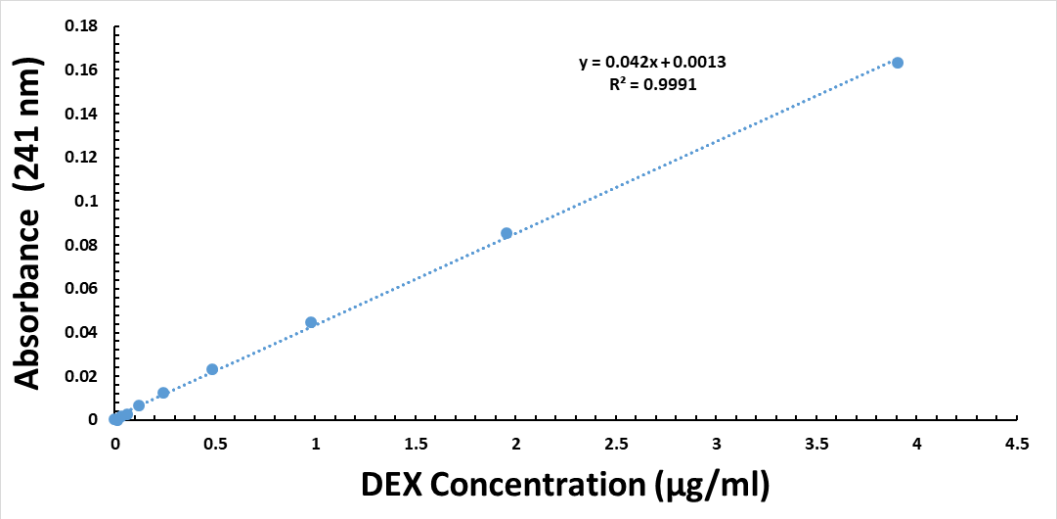


Figure 7-2: dexamethasone-cyclodextrin standard curve prepared in PBS (n=3).

Table 7-1: Drug lodging in all 3D-prented scaffolds loaded with an initial concentration of 8 mg of dexamethasone.

3D oriented scaffolds	scaffolds weight (mg)	Drug loading (mg)	Drug loading (µM)
PCL/DEX-CYD (17% wt/wt)	125.85 ± 1.47	0.221 ± 0.003	220.78 ±2.57
PCL/F127 (70:30) (17% wt/wt)	234.13 ± 23.46	0.411 ±0.04	410.76 ±41.17
PCL/F127 (60:40)(17% wt/wt)	244 ± 10.46	0.428 ±0.02	428.07 ±18.35
PCL/F68 (70:30)(17% wt/wt)	137.3 ±0.95	0.241 ±0.002	240.88 ±1.67
PCL/F68 (60:40)(17% wt/wt)	261.93 ±30.33	0.460 ±0.05	459.53 ±53.21
PCL/L31 (70:30)(17% wt/wt)	194.95 ±38.68	0.342 ±0.07	342.02 ±67.86
PCL/L31 (60:40)(17% wt/wt)	276.85 ±19.04	0.486 ±0.03	485.71 ±33.40
PCL/SPAN80 (70:30)(17% wt/wt)	277.52 ±13.56	0.487 ±0.02	486.88 ±23.95
PCL/SPAN80 (60:40)(17% wt/wt)	372.96 ±9.90	0.654 ±0.02	654.31 ±17.38
PCL/SAIB (70:30)(17% wt/wt)	271.13 ±9.91	0.476 ±0.01	475.67 ±17.38
PCL/SAIB (60:40)(17% wt/wt)	230 ±3.80	0.404 ±0.01	403.51 ±6.66
PCL/DEX-MC (0.17% wt/wt)	275.07 ±4.50	0.483 ±0.01	482.57 ±7.9
PCL/DEX-MC (0.7% wt/wt)	182.53 ±0.67	1.28 ±0.005	1280.94 ±4.68
PCL/SAIB (60:40)DEX-MC (0.7% wt/wt)	210.62 ±2.77	1.48 ±0.02	1478.06 ±19.47

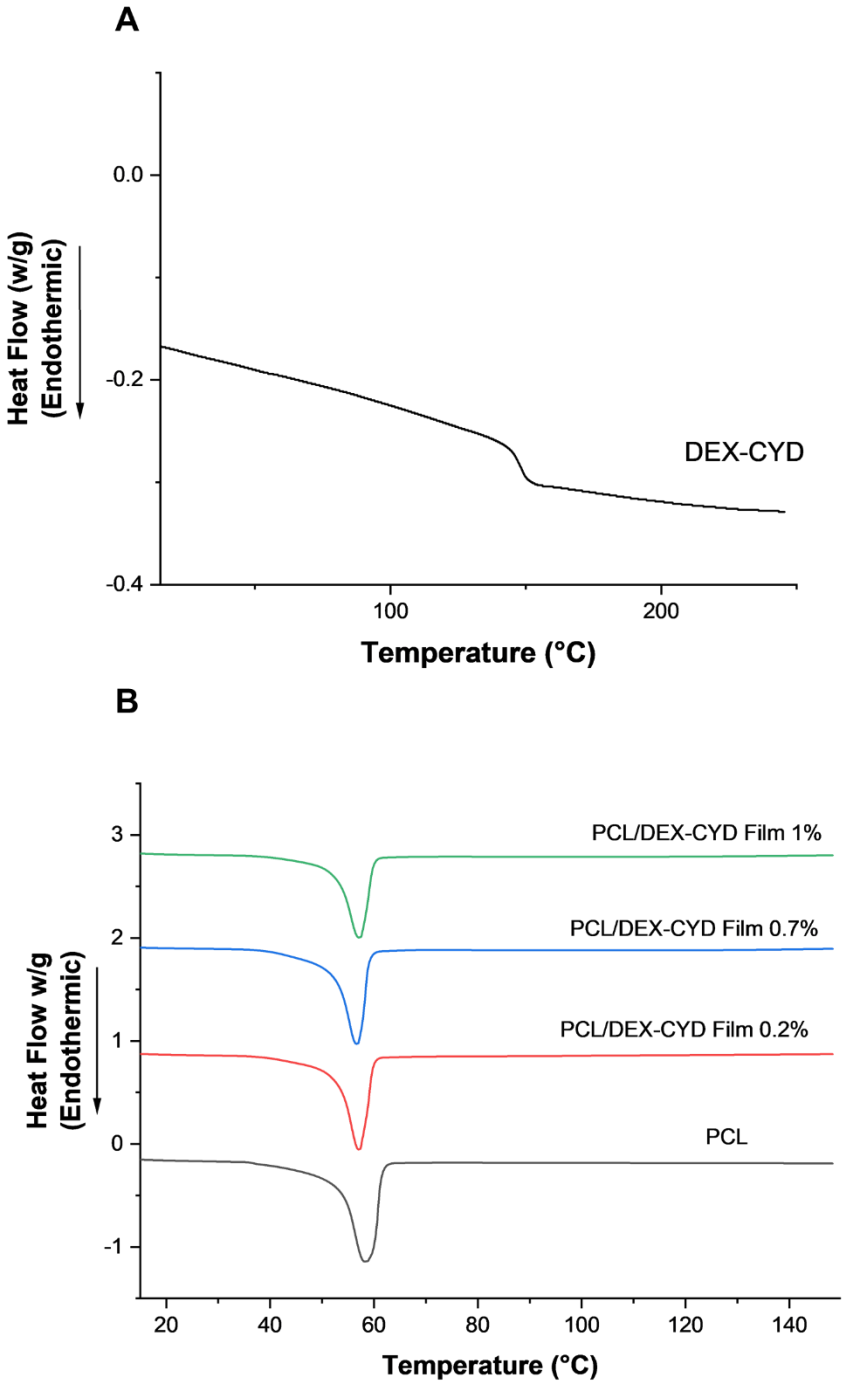


Figure 7-3: DSC thermograph. (**A**) DEX-CYD, (**B**) PCL with 0.05%, 0.1%, and 0.25% wt/wt DEX-CYD.

Table 7-2: Thermal properties of PCL loaded with different concentrations of DEX-CYD: T_m: melting temperature; ΔH_m: the enthalpy of melting; X_c: the degree of crystallinity; ND: Not Detected. (n=1).

2D PCL films	T_g (°C)	T_m (°C)	ΔH_m (J/g)	X_c (%)
PCL	45.89	57.53	65.450	46.92
PCL/DEX-CYD (0.2% wt/wt)	44.89	56.98	98.167	70.37
PCL/DEX-CYD (0.7% wt/wt)	44.94	56.29	119.40	85.59
PCL/DEX-CYD (1% wt/wt)	44.67	57.46	123.14	88.27

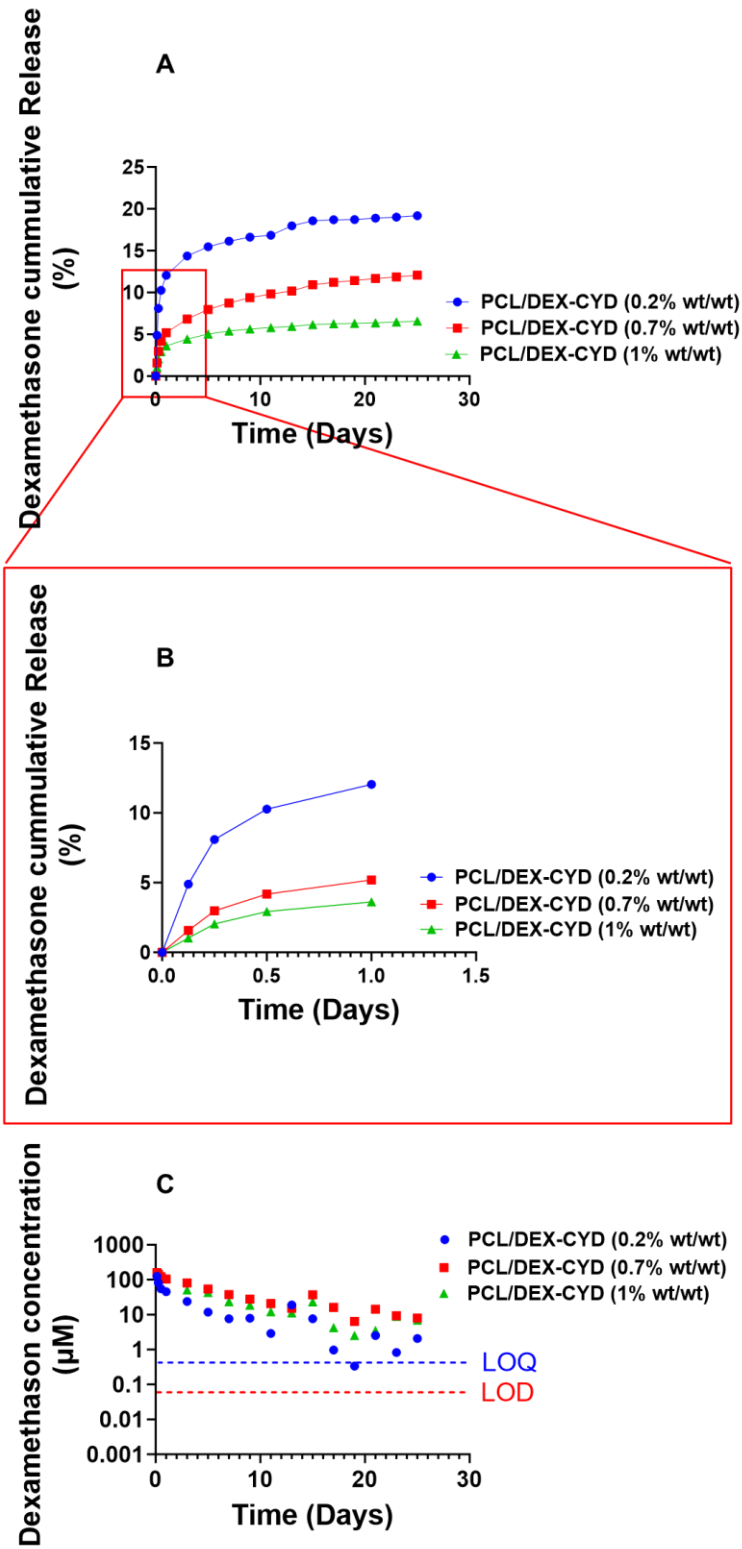


Figure 7-4: cumulative and actual release of dexamethasone from 2D PCL films incubated in 10 ml of PBS. (**A**) Cumulative release percentage of 2D PCL films loaded with 0.2%, 0.7%, and 1% wt/wt of dexamethasone-cyclodextrin over 25 days. PBS was collected at 2, 4, 6,

12, 24 h, and every 2 days. (**B**) cumulative release percentage over 24 h. (**C**) Actual release in µM showing the limit of detection (LOD) and limit of quantification (LOQ) of the released dexamethasone. All data represent the mean ± SD (n = 3).

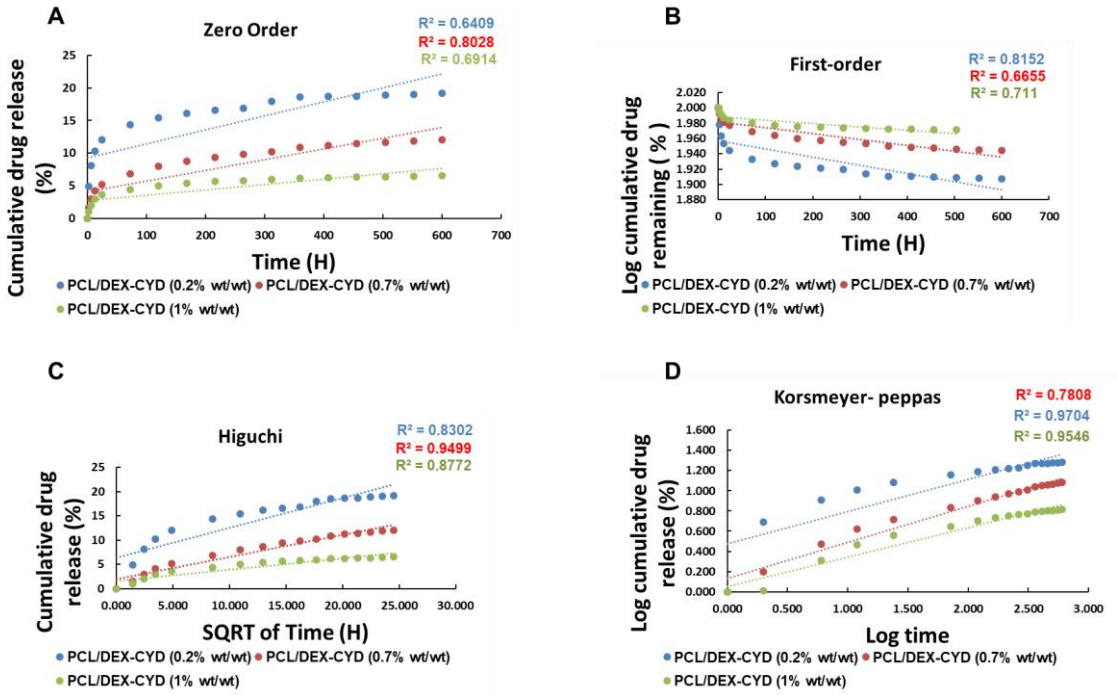


Figure 7-5: dexamethasone release kinetics of 2D PCL films loaded with various concentrations of dexamethasone (DEX-CYD) 0.2% wt/wt (blue), 0.7% wt/wt (green), and 1% wt/wt (red), fitted to various models: **A**) Zero-order, **B**) First-order, **C**) Higuchi model, and **D**) Korsmeyer-Peppas.

Table 7-3: R^2 drug release kinetics values for all 2D PCL films.

2D PCL films	Zero-order	First order	Higuchi	KMP	n value KPM
PCL/DEX-CYD (0.2% wt/wt)	0.64	0.82	0.83	0.78	0.32
PCL/DEX-CYD (0.7% wt/wt)	0.8	0.67	0.95	0.97	0.36
PCL/DEX-CYD (1% wt/wt)	0.69	0.71	0.88	0.95	0.29

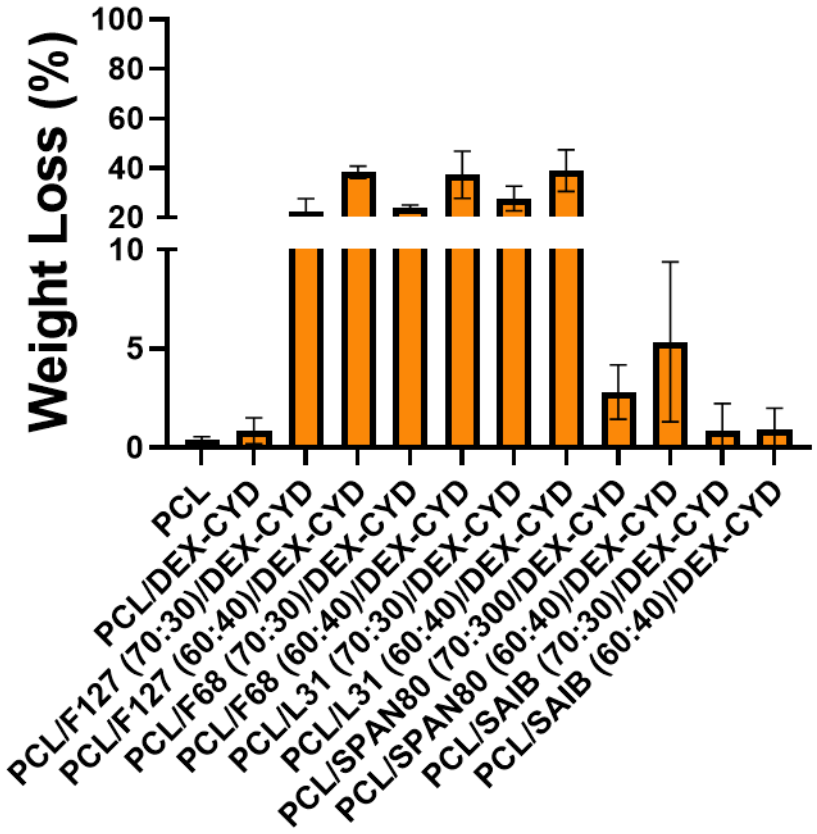


Figure 7-6:3D printed scaffold mass loss after 35 days. All data represent ±SD (n=3).

***Weight loss* (%) = W_1-W_2/W_1X100**

Where W_1 is the dried weight of the 3D printed scaffold before the controlled release, W_2 is the dried weight of the scaffold after the controlled release.

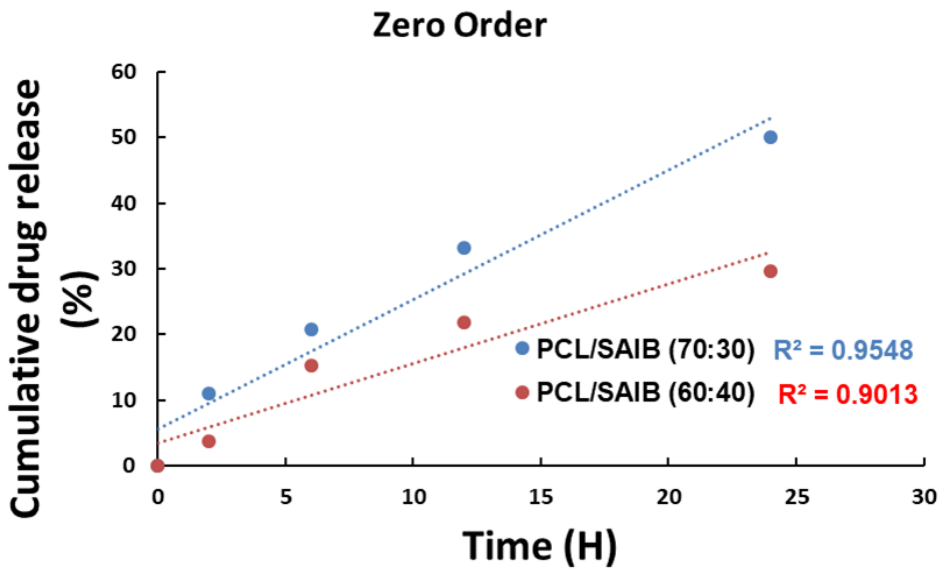


Figure 7-7: dexamethasone release kinetics of 3D printed PCL scaffolds loaded with 0.17% wt/wt of dexamethasone. PCL/SAIB (70:30) (blue), and PCL/SAIB (60:40) (red), fitted the zero-order model at 24h.

Table 7-4: media composition for αMEM and RPMI. Chemicals in (Red) are presented only in αMEM. Chemicals in (Green) are presented only in RPMI. Chemicals in (Black) are presented in both media with variable concentrations. All component concentrations are measured in (mg/L).

Medium	αMEM	RPMI
Glycine	50	10
L-Alanine	25	
L-Arginine hydrochloride	126	200
L-Asparagine-H_2O	50	50
L-Aspartic acid	30	20
L-Cysteine hydrochloride-H_2O	100	65
L-Cystine 2HCl	31	65
L-Glutamic Acid	75	20
L-Glutamine	292	300
L-Histidine	31	15
L-Histidine hydrochloride-H_2O	42	
L-Isoleucine	52	50
L-Leucine	52	50
L-Lysine hydrochloride	73	40
L-Methionine	15	15

L-Phenylalanine	32	15
L-Proline	40	20
L-Serine	25	30
L-Threonine	48	20
L-Tryptophan	10	5
L-Tyrosine disodium salt dihydrate	52	29
L-Valine	46	20
Ascorbic acid	50	
Biotin	0.1	0.2
Choline chloride	1	3
D-Calcium pantothenate	1	0.25
Folic Acid	1	1
Niacinamide	1	1
Para-Aminobenzoic Acid		1
Pyridoxal hydrochloride	1	1
Riboflavin	0.1	0.2
Thiamine hydrochloride	1	1
Vitamin B12	1.36	0.005
i-Inositol	2	35
Calcium Chloride ($CaCl_2$) (anhyd.)	200	
Calcium nitrate (Ca(NO3)2 4H2O)		100
Ferric Nitrate (Fe(NO3)3"9H_2O)		
Magnesium Sulfate ($MgSO_4$) (anhyd.)	97.67	48.84
Potassium Chloride (KCl)	400	400
Sodium Bicarbonate ($NaHCO_3$)	2200	2000
Sodium Chloride (NaCl)	6800	6000
Sodium Phosphate monobasic (NaH_2PO_4-H_2O)	140	
Sodium Phosphate dibasic (Na_2HPO_4) anhydrous		800
D-Glucose (Dextrose)	1000	2000
Lipoic Acid	0.2	
Phenol Red	10	5
Sodium Pyruvate	110	

Table 7-5: The correspondent concentration of dexamethasone from PCL/SAIB (60:40) 3D printed scaffolds in basal RPMI media was measured by UV-vis. All data represent the mean ±SD (n=3).

Release day	Correspondent Conc. in µM
Day 3	0.013 ±1.94
Day 7	0.011 ±0.18
Day 15	0.005 ±1.51
Day 25	0.002 ±1.83
Day 35	0.002 ±1.63

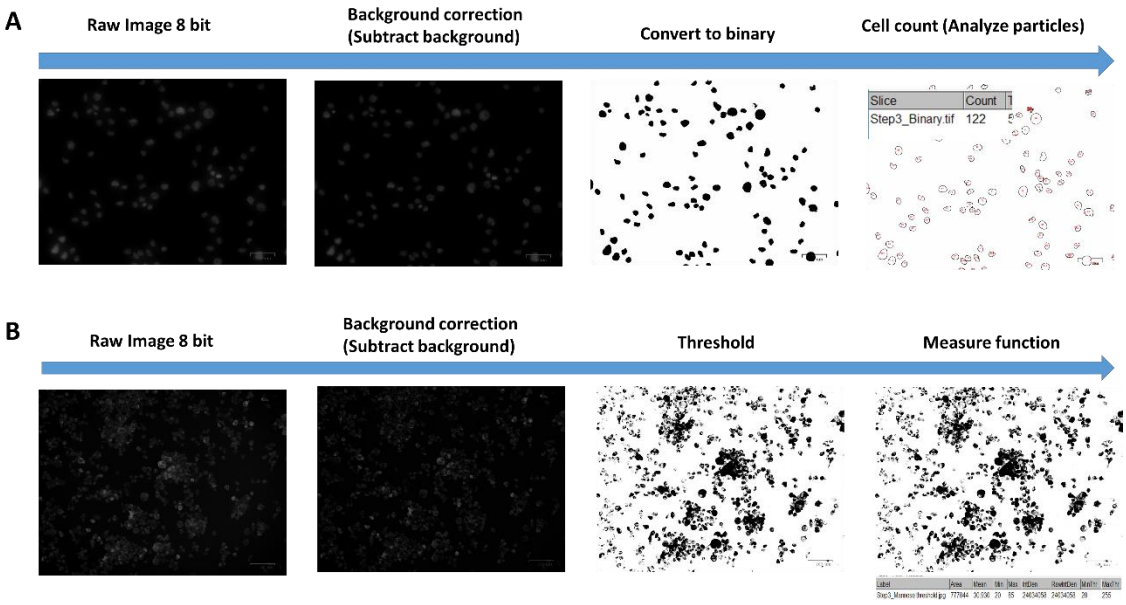


Figure 7-8: Image analysis by imageJ. (A) Schematic analysis of cell count. (B) Schematic procedure of measuring mean fluorescent intensity.

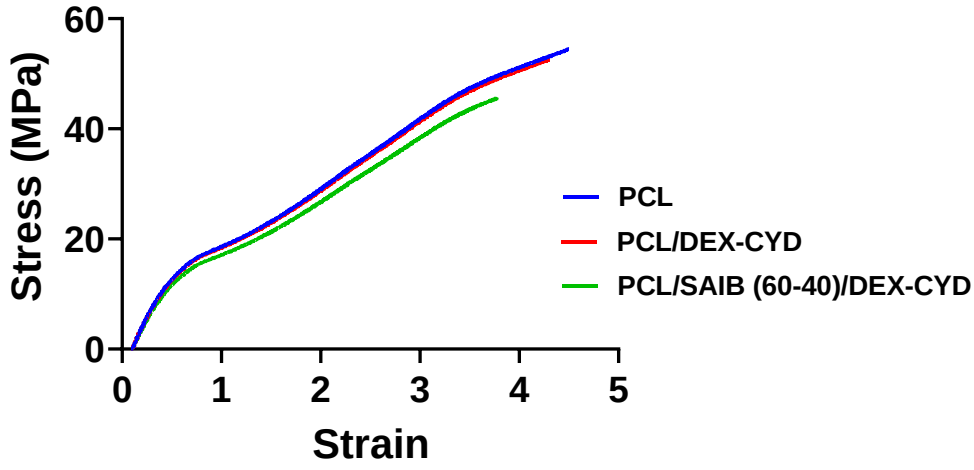


Figure 7-9: The representative stress-strain curves were measured by a Universal Texture Analyser (TA-HD Plus, Stable Microsystems, USA) with a 5 kg load cell. The steadily increasing strain was applied to a 10x10x0.5 mm3 cubic scaffold in the z-direction with a speed of 0.5 mm/s to the strain of 0.5, while the force exerted during compression was measured.